



Universidad
de Alcalá

Facultad de Biología, Ciencias Ambientales y Química

Departamento de Química Analítica,

Química Física e Ingeniería Química

**Graphene-based nanomaterials innovative
tools in electrochemical and microfluidic
(bio-)-sensing and in micromotors design**

Tesis Doctoral

Aída Martín Galán

Alcalá de Henares, Febrero 2016

ALBERTO ESCARPA MIGUEL, Profesor Titular de Química Analítica del Departamento de Química Analítica, Química Física e Ingeniería Química de la Universidad de Alcalá,

CERTIFICA:

Que el trabajo descrito en la presente memoria, titulado **“GRAPHENE-BASED NANOMATERIALS INNOVATIVE TOOLS IN ELECTROCHEMICAL AND MICROFLUIDIC (BIO-)-SENSING AND IN MICROMOTORS DESIGN”**, ha sido realizado bajo su dirección por Dña. Aída Martín Galán en el Área de Química Analítica del Departamento de Química Analítica, Química Física e Ingeniería Química de esta Universidad excepto el trabajo descrito en el Capítulo IV que ha sido llevado a cabo en el Departamento de Nanoingeniería de la Universidad de California, San Diego (UCSD) (EEUU). Asimismo, autoriza su presentación para que sea defendido como Tesis Doctoral.

Y para que conste y surta los efectos oportunos, firma el presente en Alcalá de Henares a 15 de Diciembre de 2015.

ALBERTO ESCARPA MIGUEL, Profesor Titular de Química Analítica y Director del Departamento de Química Analítica, Química Física e Ingeniería Química de la Universidad de Alcalá,

CERTIFICA:

Que el trabajo descrito en la presente memoria, titulado “**GRAPHENE-BASED NANOMATERIALS INNOVATIVE TOOLS IN ELECTROCHEMICAL AND MICROFLUIDIC (BIO-)SENSING AND IN MICROMOTORS DESIGN**”, ha sido realizado en este departamento por Dña. Aída Martín Galán bajo la dirección del Dr. Alberto Escarpa Miguel, Profesor Titular de dicho departamento. El trabajo experimental recogido en el Capítulo IV ha sido llevado a cabo en el Departamento de Nanoingeniería de la Universidad de California, San Diego (UCSD) (EEUU).

Y para que conste y surta los efectos oportunos, firma el presente en Alcalá de Henares a 15 de Diciembre de 2015.

Agradecimientos

Durante estos años de tesis, son muchas las personas y también las instituciones (Universidad de Alcalá (UAH) y Universidad de California San Diego (UCSD), así como al Ministerio de Educación Ciencia y Deportes por su beca FPU y al Banco Santander por su Beca Fórmula Santander) a las que me gustaría incluir en estos agradecimientos por toda la ayuda prestada durante este tiempo.

En primer lugar a uno de los artífices de que haya realizado este doctorado, mi director de tesis, Alberto Escarpa. Desde el momento en el que te conocí, aún tenía 18 años, encontré en ti una gran pasión por la ciencia, y en particular, por la química que nos enseñabas durante tus clases. Me gustaría agradecerte que me hayas enseñado, durante todos estos años y hasta el último día, a pensar por mí misma y me hayas dejado desarrollar mis propias ideas, a ser rigurosa y a buscar el máximo de mí misma. Y especialmente, gracias Alberto por compartir conmigo tu singular perspectiva del arte, la cultura y la ciencia.

Me gustaría muy especialmente expresar mi agradecimiento a la Profesora Cristina González. Tú fuiste, no sólo responsable de que entrara en este grupo de investigación, sino aún más importante, una buena amiga con quien he podido hablar y aprender de ciencia y de la vida. Gracias por tu ayuda, tus conversaciones y por todos los consejos que me has ido dando durante este tiempo, nunca los olvidaré.

Mi agradecimiento también al Profesor Miguel Ángel Gil, por traer al laboratorio un punto de vista no tan químico.

De forma especial y con mucho cariño me gustaría agradecer al Profesor Joseph Wang de la Universidad de California San Diego, toda su ayuda, su apoyo constante y sus enseñanzas. Gracias por hacerme ver que no hay excusas para conseguir tus sueños. Sinceramente, le agradezco la oportunidad que me ha dado de vivir mi sueño americano y sobre todo el hacerme sentir una parte importante de su grupo de investigación, permitiéndome aprender y sumergirme cada día en la ciencia de los micromotores. Gracias Profesor Wang por su continua motivación, incluso después de mi regreso a España.

To my Dear mentor Professor Joseph Wang, I want to thank you for teaching me that there are no excuses to follow your dreams. As a person, it depends on us to work hard and reach our dreams and take advantage of the opportunities that life gives to you. I was excited to learn everyday in your high class scientific lab and discover a perfect team-machine.

Thank you for seeing something in me, for the opportunity you gave me to stay longer and let me feel an important part of your team. For your continuous motivation even after I left your lab, for let me believe in the “Fantastic voyage” and in the “American dream!”

Y, por supuesto, mis agradecimientos a todo el grupo del Profesor Wang en especial a la *Motors’ Famiglia*. Berta fuiste mi soporte, mi compañera, mi gran amiga, gracias por cuidar siempre de mí y por enseñarme todo lo que sabías de ciencia. A Fernando gracias por tu apoyo, por enseñarme los entresijos del ultrasonidos y por compartir y romper mis esquemas con tus ideas filosóficas en la nanociencia... A todos los amigos que dejé en ese laboratorio, Stephano, Julian, Zhigui (gracias por compartir tu cultura y sabiduría conmigo), Miguel, Christian, Gerson, Daniela, Jahir, Kevin, Víctor, Deni, Denise, Caleb, Kyle, mis queridas Eva y Jinxin, y al resto de compañeros, Virendra, Jinxing, Tailon, Murat, Beatriz, Melek, Tailin, Amay, Jayoung, Jung-Min... Gracias a todos por todo el tiempo que compartimos, todo lo que me enseñasteis y por vuestro apoyo. Al Doctor Stuart del grupo del Profesor Esener por enseñarme la ingeniería detrás de los equipos de ultrasonido y por sus ánimos para continuar trabajando y disfrutando de San Diego.

I also want to thank all my colleges and friends in the group of Professor Wang, specially my Motors’ Famiglia. Berta, you were my great support, my college, my friend and you look after me since I arrived to San Diego and teach me all your knowledge about science. To Fernando, thank you for your support, you taught me all about ultrasound and above all thanks for sharing with me your thoughts about the true philosophy behind the nanoscience... To my dear friends, Stephano, Julian, Zhigui (thank you for sharing your culture and knowledge), Miguel, Christian, Gerson, Daniela, Jahir, Kevin, Víctor, Deni, Denise, Caleb, Kyle, my dear Eva and Jinxin and much more colleges Virendra, Jinxing, Tailon, Murat, Beatriz, Melek, Tailin, Amay, Jayoung, Jung-Min ... Thank you all for your help, encouragement and the great time we shared. To Dr Stuart from Professor Esener group for let me the opportunity to learn with him the engineering behind the ultrasound equipments and for his support to continue the good research and enjoying in San Diego.

Me gustaría agradecer igualmente tanto a María Teresa como a Javier del Instituto de Carboquímica de Zaragoza, por permitirme conocer un poco más la química orgánica del grafeno y por todo lo que fui aprendiendo tras nuestra fructífera colaboración. A Luis Vázquez por enseñarme, con mucha paciencia, el arte de buscar las láminas de grafeno con el microscopio de fuerza atómica.

Quería también agradecer al Profesor Álvaro Colina y a todo su grupo de la Universidad de Burgos, por compartir sus conocimientos y enseñarme sobre la química y la electroquímica, tanto cuando tuve la oportunidad de ir a su universidad, como todas aquellas veces que hemos coincidido, en congresos o incluso celebrando la Eurocopa juntos.

No puede faltar en estos agradecimientos el grupo de gente que ha compartido tantas horas de laboratorio conmigo. Si digo el mejor grupo igual alguien se enfada, así que diré mis *Nanochicos* que durante las 10-12 horas que hemos pasado cada día en el lab y fuera del lab han creado esos momentos imborrables, generado risas, secado llantos y animado los bajones. Miguel, de ti aprendí casi todo, el laboratorio era para ti, como la central *Nuclear* para el señor Burns, conocías todo y me enseñaste eso y más, incluso desde América cuando hablábamos por Skype y seguía preguntándote cosas. Miri, es tan difícil describir cómo puedo agradecer lo mucho que siempre me ayudaste, gracias por tus ánimos, por tu paciencia escuchándome mis largas conversaciones sobre el grafeno. Fui madurando científicamente poco a poco gracias a ti. Pilar, no tengo ni palabras, grandísima amiga, mucha ciencia juntas y además salvaste mi ojo bueno. *Moltes gràcies* por tu ánimo constante, tus continuos consejos y por mostrarme el verdadero camino de la ciencia, la perseverancia. Adrián, éramos los más pequeños del grupo pero tu ingenio, tus manos y tus ganas nos animaban a todos. Gracias por ayudarme siempre y por las gafas-lupa para hacer los electrodos. Ojalá podamos coincidir trabajando mano a mano de nuevo, ha sido genial que estuvieras a mi lado. También agradecer a toda la gente que ha pasado por el lab: Diana, gracias por enseñarme tu *chipi*, Laurita, la vida es difícil pero menos con personas como tú al lado, Flavio, *grazie mille*, Patri, por guardar el secreto del grafeno ;) Fede, MariMore por vuestros constantes ánimos. Y a toda la gente que he conocido en la uni estos años, por esas comidas tan animadas: Pati, Jochen, Romy (por las cervecitas el viernes por la tarde), María Castro, Raquel (por las tardes de conversación), Vir, Clara, Cris, Elena, Estefanía, Jesús, Laura, Miguel; y mis compis del Forensic lab: Charlie (por tus sonrisas y ánimos), André (por tus clases de baile), Valentina, María, Matías, Ignacio, Felix, Sofía, Jorge...y todos aquellos que me dejé en el tintero.

Y por supuesto a mis amigos. A María, muchas gracias por animarme siempre y por comprenderme, siempre has sido mi gran apoyo fuera del doctorado. A Jorge, por escucharme mis tonterías de ciencia e intentar aprender de grafeno y sobre todo por tus clases sobre motores, gracias amigo. A Lucía, por tus ánimos y tus muchos abrazos durante los momentos de bajón. Y a Kumiko Hayazaki y a su familia, mi hermanita de aventuras en San Diego y la que cada día me

Agradecimientos

escuchaba mis malos y buenos momentos del laboratorio y del no laboratorio, *Arigatau*, sin ti la experiencia en América no hubiera sido tan buena, gracias pequeña. *To my beloved japanese family*.

Gracias Sergio por toda tu ayuda, y por aconsejarme siempre a creer en mis ideas. Muchas gracias por todo, nunca olvidaré que siempre me entendiste y apoyaste durante el doctorado sobre todo en aquellos momentos donde las muchas horas de trabajo y la falta de resultados hacen este trabajo aún más difícil, muchas gracias por todo.

Toda mi familia ha pasado toda esta tesis a unos cientos o miles de kilómetros, pero siempre he sentido la proximidad de su afecto y su apoyo, muchísimas gracias. (Skype ha hecho que esa distancia fuera más corta).

Gracias papá por enseñarme desde pequeña los pasos para ser constante en el trabajo y a tener las ganas de afrontar cada reto cada día, sin tus ganas por hacer que cada día fuera más trabajadora nunca podría haber afrontado caminos como esta tesis. A mi madre, por enviarme cada día un poco de su continua paciencia. A mi hermano, por enseñarme que la vida pasa, y que tienes que disfrutar todas las experiencias que pasan por tu lado. A mi abuela por su apoyo, aunque le sea difícil entender lo que hago, tu compañía me relajaba muchísimos fines de semana tras el estrés de pasar tantas horas en el laboratorio. Muchas gracias a los cuatro por aguantarme con mis presiones, ánimos y desánimos, especialmente a ti papá...

Finalmente, quiero recordar a mi abuelo. Tus historias, que tanto disfruté siempre estarán conmigo, estés donde estés, gracias por tus ánimos. América vio las lágrimas por tu pérdida, pero siempre estarás conmigo.

A mi abuelo y a mi familia

Inicio del viaje...

Al caer el electrón cargado

Internamente en el material enmarañado,

De carbono, tela de grafeno,

Alcanzará el analito al ciclohexeno.

Muestras estudiadas

Analitos separados.

Resuelven los materiales

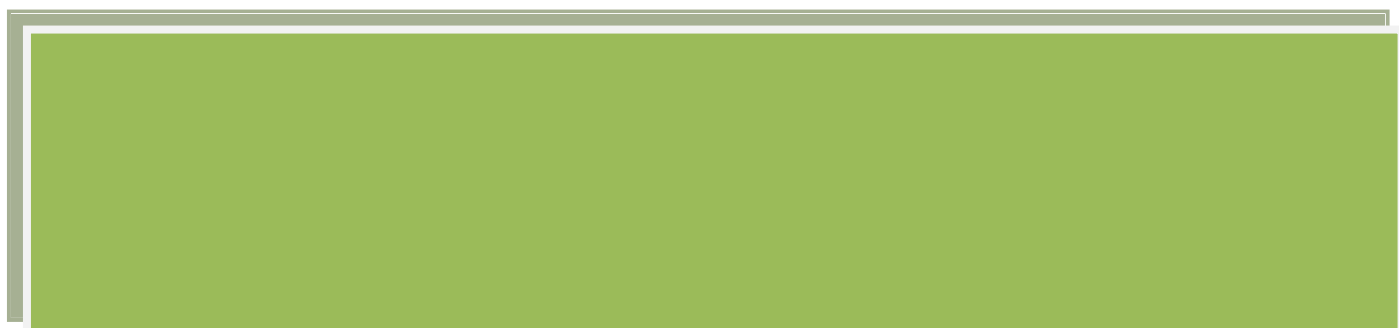
Todos ellos incrustados,

Inhomogéneos sobre un electrodo,

Nanoméricamente modificado.

A Fantastic voyage from the electrons jumping in the network of graphene to the motion of graphene motors

Summary



Graphene is an atomically thin sheet of sp^2 bonded carbon atoms forming a two dimensional (2-D) lattice. This structure provides this material its extraordinary properties such as high surface area, high electrical and thermal conductivities, optical transparence, high mechanical strength and high elasticity. These unique features of graphene plus the versatility to be synthesized with different oxygen functionalities and defects justify its exploration in different (electro-)-analytical applications.

Specifically, these 2-D structures are very valuable tools for electrochemical sensing. They offer high currents because of their large surface area, enabling fast redox conversion, enhancing the analytical sensitivity and the resistance to the passivation. Likewise, in many cases, they allow a decrease in the redox potentials due to the high presence of active sites that would improve the overall selectivity of the analysis.

Besides, the actual trend in Analytical Chemistry of developing new miniaturized and portable analytical devices capable of generating a fast response, reducing sample and reagents consumption or improving portability of the instrumentation with a low cost, became a starting point for the inclusion of nanomaterials such as graphene with the compatible screen-printed and microfluidic technologies for advanced sensing and biosensing. In addition, the electrochemical detection coupled to microfluidic systems is a valuable detection principle due to its inherent miniaturization, and high compatibility with micro- and nanotechnologies. In this sense, the integration of graphene and other nanomaterials is a very pertinent combination because of the low sensitivity that microfluidic platforms often present.

Recently, micromotors –devices that convert energy into movement– have comprised a new technological leap in science for the development of autonomous machines that could carry out a particular task. The structure,

shape and size as well as the materials constituting these micromotors are essential for an excellent propulsion and creative application. Graphene appears in this scene as a very convenient material to be part of these novel devices because of the versatility in its chemical functionalization and its outstanding physical properties such as its high mechanical strength, flexibility or elasticity, as it was previously commented.

Therefore, all the features derived from the graphene and related nanomaterials stated above convert these materials in unique and innovative tools to incorporate in the current analytical nanoscience and nanotechnology. As a consequence, the exploration and evaluation of graphene-based materials for enhancing the analytical performance of the previously identified vanguard analytical tools –electrochemical (bio)-sensors, electrochemical microfluidics and micromotors– has constituted the main motivation of this Doctoral Thesis.

To this end, this Doctoral Thesis has three defined objectives.

1. Design, characterization and development of novel electrochemical graphene-based electrochemical (bio)-sensors.
2. Design, characterization and development of novel graphene-based electrochemical detectors in microfluidic chips.
3. Design, characterization and development of novel chemically and ultrasound-powered graphene-based micromotors.

Accordingly to the previous objectives, the main milestones identified in this Thesis have been:

1.1. Analytical characterization and electrochemical evaluation of chemically synthesized graphene nanoribbons with different oxygen content using microscopy, spectroscopic and electrochemical techniques.

1.2. Design and development of graphene-based chemical sensors for fast and reliable detection of target molecules of clinical relevance (ascorbic acid, levodopa, L-tyrosine and uric acid) and its application for monitoring uric acid in urine samples.

1.3. Design and development of a novel biosensing strategy for fast and reliable detection of target D-amino acids with clinical significance (D-tyrosine in *Bacillus subtilis* and D-methionine in *Vibrio cholerae*) and its application for its monitorization in urine samples using screen-printed graphene-based electrodes.

2.1. Design and development of a novel electrochemical microfluidic biosensing strategy for fast and reliable detection of target D-amino acids (D-methionine and D-leucine) with clinical significance in *Vibrio cholerae* using screen-printed graphene-based electrodes.

2.2. Design, fabrication and characterization of exclusive carbon nanomaterial transducers (reduced graphene oxide (rGO), single-walled carbon nanotubes (SWCNTs) and multi-walled carbon nanotubes (MWCNTs)) based on teflon filter electrodes for electrochemical and microfluidic sensing.

2.3. Development of a microfluidic chip coupled to exclusive multi-walled carbon nanotube transducers for the determination of quality phenolic markers (tyrosol, hydroxytyrosol and oleuropein) in olive oils.

3.1. Optimization of the template-assisted electrosynthesis of graphene/platinum and graphene/gold micromotors using double conical polycarbonate membranes as templates.

3.2. Analytical characterization of the graphene micromotors using optical and electron microscopy techniques.

3.3. Study of the propulsion mechanisms (chemically and ultrasound powered) in the graphene/platinum and graphene/gold micromotors, respectively.

According to these objectives, the results of this Doctoral Thesis have been divided into **chapters II, III** and **IV**.

In a first stage, synthesis, characterization and applications of graphene in the development of new electrochemical sensors and innovative biosensing strategies using screen-printed technology have been studied. (**Chapter II** *Graphene nanoribbons for electrochemical (bio-)-sensing*).

Firstly, the *state of the art* of graphene materials in (bio)-sensing have been revised (**Chapter II.1.** *Graphene for electrochemical (bio-)-sensing*).

Then, the synthesis and characterization of two graphene nanoribbons with different oxygen content was carried out. Graphene oxide nanoribbons (GNRox) obtained from multi-walled carbon nanotubes (MWCNTs) and reduced graphene nanoribbons (GNRred) obtained from the chemical reduction of GNRox. GNRs were characterized by atomic force microscopy (AFM), transmission electron microscopy (TEM), X-ray photoelectron spectroscopy (XPS), infrared (IR), Raman spectroscopy, X-ray diffraction (XRD), and electrochemical techniques (cyclic voltammetry (CV), chronocoulometry, differential pulse voltammetry (DPV)). From all these techniques, the following data are summarized for GNRox (44 wt.% oxygen

content, 0.8 nm layer height, 19% Csp³, 2% Csp²) and for GNRred (14 wt. % oxygen content, 1.2 nm layer height, 47% Csp², 10% Csp³).

Afterwards, the electrochemical behavior on GNRox and GNRred for a set of analytically significant target molecules with different chemical structures was evaluated using DPV, including hydroquinone, catechol, resorcinol, levodopa, L-tyrosine, uric acid and ascorbic acid. The results showed that GNRs provided significantly better electrochemical responses compared to the controls MWCNTs (the carbon source) and the non-modified glassy carbon electrode. GNRox resulted to be the material of choice for sensing molecules with high oxidation potentials, and GNRred, on the other hand, yielded an excellent sensitivity for aromatic molecules in which π - π interactions were dominant or the number of conjugated 1,2-diols presented was high.

Then, the advantages of these materials were explored for the fabrication of disposable electrochemical sensors on carbon screen-printed (CSPE) platforms for the sensing of ascorbic acid, levodopa and uric acid. GNRred exhibited electrocatalysis towards ascorbic acid, levodopa and uric acid allowing a fast (100 s), selective, and accurate determination with quantitative recoveries (97 - 101%) of these analytes in urine samples. (**Chapter II.2. Graphene nanoribbons for electrochemical sensing**).

GNRox on disposable CSPEs were used for a straightforward *in-situ* measurement of L and D-amino acids, taking advantage of the electroactivity of certain clinically relevant amino acids such as tyrosine and methionine involved in important bacterial diseases such as, *Bacillus subtilis* and *Vibrio cholerae*, respectively. (**Chapter II.3. Graphene nanoribbons for electrochemical biosensing**). The strategy is based on a dual electrochemical and enzymatic approach, in which the H₂O₂ generated from the reaction of the D-amino acids with the class enzyme D amino acid

oxidase (DAAO) and the L-amino acids, which is an electroactive molecule, are simultaneously detected by DPV. On GNRox disposable platforms using 50 μL of sample and 360 s the simultaneous detection, calibration and quantitative analysis of both L and D enantiomers was carried out in urine samples.

In a second stage, the design and fabrication of novel electrodes based on carbon nanomaterials and their application in electrochemical microfluidics have been developed (**Chapter III. Graphene for electrochemical microfluidic (bio-)-sensing**).

Firstly, the *state of the art* of the coupling between carbon nanomaterials and electrochemical microfluidics was reviewed. (**Chapter III.1. Carbon nanomaterials for electrochemical microfluidic (bio-)-sensing: state of the art**). On the one hand, a novel strategy using an electrochemical microfluidic strategy with commercial CSPEs modified with GNRred was presented for the separation and enantiomeric detection of D-methionine and D-leucine. (**Chapter III.2. Graphene-based materials in electrochemical microfluidic biosensing**). These D-amino acids act as biomarkers involved in relevant diseases caused by *Vibrio cholerae*. The proposed electrokinetic strategy allowed the controlled microfluidic separation of the D-amino acids and the specific reaction *on-column* between DAAO and each D-amino acid as well as the electrochemical detection of hydrogen peroxide yielded from each reaction. This novel strategy offers interesting advantages because it avoids the use of additives for enantiomeric separation or any covalent immobilization of the enzyme into the wall channels or on the electrode surface such as in the biosensor-based approaches. Likewise, graphene-based electrodes *end-channel* coupled to the microfluidic system allowed to improve the electrochemical detection of the D-amino acids showing the analytical potential of graphene material.

On the other hand, new tailor-designed carbon nanomaterial-based electrodes have been proposed (**Chapter III.3. *Novel carbon nanomaterial-based electrodes for electrochemical microfluidic sensing***). These teflon filtered electrodes (TFEs) based on single-walled, multi-walled carbon nanotubes and graphene have been designed using two designs: a three-electrode configuration for electrochemical sensing and a line-electrode configuration for electrochemical microfluidics.

The characterization of these carbon nanomaterial-based electrochemical transducers by field-emission scanning electron microscopy (FE-SEM), current sensing AFM and electrochemical impedance spectroscopy revealed the porosity of the electrodic surface, the final disposition of the nanomaterials on the filter and confirmed that the nanomaterial is the exclusive transducer of the electrical signal. The coupling of these TFEs as electrochemical detectors with microfluidic chips demonstrated to be suitable in the determination of three quality phenolic markers, tyrosol, hydroxytyrosol and oleuropein in olive oil samples in less than 300 s with good accuracy and precision.

Finally, in this Doctoral Thesis, the design, characterization and development of new graphene-based micromotors chemically and ultrasound powered have been described. (**Chapter IV. *Graphene-based micromotors: electrosynthesis, characterization and applications***).

Firstly, micromotors as analytical tools and their propulsion mechanisms have been introduced (**Chapter IV.1. *Micromotors: state of the art***). Afterwards, the optimization of the electrosynthesis of graphene/metal micromotors by the direct electrodeposition of graphene oxide within the conical pores of a polycarbonate template membrane followed by deposition of the inner metal layer has been discussed (**Chapter IV.2. *Chemically powered graphene micromotors***). The presence of high number of edges and

defects in the graphene layer results in highly reactive microporous platinum or gold catalytic structures. The high catalytic activity of Pt, in the desproportion of H_2O_2 as chemical fuel, leads to an ultrafast bubble propulsion of the micromotor (with speed as high as $1700 \mu\text{m}/\text{sec}$) and operation at extremely low levels (0.1 %) of the peroxide fuel.

Furthermore, new graphene/gold micromotors, loaded in a gel matrix stabilizer with perfluorocarbon (PFC) emulsions and silica particles or nanobullets, have reached speeds in the meters per second scale. (**Chapter IV.3. *Ultrasound powered graphene micromotors***). The propulsion mechanism relies in the vaporization of the PFC emulsions contained in the micromotor after the application of ultrasound pulses, allowing the firing and ejection of the nanobullets.

Finally, considering the unifying thread of this Doctoral Thesis relying on the exploration of the graphene properties as a new tool in the electrochemical (microfluidic) (bio-)-sensing as well as in the design and development of cutting-edge micromotors as new analytical tools; the general conclusions of this Thesis have been divided into three bullet points considering the three main chapters.

1. Graphene nanoribbons (oxide and chemically reduced), obtained after opening carbon nanotubes by chemical oxidation have demonstrated that (i) they are suitable nanomaterials because of the rich edge chemistry compared to pristine graphene (ideal graphene) and (ii) there are nanoribbons with a more suitable functionalization than others for electrochemical detection, depending on the chemical structure of the target molecule. This later fact paves the way to the tailored-designed graphenes for improving the analytical detection according to the chemical structure of the target molecule.

Indeed, the reactivity (abundance in defects and C_{sp^2}/C_{sp^3} ratio) and the inherent properties of graphene nanoribbons (high surface area and excellent electrical conductivity), have demonstrated to play an important role in the design and development of electrochemical (bio-)-sensing strategies with enhanced analytical features in terms of selectivity, sensibility and reproducibility.

All in sum, the research and examination of the synergies between the analytical performance found for the graphene nanoribbons and those inherent to the screen-printed technologies have permitted to develop fast response, disposable and portable analytical innovative tools, which require low sample volumes and reagent consumption. Indeed, these graphene nanoribbons have been successfully employed in the development of electrochemical sensors (reduced graphene nanoribbons) and in the development of biosensing strategies (graphene oxide nanoribbons) for the detection of clinical and relevant markers in illnesses such as uric acid and D-amino acids, respectively.

2. The features derived from graphene have been creatively explored with the inherent advantages of microfluidic systems (fast analysis with low sample and reagent consumption, portability and flow control in the microscale), because of their compatibility between the micro and nano scales as well as in between the micro and nanotechnologies.

Certainly, graphene (chemically reduced graphene) has demonstrated to be an excellent nanomaterial for the development of electrochemical transducers coupled to microfluidic systems. In the framework of the electrochemical detection coupled to microfluidic systems, it has exhibited remarkable electrocatalysis, enhanced sensitivity and high reproducibility due to its also high surface area and conductivity. So, these evidences confer

to graphene an extra value in electrochemical microfluidics because of the low sensitivities usually presented by these platforms.

All these reasons have permitted, on the one hand, the development of innovative biosensing applications –using thin film approaches on conductive surfaces in the fabrication of electrochemical detectors– for the enantiomeric resolution and selective detection of D-amino acids with clinical relevancy in important illnesses such as *Vibrio Cholerea*.

On the other hand, in order to explore the mentioned electrocatalytic properties of graphene, new electrochemical detectors based on exclusive nanomaterials such as graphene and also extended to carbon nanotubes, have been designed, characterized and developed. The simple filtration of the nanomaterial and its disposition on flexible and non-conductive wafers has permitted the development of new nanomaterial-exclusive transducers for electrochemical microfluidics, which has been the starting point in the development of important applications in the agro-food sector such as the fast and reliable detection of phenolic markers in olive oil.

3. The exceptional contribution of graphene (graphene oxide and electrochemically reduced graphene oxide) in the design and development of catalytic micromotors, which have been electrosynthesized on the pores of a polycarbonate membrane, has been demonstrated. Clearly, the high surface area of graphene, suitably functionalized, could improve from the chemical reaction responsible for the propulsion of the micromotor to the interaction with target molecules with analytical (bio-)-sensing purposes.

The found results have underlined graphene to be the responsible for the improved propulsion in micromotors yielding fast and efficient micromotors with propulsion mechanisms relying on the generation of bubbles from a chemical reaction and assisted by acoustic energies. These finds foresees a

promising future in the development of movable sensors capable of *in situ* perform analytical tasks, swimming in small sample volumes without the use of external fluid forces.

In sum, the general conclusion of this Doctoral Thesis is that graphene –in all its different chemical forms and variants- has demonstrated to be an extraordinary material in the design and development of analytical forefront tools such as (bio-)-sensors and microfluidic electrochemical systems and in other new generation of cutting-edge tools such as micromotors in the present framework of analytical nanoscience and nanotechnology.

Resumen



El grafeno es una lámina de átomos de carbono de un átomo de espesor unidos con hibridación sp^2 . Esta estructura proporciona al material unas propiedades extraordinarias como son una elevada superficie específica, una alta conductividad eléctrica y térmica, transparencia óptica, una elevada resistencia mecánica y una extraordinaria elasticidad. Estas propiedades junto a la versatilidad del grafeno para ser sintetizado con distinta química de defectos, que permite llevar a cabo adecuadas funcionalizaciones, justifican su exploración para distintas aplicaciones (electro-)-analíticas.

Por una parte, estas estructuras 2-D son herramientas muy valiosas para el sensado electroquímico. En efecto, y debido a esta elevada superficie específica, el grafeno ofrece no sólo una rápida conversión redox que se traduce en altas intensidades de corrientes y, por ello, en un aumento de la sensibilidad analítica, sino también una disminución de la pasivación de la superficie que conlleva una mejora de la precisión del análisis. Asimismo, estas propiedades superficiales permiten una disminución de los potenciales redox pudiendo mejorar la selectividad de la detección.

Por otra parte, una de las tendencias de la Química Analítica es el desarrollo de sistemas analíticos miniaturizados y portables de respuesta rápida con bajo consumo de muestra y de reactivos. Este tipo de sistemas analíticos de nueva generación como son los sensores y bio-sensores electroquímicos así como los sistemas microfluídicos constituyen plataformas muy adecuadas donde la inclusión de nanomateriales tales como grafeno es altamente pertinente debido a que se esperan prestaciones analíticas muy mejoradas. Asimismo, la detección electroquímica acoplada a los microchips analíticos, como ejemplo revelador de sistemas microfluídicos, es una valiosa herramienta debido a su miniaturización inherente y a su elevada sensibilidad así como su alta compatibilidad con las micro y nanotecnologías. En este sentido, la incorporación del grafeno y otros

nanomateriales constituye una aproximación analítica conveniente debido a la baja sensibilidad que muchas veces presentan los sistemas microfluídicos.

Por su parte, recientemente, los micromotores –dispositivos que transforman la energía en movimiento– han constituido un paso tecnológico muy importante en el desarrollo de nuevas máquinas químicas capaces de llevar a cabo operaciones analíticas aprovechando su movimiento autónomo debido a la generación de burbujas a través de reacciones químicas o por aplicación de pulsos de ultrasonidos (entre otros mecanismos). Resulta preciso destacar que la estructura, forma, tamaño y, particularmente, los materiales que constituyen estos micromotores juegan un papel esencial para conseguir una propulsión óptima y el desarrollo de aplicaciones novedosas dentro del ámbito del biosensado. En este sentido, el grafeno se constituye como un material muy adecuado para formar parte de estas nuevas máquinas moleculares debido a su versatilidad en su funcionalización química y a sus extraordinarias propiedades físicas como alta conductividad, resistencia mecánica, flexibilidad o elasticidad, tal y como se ha comentado precedentemente.

Todas estas características derivadas del grafeno convierten a este nanomaterial de carbono en una herramienta innovadora dentro del ámbito de la nanociencia y nanotecnología analíticas. De esta manera, la exploración y evaluación de los materiales basados en grafeno para la mejora de las características analíticas en las herramientas analíticas de vanguardia previamente identificadas como son los (bio-)sensores electroquímicos, la microfluídica electroquímica y los micromotores, ha constituido la principal motivación de esta Tesis Doctoral.

Dentro de este contexto químico-analítico, esta Tesis Doctoral presenta tres objetivos claramente definidos.

1. Diseño, caracterización y desarrollo de nuevos (bio-)sensores electroquímicos basados en grafeno.
2. Diseño, caracterización y desarrollo de nuevos detectores electroquímicos basados en grafeno para su acoplamiento en microchips analíticos.
3. Diseño, caracterización y desarrollo de nuevos micromotores basados en grafeno con mecanismo de autopropulsión química o ultrasónica.

De acuerdo con dichos objetivos, los principales hitos identificados en esta Tesis Doctoral han sido:

- 1.1. Caracterización analítica y evaluación electroquímica de nanocintas de grafeno sintetizadas químicamente con distinto grado de oxidación empleando técnicas de microscopía electrónica, técnicas espectroscópicas y técnicas electroquímicas.
- 1.2. Diseño y desarrollo de sensores químicos basados en grafeno para la detección rápida y fiable de moléculas objetivo de relevancia clínica (ácido ascórbico, levodopa, L-tirosina y ácido úrico) y su aplicación para la monitorización de ácido úrico en muestras de orina.
- 1.3. Diseño y desarrollo de una nueva estrategia biosensora para la detección rápida y fiable de D-amino ácidos con relevancia clínica (D-tirosina en *Bacillus subtilis* y D-metionina en *Vibrio cholera*) y su aplicación para su monitorización en muestras de orina usando electrodos serigrafiados basados en grafeno.

2.1. Diseño y desarrollo de una nueva estrategia biosensora para la detección rápida y fiable de D-amino ácidos con relevancia clínica en *Vibrio cholerae* (D-metionina y D-leucina) utilizando microchips analíticos acoplados con electrodos basados en grafeno.

2.2. Diseño, fabricación y caracterización de transductores exclusivos basados en grafeno reducido (rGO), nanotubos de carbono de pared sencilla (SWCNTs) y nanotubos de carbono de pared múltiple (MWCNTs) para sensado electroquímico y microfluídico.

2.3. Desarrollo de microchips analíticos acoplados a transductores constituidos exclusivamente por MWCNTs para la determinación de compuestos fenólicos (tiroso, hidroxitiroso y oleuropeína) como marcadores de calidad en aceite de oliva.

3.1. Optimización de la electrosíntesis de micromotores basados en grafeno/platino y grafeno/oro usando membranas de policarbonato de doble cono como molde.

3.2. Caracterización analítica de los micromotores basados en grafeno utilizando microscopía óptica y electrónica.

3.3. Estudio de los mecanismos de propulsión (química y por ultrasonidos) en los micromotores basados en grafeno/platino y grafeno/oro.

A continuación, se expondrán brevemente los resultados más relevantes obtenidos durante el desarrollo de esta Tesis Doctoral.

En una primera etapa, se estudió la síntesis, caracterización y aplicaciones del grafeno en el desarrollo de nuevos sensores electroquímicos y de estrategias innovadoras de biosensado, empleando tecnología serigrafada.

(Capítulo II. Nanocintas de grafeno para el (bio)-sensado electroquímico).

En primer lugar, se han revisado los antecedentes bibliográficos relacionados con el grafeno en el ámbito de detección electroquímica **(Capítulo II.1. Grafeno en el (bio)-sensado electroquímico: state of the art)**. A continuación, se ha llevado a cabo la caracterización completa de las nanocintas de grafeno y su aplicación para el desarrollo de nuevas estrategias electroquímicas sensoricas y biosensoricas. Se han sintetizado y caracterizado nanocintas de grafeno con distinto contenido en oxígeno: nanocintas de grafeno oxidado (GNRox) obtenidas a partir de MWCNTs y nanocintas de grafeno reducidas (GNRred) obtenidas a partir de la reducción química de GNRox. Ambas nanocintas de grafeno fueron caracterizadas utilizando microscopía de fuerza atómica (AFM), microscopía de transmisión electrónica (TEM), espectroscopía de fotoelectrones emitidos por rayos X (XPS), espectroscopía de infrarrojo (IR), espectroscopía Raman, difracción de rayos X (XRD) y técnicas electroquímicas (voltametría cíclica (CV) y voltametría diferencial de impulsos (DPV)). Estos estudios arrojaron para GNRox un 44% de contenido en oxígeno, 0,8 nm de altura de lámina y un contenido del 19% en Csp³ y de un 2% en Csp² y para GNRred un 14 % de contenido en oxígeno, 1,2 nm de altura de láminas y un contenido del 47% en Csp² y de un 10% en Csp³.

A continuación, se evaluó el comportamiento electroquímico sobre GNRox y GNRred de un conjunto de moléculas relevantes con estructuras químicas

diferentes (hidroquinona, catecol, resorcinol, levodopa, L-tirosina, ácido úrico y ácido ascórbico), empleando DPV. Los resultados obtenidos desvelaron que las nanocintas de grafeno mostraron una respuesta electroquímica significativamente mejorada en comparación con los MWCNTs (material de origen de la nanocintas) y el electrodo de carbono vitrificado sin modificar. Las GNROx resultaron ser el material óptimo para el sensado de moléculas cuya oxidación se produce a elevados potenciales de oxidación y las GNRred ofrecieron mejor sensibilidad en la detección de moléculas aromáticas en las cuáles las interacciones π - π fueron dominantes.

Posteriormente, se exploraron las ventajas de estos nanomateriales para la construcción de plataformas electroquímicas sensoras desechables sobre electrodos de carbono serigrafiados (CSPE) para el sensado de ácido ascórbico, levodopa y ácido úrico en muestras de orina. GNRred exhibió una profunda electrocatálisis para la oxidación de ácido ascórbico, levodopa y ácido úrico permitiendo una detección rápida (100 s), selectiva y con recuperaciones cuantitativas (97-101%). (**Capítulo II.2. Nanocintas de grafeno para el sensado electroquímico**).

Asimismo, se han empleado GNROx como material de grafeno óptimo sobre electrodos desechables de CSPEs para la medida *in-situ* de amino ácidos L y D, aprovechando la electroactividad de ciertos amino ácidos clínicamente relevantes como son la tirosina y la metionina, presentes en enfermedades bacterianas importantes como son *Bacillus subtilis* y *Vibrio cholerae*, respectivamente (**Capítulo II.3. Nanocintas de grafeno para el biosensado electroquímico**). Esta estrategia se basó en la detección simultánea del peróxido de hidrógeno (generado tras la reacción de los D-amino ácidos con la enzima de clase D-amino ácido oxidasa) y de los L-amino ácidos electroactivos. En una plataforma desechable de GNROx empleando sólo 50 μ L de muestra y un tiempo total de análisis de 360 s, se llevó a cabo la detección simultánea de ambos enantiómeros en muestras de orina.

A continuación, en una segunda etapa, se llevó a cabo el diseño y fabricación de nuevos electrodos, exclusivamente constituidos por nanomateriales de carbono, así como el desarrollo de nuevas aplicaciones en el ámbito de la microfluídica electroquímica (**Capítulo III. Grafeno para el (bio)-sensado electroquímico microfluídico**).

En primer lugar se revisaron los antecedentes bibliográficos (**Capítulo III.1. Nanomateriales de carbono para (bio)-sensado electroquímico microfluídico: state of the art**), relacionados con el acoplamiento de los nanomateriales de carbono en microfluídica electroquímica.

Por una parte, se ha propuesto una estrategia novedosa que emplea microchips analíticos acoplados a CSPEs comerciales modificados con GNRred para la separación y detección enantiomérica de D-metionina y D-leucina. (**Capítulo III.2. Materiales basados en grafeno para el biosensado microfluídico electroquímico**). Estos D-amino ácidos actúan como biomarcadores en distintas enfermedades relevantes causadas por la bacteria *Vibrio cholerae*. La estrategia electrocinética propuesta, mediante un control adecuado de los fluidos, permitió la separación microfluídica de los D-amino ácidos, la reacción enzimática específica dentro del microchip (*on-column*) entre la DAAO y cada D-amino ácido así como la detección electroquímica del peróxido de hidrógeno obtenido en cada reacción. Esta estrategia innovadora ofrece ventajas importantes dado que evita el uso de aditivos externos para la separación enantiomérica, así como la inmovilización covalente de la enzima en las paredes de los canales microfluídicos o en la superficie electródica como en otras aproximaciones biosensoras. Asimismo, los electrodos basados en grafeno acoplados al sistema microfluídico permitieron mejorar la detección electroquímica de los D-amino ácidos, revelándose de nuevo el potencial analítico del grafeno.

Por otra parte, se han propuesto nuevos electrodos basados en nanomateriales de carbono como único material conductor sobre sustratos adaptables no conductores. (**Capítulo III.3. Nuevos electrodos basados en nanomateriales de carbono para el sensado microfluídico electroquímico**). Estos electrodos de teflón filtrados con dispersiones de grafeno, así como de SWCNTs y MWCNTs (TFEs) se han diseñado en configuración de tres electrodos para el sensado electroquímico miniaturizado y en configuración de línea para microfluídica electroquímica.

La caracterización de estos electrodos basados en nanomateriales de carbono por microscopía electrónica de barrido de alta emisión (FE-SEM), AFM de sensado de corriente e impedancia electroquímica, revelaron la porosidad de la superficie del electrodo, la disposición final de los nanomateriales en el filtro y confirmaron que el nanomaterial era el único transductor de la señal eléctrica. El acoplamiento de estos TFEs como detectores electroquímicos en microchips analíticos demostró ser muy adecuado en la determinación del tirosol, hidroxitirosol y oleuropeina en aceites de oliva en menos de 300 s con una buena exactitud (recuperaciones cuantitativas) y precisión (RSDs $\leq 4\%$).

En la última etapa de esta Tesis Doctoral, se han diseñado, caracterizado y desarrollado nuevos micromotores basados en grafeno propulsados por reacciones químicas o por pulsos de ultrasonidos. (**Capítulo IV. Micromotores basados en grafeno: electrosíntesis, caracterización y aplicaciones**).

En primer lugar, se ha descrito el concepto de micromotor y los métodos de propulsión más utilizados. (**Capítulo IV.1. Micromotores: state of the art**). A continuación se recogen los resultados obtenidos en la electrosíntesis de nuevos micromotores de grafeno/metal a través de la electrodeposición directa de óxido de grafeno sobre los poros cónicos de una membrana de

policarbonato y posterior electrodeposición de una lámina interna de metal. (**Capítulo IV.2. *Micromotores de grafeno propulsados por reacciones químicas***). La presencia de un elevado número de defectos en este grafeno permitió la formación de estructuras microporosas altamente reactivas de metales catalíticos (platino y oro), depositados sobre grafeno. Esta elevada actividad catalítica del platino, mejorada por la presencia del grafeno, proporcionó una ultra propulsión del micromotor (con velocidades hasta los 1700 $\mu\text{m/s}$) utilizando muy bajos niveles de peróxido de hidrógeno.

Asimismo y dentro de este ámbito, se han diseñado nuevos micromotores de grafeno/oro que alojan en su interior estructuras analíticas (microbolas de sílice o nanoproyectiles) y emulsiones de perfluorocarbono (PFC), exhibiendo velocidades extraordinarias (del orden de m/s). (**Capítulo IV.3. *Micromotores de grafeno propulsados por ultrasonidos***). El mecanismo de propulsión de los mismos, radica en que, tras la exposición de una serie de pulsos ultrasonidos focalizados sobre el micromotor, las emulsiones de PFC se vaporizan dentro del mismo permitiendo la eyección y disparo de los nanoproyectiles. Se ha demostrado también que estas estructuras analíticas incorporados en los micromotores son capaces de penetrar en un tejido gelatinoso, lo que les convierte en futuras herramientas de liberación de moléculas y/o partículas en muestras biológicas.

Por último, a la luz del hilo conductor de esta Tesis Doctoral –exploración de las propiedades del grafeno como nueva herramienta en el (bio-)-sensado (microfluídico) electroquímico y en el diseño y desarrollo de micromotores– y todo ello dentro del marco más actual de la nanociencia y nanotecnología analíticas, se describen con arreglo a los tres capítulos donde se han agrupado y discutido los resultados, las conclusiones generales de esta Tesis Doctoral.

1. Las nanocintas de grafeno (oxidadas y reducidas químicamente), han demostrado ser unos nanomateriales muy adecuados debido a su química rica en defectos en comparación con el grafeno ideal (conceptualmente constituido por una lámina carbonácea perfecta). Asimismo, se han encontrado evidencias de la influencia que ejerce la química de funcionalización en la detección electroquímica de las moléculas diana con arreglo a su estructura química. Este hecho conduce al diseño de nanocintas de grafeno con química de funcionalización dirigida a una detección electroquímica mejorada dependiendo de la estructura química del analito.

En efecto, la reactividad (abundancia de defectos y la relación C_{sp^2}/C_{sp^3}) y las propiedades inherentes de las nanocintas de grafeno (elevada superficie específica y excelente conductividad eléctrica), han demostrado ejercer un papel predominante en el diseño y en el desarrollo de estrategias de (bio-)sensado electroquímicas con propiedades analíticas muy mejoradas en términos de selectividad, sensibilidad y reproducibilidad de los análisis.

Por todo ello, la búsqueda y exploración de sinergias entre las prestaciones analíticas encontradas para las nanocintas de grafeno y aquellas inherentes a la tecnología serigrafiada han permitido desarrollar y proponer herramientas analíticas innovadoras de respuesta rápida, desechables y portables que exigen bajos volúmenes de muestra y bajo consumo de reactivos. En efecto, estas nanocintas de grafeno se han empleado con éxito en la construcción de sensores electroquímicos (nanocintas de grafeno ricas en C_{sp^2}) y en el desarrollo de estrategias biosensoras (nanocintas de grafeno ricas en C_{sp^3}) para la detección de marcadores de enfermedades de elevada importancia clínica como son el ácido úrico y los D-amino ácidos, respectivamente.

2. Las propiedades del grafeno han sido creativamente exploradas junto con las inherentes ventajas de los sistemas microfluídicos (análisis rápidos, bajo consumo de muestra y reactivos, portabilidad y control de fluidos en la

microescala) debido a la compatibilidad entre la micro y la nanoescala, así como entre las micro y las nanotecnologías.

En efecto, se ha demostrado que el grafeno (grafeno reducido químicamente) es un nanomaterial excelente para la construcción de transductores electroquímicos acoplados a microchips analíticos debido a que ha exhibido –en el marco de la detección electroquímica acoplada a estos sistemas microfluídicos– una marcada electrocatálisis, un aumento de sensibilidad y una elevada reproducibilidad debido también a su elevada superficie específica y conductividad. Estos hallazgos confieren al grafeno un valor añadido dentro de la microfluídica electroquímica dado que ésta presenta muy frecuentemente bajas sensibilidades.

Todo ello ha permitido, por una parte, el desarrollo de aplicaciones innovadoras de biosensado –empleando métodos de formación de película delgada sobre superficies conductoras para la construcción de los detectores electroquímicos– basadas en la resolución enantiomérica y detección selectiva de los D-amino ácidos con relevancia clínica en enfermedades importantes como el *Vibrio cholerae*.

Por otra parte, y en aras de explotar esas propiedades electrocatalíticas del grafeno se han diseñado, caracterizado y desarrollado nuevos detectores electroquímicos constituidos exclusivamente por grafeno, que se han extendido de forma natural a otros nanomateriales de carbono como son los nanotubos. La simple filtración del nanomaterial y su adecuada disposición sobre soportes flexibles no conductores, ha permitido desarrollar nuevos transductores para microfluídica electroquímica constituidos exclusivamente por el nanomaterial y ha supuesto ser el punto inicial para el desarrollo de aplicaciones tal y como es la detección rápida y fiable de marcadores fenólicos en aceite de oliva.

3. Se ha demostrado la excepcional contribución del grafeno (grafeno oxidado y electroquímicamente reducido) dentro del ámbito del diseño y construcción de micromotores catalíticos electrosintetizados sobre poros de membranas de policarbonato. La elevada superficie del grafeno, adecuadamente funcionalizada, puede mejorar tanto las reacciones químicas en las cuales se basa la propulsión de estos micromotores como las interacciones con otras moléculas con fines analíticos de (bio-)-sensado.

En efecto, se han encontrado resultados conducentes a que el grafeno ha dotado a los micromotores de propiedades propulsoras mejoradas que han permitido la obtención de micromotores mucho más rápidos y eficaces, tanto en aquellos cuyo mecanismo de propulsión es la generación de burbujas a través de reacciones químicas como en aquellos asistidos por aplicación de pulsos de ultrasonidos. Estos hallazgos hacen prever un futuro muy prometedor para el desarrollo de nuevos sensores móviles capaces de realizar operaciones analíticas *in situ*, navegando en pequeñas cantidades de muestra y sin necesidad del empleo de fuerzas impulsoras de fluidos.

Por todo ello, finalmente se podría establecer como conclusión general de esta Tesis Doctoral que el grafeno –en sus distintas variantes y formas químicas– ha demostrado ser un material extraordinario en el diseño y desarrollo de herramientas analíticas de vanguardia tales como los (bio-)-sensores y sistemas microfluídicos electroquímicos así como en otras que podrían decirse de nueva generación como son los micromotores, todo ello dentro del marco más actual de la nanociencia y nanotecnología analíticas.

I. Hypothesis, motivation and milestones	1
II. Graphene nanoribbons for electrochemical (bio-)-sensing	9
II.1. Graphene for electrochemical (bio-)-sensing:	
<i>State of the art</i>	11
II.1.1. What graphene stands for?	13
II.1.2. Graphene: properties, synthesis and characterization	16
II.1.3. Graphene for electrochemical (bio-)-sensing	21
II.1.3.1. Graphene oxide: electrochemistry and applications	24
II.1.3.2. Reduced graphene oxide: electrochemistry and applications	29
II.1.3.3. Graphene nanoribbons: electrochemistry and applications	37
II.1.4. Outlook and perspectives	43
II.1.5. References	53
II.2. Graphene nanoribbons for electrochemical sensing	63
II.2.1. Introduction and objectives	65
II.2.2. Synthesis and characterization of graphene nanoribbons	70

II.2.3. Tailored graphene nanoribbons for electrochemical sensing	81
II.2.4. Graphene nanoribbon-based electrochemical sensors on screen-printed platforms	88
II.2.5. Conclusions	93
II.2.6. Experimental section	95
II.2.7. Appendix	101
II.2.8. References	102
II.3. Graphene nanoribbons for electrochemical biosensing	107
II.3.1. Introduction and objectives	109
II.3.2. Strategy for the enantiomeric amino acid analysis	111
II.3.3. Optimization of the enantiomeric amino acid analysis	112
II.3.4. Enantiomeric amino acid calibration and analysis	117
II.3.5. Conclusions	120
II.3.6. Experimental section	121
II.3.7. Appendix	123
II.3.8. References	125

III. Graphene for electrochemical microfluidic (bio-)-sensing	127
III.1. Carbon nanomaterials for electrochemical microfluidic (bio-)-sensing: <i>State of the art</i>	129
III.1.1. Microfluidic chips coupled to electrochemical detection	131
III.1.2. Carbon nanomaterials in microfluidic chips	138
III.1.2.1. Carbon nanotubes in microfluidic chips	139
III.1.2.2. Graphene in microfluidic chips	149
III.1.3. Outlook and perspectives	152
III.1.4. References	155
III.2. Graphene-based materials in electrochemical microfluidic biosensing	161
III.2.1. Introduction and objectives	163
III.2.2. Enzyme-based microfluidic chip for D- amino acid enantiomer biomarkers detection	166
III.2.3. Conclusions	172
III.2.4. Experimental section	173
III.2.5. References	176

III.3. Novel carbon nanomaterial-based electrodes for electrochemical microfluidic sensing	179
III.3.1. Introduction and objectives	181
III.3.2. Graphene and carbon nanotubes teflon-filtered electrodes for electrochemical microfluidic sensing	183
III.3.3. Characterization of the carbon nanomaterial-based teflon filter electrodes	190
III.3.4. Application of the carbon nanomaterial-based teflon filter electrodes for phenolic detection in olive oil	195
III.3.5. Conclusions	202
III.3.6. Experimental section	204
III.3.7. References	210
IV. Graphene-based micromotors: electro-synthesis, characterization and applications	213
IV.1. Micromotors: <i>State of the art</i>	215
IV.1.1. Micromotors: novel analytical tools	217
IV.1.2. Micromotors: propulsion methods	219
IV.1.3. Nanomaterials in micromotors	234
IV.1.4. Outlook and future perspectives	236
IV.1.5. References	237

IV.2. Chemically powered graphene micromotors	243
IV.2.1. Introduction and objectives	245
IV.2.2. Synthesis and characterization of chemically powered graphene micromotors	247
IV.2.3. Propulsion of chemically powered graphene micromotors	253
IV.2.4. Conclusions	261
II.2.5. Experimental section	262
II.2.6. Appendix	265
II.2.7. References	267
IV.3. Ultrasound powered graphene micromotors	271
IV.3.1. Introduction and objectives	273
IV.3.2. Synthesis and characterization of ultrasound powered graphene-gold microcannons	276
IV.3.3. Penetration of nanobullets fired from graphene-gold microcannons	280
IV.3.4. Conclusions	284
IV.3.5. Experimental section	285
IV.3.6. Appendix	289
IV.3.7. References	295

V. Conclusions	301
General conclusions	303
Conclusiones generales	309
VI. Appendices	315
List of Figures and Tables	317
Acronyms	325
VII. Publications and conferences	329

Chapter I

Hypothesis, motivation and milestones

El conocimiento científico es magnífico, racional y luminoso aunque en ocasiones problemático, pero siempre al servicio de las necesidades humanas (J.M. Sánchez Ron)



The recent discovery of graphene has opened new opportunities in the development of creative and innovative works.

Graphene is an atomically thin sheet of sp^2 bonded carbon atoms forming a two dimensional (2-D) lattice. This structure provides this material its extraordinary properties such as high surface area, high electrical and thermal conductivities, optical transparency, high mechanical strength and high elasticity. These unique features of graphene plus the versatility to be synthesized with different oxygen functionalities and defects, such as graphene oxide, or reduced graphene oxides are a merit to be exploited in different analytical applications. Specifically, these 2-D structures are very valuable tools for electrochemical sensing. They offer high currents because of its high surface area enabling fast redox conversion, enhancing the analytical sensitivity and resist to the passivation, yielding good reproducibility. Furthermore, in many cases a decrease in redox potentials due to the high presence of active sites could enhance the overall selectivity of the analysis.

Besides, the actual tendency of improving the analytical performance by reducing sample and reagents consumption, generating a fast response, improving portability with a low cost, make screen-printed and microfluidic technologies compatible platforms to include nanomaterials such as graphene for advanced sensing and biosensing.

In microfluidic systems, additionally, electrochemistry is a valuable detection principle due to its inherent miniaturization and high compatibility with micro and nanotechnologies. Although the sensitivity is often a drawback because of the small volumes of sample, the use of nanomaterials overcome this sensitivity problem

enhancing the surface area features. Thus, these microfluidic platforms combining nanomaterials are extremely pertinent and demanded as a novel horizon in the laboratories.

On the other hand, micromotors are devices capable of converting energy into movement. The structure, shape and size as well as the materials constituting these devices are essential for an excellent propulsion and creative applications. Commonly, these micromotors are particles or structures with a few microns dimensions, creatively designed with certain asymmetry. Therefore, the application of certain energy in the system permits a local gradient and the uneven distribution of the forces in the micromotor, permitting the expected movement. In general, when the energy responsible for the movement comes from a chemical reaction or an acoustic energy, chemically-driven micromotors mainly powered by bubbles and ultrasound-propelled micromotors are found, respectively.

Graphene and nanomaterials may be used to improve the autonomous motion and, interestingly, creative research may be performed because graphene gives an additional value in the micromotor structure since it may be functionalized or anchored to other molecules by its oxygen functionalities and it presents high edge chemistry capable to react with many other materials. Thus, the employment of graphene and nanomaterial-based micromotors present a wide variety of analytical applications such as the removal of interferences and or chemical (bio-)-sensing.

Therefore, all the features derived from the graphene and related materials stated above convert these materials in unique tools in the current analytical nanoscience and nanotechnology. As a consequence, the exploration and evaluation of graphene-based

materials for enhancing the analytical performance of the previously identified vanguard analytical tools –electrochemical (bio-)-sensors, electrochemical microfluidics and micromotors– has constituted the main motivation of this Doctoral Thesis.

Accordingly, this Doctoral Thesis has three well-defined objectives.

- 1-** Design, characterization and development of novel electrochemical graphene-based (bio-)-sensors
- 2-** Design, characterization and development of novel graphene-based electrochemical detectors in microfluidic chips
- 3-** Design, characterization and development of novel chemically and ultrasound powered graphene-based micromotors

Accordingly to the previously objectives, the main milestones identified in this Thesis have been:

1.1 Analytical characterization and electrochemical evaluation of chemically synthesized graphene nanoribbons with different oxygen content using microscopy techniques (atomic force microscopy (AFM), transmission electron microscopy (TEM) and field emission-scanning electron microscopy (FE-SEM)), spectroscopic techniques (X-ray photoelectron spectroscopy (XPS), infrared (IR) and Raman spectroscopy), X-ray diffraction (XRD) and electrochemical techniques (chronocoulometry, cyclic voltammetry (CV) and differential pulse voltammetry (DPV)).

1.2. Design and development of graphene-based chemical sensors for fast and reliable detection of target molecules of clinical relevance (ascorbic acid, levodopa, L-tyrosine, uric acid) and its application for uric acid monitoring in urine samples

1.3. Design and development of a novel biosensing strategy for fast and reliable detection of target D-amino acids with clinical significance (D-Tyr in *Bacillus subtilis* and D-Met in *Vibrio cholerae*) and its application for its monitorization in urine samples using screen-printed graphene-based electrodes.

2.1. Design and development of a novel electrochemical microfluidic biosensing strategy for fast and reliable detection of target D-amino acids with clinical significance in *Vibrio cholerae* using screen-printed graphene-based electrodes.

2.2. Design, fabrication and characterization of exclusive carbon nanomaterial (reduced graphene oxide (rGO), single-walled carbon nanotubes (SWCNTs) and multi-walled carbon nanotubes (MWCNTs)) transducers based on teflon filter electrodes for electrochemical and microfluidic sensing.

2.3. Development of a microfluidic chip coupled to exclusive multi-walled carbon nanotube transducers for the determination of quality phenolic markers in olive oils.

3.1. Optimization of the template-assisted electrosynthesis of graphene-based micromotors using double conical polycarbonate membranes as templates.

3.2. Analytical characterization of the graphene micromotors using optical and electron microscopy techniques.

3.3. Study of the propulsion mechanisms (chemically and ultrasound powered) in the graphene-based micromotors.

According to these objectives, the results obtained in this Doctoral Thesis has been classified and discussed in three main chapters. In the first one (**chapter II**), the design and development of graphene-based chemical sensors and biosensing strategies for the fast and reliable detection of target analytes of clinical relevance are described. In the second one (**chapter III**), novel electrochemical microfluidic chips coupled to graphene-based detectors are proposed. The design and development of a graphene-based biosensing strategy for the fast and reliable detection of D-amino acid biomarkers in *Vibrio Cholerae* as well as the pioneering design, fabrication and characterization of carbon nanomaterial exclusive transducers based on teflon filter electrodes and its application to the determination quality phenolic markers in olive oils are presented and discussed. Finally, in the last one (**chapter IV**), the electrosynthesis, characterization and applications of bubble-propelled graphene-based micromotors (powered by chemical and acoustic energies) are described. Firstly, the pioneering electrochemical template-based synthesis of ultrafast oxygen-propelled graphene-based micromotors resulting from the electrochemical reduction of graphene oxide and secondly, ultrasound powered electrochemically reduced graphene oxide/gold micromotors are presented and discussed.

Chapter II

Graphene nanoribbons for electrochemical (bio-)-sensing

*Chemistry is not limited to beakers and laboratories.
It is all around us, and the better we know chemistry,
the better we know our world. (ACS, Chemistry is Everywhere)*



II.1. Graphene for electrochemical (bio-)-sensing: *State of the art*



II.1.1. What graphene stands for?

The definition of nanomaterial was established by the European Commission, recommendation of the 18th October 2011.¹

A natural, incidental or manufactured material containing particles, in an unbound state or as an aggregate or as an agglomerate and where, for 50 % or more of the particles in the number size distribution, one or more external dimensions is in the size range 1 nm - 100 nm. In specific cases and where warranted by concerns for the environment, health, safety or competitiveness the number size distribution threshold of 50 % may be replaced by a threshold between 1 and 50 %. By derogation from the above, fullerenes, graphene flakes and single wall carbon nanotubes with one or more external dimensions below 1 nm should be considered as nanomaterials.

It is worth noting that the definition includes all the carbon allotropes that have dimensions below the nanometer scale. In this thesis, carbon nanomaterials and, in particular, graphene has been the employed material to develop the majority of the working plan. Graphene is one of the newest carbon nanomaterials in the scientific scenario. Since the isolation of graphene sheets in 2004 by a simple technique using cello-tape,² graphene has captured incessant interest for the scientific community. **Figure II.1** shows the molecular models of the carbon family, where fullerenes zero-dimension (0-D) materials, single-walled carbon nanotubes (SWCNT) one-dimension (1-D) materials and graphite three-dimension (3-D) materials are identified. Graphene is the youngest member and filled the second dimension (2-D) of the carbon nanomaterials in the multidimensional family of the carbon allotropes.

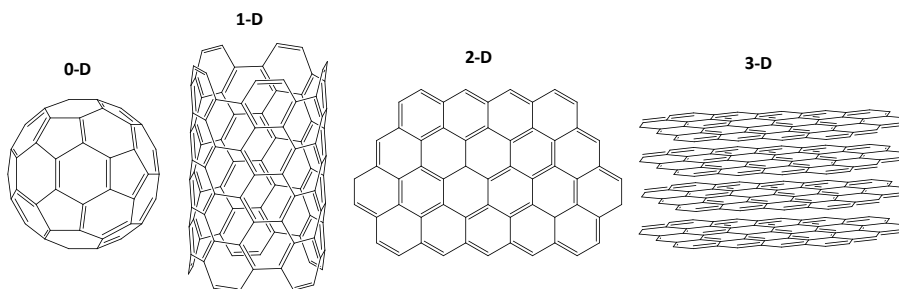


Figure II.1. Multidimensional carbon allotrope family. Fullerene (0-D), SWCNTs (1-D), graphene (2-D) and graphite (3-D)

According to the IUPAC, graphene is: “A *single carbon layer of the graphite structure, describing its nature by analogy to a polycyclic aromatic hydrocarbon of quasi infinite size*”. For that “*previously, descriptions such as graphite layers, carbon layers or carbon sheets have been used for the term graphene. Because graphite designates that modification of the chemical element carbon, in which planar sheets of carbon atoms, each atom bound to three neighbors in a honeycomb-like structure, are stacked in a three-dimensional regular order, it is not correct to use for a single layer a term which includes the term graphite, which would imply a three dimensional structure. The term graphene should be used only when the reactions, structural relations or other properties of individual layers are discussed*”.³

In the “graphene” field, terminology is an important issue and, in the bibliography, we can notice differences when referring to graphene. Firstly, according to the number of layers, three different groups are established: a single-layer, few-layers from 2 to 9 layers and multi-layer or graphite more than 10 layers. **Figure II.2** illustrates this classification showing single, few and multi-layer graphene structures.⁴ Although the true graphene is only a single-layer, the

easy π - π interaction between layers provokes a truly challenge to obtain one layer, in the synthesis process, as well as, in the works published in the bibliography. Another classification is established considering the chemical synthesis of the graphene, in this group we could include the following terminology depending on the carbon source. When the carbon source is graphite we could obtain chemically modified graphene that includes either graphene oxide (GO) or reduced graphene oxide (rGO). While, if the carbon source are carbon nanotubes, graphene nanoribbons (GNR) are synthesized after the unzipping of the CNTs.

Thirdly, and with independence of the previous terminology, two more terms are commonly employed in the literature. Graphene nanosheets and graphene nanoplatelets, these nanomaterials are commonly related to the number of layers. Therefore, graphene nanosheets are the open-equivalent to a SWCNT, which is one layer of graphene thick, and graphene nanoplatelets are consequently, the open-equivalent to the multi-walled carbon nanotubes (MWCNTs), which consist of few layers.

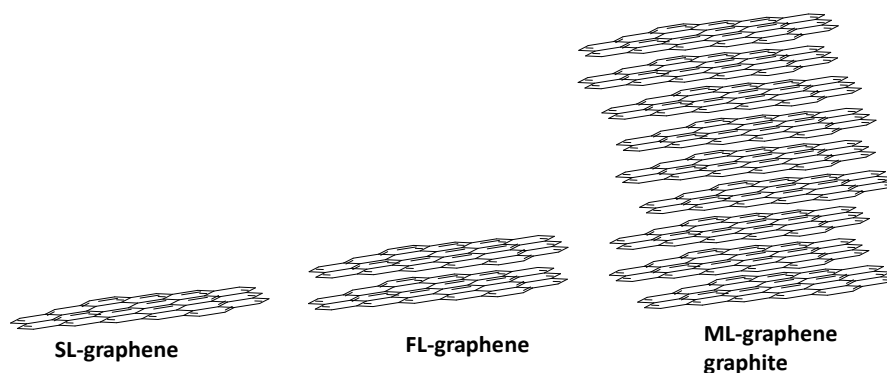


Figure II.2. Representation of graphene: single-layer (SL), few-layer (FL) and multilayer (ML) graphene

All these terms are broadly used referring to graphene in the bibliography. As a result, the researcher must be critical with the material considered. And above all, the most important issue is to differ between graphite and graphene.

II.1.2. Graphene: properties, synthesis and characterization

Graphene is a 2-D sheet of carbon atoms bonded by sp^2 bonds. This configuration provides this material of extraordinary properties such as high surface area, theoretically $2630 \text{ m}^2/\text{g}$ for single-layer,⁵ and double than single-walled carbon nanotubes. It also shows excellent thermal ($k = 5 \cdot 10^3 \text{ Wm}^{-1}\text{K}^{-1}$)⁶ and electrical conductivity ($\sigma = 64 \text{ mS cm}^{-1}$). Graphene is considered a zero-gap semiconductor, because it presents no gap between conduction and valence bands, so it might be considered either a semiconductor or as a metal. According to the physical properties, graphene presents optical transparency, high mechanical strength (Young's modulus, $\sim 1100 \text{ GPa}$),⁷ high elasticity and flexibility.

Graphene has been synthesized by several methods, Geim et al. obtained it by the simple approach of peeling-off or "Scotch tape" method, using a sticky tape and a pencil in 2004. However, the first approach of synthesis in 1979⁸ was chemical vapour deposition (CVD) and epitaxial growth on a nickel surface by the decomposition of ethylene. During the last years, various methods for producing this carbon allotrope have been developed, including epitaxial growth and chemical synthesis from graphite.⁹ In **Table II.1** (see page 45) is summarized the synthesis process and some electrochemical applications of those graphenes.

II.1. Graphene for electrochemical (bio)-sensing: *State of the art*

After the synthesis process, the material needs to be characterized by a wide number of techniques¹⁰⁻¹² to obtain reliable and complete analytical information about the morphological, physical and chemical structure. **Table II.2** summarizes the main techniques involved in graphene characterization.

Table II.2. Selected analytical techniques for characterization of graphene

Technique		Analytical information		Analytical data for <i>true</i> graphene
Microscopy	TEM	Morphological	Length layer	Height of a layer ~0.34 nm
	SEM			
	AFM			
Spectroscopy	Raman	Inner structure	Chemical groups and defects of the lattice	Only sp ² -carbons
	IR			
	UV-Vis			
	NMR			
	XPS			
Electrochemical techniques	Cyclic Voltammetry	Inherent electrical properties	Heterogeneous electron transfer rate	Enhanced kinetics, Electrocatalysis and Current densities
	Chronoamperometry			
	Chronocoulometry			
	Impedance			

Microscopy techniques such as scanning electron microscopy (SEM), transmission electron microscopy (TEM) and atomic force microscopy (AFM) are required to evaluate morphological aspects. Certainly, SEM images are mainly used to understand how the graphene material is deposited on different surfaces, chiefly onto

II.1. Graphene for electrochemical (bio)-sensing: *State of the art*

electrode surfaces.¹³ Meanwhile, TEM permits an accurate morphological and topographical evaluation of the carbonaceous material.¹⁴

Complementary information to TEM is given by AFM. This is a powerful technique that plays a decisive role in graphene characterization because it permits to estimate the number of layers.^{15,16} A pristine single layer of graphene or “true graphene” consists in one layer thick with van der Waals thickness around 0.34 nm. ² In GO the compromise is that these sheets are expected to be thicker than pristine graphene because of the presence of sp³-carbon atoms. Oxygen functionalities above and below the original plane suggest that one layer is approximately 0.8 nm.¹⁷

Raman, IR, nuclear magnetic resonance (NMR) and UV–Vis spectroscopies have also been used in order to know characteristics of the inner structure (defects and moieties in the sheet).¹¹ Above all the techniques, Raman gives extraordinary analytical information, about the number of layers in the structure ^{12,18} and the inner structure of graphene. While graphite exhibits a Raman spectrum with a typical G-band at 1590 cm⁻¹, GO and rGO samples show differences in their Raman spectra and display a G band at 1590 cm⁻¹ and a D band at 1360 cm⁻¹. G band corresponds to the carbon sp² vibrations of the domains in-plane, as in graphite spectrum.¹⁹ D-band arises from the out-of-plane vibrational modes and is indicative of sp³ carbons present.²⁰ The intensity ratio of the D and G lines (I_D/I_G ratio), therefore, provides important information because is proportional to the average size of the sp² carbon domain, as a result, a decrease in the ratio I_D/I_G is attributed to the removal of defects.²⁰ However, in some cases, rGO can present higher I_D/I_G ratio than GO which would

indicate that reduced graphene oxide present much more edges and would have been broken into more fragments.²¹

IR spectra permit an analysis of the functional moieties present in the graphene samples and an estimation of the Csp^2 and Csp^3 content, comparing vibrations from graphitic domains. In general, the most probable bands are provoked by stretching and bending vibrations from hydroxyl, epoxy or carboxyl groups.²² In the case of rGO, the intensities of the bands associated to oxygen moieties strongly decrease compared to GO. NMR is not a widely employed technique in graphene characterization but, as well as for IR, it allows to difference between reduced and graphene oxides. The ^{13}C spectra are the analysis used to determine the presence or absence of oxygen groups, meanwhile wide bands are found in rGO due to the presence of different carbon atom environments in the material.²³ The UV-Vis spectroscopy mainly allows to monitor reduction reaction from GO to rGO. GO displays an absorption peak at around 230 nm due to the $\pi-\pi^*$ transition of aromatic C=C bonds and a weak peak at around 290 nm due to the $n-\pi^*$ transition of the C=O bond. As the reaction yields rGO, the peak at 230 nm increases with the decrease in intensity of the 290 nm band.¹¹

Furthermore, the moieties that are part of the graphene layer could be confirmed by X-ray photoelectron spectroscopy (XPS) and elemental analysis techniques. XPS of C 1s is a powerful tool to study the reduction of the oxygen content of the graphene films.¹¹ XPS permits to distinguish the groups of bonds and the oxidation state of carbons that are presented in GO and rGO. Therefore, GO presents a complex spectrum due to the presence of oxide-moieties and rGO mainly presents C-C and C=C bonds and its spectrum, centered at 285 eV. Thus, the decrease in oxygen-groups and the generation of

II.1. Graphene for electrochemical (bio)-sensing: *State of the art*

large domains of π -conjugated structures in rGO make simpler its spectrum. ²¹

Powder X-ray diffraction (XRD) allows comparing between patterns of graphite and the synthesized graphene and permits to know the interlayer distance between layers. ²⁴

Additional techniques employed are thermal gravimetric analysis (TGA) to know the oxygen content of the graphene sample. This measurement permits to compare different graphene samples with different oxygen content. GO is thermally unstable and loses mass at 200 °C because of the pyrolysis of the labile oxygen-moieties and yields CO, CO₂ and water vapour. ¹⁰

The electrochemical behavior and electrochemical characteristics of graphene are evaluated using techniques such as cyclic voltammetry (CV), chronoamperometry or chronocoulometry. Outer and inner sphere redox systems are commonly scanned by electrochemical techniques to characterize the electrochemical behavior of the graphene materials.²⁵

II.1.3. Graphene for electrochemical (bio)-sensing

Despite being a material with plenty of properties,²⁶ just some of them, the large surface area and high electrical conductivity, are some of the most relevant properties for electrochemical applications. A comparison between two of the most important carbon allotropes such as, SWCNTs (1-D nanomaterial) and graphene (2-D nanomaterial), shows the following advantages for the 2-D material compared to 1-D.²⁷ In comparison to CNTs, graphene exhibits several advantages such as lower costs, high surface area and easy processing. Moreover, graphene synthesized from graphite does not contain metallic impurities from its synthesis and it is cheaper because its carbon source is graphite.²⁶ In graphene, in contrast with CNTs, the large number of edges per mass of the material permits higher heterogeneous electron transfer (HET) rates.^{28,29} Pumera et al. studied by cyclic voltammetry the HET rate for different chemically modified graphene materials as well as graphite and glassy carbon electrodes (GCE) as controls.¹⁴ Furthermore, in a previous work,³⁰ Pumera et al. also calculated the HET for MWCNTs and samples of MWCNT with different content of nanographite impurities. **Table II.3** summarizes the data obtained in both works. It indicates that reduced graphene material offers better electrochemical performance than graphite and MWCNTs and close to the found for GCE. In other words, the electrochemical activity of graphene is due to the presence of a higher density of sp² domains and planes and to the higher number of edges planes, which present defects. On the other hand, in the case of CNTs it is also due to the presence of the impurities from the synthesis process.³¹

II.1. Graphene for electrochemical (bio)-sensing: *State of the art*

Table II.3. HET rates for carbon material-based electrodes

Carbon materials	k^0_{obs} (cm s ⁻¹)	Carbon materials	k^0_{obs} (cm s ⁻¹)
GCE	0.003	MWCNT	2×10^{-5}
Pyrolytic Graphite	$2 - 3 \times 10^{-5}$	MWCNT- 10% impurity	6×10^{-4}
GO	5×10^{-5}	MWCNT- 30% impurity	2×10^{-3}
rGO	4×10^{-4} to 0.005		

Values taken from references 14,30

Therefore the improvement of graphene in the electron-transfer kinetics facilitates the redox processes for molecules that usually require high over-potentials to be oxidized or reduced.

The role of graphene as electrochemical transducer is nowadays a matter of great interest, being characteristic: (a) The low detection potentials. The electrocatalytic effect induced by graphene materials might have a strong effect on the electrocatalysis of analytes and, therefore, on the substantial reduction of the detection potentials, which would improve the overall *selectivity* of the analysis. (b) The high currents obtained. The greater surface area of graphene detectors enables larger scale redox conversion, which implies an increase in *sensitivity* in the analytical procedure. (c) The high stability and resistance to passivation originated from the greater surface area of the graphene-based detectors. This characteristic implies better *reproducibility* in analysis, since the resulting signal tends to foul in analytical environments.

On the other hand, Electroanalysis is living a true *Renaissance* due to the discovery of novel nanomaterials.³² After the appearance of carbon nanotubes, which evolved nanotechnology, graphene is the *novelty* in the electroanalysis field. Lots of target molecules of high significance in diverse fields are electroactive. Therefore, their

electrochemical detection has been enhanced because nanomaterials offer excellent selectivity and sensitivity in their direct detection without the necessity of any derivatization step.

The properties of graphene materials have recently improved the electrochemical sensing and biosensing.^{29,33-39} As in other carbon and metallic nanomaterials, graphene has been broadly used under two approaches: building thin film and composite electrodes in sensing approaches and as electrochemical transducers in biosensing coupling with biomolecules (enzymes, antibodies, DNA) for high selective and sensitive molecule detection.

In the thin film approach, the design of graphene-film electrodes is very simple. The underlying bulk electrode is modified with graphene films, usually by the deposition of a suspension of graphenes in solvent (e.g., dimethylformamide (DMF) or other organic solvent in the case of reduced graphene samples,⁴⁰ water in graphene oxides¹⁰ and surfactant solutions⁴¹ in both cases) and then, the solvent is evaporated. As a result, random graphene films are created on the surface of the electrodes.

In the composite electrodes, graphene is mixed with other components or embedded in a polymer matrix. The main advantage of this design over graphene-film detectors is that graphene-composites are mechanically stable and significantly reduce noise levels. This is a classic characteristic of composite electrodes, which are capable of acting as an array of micro/nanoelectrodes with heavy overlapping diffusion zones. Thus, it provides signals equivalent to macroelectrodes with the advantage of reducing noise and a high signal-to-noise ratio. Furthermore, graphene easily suffers from π - π stacking interactions; so the prevention of aggregation, using

polymers or other materials onto the graphene surfaces, permits to obtain individual sheets.

Finally, beyond the chemical sensing, graphene has been also explored in biosensing by using the same approach that have been studied with several forms of carbon materials such as graphite, carbon nanofibers or carbon nanotubes, among other examples. Redox enzymes as glucose oxidase, or proteins are some of the examples that usually integrate via assembling with graphene surface.

II.1.3.1. Graphene oxide: electrochemistry and applications

Graphene oxide includes a variety of reactive oxygen groups such as, carboxyl (COOH), carbonyl (C=O), epoxyde (-O-) and hydroxyl (-OH) linked to a network of Csp³ structure. The precise chemical structure of GO has been an item of considerable discussion during the last years,⁴² being the most accepted model published by Anton Lerf and Jacek Klinowski.^{43,44} In this model, schematized in **Figure II.3**, alcohols and epoxides form the basal plane, meanwhile carboxyl and carboxylic acid moieties are located in the edges. As discussed in the previous section of synthesis, this material may be obtained by thermal or mechanical exfoliation of graphite oxide through sonicating and/or stirring it in water,⁴⁵ with the undesirable disadvantage of damaging the platelets.¹² Furthermore, GO presents negative charge when dispersed in water, which suggests that electrostatic repulsion between negatively charged GO sheets could generate a stable aqueous suspension of them. Apart from that, it is also possible to functionalize this GO considering various chemical reactions that provide chemically modified graphenes.⁴² These

II.1. Graphene for electrochemical (bio)-sensing: *State of the art*

functionalizations consist in the reaction at the carboxylic acid or epoxy groups that reduce the hydrophilic GO or the non-covalent functionalization of GO via π - π stacking, cation- π or van der Waals interactions on the sp^2 system.

The main characteristic in the GO structure is the high percentage of sp^3 carbons as consequence of the oxidation treatment. This causes a decrease of sp^2 carbon content compared to rGO, which provokes the aromatic loss in GO, and the consequent deficit in HET rate (see **Table II.3**). This structure of GO provides the material special features ^{46,47} and its use for many applications, as remarkable as, polymer composites, energy-related material, sensors, field emission transistors and biomedical applications.

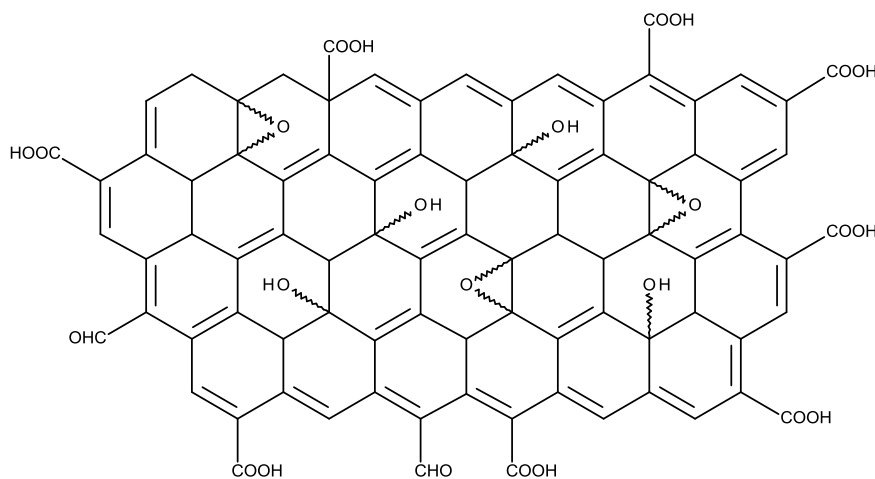


Figure II.3. Schematic model of graphene oxide

Table II.4 (see page 47) shows the GO materials used in the electrochemical detection of different analytes, some of them explored in real samples. Towards the selected examples, the potential of GO as an electrochemical transducer will be critically stated following the before explained approaches (thin film,

composite and biosensor based electrodes) and remarking the chemical interaction with the detected molecule.

As regards to the thin-film approach, Chang et al. reported studies of the improved voltammetric detection in terms of sensitivity and selectivity of uric acid (UA) and ascorbic acid (AA) at a carbon screen-printed electrode (CSPE) modified with nanoplatelets of graphitic oxide. They used an original microwave-assisted hydrothermal elimination method⁴⁸ to explore the role of oxygen functionalities and edge plane sites on the electrochemical behavior of UA and AA. This method implies the generation of supercritical water, which acts as reducing agent under the solvothermal condition, deoxygenating the oxygen moieties of the basal plane.⁴⁹ Therefore, it is removed the oxygen-containing functional groups from the basal surface of the GO maintaining the edge plane groups. By varying the microwave treatment temperature, it is controlled the reduction of the oxygen functional groups. Furthermore, as the edge-plane-like sites are, in fact, the electroactive sites; this platform, which retained the edge plane with tunable oxygen-containing functional groups, allowed a deep study of comparison between different GO-modified electrodes and a non-modified CSPE.

Surprisingly, meanwhile using a CSPE, AA and UA are oxidized at the same potential, a large shift in the oxidation potential of AA in cathodic direction was observed when using GO-modified electrodes not being shifted the peak potential for UA. Therefore, the increment in potential (ΔE) shifted from 0 mV in the case of CSPE to 19 mV, 58 mV and 158 mV for graphene oxide with 6.3%, 7.7% and 9.9 % in COOH moieties, respectively. UA did not experiment any electrocatalytic effect when a GO-modified electrode was used. Authors attributed the shift in oxidation potential to the very distinct

ability of AA and UA to form hydrogen bonds with oxo-surface groups (especially COOH group). The result of potential shift observed for AA indicates that a direct chemical interaction between oxo-surface groups and AA is involved in the reaction center during the oxidation step. In the case of UA the hydrogen bond interaction is far from the reaction center and therefore, it is not interfering in the oxidation step.

A new 4-nitrophenol sensor was developed based on a GO film coated GCE due to the special importance of the analysis of aromatic nitrocompounds in natural waters and effluents.⁵⁰ The GO has strong adsorptive capability for 4-nitrophenol, because they easily interact by both hydrogen bonds and π - π stacking, as well as, by electrostatic interactions since nitrogen atom may be positively charged. Therefore, the GO films exhibit electrocatalytic activity towards the reduction of 4-nitrophenol, because they decreased the reduction potential in 54 mV and also showed good sensitivity because the current in GO-modified electrode increased in four times compared to GCE.

As it has been indicated before, the chemical functionalization of graphene has been also explored in electrochemical applications. A carboxylic acid functionalized graphene (graphene-COOH) was prepared and used to make a novel sensor for the simultaneous detection of adenine and guanine.⁵¹ The negatively charged graphene-COOH nano-film could interact with the positive charged guanine and adenine analytes, and this led to effectively improve the sensitivity of the proposed method. As a result, in the modified electrode the peak currents increased near four times in contrast to the response of the bare GCE.

II.1. Graphene for electrochemical (bio)-sensing: *State of the art*

Two voltammetric sensors have been developed using GO composite electrodes. In both cases, nafion has been the added material mixed with GO. Important alkaloids, such as the natural and daily life caffeine⁵² and colchicines,⁵³ have been detected using a nafion/GO/GCE sensor. Nafion increases the immobilization stability of GO on the electrode surface due to its ability to form excellent films, and furthermore, nafion may also interact with the positive charged analytes permitting the adsorption of certain molecules as caffeine or colchicines, which are positively charged at acid pH.

GO has also been explored in the design of biosensors. While using GO, an increase in the signal and a significant change in potential detection have been achieved; the use of chitosan has also increased the stability of GO on the GCE. The nanocomposite is based on chitosan-ferrocene, graphene and glucose oxidase that catalyze the oxidation of glucose on a glassy carbon electrode.⁵⁴ Although GO has been used in biosensing,⁵⁵ it is also true that the biological activity of the GO–enzyme conjugate decreases when there is an electrostatic interaction between the enzymes and the oxygen groups of GO.⁵⁶ For that reason, depending on the application the most appropriate graphene would be the one which improves the molecule determination.

II.1.3.2. Reduced graphene oxide: electrochemistry and applications

Reduced graphene oxide is usually synthesized by chemical, thermal or electrochemical reduction of GO or by other methods explained in the previous sections and summarized in **Table II.1** (see page 45). The most common route for the synthesis of rGO is the chemical one, which uses chemical compounds such as hydrazine in ammonia media. In **Figure II.4A**, this reduction is schematized. The chemical treatment provokes the reduction of epoxide groups mainly located in the basal plane, whereas, reductions of the hydroxyl, carbonyl, and carboxyl groups are caused by thermal treatment during reduction process.⁵⁷ **Figure II.4B** represents the rGO layer, in which a few oxygen groups remain in the sheet. The properties of this material are mainly the ones explained in the generalities for one graphene sheet, however, it may contain some oxygenated moieties that belonged to the GO sheet. As a result, the elemental analysis of the rGOs measured by combustion revealed the existence of a significant amount of oxygen (atomic C/O ratio, ~ 10), indicating that rGO is not the same as a pristine graphene sheet. Theoretical calculations of the rGO (the model used for GO had the graphene modified with hydroxyl and epoxide groups) suggest that reduction below 6.25% of the area of the GO (C/O = 16 in atomic ratio) may be difficult in terms of removing the remaining hydroxyl groups.^{6,58}

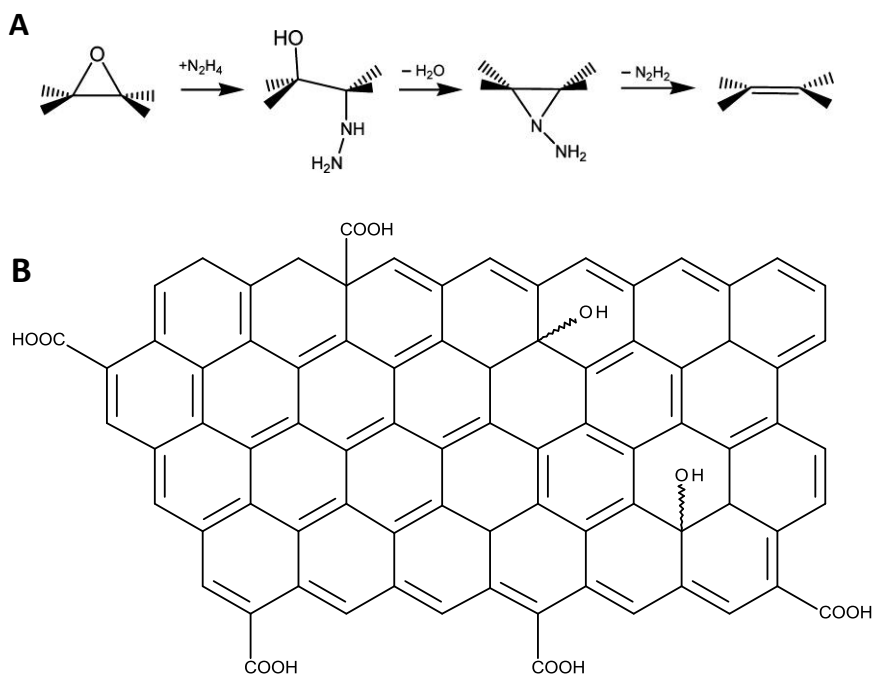


Figure II.4. (A) Reduction of epoxide group with hydrazine in NH_3 media and (B) schematic model of reduced graphene oxide. Modified with permission of reference 57

The main characteristic of the rGO is the higher content of sp^2 -carbon compared with GO. The natural consequence is the presence of an enormous orbital π , which permits a higher HET rates than GO (see **Table II.3**). For this reason, it is the most employed graphene in the bibliography for electrochemical sensing.

Owing to the strong tendency between graphene sheets to stack by π - π interaction, the layers easily aggregate. However, this aggregation could be overcome by the insertion of molecules that stabilize the structure, dispersion in organic solvents or addition of polymers onto the nanosheets. Thus, the habitual solvents used to disperse this material are mainly organic solvent such as, DMF, N,N' -

dimethylacetamide, and N-methyl-2-pyrrolidone at concentrations up to 1 mg mL⁻¹.¹⁰ Despite being very hydrophobic molecule, it is also dispersed in water using surfactants as cetyl trimethylammonium bromide (CTAB), sodium dodecyl benzyl sulfate (SDBS) or sodium dodecyl sulfate (SDS).⁵⁹ It is of relevant importance that often the presence of some stabilizers is undesirable for most applications.⁶⁰

This unique nanostructure holds great promise for potential applications in many technological fields such as nanoelectronics, sensors, capacitors, and nanocomposites.⁶¹⁻⁶³

Table II.5 (see page 48) shows the rGO materials used in the electrochemical detection of different analytes, some of them explored in real samples. Towards the selected examples, the potential of rGO as an electrochemical transducer will be critically stated following the before explained approaches (thin film, composite and biosensor based electrodes) and remarking the chemical interaction with the detected molecule. Reduced graphene oxide is widely used in analytical and electrochemical applications because of the excellent properties of this carbon material. Its chemical inertness, potential window and electrocatalytic activity to a variety of redox reactions are the most prominent properties that permit its electrochemical application.

Using the thin-film approach by a simple casting of the electrode with the rGO material, different electrode substrates such as GCE and CSPEs have been used to detect important target molecules. Indeed, chemically reduced graphene nanosheets modified GCE have been explored for the simultaneous determination of morphine, noscapine and heroin, which are important, opiate drugs⁶⁴ as well as for the

simultaneous determination of hydroquinone (HQ) and catechol (CT).⁶⁵

Certainly, graphene films on electrodes usually have been obtained by drop-casting solution based on reduced graphene oxide obtained from chemical reduction with $\text{N}_2\text{H}_4/\text{NH}_3$ or other reagents from GO sheets. But the main limitation of this approach is the lack of control in the film thickness, and clearly, the toxic chemicals that are involved. As consequence of it, nowadays, electrochemical reduction of GO has drawn great attention because of its fast and environmental friendly synthesis. This modified electrode was used for the simultaneous determination of HQ and CT ⁶⁶ as well as for nitric oxide sensing.⁶³

The advantages of rGO in connection with the inherent advantages of screen-printed technology were also explored for detection of AA, dopamine (DA) and UA, finding an excellent electrocatalysis from rGO on these important analytes.⁶⁷

Another interesting approach consists of a good stability, uniform, and rich-wrinkled electrophoretic deposited graphene film, ^{68,69} which was utilized as an analytical platform for the determination of nitroaromatic explosive compounds such as, 2,4,6-trinitrotoluene.⁷⁰ This methodology is based on high deposition rate and throughput, good uniformity and controlled thickness of the obtained films, without need of binders, and simplicity of scaling up. Trinitrotoluene is a good π -electron acceptor and it easily adsorbs on graphene surface through hydrogen bond and/or π - π stacking interaction with reduced graphene oxide. Therefore, trinitrotoluene sensing can be attributed to those interactions with graphene. In this article, it was evaluated analytical detection of trinitrotoluene and the electrochemical activity of this graphene-based electrode containing

either 4-nitrotoluene or 2,4-dinitrotoluene. Authors found that the number of reduction peaks for nitroaromatic compounds were dependent on the number of nitro groups on the aromatic ring. Therefore, the graphene may have potential in the electrochemical detection of nitroaromatic compounds with distinguishable voltammogram features.

These of aromatic molecules might foul the graphene electrodes because they adsorb in the carbon surfaces, in order to avoid this fouling and clean the nanomaterial surface, cyclic voltammeteries with the buffer of measurement are commonly employed scanning in the redox potential window. Therefore, in the general literature, graphene has demonstrated its excellent repeatability and reproducibility as electrochemical detector compared with conventional electrodes.⁷¹ However, there are also some examples showing that graphene-modified electrodes are worse than conventional carbon-based electrodes.⁷²

On the other hand, rGO mixed with other components or embedded in a polymer matrix into composite approach is a promising cutting edge in graphene-detectors. Indeed, as we have already mentioned before, the presence of polymers as nafion or chitosan permit not only to stabilize the material on the electrode but also to avoid aggregation of sheets because the positively charged chitosan interacts with the negatively charged graphene. A fast method for the simultaneous determination of CT, resorcinol (RS) and HQ at graphene–chitosan composite film modified GCE has been reported.⁷³ Another application for the simultaneous determination of dopamine and ascorbic acid utilized a green-synthesis graphene obtained with non-toxic solvents by reduction of GO using ascorbic acid and chitosan on the GCE.⁷⁴ Furthermore, rGO polymerization

synthesis has been completed in one-step with electro-synthesis applying cyclic sweeping on the GCE and then applied for the simultaneous determination of UA, xanthine and hypoxanthine.⁷⁵

Although graphene properties permits, in some cases, the simultaneous determination of several compounds because of the graphene electrocatalysis on some molecules, the different π - π interaction between target analytes and graphene allowed to differentiate the presence of two analogous structural species. Aloe-emodin and aloin are one studied example using a graphene-nafion GCE.⁷⁶ It is remarkable, the much higher current intensities in the case of aloe-emodin and emodin (structural analogous) obtained with graphene and MWCNT than the conventional GCE, and more importantly, the non-presence of oxidation peak in the case of aloin. Remarkably, this is an excellent example in which the high electroactive surface area of graphene provides enhanced the sensitivity for both aloe-emodin and emodin in comparison to non-modified and MWCNTs modified GCE surfaces. Furthermore, interestingly, in the analysis the redox peak of aloin (analogous compound with a glycosyl group) is not found. Authors explained the non-oxidation peak and the non-presence of peak for aloin due to the steric hindrance of glycosyl group of aloin to interact with graphene surface. While aloe-emodin structure easily interacts via π - π with graphene structure; aloin, a non-planar and hydrophile molecule, provokes the impeded adsorption on graphene surface.

Moreover, other molecules had been embedded in the graphene structure in order to enhance the response of an analyte. To stabilize chemically reduced graphene, an anion porphyrin, meso-tetra(4-carboxyphenyl) porphine was incorporated in graphene structure and used for highly selective and sensitive detection of DA on GCE.⁷⁷ The

aromatic π - π stacking and electrostatic attraction between positively-charged DA and negatively-charged porphyrin-modified graphene could accelerate the electron transfer and the analyte response.

The recognition of chiral molecules is an important task, especially in the detection of chiral drugs. A key step in selectively sensing chiral molecules such as binaphthol is to build a chiral surface that can identify the minute differences between the two especial enantiomers. A chiral surface using the self-assembly method to anchor chiral osmium complex Λ -[Os(phen)₃(ClO₄)₂] onto a single-layered rGO film that is attached to the 3-aminopropyltriethoxysilane modified indium tin oxide (ITO) substrate was developed.⁷⁸ The use of single-layered rGO in the hybrid film has greatly improved the detection sensitivity of chiral binaphthol, indicating that functionalized graphene film has promising potential in analyzing chiral molecules.

Owing to the tendency of rGO to aggregate by π - π stacking interactions, it is necessary to improve its stability. Another route to avoid this problem consists of the inclusion of MWCNTs between graphene layers creating a three dimensional, porous, conductive and catalytic matrix on the electrode surface.⁷⁹ It was synthesized the rGO-MWCNTs hybrid materials through a facile chemical reduction method with polyethyleneimine (PEI) as the reductant and the dispersion of rGO-MWCNTs was dropped on the GCE surface obtaining rGO-MWCNTs/GCE to simultaneously detect HQ, CT, p-cresol and nitrite. Interestingly, when using GCE, only two oxidation peaks were found with really low intensity, however, the presence of MWCNTs improved the selectivity, and four peaks were depicted. Then, hybrid MWCNT-graphene material enhanced the sensitivity of

the electrochemical measurements and the current intensity was improved compared to MWCNT modified electrode.

Finally, as regards to biosensing field, the main drawback in biosensor building is that proteins usually have their redox centers deeply buried. Therefore, it is difficult for electrons to be transferred between protein molecule and electrode surface. The question is whether graphene constitutes a new promise or not. In this sense, rGO has demonstrated its capacity for acting as electron donor, in which the protein can keep stability and its direct electron-transfer rate can be enhanced. Redox enzymes as glucose oxidase or proteins as hemoglobin are some of the examples that integrate via assembling with graphene surface as we will discuss below.

The direct detection of glucose based on the electrocatalytic reduction of oxygen using an electrode of glucose oxidase integrated with graphene⁸⁰ and with graphene/nafion film was studied.⁸¹ The voltammetric results indicated that glucose oxidase assembled on graphene retained its native structure and bioactivity. Besides, when graphene material was on the electrode, the currents were double than in the non-modified electrodes. The higher sensitivity and currents obtained using glucose oxidase /graphene-modified electrode compared to glucose oxidase /non-modified ones are due to the higher adsorption capacity and stronger interaction between glucose oxidase and graphene rather than between the oxidase and GCE, therefore, it suggests that a larger quantity of enzyme is assembled in the surface of the electrode.

A new biocomposite film based on graphene, zinc oxide nanospheres and hemoglobin has been developed for sensing hydrogen peroxide.⁸² It was obtained a biosensor that could retain the bioactivity and native structure of hemoglobin, indicating that the composite film

could provide a favorable environment for the immobilization of hemoglobin.

Cytochrome c embedded in a novel support matrix of graphene/poly (3,4-ethylenedioxythiophene) nano composite on a glassy carbon electrode was also studied.⁸³ The immobilized cytochrome c in the graphene matrix displays excellent direct electrochemistry and retains its biocatalytic activity towards the reduction of hydrogen peroxide.

II.1.3.3. Graphene nanoribbons: electrochemistry and applications

Graphene nanoribbons are unzipped CNTs with structural control. **Figure II.5** illustrates the different routes to open nanotubes that yield GNRs:⁸⁴ by chemical oxidation of the nanotubes,⁸⁴ by plasma etching of CNTs embedded in a polymer film,⁸⁵ by the intercalation of metals ⁸⁶ or nanoparticles ⁸⁷ and the posterior exfoliation or by the unwrapping MWCNTs using electrical current and nanomanipulation to produce a GNR of the desired width and length,⁸⁷ among others.

Considering their atomic structures, graphene edges are usually classified as zigzag, armchair, combined, and reconstructed types. Physical properties of finite-size graphene nanostructures are often determined by properties of the edge itself, and may substantially differ from those of perfect graphene sheet.

II.1. Graphene for electrochemical (bio)-sensing: *State of the art*

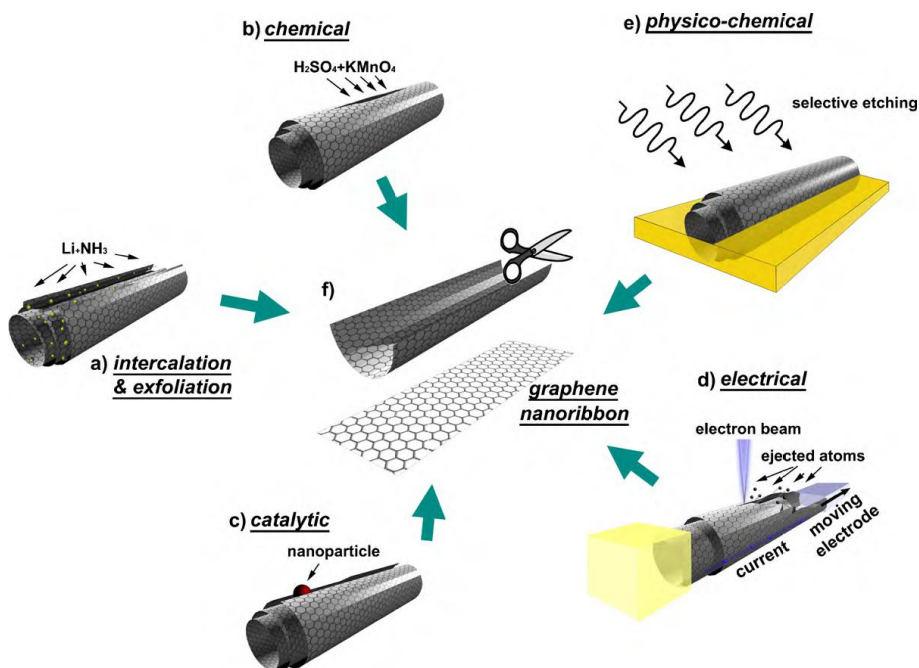


Figure II.5. Synthetic routes to yield GNRs from the unzipping of carbon nanotubes: (a) Intercalation-exfoliation of MWCNTs, involving treatments in liquid NH₃ and Li, and subsequent exfoliation using HCl and heat treatments; (b) chemical route, involving acid reactions (e.g. H₂SO₄ and KMnO₄ as oxidizing agents) that break carbon-carbon bonds; (c) catalytic approach, in which metal nanoparticles “cut” the nanotube longitudinally like a pair of scissors, (d) electrical method, by passing an electric current through a nanotube, and (e) physicochemical method by embedding the tubes in a polymer matrix followed by argon plasma treatment. The resulting structures are either GNRs or graphene sheets (f). Reprinted with permission of reference 84

Taking into account the most known chiral edge configurations of CNTs, at 0° (armchair) and at 30° (zigzag), it is possible to find armchair and zigzag nanoribbons, respectively. Moreover, armchair ones are semiconductors or conductors depending on the width of the ribbon, and zigzag ones are always conductors or present metallic behaviour, but they could also induce an energy gap depending on the field strength applied.⁸⁸ Furthermore, edge chemistry is an important characteristic of nanoribbons, because the edges present chemical functionalities such as carboxylic acid, carbonyl and amine, among others. Therefore, GNRs are significantly more chemically reactive than crystalline graphene, because graphene surfaces seem to be chemically inert and could only interact with other molecules by physical adsorption via π - π interaction and GNRs.²¹

Table II.6 (see page 52) shows the GNR materials used in the electrochemical detection of different analytes, some of them explored in real samples. Towards the selected examples, the potential of GNRs as an electrochemical transducer will be critically stated following the before explained approaches –thin film, composite and biosensor based electrodes– and remarking the chemical interaction with the detected molecule.

Graphene nanoribbons present an extreme reactivity due to the existing of open-ended graphene sheets. Thus, using GNRs as an electrocatalytic material for preparation of electrochemical sensors and biosensors would be worthy. The presence of a larger amount of edge plane-like defects on graphene and more sp^2 domains facilitates the rapid detection of several interesting molecules such as, catecholamines, neurotransmitters, NADH, H_2O_2 , guanine, tyrosine, adenine, etc., with better results than SWCNT and MWCNT.

However, GNRs for electrochemical sensing have been used in smaller extent than other graphenes.

As a result, functionalized GNRs obtained by the unzipping using a chemical oxidation of SWCNTs and its deposition on CSPEs has been evaluated for the detection of important molecules.⁸⁹ In general terms, the electrochemical response improved when graphene was used as electrochemical transducer around double or several times more the signal found in CSPEs. One isolated example where graphene did not improve the electrochemical sensing has been the detection of trinitrotoluene in seawater where no significant difference was found in the performance of graphite microparticles and single-, few-, and multilayer graphene nanoribbons, the sensitivities found were in the same range, being 40% higher in graphite material than in single-layer graphene materials.⁹⁰ However, recently the electrochemical potential of GNRs has been demonstrated in a deep study using three dihydroxybenzene isomers and other target molecules such as UA, AA, levodopa (LD) and L-tyrosine (L-Tyr),²¹ displaying reduced graphene nanoribbons analytical responses from 5 to 10-fold higher compared to the response of the GCE. Apart from the excellent responses obtained in all the cases, the interaction between oxygen groups of the graphene oxide nanoribbons and these target molecules plus the π - π interaction highly found with reduced graphene materials are described. Consequently, they open new opportunities for tailoring graphene to optimizing the sensing application based on the chemistry of the molecule.

1-hydroxypyrene is considered one of the metabolites of polycyclic aromatic hydrocarbons, and has been widely used as a urinary valuable biomarker for evaluation of human exposure to polycyclic

aromatic hydrocarbons.⁹¹ To reduce matrix interference in the real sample and achieve the required sensitivity, the analysis of 1-hydroxypyrene needs a pre-concentration procedure with a C18 and copper phthalocyanine that can selectively adsorb 1-hydroxypyrene via $\pi - \pi$ interaction due to the small π -electron system on it. Then, as graphene tends to be re-aggregated owing to π - π interactions between graphene layers, the authors designed a new route by inserting positively charged polyhedral oligomeric silsesquioxane nanocages into negatively charged graphene oxide nanoribbon layers. Apart from that, 1-hydroxypyrene has planar aromatic structures with a π -electron system, which interacts via π - π with graphene. When 1-hydroxypyrene is pre-concentrated on the composite graphene electrode, as the concentration is increased, the response signal is enhanced significantly. In this case, when graphene oxide nanoribbons were deposited on the electrode the response of the bare electrode improved 2 times but when 1-hydroxypyrene was evaluated with the composite framework the response increased in 12 times from that found in the bare electrode.

GNRs have been rarely explored in the biosensors building. A less toxic, reproducible, and easy method for producing functionalized multilayer graphene from MWCNTs in mass scale using only concentrated $\text{H}_2\text{SO}_4/\text{HNO}_3$ has been proposed. The thin film of functionalized multilayer graphene has been fabricated onto an ITO substrate by electrophoretic deposition technique. Then, urease and glutamate dehydrogenase has been immobilized using ethyl(dimethylaminopropyl) carbodiimide and N-hydroxy-succinimide chemistry.⁹² The biochemical reaction supposes the decomposition of urea into bicarbonate (HCO_3^-) and ammonium ions (NH_4^+) which is catalyzed by urease. Then, it is needed the addition of glutamate dehydrogenase that catalyzes the reaction between

II.1. Graphene for electrochemical (bio)-sensing: *State of the art*

NH_4^+ , α -ketoglutarate and NADH to obtain electrons that are transferred to the electrode.

Moreover, the integration of one model enzyme, glucose oxidase, has also been explored using GNRs. Firstly, reduced graphene nanoribbons non-covalently functionalized with water-soluble iron(III) meso-tetrakis(N-methylpyridinium-4-yl) porphyrin via π - π non-covalent interaction were deposited on GCE surface.⁹³ Using glucose oxidase as model enzyme, a biosensor based on the consumption of O_2 was developed and could be successfully applied in the detection of glucose in human serum.

II.1.4. Outlook and perspectives

In this section, the terminology in the graphenes field has been clarified to avoid misunderstandings. Furthermore, a complete analytical characterization of graphene is crucial to know the morphology and structure of the synthesized material.

Interestingly, the *state of the art* of graphene in electrochemical detection shows how some graphenes (tailored graphene) are more suitable than others to detect a target molecule. Furthermore, the interactions between these target molecules and either moieties or graphene lattice should be the objective to optimize and elucidate the best electrochemical sensing or biosensing. To sum up, graphene is a true new promise for selective and sensitive electrochemical sensing and biosensing.

Finally, in order to give a conceptual overview about the chemistry behind the electrochemistry, **Table II.7** summarizes the typical interactions that govern the enhancement in sensing and biosensing between graphenes and the target analytes.

II.1. Graphene for electrochemical (bio)-sensing: *State of the art*

Table II.7. Electrochemical detection with graphenes

Graphene	Structure	Target molecule	Interaction graphene-molecule	Analytical performance features	Ref
Graphene nanoplatelets	GO (few layers)	AA, UA	Hydrogen bond	Electrocatalysis and enhanced sensitivity	48
GO	GO (few layers)	4-nitrophenol	Hydrogen bonds plus π - π stacking	Low electrode fouling	50
GO	Graphene-COOH (few layers)	Adenine and guanine	Electrostatic	Enhanced sensitivity	51
rGO	Graphene film	Trinitrotoluene	Hydrogen bond and π - π stacking.	Improved limit of detection	70
rGO	Graphene film	Anthraquinones	π - π stacking	Enhanced sensitivity	76
GNR	rGO	CT, RS, AA, L-Tyr	Hydrogen bond and π - π	Electrocatalysis and enhanced sensitivity	21
GNR	GO	HQ, LD, UA	Hydrogen bond and π - π	Electrocatalysis and enhanced sensitivity	21
GNR	GO	1-hydroxypyrene	π - π	Low electrode fouling	91

Table II.1. Terminology and synthesis of graphene in Electroanalysis

Terminology	Synthetic Route	Synthesis conditions	Target molecule	Remarks	Ref	
Single layer	“Peeling off” highly oriented pyrolytic graphite		ND	First isolation of one layer of graphene	2	
Single layer	Mechanical cleavage		ND	Large surface area	94	
Single layer	Intercalation of small molecules in a graphite layer and exfoliation	Thermal shock	Neurotransmitters	Simple approach to obtain one layer. Possible structural defects	95	
		Ultrasonication			96	
Single and few layers	Epitaxial grown on silicon wafers		ND	Study of Dirac nature of the charge carriers	97	
Single and few-layers	CVD and epitaxial growth. Exposure of the metallic surface to H ₂ and CH ₄ gases. Isolation of graphene	On single crystalline transition metal: Cu, Co, Pt, Ir, Ru and Ni.		Bottom-up strategy. Metallic impurities contained in the layer	98	
Few- layers. Chemically modified graphene: GO and rGO.	Chemical treatment. ⁴² Oxidation of graphite to obtain graphite oxide, exfoliation (GO) and reduction (rGO)	Oxidation	Reduction	Cheap synthesis Low monolayer yields (1%). Structural defects. Small surface of layer. Introduction of heteroatomic impurities (almost N ₂ H ₄)	98	
		Hummer and Offerman’s method ⁹⁹	Chemical reduction			Catecholamines, neurotransmitters, drugs, hydroquinone, H ₂ O ₂ , adenine, guanine, tryptophan, tyrosine, uric acid, ascorbic acid, glucose, trinitrotoluene
		Brodie’s method ¹⁰⁰	Thermal reduction			
		Stadenmeier’s method ¹⁰¹	Electrochemical reduction			

ND. Not detected

Terminology	Synthetic Route	Synthesis conditions	Target molecule	Remarks	Ref
GNRs	“Unzipping” CNTs	Chemical oxidation of SWCNTs, open up after treatment ⁸⁴	Catecholamines, neurotransmitters, NADH, H ₂ O ₂ , guanine, tyrosine, adenine, urea, glucose, trinitrotoluene	Top-down strategy. Possible presence of unzipped CNTs	102, 103
		Plasma etching, opening up MWCNTs ⁸⁵			
		Lithium intercalation and exfoliation of MWCNTs ⁸⁶			
		Nanoparticles of Ni are used as nano-knives in a hydrogen atmosphere to act as catalytic hydrogenation of carbon ^{104,105}			
		Electrically unwrapping CNTs ⁸⁷			
		Ionic liquid assisted splitting action under microwave radiation ¹⁰⁶			
Graphene nanosheets	Chemical reduction of graphite oxide by environmental friendly agents: saccharides	Reduction with fructose, glucose, sacarose	Neurotransmitters: dopamine, adrenaline and noradrenalin	Green synthesis	107
Graphene nanosheets	Solvothermal synthesis using ethanol and sodium. By pyrolysis of the NaOEt obtained	Bottom-up approach	ND	Common reagents. Low cost. Bulk quantities	108

ND. Not detected

Table II.4. Graphene oxide applications in electrochemistry

GRAPHENE			ANALYTE DETECTION			SAMPLE ANALYSIS		Ref
Material	Graphene synthesis	Electrode (modification)	Analyte	Electrochemical technique	Measurement media	Sample	Sample preparation	
Nanoplatelets of graphitic oxide	Hummer's method. Microwave-solvothermal reduction.	GO/CSPE	Uric acid and ascorbic acid	Linear voltamperometry. +0.80 to -0.20 V.	Phosphate buffer 0.1 M, pH 7.40	ND	ND	48
GO	Hummer's method and suspended in DMF and ultrasonication	GO/GCE	4-nitrophenol	Linear voltamperometry +0.20 to -1.00 V	Acetate buffer 0.1 M, pH 4.80	Water sample	Spiking the sample.	50
Graphene-COOH	Hummer's modified method. Heat and acid media to oxidize	Graphene-COOH/GCE	Adenine and guanine	DPV. +0.60 to +1.50 V	Acetate buffer 0.1 M, pH 4.50	Blood serum and plasma.	Thermal denaturation of dsDNA.	51
GO	Hummer's and ultrasonication.	Nafion/GO/GCE	Caffeine	DPV. +0.80 to +1.60 V	H ₂ SO ₄ 0.1 M, pH 0.95	Cola, Tea and energy drinks.	Degasification and spiking.	52
GO	Hummer's method and ultrasonication.	Nafion/GO/GCE	Colchicine	Square wave voltammetry. +0.50 to +1.10 V	H ₂ SO ₄ 0.1 M	Drug tablet	Tablets are grinding, extracted with NaOH and centrifugated.	53
GO	Modified Hummer's method.	Ferrocene-chitosan/GO/enzyme GCE	Glucose	Amperometry +0.30 V vs. Ag/AgCl (sat. KCl)	Phosphate buffer saline 0.1 M, pH 6.98	ND	ND	54

ND. Not detected

Table II.5. Reduced graphene oxide applications in electrochemistry.

GRAPHENE			ANALYTE DETECTION			SAMPLE ANALYSIS		Ref
Material	Graphene synthesis	Electrode (modification)	Analyte	Electrochemical technique	Measurement media	Sample	Sample preparation	
Chemically rGO	GO reduced with N_2H_4/NH_3 .	Electrophoretic deposition. Graphene film/GCE	Trinitrotoluene	DPV. -0.10 to -0.80 V	Phosphate buffer 0.1 M, pH 6.50	ND	ND	70
Chemically rGO	GO reduced with N_2H_4/NH_3 .	Graphene/GCE	Dopamine	DPV. -0.20 to +0.50 V.	Phosphate buffer 0.01 M, pH 7.40	ND	ND	87
Electrochemically reduced graphene oxide (erGO)	GO reduced by CVs.	Graphene/GCE	Hydroquinone and catechol	DPV. -0.10 to +0.50 V.	Acetate buffer 0.2 M, pH 5.80	ND	ND	66
Chemically rGO	GO reduction by N_2H_4/NH_3	rGO/GCE	Catechol and hydroquinone	DPV. 0.00 to +0.60 V.	Acetate buffer 0.1 M pH 4.50	Tap water	Samples are spiked.	65

ND. Not detected

GRAPHENE			ANALYTE DETECTION			SAMPLE ANALYSIS		Ref
Material	Graphene synthesis	Electrode (modification)	Analyte	Electrochemical technique	Measurement media	Sample	Sample preparation	
Chemically rGO	GO reduced with N ₂ H ₄ /NH ₃ .	Graphene/ layered double hydroxides /GCE	Dopamine	Square wave voltammetry. -0.20 to +0.50 V.	Phosphate buffer 0.1 M pH 7.00	Dopamine hydrochloride injection	Spiked sample	109
Chemically rGO	GO reduced with N ₂ H ₄ /NH ₃ .	Graphene-chitosan/GCE	Catechol, resorcinol and hydroquinone	DPV -0.20 to +0.70 V	Phosphate buffer 0.1 M pH 7.00	Tap, river, lake and sanitary waste water	Spiked sample	73
Thermally rGO	GO reduced by solvothermal process.	Cu ₂ O/Graphene/ GCE	Dopamine	CV -0.10 to +0.80 V	Phosphate buffer 0.1 M pH 5.00	Dopamine hydrochloride injection	Dilution	110
Chemically rGO	GO reduced with N ₂ H ₄ /NH ₃ .	Nafion/TiO ₂ -graphene	L-tryptophan and L-tyrosine	DPV. +0.50 to +0.90 V.	Phosphate buffer 0.1 M pH 6.00	ND	ND	111
Chemically rGO	GO reduced with N ₂ H ₄ /NH ₃ .	Porphyrin-graphene/ GCE	Dopamine	DPV. 0.00 to +0.50 V.	Phosphate buffer 0.1 M pH 7.00	Hydrochloride injection, human urine and serum samples	Serum and urine were diluted. Injection was spiked.	77
Chemically rGO	GO ultrasonicated and reduced.	Siloxane-rGO-osmium complex-ITO	R and S-1,1'-2-binaphthol	DPV. -0.10 to +1.00 V.	0.05 M NaClO ₄ (H ₂ O/CH ₃ CN 2:1 v/v).	ND	ND	78

GRAPHENE			ANALYTE DETECTION			SAMPLE ANALYSIS		Ref
Material	Graphene synthesis	Electrode (modification)	Analyte	Electrochemical technique	Measurement media	Sample	Sample preparation	
Chemically rGO	Commercial GO reduced with PEI	rGO-MWCNTs	Catechol, hydroquinone, p-cresol and nitrite	CV. -0.20 to +1.00 V	Phosphate buffer 0.1 M, pH 7.00	River water sample	Spiked samples	79
Chemically rGO	GO reduced with ascorbic acid.	Chitosan/rGO/GCE	Dopamine and ascorbic acid	DPV. -0.20 to 0.80 V.	Phosphate buffer 0.1 M, pH 4.00	Human serum sample	Spiked samples	74
Electrochemically rGO	Reduction of GO at -1.3 V vs. SCE for 300 s.	erGO-ion liquid/GCE	Rutin	DPV. +0.80 to +0.10 V.	Phosphate buffer 0.1 M, pH 2.50	Tablets, human serum and urine.	Tablets were ground and diluted. Serum and urine were diluted and spiked.	112
Electrochemically rGO	GO reduced by CV.	Poly (L-Arginine)/erGO/GCE	Uric acid, xanthine, hypoxanthine	DPV. 0.00 to +1.20 V	Phosphate buffer 0.1 M, pH 7.00	Human urine	Dilution	75
Thermal rGO	Commercial GO reduced at 90 °C.	AuNPs- β -cyclodextrin-GO	Ascorbic acid, dopamine and uric acid	Square wave voltammetry. 0.00 to +0.70 V	0.1 M NaH ₂ PO ₄ /HCl pH 2.00	Urine	Dilution	113
Chemically rGO	GO reduced with N ₂ H ₄ /NH ₃ .	glucose oxidase-graphene/GCE	Glucose	CV. -0.05 to -0.65 V.	Phosphate buffer 0.1 M, pH 6.90	Human blood serum	Dilution	80

GRAPHENE			ANALYTE DETECTION			SAMPLE ANALYSIS		Ref
Material	Graphene synthesis	Electrode (modification)	Analyte	Electrochemical technique	Measurement media	Sample	Sample preparation	
Chemically rGO	GO reduced with H_2O_2/H^+ .	Hemoglobin/graphene-ZnO nanosphere/ Au electrode	Hydrogen peroxide	Chronoamperometry -0.30 V vs. not-reported	Phosphate buffer 0.1 M, pH 6.50	ND	ND	82
Not reported (Graphene)	Not reported	Graphene-chitosan /hemoglobin/ graphene/ ion liquid/GCE	Nitromethane	Chronoamperometry -0.35 V vs. saturated calomel electrode (SCE)	Phosphate buffer 0.1 M, pH 7.00	Freshwater	Direct amperometric measure	114
Chemically rGO	GO reduced with N_2H_4/NH_3 .	GO/PEDOT	Cytocrome C. (H_2O_2)	Chronoamperometry 0 V vs. Ag/AgCl (3 M KCl)	Phosphate buffer 10 mM, pH 7.00	ND	ND	83
Graphene	Not reported	Enzyme/AgNPs/ graphene-chitosan/GCE	Sarcoxine oxidase (H_2O_2)	Chronoamperometry -0.45 V vs. SCE	Phosphate buffer 0.1 M, pH 7.00	ND	ND	115
Graphene sheet	Direct Arc-discharge method	Enzyme/graphene/ Nafion/ GCE	Glucose	CV. -0.80 to +0.80 V	Phosphate buffer 0.2 M, pH=7.40	ND	ND	81

Table II.6. Graphene nanoribbons applications in electrochemistry

GRAPHENE			ANALYTE DETECTION			SAMPLE ANALYSIS		Ref
Material	Graphene synthesis	Electrode (modification)	Analyte	Electrochemical technique	Measurement media	Sample	Sample preparation	
Functionalized multilayer graphene	Unzipping MWCNTs. Sonication and oxidation under H ₂ SO ₄ /HNO ₃	Electrophoretic deposition on ITO and covalent immobilization of enzymes	Urea	CV. -0.75 to +0.75 V	Phosphate buffer 50 mM, pH 7.00, 0.9% NaCl	ND	ND	92
GNRred	Unzipping MWCNTs by oxidation	GNRs/GCE and immobilization glucose oxidase	Glucose	Amperometry -0.41 V vs. SCE	Phosphate buffer 0.1 M, pH 7.40	Human serum	Dilution	93
GNRox	Unzipping MWCNTs by oxidation with KMnO ₄ and H ₂ SO ₄	Deposition of GNRox/polymer on GCE	1-hydroxypyrene	DPV. -0.30 to +0.80 V.	Phosphate buffer 50 mM, pH 2.00 NaCl 0.2 M	ND	ND	91
Single, few and multilayer GNRs (commercial)	Commercial synthesis	Deposition of GNR on GCE	2,4,6-trinitrotoluene	DPV. +0.60 to -1.00 V	0.5 M NaCl	Seawater	Spiked with trinitrotoluene	90

II.1.5. References.

1. <http://ec.europa.eu/environment/chemicals/nanotech/#definition>. (August 9, 2015).
2. Novoselov, K. S.; Geim, A. K.; Morozov, S. V.; Jiang, D.; Zhang, Y.; Dubonos, S. V.; Grigorieva, I. V.; Firsov, A. A. Electric field effect in atomically thin carbon films. *Science* **2004**, *306*, 666-669.
3. Fitzer, E.; Kochling, K.-H.; Boehm, H. P.; Marsh, H. Recommended terminology for the description of carbon as a solid. *Pure Appl. Chem.* **1995**, *67*, 473-506.
4. Goh, M. S.; Pumera, M. Multilayer graphene nanoribbons exhibit larger capacitance than their few-layer and single-layer graphene counterparts. *Electrochem. Commun.* **2010**, *12*, 1375-1377.
5. Stankovich, S.; Dikin, D. A.; Dommett, G. H. B.; Kohlhaas, K. M.; Zimney, E. J.; Stach, E. A.; Piner, R. D.; Nguyen, S. T.; Ruoff, R. S. Graphene-based composite materials. *Nature* **2006**, *442*, 282-286.
6. Park, S.; Ruoff, R. S. Chemical methods for the production of graphenes. *Nat. Nanotechnol.* **2009**, *4*, 217-224.
7. Lee, C.; Wei, X.; Kysar, J. W.; Hone, J. Measurement of the elastic properties and intrinsic strength of monolayer graphene. *Science* **2008**, *321*, 385-388.
8. Eizenberg, M.; Blakely, J. M. Carbon Monolayer Phase Condensation on Ni(111). *Surf. Sci.* **1979**, *82*, 228-236.
9. Singh, V.; Joung, D.; Zhai, L.; Das, S.; Khondaker, S. I.; Seal, S. Graphene based materials: Past, present and future. *Prog. Mater. Sci.* **2011**, *56*, 1178-1271.
10. Paredes, J. I.; Villar-Rodil, S.; Martinez-Alonso, A.; Tascon, J. M. D. Graphene oxide dispersions in organic solvents. *Langmuir* **2008**, *24*, 10560-10564.
11. Stankovich, S.; Dikin, D. A.; Piner, R. D.; Kohlhaas, K. A.; Kleinhammes, A.; Jia, Y.; Wu, Y.; Nguyen, S. T.; Ruoff, R. S. Synthesis of graphene-based nanosheets via chemical reduction of exfoliated graphite oxide. *Carbon* **2007**, *45*, 1558-1565.
12. Koh, Y. K.; Bae, M.; Cahill, D. G.; Pop, E. Reliably Counting Atomic Planes of Few-Layer Graphene ($n > 4$). *Acs Nano* **2011**, *5*, 269-274.
13. Zhang, L.; Li, Y.; Zhang, L.; Li, D.; Karpuzov, D.; Long, Y. Electrocatalytic Oxidation of NADH on Graphene Oxide and Reduced Graphene Oxide Modified Screen-Printed Electrode. *Int. J. Electrochem. Sc.* **2011**, *6*, 819-829.
14. Ambrosi, A.; Bonanni, A.; Sofer, Z.; Cross, J. S.; Pumera, M. Electrochemistry at Chemically Modified Graphenes. *Chem.-Eur. J.* **2011**, *17*, 10763-10770.

II.1. Graphene for electrochemical (bio)-sensing: *State of the art*

15. Valles, C.; Drummond, C.; Saadaoui, H.; Furtado, C. A.; He, M.; Roubeau, O.; Ortolani, L.; Monthieux, M.; Penicaud, A. Solutions of Negatively Charged Graphene Sheets and Ribbons. *J. Am. Chem. Soc.* **2008**, *130*, 15802-15804.
16. Novoselov, K. S.; Jiang, D.; Schedin, F.; Booth, T. J.; Khotkevich, V. V.; Morozov, S. V.; Geim, A. K. Two-dimensional atomic crystals. *Proc. Natl. Acad. Sci. USA* **2005**, *102*, 10451-10453.
17. Zhou, M.; Zhai, Y.; Dong, S. Electrochemical Sensing and Biosensing Platform Based on Chemically Reduced Graphene Oxide. *Anal. Chem.* **2009**, *81*, 5603-5613.
18. Ferrari, A. C.; Meyer, J. C.; Scardaci, V.; Casiraghi, C.; Lazzeri, M.; Mauri, F.; Piscanec, S.; Jiang, D.; Novoselov, K. S.; Roth, S.; Geim, A. K. Raman spectrum of graphene and graphene layers. *Phys. Rev. Lett.* **2006**, *97*, 187401.
19. Tuinstra, F.; Koenig, J. L. Raman Spectrum of Graphite. *J. Chem. Phys.* **1970**, *53*, 1126-&.
20. Cheng, M.; Yang, R.; Zhang, L.; Shi, Z.; Yang, W.; Wang, D.; Xie, G.; Shi, D.; Zhang, G. Restoration of graphene from graphene oxide by defect repair. *Carbon* **2012**, *50*, 2581-2587.
21. Martín, A.; Hernández, J.; Vázquez, L.; Martínez, M. T.; Escarpa, A. Controlled chemistry of tailored graphene nanoribbons for electrochemistry: a rational approach to optimizing molecule detection. *RSC Adv.* **2014**, *4*, 132-139.
22. Acik, M.; Lee, G.; Mattevi, C.; Pirkle, A.; Wallace, R. M.; Chhowalla, M.; Cho, K.; Chabal, Y. The Role of Oxygen during Thermal Reduction of Graphene Oxide Studied by Infrared Absorption Spectroscopy. *J. Phys. Chem. C* **2011**, *115*, 19761-19781.
23. He, H. Y.; Riedl, T.; Lerf, A.; Klinowski, J. Solid-state NMR studies of the structure of graphite oxide. *J. Phys. Chem.* **1996**, *100*, 19954-19958.
24. He, G.; Chen, H.; Zhu, J.; Bei, F.; Sun, X.; Wang, X. Synthesis and characterization of graphene paper with controllable properties via chemical reduction. *J. Mater. Chem.* **2011**, *21*, 14631-14638.
25. Pumera, M. Electrochemistry of graphene, graphene oxide and other graphenoids: Review. *Electrochem. Commun.* **2013**, *36*, 14-18.
26. Pumera, M.; Ambrosi, A.; Bonanni, A.; Chng, E. L. K.; Poh, H. L. Graphene for electrochemical sensing and biosensing. *Trends Anal. Chem.* **2010**, *29*, 954-965.
27. Yang, W.; Ratinac, K. R.; Ringer, S. P.; Thordarson, P.; Gooding, J. J.; Braet, F. Carbon Nanomaterials in Biosensors: Should You Use Nanotubes or Graphene? *Angew. Chem. Int. Ed.* **2010**, *49*, 2114-2138.

II.1. Graphene for electrochemical (bio)-sensing: *State of the art*

28. Brownson, D. A. C.; Kampouris, D. K.; Banks, C. E. Graphene electrochemistry: fundamental concepts through to prominent applications. *Chem. Soc. Rev.* **2012**, *41*, 6944-6976.
29. Pumera, M. Graphene-based nanomaterials and their electrochemistry. *Chem. Soc. Rev.* **2010**, *39*, 4146-4157.
30. Ambrosi, A.; Pumera, M. Nanographite Impurities Dominate Electrochemistry of Carbon Nanotubes. *Chem.-Eur. J.* **2010**, *16*, 10946-10949.
31. Banks, C. E.; Crossley, A.; Salter, C.; Wilkins, S. J.; Compton, R. G. Carbon nanotubes contain metal impurities which are responsible for the "electrocatalysis" seen at some nanotube-modified electrodes. *Angew. Chem. Int. Ed.* **2006**, *45*, 2533-2537.
32. Escarpa, A. Food electroanalysis: sense and simplicity. *Chemical Rec.* **2012**, *12*, 72-91.
33. Pumera, M. Electrochemistry of Graphene: New Horizons for Sensing and Energy Storage. *Chemical Rec.* **2009**, *9*, 211-223.
34. Shao, Y.; Wang, J.; Wu, H.; Liu, J.; Aksay, I. A.; Lin, Y. Graphene Based Electrochemical Sensors and Biosensors: A Review. *Electroanalysis* **2010**, *22*, 1027-1036.
35. Wu, S.; He, Q.; Tan, C.; Wang, Y.; Zhang, H. Graphene-Based Electrochemical Sensors. *Small* **2013**, *9*, 1160-1172.
36. Kuila, T.; Bose, S.; Khanra, P.; Mishra, A. K.; Kim, N. H.; Lee, J. H. Recent advances in graphene-based biosensors. *Biosens. Bioelectron.* **2011**, *26*, 4637-4648.
37. Ratnac, K. R.; Yang, W.; Gooding, J. J.; Thordarson, P.; Braet, F. Graphene and Related Materials in Electrochemical Sensing. *Electroanalysis* **2011**, *23*, 803-826.
38. Artiles, M. S.; Rout, C. S.; Fisher, T. S. Graphene-based hybrid materials and devices for biosensing. *Adv. Drug Deliv. Rev.* **2011**, *63*, 1352-1360.
39. Alwarappan, S.; Erdem, A.; Liu, C.; Li, C. Probing the Electrochemical Properties of Graphene Nanosheets for Biosensing Applications. *J. Phys. Chem. C* **2009**, *113*, 8853-8857.
40. Park, S.; An, J.; Jung, I.; Piner, R. D.; An, S. J.; Li, X.; Velamakanni, A.; Ruoff, R. S. Colloidal Suspensions of Highly Reduced Graphene Oxide in a Wide Variety of Organic Solvents. *Nano Lett.* **2009**, *9*, 1593-1597.
41. Lotya, M.; King, P. J.; Khan, U.; De, S.; Coleman, J. N. High-Concentration, Surfactant-Stabilized Graphene Dispersions. *ACS Nano* **2010**, *4*, 3155-3162.

II.1. Graphene for electrochemical (bio)-sensing: *State of the art*

42. Dreyer, D. R.; Park, S.; Bielawski, C. W.; Ruoff, R. S. The chemistry of graphene oxide. *Chem. Soc. Rev.* **2010**, *39*, 228-240.
43. He, H. Y.; Klinowski, J.; Forster, M.; Lerf, A. A new structural model for graphite oxide. *Chem. Phys. Lett.* **1998**, *287*, 53-56.
44. Lerf, A.; He, H. Y.; Forster, M.; Klinowski, J. Structure of graphite oxide revisited. *J. Phys. Chem. B* **1998**, *102*, 4477-4482.
45. Li, D.; Mueller, M. B.; Gilje, S.; Kaner, R. B.; Wallace, G. G. Processable aqueous dispersions of graphene nanosheets. *Nat. Nanotechnol.* **2008**, *3*, 101-105.
46. Dikin, D. A.; Stankovich, S.; Zimney, E. J.; Piner, R. D.; Dommett, G. H. B.; Evmenenko, G.; Nguyen, S. T.; Ruoff, R. S. Preparation and characterization of graphene oxide paper. *Nature* **2007**, *448*, 457-460.
47. Mkhoyan, K. A.; Contryman, A. W.; Silcox, J.; Stewart, D. A.; Eda, G.; Mattevi, C.; Miller, S.; Chhowalla, M. Atomic and Electronic Structure of Graphene-Oxide. *Nano Letters* **2009**, *9*, 1058-1063.
48. Chang, J.; Chang, K.; Hu, C.; Cheng, W.; Zen, J. Improved voltammetric peak separation and sensitivity of uric acid and ascorbic acid at nanoplatelets of graphitic oxide. *Electrochem. Commun.* **2010**, *12*, 596-599.
49. Zhou, Y.; Bao, Q.; Tang, L. A. L.; Zhong, Y.; Loh, K. P. Hydrothermal Dehydration for the "Green" Reduction of Exfoliated Graphene Oxide to Graphene and Demonstration of Tunable Optical Limiting Properties. *Chem. Mat.* **2009**, *21*, 2950-2956.
50. Li, J.; Kuang, D.; Feng, Y.; Zhang, F.; Xu, Z.; Liu, M. A graphene oxide-based electrochemical sensor for sensitive determination of 4-nitrophenol. *J. Hazard. Mater.* **2012**, *201*, 250-259.
51. Huang, K.; Niu, D.; Sun, J.; Han, C.; Wu, Z.; Li, Y.; Xiong, X. Novel electrochemical sensor based on functionalized graphene for simultaneous determination of adenine and guanine in DNA. *Colloid. Surface. B* **2011**, *82*, 543-549.
52. Zhao, F.; Wang, F.; Zhao, W.; Zhou, J.; Liu, Y.; Zou, L.; Ye, B. Voltammetric sensor for caffeine based on a glassy carbon electrode modified with Nafion and graphene oxide. *Microchim. Acta* **2011**, *174*, 383-390.
53. Wang, F.; Zhou, J.; Liu, Y.; Wu, S.; Song, G.; Ye, B. Electrochemical oxidation behavior of colchicine on a graphene oxide-Nafion composite film modified glassy carbon electrode. *Analyst* **2011**, *136*, 3943-3949.
54. Qiu, J.; Huang, J.; Liang, R. Nanocomposite film based on graphene oxide for high performance flexible glucose biosensor. *Sensor. Actuat. B-Chem.* **2011**, *160*, 287-294.

II.1. Graphene for electrochemical (bio)-sensing: *State of the art*

55. Zhang, J.; Zhang, F.; Yang, H.; Huang, X.; Liu, H.; Zhang, J.; Guo, S. Graphene Oxide as a Matrix for Enzyme Immobilization. *Langmuir* **2010**, *26*, 6083-6085.
56. Zhang, Y.; Zhang, J.; Huang, X.; Zhou, X.; Wu, H.; Guo, S. Assembly of Graphene Oxide-Enzyme Conjugates through Hydrophobic Interaction. *Small* **2012**, *8*, 154-159.
57. Gao, X.; Jang, J.; Nagase, S. Hydrazine and Thermal Reduction of Graphene Oxide: Reaction Mechanisms, Product Structures, and Reaction Design. *J. Phys. Chem. C* **2010**, *114*, 832-842.
58. Boukhalov, D. W.; Katsnelson, M. I. Modeling of graphite oxide. *J. Am. Chem. Soc.* **2008**, *130*, 10697-10701.
59. Pu, N.; Wang, C.; Liu, Y.; Sung, Y.; Wang, D.; Ger, M. Dispersion of graphene in aqueous solutions with different types of surfactants and the production of graphene films by spray or drop coating. *J. Taiwan Inst. Chem. E.* **2012**, *43*, 140-146.
60. Brownson, D. A. C.; Metters, J. P.; Kampouris, D. K.; Banks, C. E. Graphene Electrochemistry: Surfactants Inherent to Graphene Can Dramatically Effect Electrochemical Processes. *Electroanalysis* **2011**, *23*, 894-899.
61. Cao, A.; Liu, Z.; Chu, S.; Wu, M.; Ye, Z.; Cai, Z.; Chang, Y.; Wang, S.; Gong, Q.; Liu, Y. A Facile One-step Method to Produce Graphene-CdS Quantum Dot Nanocomposites as Promising Optoelectronic Materials. *Adv Mater* **2010**, *22*, 103-106.
62. Guo, S.; Dong, S.; Wang, E. Three-Dimensional Pt-on-Pd Bimetallic Nanodendrites Supported on Graphene Nanosheet: Facile Synthesis and Used as an Advanced Nanoelectrocatalyst for Methanol Oxidation. *Acs Nano* **2010**, *4*, 547-555.
63. Wang, Y. L.; Zhao, G. C. Electrochemical Sensing of Nitric Oxide on Electrochemically reduced Graphene-Modified Electrode. *J. Electrochem.* **2011**, 482780.
64. Navaee, A.; Salimi, A.; Teymourian, H. Graphene nanosheets modified glassy carbon electrode for simultaneous detection of heroine, morphine and noscapine. *Biosens. Bioelectron.* **2012**, *31*, 205-211.
65. Du, H.; Ye, J.; Zhang, J.; Huang, X.; Yu, C. A voltammetric sensor based on graphene-modified electrode for simultaneous determination of catechol and hydroquinone. *J Electroanal Chem* **2011**, *650*, 209-213.
66. Chen, L.; Tang, Y.; Wang, K.; Liu, C.; Luo, S. Direct electrodeposition of reduced graphene oxide on glassy carbon electrode and its electrochemical application. *Electrochem. Commun.* **2011**, *13*, 133-137.
67. Ping, J.; Wu, J.; Wang, Y.; Ying, Y. Simultaneous determination of ascorbic acid, dopamine and uric acid using high-performance screen-printed graphene electrode. *Biosens. Bioelectron.* **2012**, *34*, 70-76.

II.1. Graphene for electrochemical (bio)-sensing: *State of the art*

68. Wu, Z.; Pei, S.; Ren, W.; Tang, D.; Gao, L.; Liu, B.; Li, F.; Liu, C.; Cheng, H. Field Emission of Single-Layer Graphene Films Prepared by Electrophoretic Deposition. *Adv Mater* **2009**, *21*, 1756-1760.
69. Chavez-Valdez, A.; Shaffer, M. S. P.; Boccaccini, A. R. Applications of Graphene Electrophoretic Deposition. A Review. *J Phys Chem B* **2013**, *117*, 1502-1515.
70. Tang, L.; Feng, H.; Cheng, J.; Li, J. Uniform and rich-wrinkled electrophoretic deposited graphene film: a robust electrochemical platform for TNT sensing. *Chem. Commun.* **2010**, *46*, 5882-5884.
71. Xiong, H.; Jin, B. The electrochemical behavior of AA and DA on graphene oxide modified electrodes containing various content of oxygen functional groups. *J Electroanal Chem* **2011**, *661*, 77-83.
72. Chee, S. Y.; Pumera, M. Comparison of the electroanalytical performance of chemically modified graphenes (CMGs) using uric acid. *Electrochem. Commun.* **2012**, *20*, 141-144.
73. Yin, H.; Zhang, Q.; Zhou, Y.; Ma, Q.; Liu, T.; Zhu, L.; Ai, S. Electrochemical behavior of catechol, resorcinol and hydroquinone at graphene-chitosan composite film modified glassy carbon electrode and their simultaneous determination in water samples. *Electrochim. Acta* **2011**, *56*, 2748-2753.
74. Zhu, X.; Liu, Q.; Zhu, X.; Li, C.; Xu, M.; Liang, Y. Reduction of Graphene Oxide Via Ascorbic Acid and Its Application for Simultaneous Detection of Dopamine And Ascorbic Acid. *Int. J. Electrochem. Sc.* **2012**, *7*, 5172-5184.
75. Zhang, F.; Wang, Z.; Zhang, Y.; Zheng, Z.; Wang, C.; Du, Y.; Ye, W. Simultaneous electrochemical determination of uric acid, xanthine and hypoxanthine based on poly(L-arginine)/graphene composite film modified electrode. *Talanta* **2012**, *93*, 320-325.
76. Li, J.; Chen, J.; Zhang, X.; Lu, C.; Yang, H. A novel sensitive detection platform for antitumor herbal drug aloe-emodin based on the graphene modified electrode. *Talanta* **2010**, *83*, 553-558.
77. Wu, L.; Feng, L.; Ren, J.; Qu, X. Electrochemical detection of dopamine using porphyrin-functionalized graphene. *Biosens. Bioelectron.* **2012**, *34*, 57-62.
78. Bu, Y.; Wang, S.; Chen, Q.; Jin, H.; Lin, J.; Wang, J. Self-assembly of osmium complexes on reduced graphene oxide: A case study toward electrochemical chiral sensing. *Electrochem. Commun.* **2012**, *16*, 80-83.
79. Hu, F.; Chen, S.; Wang, C.; Yuan, R.; Yuan, D.; Wang, C. Study on the application of reduced graphene oxide and multiwall carbon nanotubes hybrid materials for simultaneous determination of catechol, hydroquinone, p-cresol and nitrite. *Anal. Chim. Acta* **2012**, *724*, 40-46.
80. Wu, P.; Shao, Q.; Hu, Y.; Jin, J.; Yin, Y.; Zhang, H.; Cai, C. Direct electrochemistry of glucose oxidase assembled on graphene and application to glucose detection. *Electrochim. Acta* **2010**, *55*, 8606-8614.

II.1. Graphene for electrochemical (bio)-sensing: *State of the art*

81. Zhang Yanqin; Fan Youjun; Wang Shanshan; Tan Yiliang; Shen Xingcan; Shi Zujin Facile Fabrication of a Graphene-based Electrochemical Biosensor for Glucose Detection. *Chinese J. Chem.* **2012**, *30*, 1163-1167.
82. Xu, J.; Liu, C.; Wu, Z. Direct electrochemistry and enhanced electrocatalytic activity of hemoglobin entrapped in graphene and ZnO nanosphere composite film. *Microchim. Acta* **2011**, *172*, 425-430.
83. Wang, G.; Qian, Y.; Cao, X.; Xia, X. Direct electrochemistry of cytochrome c on a graphene/poly (3,4-ethylenedioxythiophene) nanocomposite modified electrode. *Electrochem. Commun.* **2012**, *20*, 1-3.
84. Kosynkin, D. V.; Higginbotham, A. L.; Sinitskii, A.; Lomeda, J. R.; Dimiev, A.; Price, B. K.; Tour, J. M. Longitudinal unzipping of carbon nanotubes to form graphene nanoribbons. *Nature* **2009**, *458*, 872-U5.
85. Jiao, L.; Zhang, L.; Wang, X.; Diankov, G.; Dai, H. Narrow graphene nanoribbons from carbon nanotubes. *Nature* **2009**, *458*, 877-880.
86. Cano-Marquez, A. G.; Rodriguez-Macias, F. J.; Campos-Delgado, J.; Espinosa-Gonzalez, C. G.; Tristan-Lopez, F.; Ramirez-Gonzalez, D.; Cullen, D. A.; Smith, D. J.; Terrones, M.; Vega-Cantu, Y. I. Ex-MWNTs: Graphene Sheets and Ribbons Produced by Lithium Intercalation and Exfoliation of Carbon Nanotubes. *Nano Letters* **2009**, *9*, 1527-1533.
87. Kim, K.; Sussman, A.; Zettl, A. Graphene Nanoribbons Obtained by Electrically Unwrapping Carbon Nanotubes. *Acs Nano* **2010**, *4*, 1362-1366.
88. Huang, Y. C.; Chang, C. P.; Lin, M. F. Electric-field induced modification of electronic properties of few-layer graphene nanoribbons. *J. Appl. Phys.* **2008**, *104*, 103714.
89. Valentini, F.; Romanazzo, D.; Carbone, M.; Palleschi, G. Modified Screen-Printed Electrodes Based on Oxidized Graphene Nanoribbons for the Selective Electrochemical Detection of Several Molecules. *Electroanalysis* **2012**, *24*, 872-881.
90. Goh, M. S.; Pumera, M. Graphene-based electrochemical sensor for detection of 2,4,6-trinitrotoluene (TNT) in seawater: the comparison of single-, few-, and multilayer graphene nanoribbons and graphite microparticles. *Anal. Bioanal. Chem.* **2011**, *399*, 127-131.
91. Shen, X.; Cui, Y.; Pang, Y.; Qian, H. Graphene oxide nanoribbon and polyhedral oligomeric silsesquioxane assembled composite frameworks for pre-concentrating and electrochemical sensing of 1-hydroxypyrene. *Electrochim. Acta* **2012**, *59*, 91-99.
92. Srivastava, R. K.; Srivastava, S.; Narayanan, T. N.; Mahlotra, B. D.; Vajtai, R.; Ajayan, P. M.; Srivastava, A. Functionalized Multilayered Graphene Platform for Urea Sensor. *Acs Nano* **2012**, *6*, 168-175.

II.1. Graphene for electrochemical (bio)-sensing: *State of the art*

93. Zhang, S.; Tang, S.; Lei, J.; Dong, H.; Ju, H. Functionalization of graphene nanoribbons with porphyrin for electrocatalysis and amperometric biosensing. *J. Electroanal. Chem.* **2011**, *656*, 285-288.
94. Jayasena, B.; Subbiah, S. A novel mechanical cleavage method for synthesizing few-layer graphenes. *Nanoscale Res. Lett.* **2011**, *6*, 95.
95. Yu, A.; Ramesh, P.; Itkis, M. E.; Bekyarova, E.; Haddon, R. C. Graphite nanoplatelet-epoxy composite thermal interface materials. *J. Phys. Chem. C* **2007**, *111*, 7565-7569.
96. Ang, P. K.; Wang, S.; Bao, Q.; Thong, J. T. L.; Loh, K. P. High-Throughput Synthesis of Graphene by Intercalation - Exfoliation of Graphite Oxide and Study of Ionic Screening in Graphene Transistor. *ACS Nano* **2009**, *3*, 3587-3594.
97. de Heer, W. A.; Berger, C.; Wu, X.; First, P. N.; Conrad, E. H.; Li, X.; Li, T.; Sprinkle, M.; Hass, J.; Sadowski, M. L.; Potemski, M.; Martinez, G. Epitaxial graphene. *Solid State Commun.* **2007**, *143*, 92-100.
98. Reina, A.; Jia, X.; Ho, J.; Nezich, D.; Son, H.; Bulovic, V.; Dresselhaus, M. S.; Kong, J. Large Area, Few-Layer Graphene Films on Arbitrary Substrates by Chemical Vapor Deposition. *Nano Letters* **2009**, *9*, 30-35.
99. Hummers, W. S.; Offeman, R. E. Preparation of Graphitic Oxide. *J. Am. Chem. Soc.* **1958**, *80*, 1339-1339.
100. Brodie, B. C. Sur le poids atomique du graphite *Ann Chim Phys* **1860**, *59*, 466-472.
101. Staudenmaier, L. Verfahren zur Darstellung der Graphitsäure. *Ber Dtsch Chem Ges* **1898**, *41*, 1481-1487.
102. Terrones, M. Materials science: Nanotubes unzipped. *Nature* **2009**, *458*, 845-846.
103. Terrones, M.; Botello-Mendez, A. R.; Campos-Delgado, J.; Lopez-Urias, F.; Vega-Cantu, Y. I.; Rodriguez-Macias, F. J.; Elias, A. L.; Munoz-Sandoval, E.; Cano-Marquez, A. G.; Charlier, J.; Terrones, H. Graphene and graphite nanoribbons: Morphology, properties, synthesis, defects and applications. *Nano Today* **2010**, *5*, 351-372.
104. Ci, L.; Xu, Z.; Wang, L.; Gao, W.; Ding, F.; Kelly, K. F.; Yakobson, B. I.; Ajayan, P. M. Controlled Nanocutting of Graphene. *Nano Research* **2008**, *1*, 116-122.
105. Laura Elias, A.; Botello-Mendez, A. R.; Meneses-Rodriguez, D.; Jehova Gonzalez, V.; Ramirez-Gonzalez, D.; Ci, L.; Munoz-Sandoval, E.; Ajayan, P. M.; Terrones, H.; Terrones, M. Longitudinal Cutting of Pure and Doped Carbon Nanotubes to Form Graphitic Nanoribbons Using Metal Clusters as Nanoscalpels. *Nano Letters* **2010**, *10*, 366-372.

II.1. Graphene for electrochemical (bio)-sensing: *State of the art*

106. Vadahanambi, S.; Jung, J.; Kumar, R.; Kim, H.; Oh, I. An ionic liquid-assisted method for splitting carbon nanotubes to produce graphene nano-ribbons by microwave radiation. *Carbon* **2013**, *53*, 391-398.
107. Zhu, C.; Guo, S.; Fang, Y.; Dong, S. Reducing Sugar: New Functional Molecules for the Green Synthesis of Graphene Nanosheets. *Acs Nano* **2010**, *4*, 2429-2437.
108. Choucair, M.; Thordarson, P.; Stride, J. A. Gram-scale production of graphene based on solvothermal synthesis and sonication. *Nat. Nanotechnol.* **2009**, *4*, 30-33.
109. Wang, Y., Peng, W., Liu, L., Tang, M., Gao, F., Li, M. Enhanced conductivity of a glassy carbon electrode modified with a graphene-doped film of layered double hydroxides for selectively sensing of dopamine. *Microchim. Acta* **2011**, *174*, 41-46.
110. Zhang, F., Li, Y., Gu, Y., Wang, Z., Wang, C. One-pot solvothermal synthesis of a Cu₂ O/Graphene nanocomposite and its application in an electrochemical sensor for dopamine. *Microchim. Acta* **2011**, *173*, 103-109.
111. Fan, Y., Liu, J., Lu, H., Zhang, Q. Electrochemistry and voltammetric determination of L-tryptophan and L-tyrosine using a glassy carbon electrode modified with a Nafion/TiO₂-graphene composite film. *Microchim. Acta*, **2011**, *173*, 241-247.
112. Gao, F.; Qi, X.; Cai, X.; Wang, Q.; Gao, F.; Sun, W. Electrochemically reduced graphene modified carbon ionic liquid electrode for the sensitive sensing of rutin. *Thin Solid Films* **2012**, *520*, 5064-5069.
113. Tian, X.; Cheng, C.; Yuan, H.; Du, J.; Xiao, D.; Xie, S.; Choi, M. M. F. Simultaneous determination of l-ascorbic acid, dopamine and uric acid with gold nanoparticles-β-cyclodextrin-graphene-modified electrode by square wave voltammetry. *Talanta* **2012**, *93*, 79-85.
114. Wang, L.; Zhang, X.; Xiong, H.; Wang, S. A novel nitromethane biosensor based on biocompatible conductive redox graphene-chitosan/hemoglobin/graphene/room temperature ionic liquid matrix. *Biosens. Bioelectron.* **2010**, *26*, 991-995.
115. Zhou, Y.; Yin, H.; Meng, X.; Xu, Z.; Fu, Y.; Ai, S. Direct electrochemistry of sarcosine oxidase on graphene, chitosan and silver nanoparticles modified glassy carbon electrode and its biosensing for hydrogen peroxide. *Electrochim. Acta* **2012**, *71*, 294-301.

II.2. Graphene nanoribbons for electrochemical sensing



II.2.1. Introduction and objectives

Graphene structure confers extraordinary properties¹⁻³ to the material, as mentioned in section II.1. Of the previously listed properties, mainly its large surface area and its high electrical conductivity have been exploited for its application in electrochemistry.⁴ This general definition and properties describe the theoretical or pristine graphene, however, considering synthesized graphenes, graphene family includes a broad variety of terms that describe different materials with different physical structure and properties.⁵

Basically, the most applied graphenes in analytical electrochemistry present as main sources graphite or CNTs in top-down scheme synthesis. On the one hand, the oxidation and exfoliation of graphite yield GO, this material loses the aromaticity and the HET rate is lower than in pristine graphene. Furthermore, the reduction of GO via chemical, thermal or electrochemical treatments generate rGO.⁶ Although this material recovers the aromaticity and increases the HET compared with GO,⁷ this material presents defects and new heteroatoms in the carbon lattice compared with the pristine graphene.⁸ These GO and rGO materials cover more than half of the analytical literature about graphene in electrochemical applications.^{5,9-15}

From the controlled structural opening process or unzipping of CNTs, GNRs are produced.¹⁶ These graphitic structures are dimensionally limited in the basal plane x-y, from a few to some hundred nanometers, because the diameter of the CNT limits the final dimension. Although many synthetic processes have been described in the literature¹⁷⁻²⁰ for synthesizing GNRs, again, the

oxidation step to open the CNT and the reduction process of the generated nanoribbon are the most cited in analytical electrochemistry.

In contrast with pristine graphene, GNRs obtained by chemical oxidation of CNTs are really promising in electrochemistry, because of the edge chemistry involved in GNR. Whereas pristine graphene has an inert chemical surface, no defects, showing poor electrochemical behavior,²¹ these graphene nanoribbons are more reactive. This reactivity can be caused by the adsorption of analytes via π - π stacking interaction, and by electrostatic or hydrogen bond interactions with functionalities of the target molecules and the oxygen moieties located at the edges of the graphene material.²² Remarkably, the main applications¹⁸ of GNRs are focused on the fields of physics, nanoelectronics, spintronics, and nanoelectromechanical systems,²³ however, they are also relevant to sensing and biosensing applications.^{22,24}

Although the longitudinal unzipping techniques used to synthesize GNRs result in over-oxidation and a plethora of defect sites that do not, in general, benefit electronic applications,¹⁷ these characteristics can actually be useful for certain electrochemical applications, as it has previously been stated.

A handful of studies have examined the use of GNRs in electrochemical sensing applications. The electrochemical sensing of model electroactive molecules in the presence of reduced GNR-modified screen-printed electrodes have displayed higher sensitivities compared to the ones of a bare screen-printed electrode.¹⁷ Various GNR-based sensors and biosensors^{14,25,26} have been developed for the detection of urea,²⁷ glucose,²⁸ 1-hydroxypyrene,²⁹ cysteine,³⁰ brevetoxin B,³¹ and 2,4,6-

trinitrotoluene.^{32,33} These sensors displayed excellent electrochemical responses in terms of reproducibility, low detection limits, and a high selectivity in all cases. In other approaches, GNRs have been incompletely unzipped to develop mixtures of GNR/MWCNTs³⁴ yielding also good responses.

Taking into consideration the literature of graphenes in electrochemistry, GNR is an under exploited carbon nanomaterial full of properties which need to be demonstrated. The most relevant and expected promises derived from the use of these carbon nanomaterials in electrochemical sensing should be:

(i) The electrocatalytic effect induced by graphene materials might have an effect on the redox capacity of analytes and, consequently, on the decrease of the detection potentials, which would improve the overall *selectivity* of the analysis.

(ii) Enhancement of faradaic currents since the large surface area of graphene detectors would permit rapid redox conversion. This implies the increase in *sensitivity* in the analytical procedure.

(iii) Increase the resistance to passivation originated from the greater surface area of the graphene-based detectors. It implies better *reproducibility* in analysis, because of the lower electrode fouling.

On the other hand, screen-printing technology represents a well-established technique for the fabrication of electrochemical sensors with high sensitivity and selectivity, with all the benefits of an easily renewable sensor. In particular, the possibility to regularly change the sensor allows reducing the risk of contamination from one analysis to another. In addition, the incorporation of carbon nanostructures such as carbon nanotubes first, and more recently

graphene, have considerably changed the scope of carbon-based electrodes in electroanalysis.³⁵

In this works involving GNRs, the first objective has been the analytical characterization of two graphene nanoribbons with different oxygen content. Since oxide graphene nanoribbons (GNRox) were obtained from MWCNTs and reduced graphene nanoribbons (GNRred) were obtained from the chemical reduction of GNRox, a reliable and valuable comparison with the controls such as the bare electrode GCE or disposable CSPes and MWCNTs could be made. Thus, this traceability is of paramount importance for ascertaining the advantages of GNRs.

The second objective sought to explore the electrochemical performances of fully characterized GNRs with respect to the detection of significant target molecules, as well as to elucidate the chemical interactions between target molecules and GNRs in the context of electrochemical sensing for seeking tailored graphenes and carbon nanomaterials for future electrochemical sensing and biosensing. For that, a set of analytically significant target molecules were evaluated using differential pulse voltammetry (DPV). Those included three dihydroxybenzene isomers:³⁶ CT, RS, and HQ; the neurotransmitter levodopa (LD); the amino acid L-tyrosine (L-Tyr); UA and AA, which are present in urine and blood serum.³⁷⁻³⁹ These target molecules are usually oxidized at approximately the same potential; therefore, discrimination among these species in a mixture can be extremely difficult using most solid electrodes.⁴⁰ Furthermore, AA, LD and UA have been chosen because they are electroactive molecules with high clinical significance, which has been scarcely reported in the bibliography, using these nanomaterials.^{22,24,39,41}

Besides, a third objective was to include these carbon nanomaterials on screen-printed electrodes as a new analytical tool, easy to use, fast and reliable, competitive in comparison with the other electrochemical approaches, because they offer a very fast response, low sample consumption (just 50 μL) and single use, disposability. In addition, in comparison with others methodologies such as, HPLC or capillary electrophoresis (CE), they represent a fast and simple alternative, which avoids even the large use of toxic solvents.

II.2.2. Synthesis and characterization of graphene nanoribbons

The carbon source used for the synthesis of graphene nanoribbons, MWCNTs (0.2% oxygen content) was produced by the arc-discharge method⁴² in a home-built electric arc-discharge apparatus under standard conditions.⁴³ The MWCNTs were characterized as being straight and highly graphitized.

GNRox, 44 wt.% oxygen, were synthesized from the MWCNTs via the longitudinal unzipping method in $\text{H}_2\text{SO}_4/\text{KMnO}_4$.¹⁶ These oxidized nanoribbons were used as starting materials to produce GNRred, 14% oxygen, via chemical reduction with $\text{N}_2\text{H}_4/\text{NH}_3$.⁴⁴

Afterwards, the structures and morphologies of the graphene samples were characterized using AFM, as shown in **Figure II.6**. This figure shows AFM images for a small GNRox sheet with an average thickness of about 0.8 nm and an area of 200 x 150 nm². The theoretical thickness of a perfectly flat unoxidized sp²-carbon-atom network is predicted to be 0.4 nm.¹ The thickness of the GNRox sample measured here was consistent the thickness of two stacked graphene sheets; however, this thickness may also indicate a single layer graphene structure having oxygen functionalities on the surface.⁴⁵ **Figure II.6** shows that the GNRred surface was rough due to the presence of stacked small fragments of the reduced graphene sheets. The average thickness of this graphene sample was 1.2 nm, suggesting that the stacked layers extended over an area of 120 x 50 nm². The GNRred sample displayed a larger number of layers than the graphene oxide sample because the high proportion of sp²-carbons in GNRred increased the extent of π - π stacking interactions.

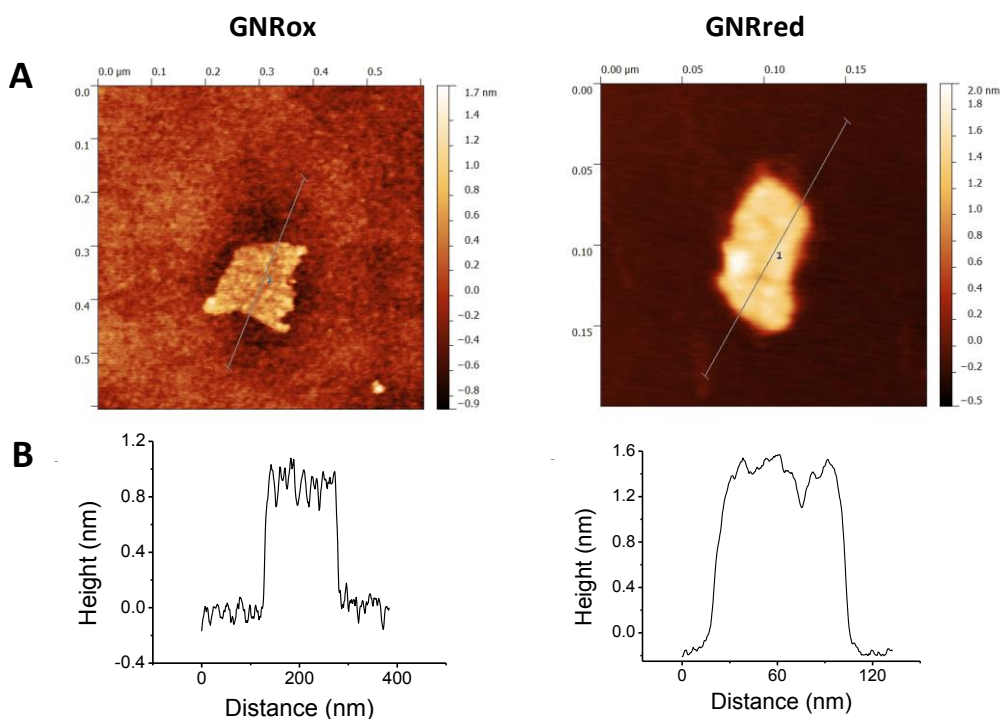


Figure II.6. (A) Tapping mode AFM images and (B) height profiles along the dashed lines of GNROx (left) and GNRred (right)

The graphene morphologies were imaged using TEM, which also demonstrated the successful synthetic process based on the chemical unzipping of MWCNTs. **Figure II.7** shows TEM images of a MWCNT sample (A), GNROx (B), and GNRred (C). The MWCNTs were more than 1 μm long and had an outer diameter of approximately 12 nm; GNROx displayed stacked layers and folds, and GNRred appeared to form thin layers with folds in the sheets. These micrographs could be used to visualize the openings of the MWCNTs used to generate the graphene layers, as well as the anisotropy of the GNR structures.

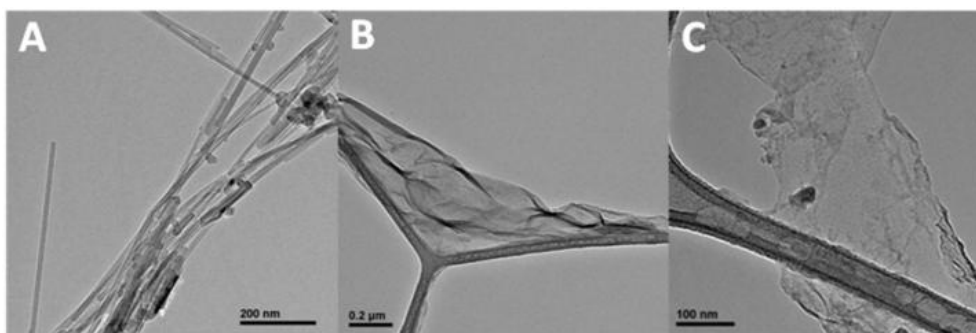


Figure II.7. TEM images of the (A) MWCNTs, (B) GNROx, and (C) GNRred samples

X-Ray diffraction studies were performed to estimate the average distance between layers in the carbon allotropes. The crystalline structures of graphite, graphene, and carbon nanotubes permit the measurement of the inter-planar spacing and lattice parameters (see **Figure II.8**). The XRD patterns obtained from the MWCNTs presented a peak at 26° corresponding to a basal plane of $d_{002}=3.34$ Å. This peak matched the distance found in the graphite layer structure. The GNROx sample displayed a new peak at 10° , which was attributed to a plane at $d_{001}=7.33$ Å. The separation between layers in the GNROx sample was high due to the presence of oxygen moieties in the lattice. The GNRred peak intensity at 10° was lower and the peak at 26° was higher than the corresponding peak intensities obtained from the GNROx diffractogram. The recovery of sp^2 -carbon in GNRred facilitated π - π stacking among the layers, and the distance between layers was smaller than the interlayer distance measured in the GNROx sample. XRD studies confirmed the change in the distance between these crystalline structures and the presence of a new graphitic structure.

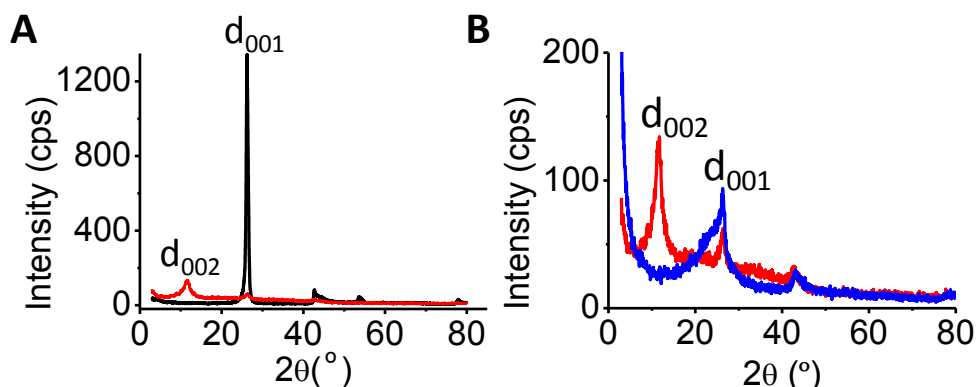


Figure II.8. X-ray diffractograms for (A) the MWCNTs (black) and GNRox (red) (scale x5 in GNRox), and (B) GNRox (red) and GNRred (blue)

The Raman spectra of graphite-derived materials usually display a D band at 1360 cm^{-1} and a G band at 1590 cm^{-1} , and an overtone of the D band occurs at 2650 cm^{-1} (the 2D or G' band).^{7,46} The D band arises from the out-of-plane vibrational modes and is indicative of the number of sp^3 carbon atoms present, whereas the G band arises from the presence of in-plane sp^2 vibrations. The intensity ratio of the D and G lines (I_D/I_G ratio), therefore, provides important information about the composition and domains in-plane giving valuable information regarding the average size of the sp^2 carbon domains as well.^{47,48} **Figure II.9** illustrates the Raman spectra of the three materials, showing the D, G, and G' bands. The I_D/I_G ratio was calculated to be 0.075, 0.52, and 0.66 for the MWCNTs, GNRox, and GNRred samples, respectively. This increase also suggested a decrease in the average size of the sp^2 graphitic domains, suggesting that the new graphitic domains created in the GNRred sample were smaller in size but more numerous than in the GNRox sample.⁷ Because the I_D/I_G ratio is proportional to the average size of the sp^2 carbon domains, a higher I_D/I_G was attributed to the presence of

additional edges (more defects)⁴⁹ and shorter layers in the GNRred surface, consistent with the AFM results.

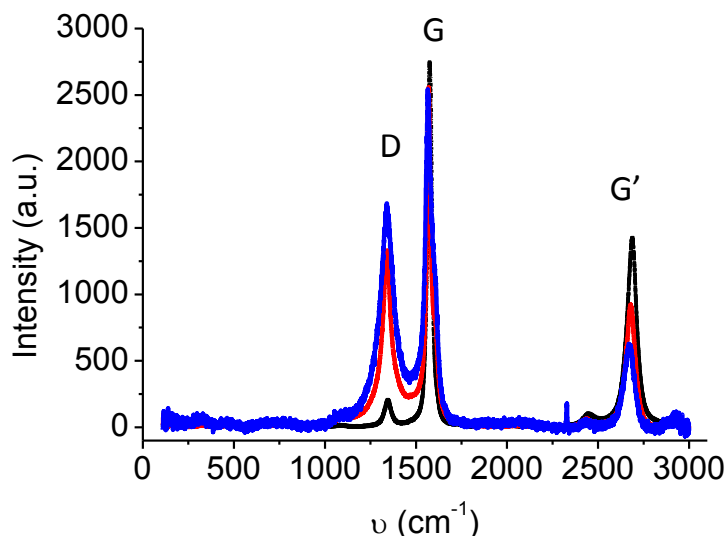


Figure II.9. Raman spectra of the MWCNTs (black), GNRox (red), and GNRred (blue). The scale of the GNRred sample is 10x the scale of the other sample spectra

XPS was used to study the oxygen content and changes in the sp^2 - sp^3 carbon structure in the graphene layers after chemical reduction of GNRox to obtain GNRred. The presence of sp^2 -carbon atoms increased significantly and the presence of sp^3 -carbon and oxygen moieties decreased correspondingly upon reduction of GNRox to GNRred. The presence of carboxyl, carbonyl, alcohol, epoxy, and ether moieties decreased to the same extent. The XPS results revealed the presence of C-N bonds in the as-synthesized GNRred sample as a result of the N_2H_4/NH_3 reduction step (see **Figure II.10**). Considering that XPS measurements are sensitive to the elemental composition of the material surface, XPS offers an accurate

measure of the oxygen content in the material. Direct determination of oxygen content was directly determined to be 0.2 wt.% in the MWCNTs, 44 wt.% in the GNRox, and 14 wt.% in the GNRred. Clearly, these data slightly differed from the XPS results because the XPS technique is not sensitive to the presence of oxygen groups below the surface and because some of the groups may be lost due to decomposition in the presence of the harsh XPS measurement conditions.

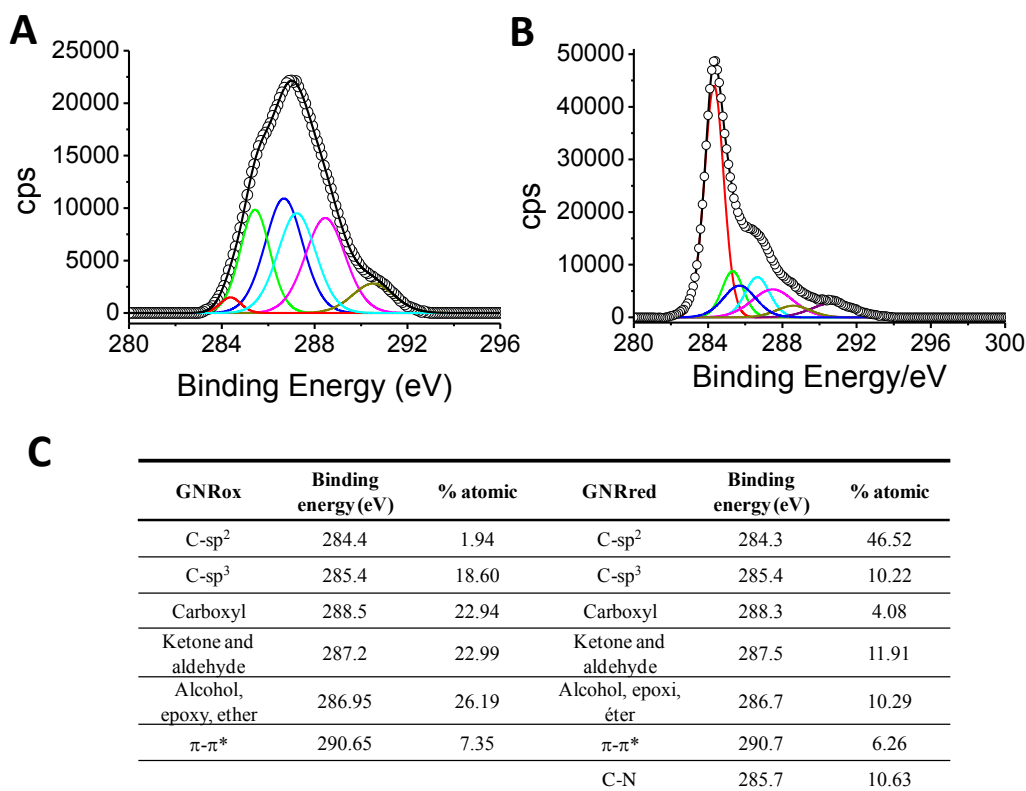


Figure II.10. (A) C1s XPS spectra of the GNRox and (B) GNRred samples, recorded with a photon energy of $h\nu = 400$ eV. (C) Table of the binding energies and atomic percentages estimated from the XPS spectra in A and B

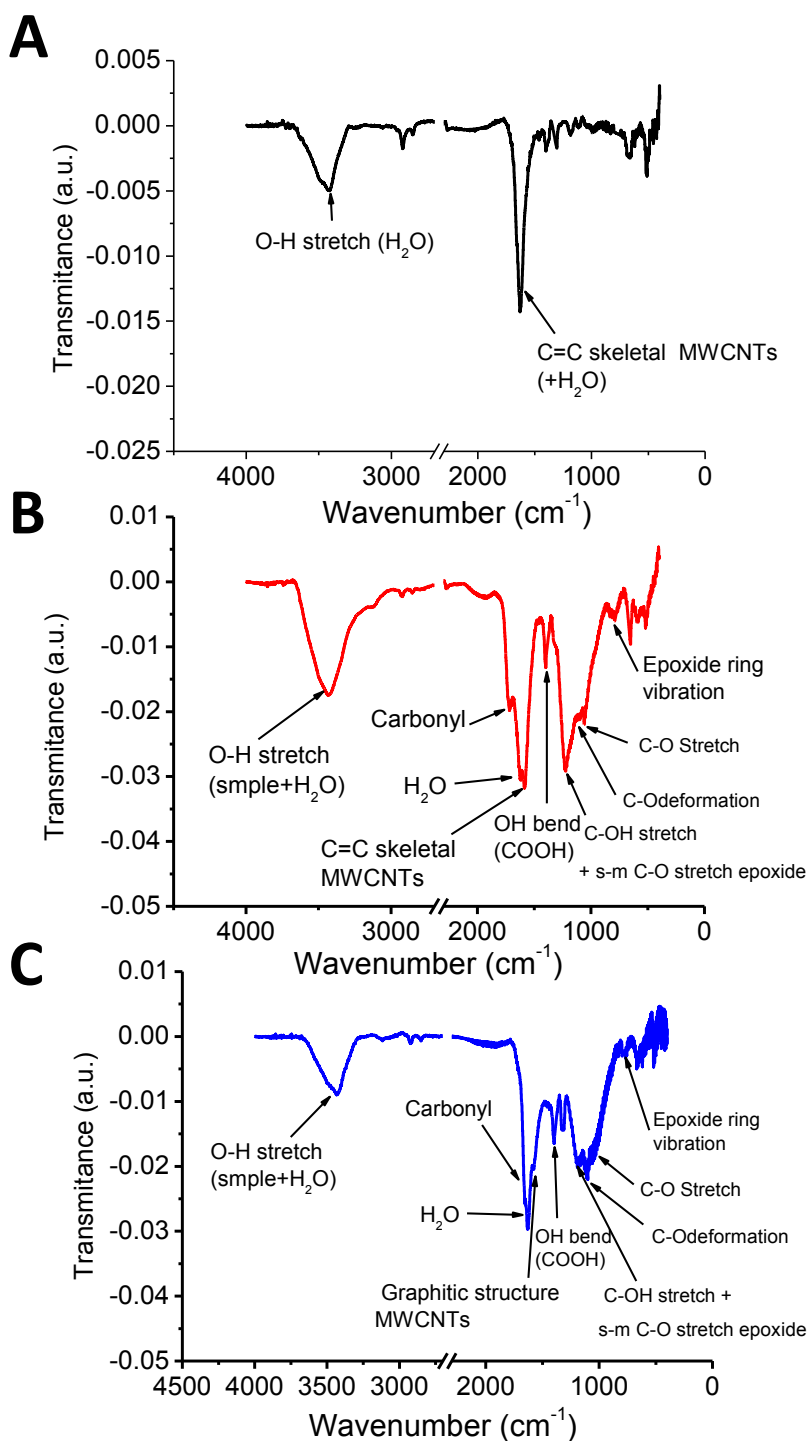


Figure II.11. IR spectra of the (A) MWCNTs, (B) GNRox, and (C) GNRred materials

Furthermore, the IR spectra were evaluated to corroborate the analysis of the functional moieties present in the GNRs, already quantified by XPS. **Figure II.11** shows the sp^2 -carbon vibrational bands obtained from the MWCNTs (**Figure II.11.A**). The GNRox spectra indicated the presence of oxygen moieties due to carboxyl, epoxy, and hydroxyl groups (**Figure II.11.B**). The GNRred spectrum shows the remained oxygen moiety signals between 1400 and 1700 cm^{-1} , however, the vibrations corresponding to the C-O stretch between 1250 and 1000 cm^{-1} were reduced to a greater extent, as compared to the GNRox spectrum. Vibrations at 3200 cm^{-1} due to the C-N bonds arose from the chemical reduction step (**Figure II.11.C**). The GNRred spectrum displayed a lower band intensity compared to the GNRox spectrum, confirming that the oxygen moieties had been reduced. These results were consistent with the Lerf–Klinowsky model.

In the last analytical characterization step, the GNR-based electrodes were explored. Firstly, the dispersion of the graphene material was of paramount importance for obtaining these results (see **Figure II.12**). Stronger sonication conditions were required to prepare the GNRred dispersion. Because GNRred includes high sp^2 content, the material readily stacks to form small piles on an electrode surface that increase the resistivity and reduce the current. The strongest sonication conditions were not necessary to obtain a good GNRox dispersion because the layers did not stack as readily, the material was not found to accumulate, and the signals obtained with or without tip sonication were indistinguishable.

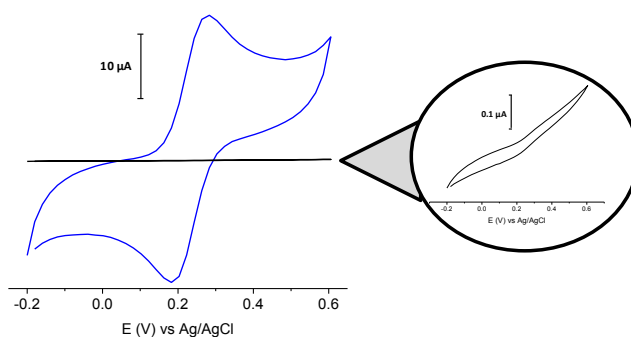


Figure II.12. Cyclic voltammetry of 1 mM $\text{K}_3[\text{Fe}(\text{CN})_6]$ in 0.1 M $\text{NaH}_2\text{PO}_4/\text{Na}_2\text{HPO}_4$ on GNRred modified electrodes dispersed without (black line) or with tip sonication (blue line) (left panel). Magnified view of the CV black line in left panel (right panel)

Secondly, the casting electrode was prepared using an optimized volume of 10 μL drop of the GNR suspensions (see **Table II.8**).

Table II.8. Cathodic current intensities in the CV study of 1 mM $[\text{Ru}(\text{NH}_3)_6]^{3+}$ in 1 M KCl, using the GNRox/GCE prepared by depositing different volumes of a 0.5 mg/mL graphene dispersion

Volume (μL)	0	1	5	10	20
i_{cat} (μA)	-6.2	-8.7	-11.7	-21.8	-24.1
RSD (% , n=3)	2.0	0.6	2.4	3.3	3.6

Thirdly, the effective electrochemical surface area was evaluated by chronocoulometry charge-time plots for the reduction of $\text{K}_3[\text{Fe}(\text{CN})_6]$ (see **Figure II.13** and equation in section **II.2.6**). The estimated areas were obtained from the slopes of the Q vs $t^{1/2}$ plots (see **Figure II.13.B**) yielding values of 0.030, 0.071, 0.113, and 0.267 cm^2 for the

non-modified GCE, MWCNTs, GNROx, and GNRred electrodes, respectively. These results revealed that GNROx and GNRred significantly increased the electrochemical surface area of the electrode. This increase corresponded to a 4-fold increase, in the case of GNROx, and a 10-fold increase, in the case of GNRred, over the electrochemical surface area of the bare GCE. The surface areas were higher than the surface area of the MWCNTs by factors of 2 and 5 for the GNROx and GNRred samples, respectively. Good interelectrode precision ($n=3$ electrodes) was obtained, with relative standard deviation (RSD) values of 2, 7, and 6% for the MWCNTs, GNROx and GNRred, respectively. These results indicated that the GNRs offered consistently high and reproducible electroactive areas, as predicted.

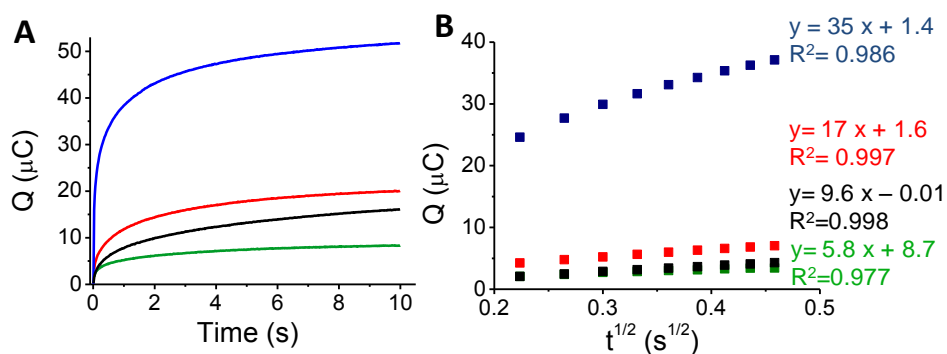


Figure II.13. (A) Chronocoulometric charge-time plots for the reduction of 0.45 mM $\text{K}_3[\text{Fe}(\text{CN})_6]$ in 0.1 M $\text{NaH}_2\text{PO}_4/\text{Na}_2\text{HPO}_4$ (pH=7.40). GCE (green), GCE/MWCNTs (black), GCE/GNROx (red), and GCE/GNRred (blue). (B) Chronocoulometric plots of the charge versus $t^{1/2}$ and linear fits for GCE (black), GCE/MWCNTs (green), GCE/GNROx (red), and GCE/GNRred (blue)

Furthermore, the morphology of GNROx and GNRred on the screen-printed platform surface was explored by field emission scanning electron microscopy (FE-SEM) in order to explore the material

deposition on the screen-printed platforms. **Figure II.14 A-C** shows the micrographs for graphene nanoribbons on CSPE. As it is indicated on the **Figure II.14 A**, the non-modified CSPE surface was homogeneous and porous. In the case of GNROx on the CSPE, the morphology resembles thin curtains, and layers seem to be overlapped rather than aggregated. As for GNRred, these small fragments of graphene easily stack and accumulate on CSPE surface forming aggregated graphene mass piles randomly distributed on the CSPE electrode surface.

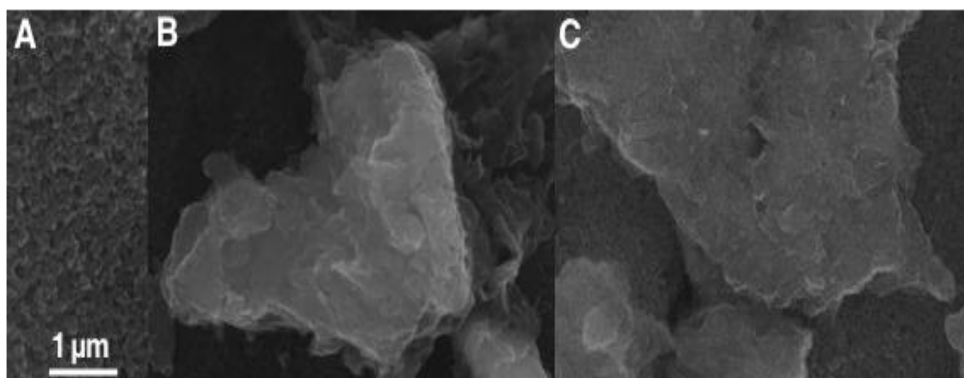


Figure II.14. FE-SEM images of (A) non-modified CSPE and (B) GNRred and (C) GNROx modified CSPEs

II.2.3. Tailored graphene nanoribbons for electrochemical sensing

The electrochemical behaviors of the isomers HQ (1,4-diol), CT (1,2-diol), and RS (1,3-diol) were explored on bare GCE, and all the carbon materials (MWCNTs, GNROx, and GNRred) on the GCE, respectively. **Figure II.15 Top** illustrates the electrochemical responses of each electrode to the target molecules. The extraordinarily high oxidation peak currents on the graphene-modified electrodes, as compared to the bare electrode, in the presence of the three target molecules reflected the high conductivity of the GNRs. The high conductivity of the GNRred electrode was particularly remarkable as a result of the high sp^2 -carbon content, which increased the electrical conductivity of this material. As an example, the electrochemical response of GNRred to CT was one order of magnitude higher than the response to HQ, (see **Table II.S1**, in Appendix II.2.7). The presence of incompletely unzipped MWCNTs, if any, was not expected to significantly affect the detection performance because the MWCNT electrode displayed a low signal level.

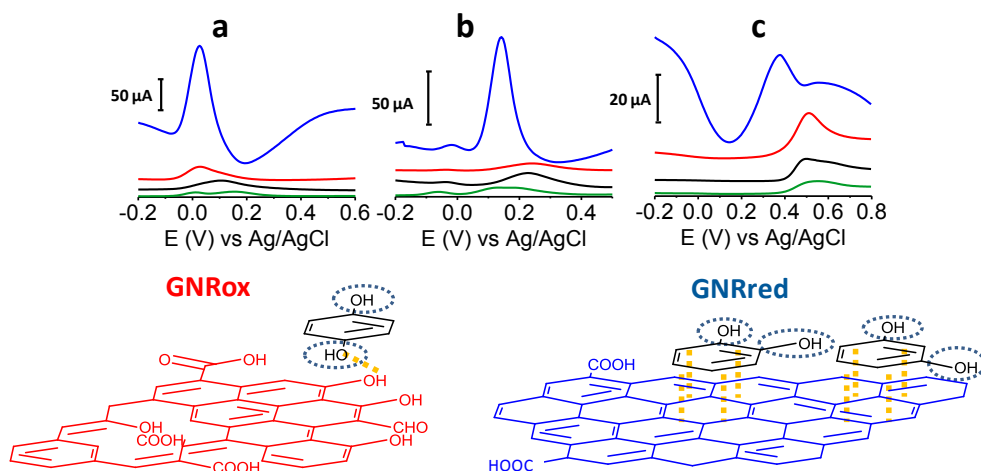


Figure II.15 (Top) Differential pulse voltammograms obtained from (a) 1 mM HQ, (b) CT, and (c) RS. (—) Bare GCE, (—) MWCNTs, (—) GNRox, and (—) GNRred. In 0.10 M $\text{NaH}_2\text{PO}_4/\text{Na}_2\text{HPO}_4$ (pH 7.40). DPV at 50 mV pulse and 0.05 s frequency and potentials versus Ag/AgCl (3 M KCl). **(Bottom)** Schematic diagram of the interactions between the target molecules (black) and the graphene materials which showed the lower oxidation potential. The oxidation reaction center is indicated by the blue circles and the main interactions are indicated in yellow

The chemistry underlying the shifts in oxidation potentials in the electrochemical detection of the target molecules may be understood as follows. 1,4-Benzenediol readily oxidizes at low potentials to produce 1,4-benzoquinones, whereas the oxidation of 1,3-diol is less favorable due to the lack of conjugation, thereby preventing the formation of the benzoquinone, as it occurs with 1,4 and 1,2-benzenediols. **Figure II.15 Bottom** illustrates the possible interaction processes between the target molecules and the graphene material. We hypothesized that the availability of more π - π interactions in GNRred than in GNRox facilitated the electrocatalysis of CT and RS and, as a consequence, facilitated oxidation of both

benzenediols with GNRred. By contrast, 1,4-benzenediol displayed similar oxidation potentials on both GNRs, suggesting that hydrogen bonds dominated the interactions between the oxide moieties on the edges of the GNR surfaces and the molecules, due to the similar potential of the HQ in the presence of GNRred and GNRox.

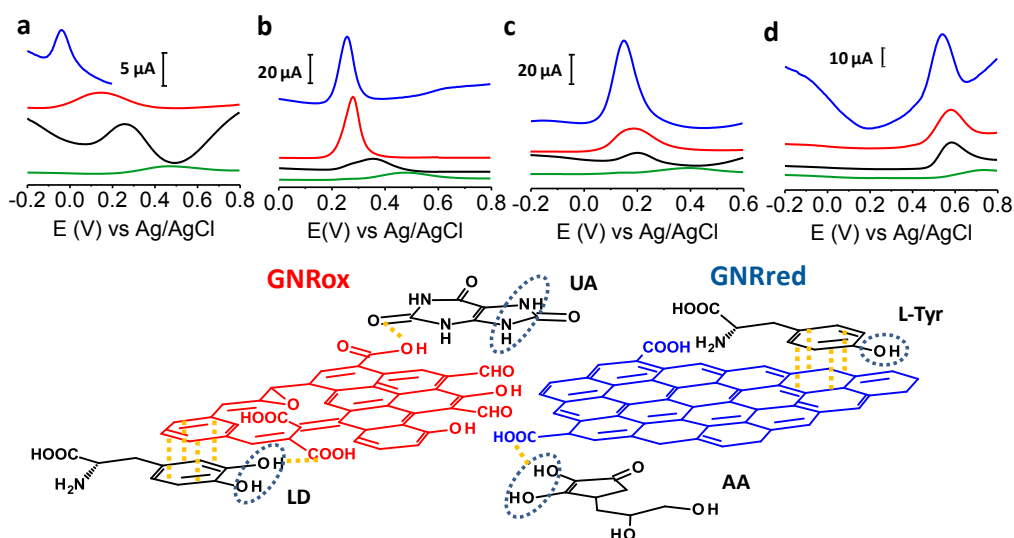


Figure II.16. (Top) Differential pulse voltammograms for 1 mM (a) AA, (b) LD, (c) UA and (d) L-Tyr. (—) Bare GCE, (—) MWCNTs, (—) GNRox and (—) GNRred. (See Figure II.15 for working conditions). (Bottom) Schematic diagram illustrating the interactions between the analytes (black) and graphene surfaces which showed the lower oxidation potential. The oxidation reaction centers are indicated by the blue circle and the main interactions are indicated in yellow

Figure II.16 Top presents the detection results of LD, AA, L-Tyr, and UA on GCE, MWCNTs, GNRox, and GNRred. A comparison of the graphene modified electrodes and the GCE and MWCNTs controls revealed that both graphene electrodes displayed significantly higher current peaks compared to the MWCNT control.

The results obtained from GNRred were particularly spectacular. The exceptional electrocatalytic properties exhibited by this material enabled the detection of AA, even below 0 V. Moreover, GNRred displayed analytical response from 5 to 10-fold higher compared to the response of the GCE.

Table II.S2 (see Appendix II.2.7) summarizes the oxidation potentials and analytical signals obtained during the DPV measurements for the four molecules.

The enhanced sensitivity of the GNRred electrode was attributed to the good conductivity of the material. These results may be understood in terms of the previous results obtained in analytical characterization studies, which identified a high electrochemical surface area and the presence of high sp^2 -carbon content. **Figure II.16 Bottom** provides a schematic diagram illustrating our rationalization of the interactions between the GNR and the target molecules. The oxygen groups of the GNRox layers and those oxygen functionalities remaining in the GNRred lattice (this latter material supposed to be in the form of carboxylic acids and carbonyls, as described in the model proposed by Lerf-Klinowski^{44,50,51}) are expected to interact with the target molecules via hydrogen bonds. In the detection of AA, GNRred yielded the strongest electrocatalysis compared to UA, where similar electrocatalytic effect was found for both graphenes. This shift could be explained considering interactions with the oxidation center of AA and GNRred and without this oxidation center in the case of UA.

LD, which basic structure derived from CT, displayed indistinguishable behaviour for GNRred and GNRox. Therefore, the predominant π - π interactions plus hydrogen interactions between

the benzenediol group and the GNRred and GNRox surfaces appeared to be responsible for the similar responses.

The oxidation process of L-Tyr was more difficult due to the presence of only one hydroxyl group. For this reason the similar oxidation potentials observed on all carbon materials (MWCNTs, GNRox, and GNRred) could be explained in terms of weak π - π interactions between the L-Tyr and the carbon materials.

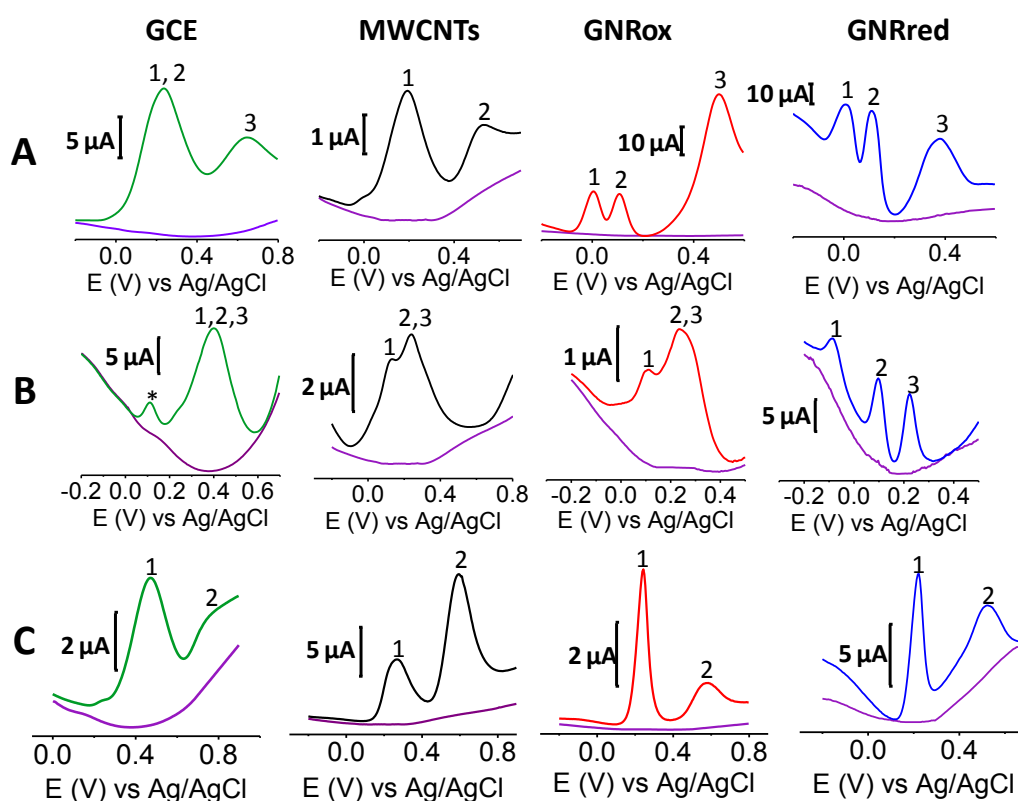


Figure II.17. (A) Voltammograms for the detection of: HQ 0.25 mM (peak 1); CT 0.25 mM (peak 2) and RS 1.0 mM (peak 3). (B) AA 0.5 mM (peak 1); LD 0.05 mM (peak 2), and UA 0.05 mM (peak 3). (C) UA 1.0 mM (peak 1) and L-Tyr 1.0 mM (peak 2). (—) Background signal, (—) bare GCE, (—) MWCNTs, (—) GNRox, and (—) GNRred. Note: * Pre-peak oxidation in LD. (See Figure II.15 for a description of the working conditions)

Figure II.17A shows the electrochemical responses of mixtures of the three isomers: HQ, CT, and RS on GCE, MWCNTs, GNRox, and GNRred. The responses revealed that although the bare GCE did not permit the simultaneous detection of the benzene 1,2 and 1,4-diols, the electrocatalytic properties of GNRox and GNRred allowed the simultaneous and separate detection of the three target molecules. **Figure II.17B** shows that the selective detection of LD, AA, and UA could only be achieved using the GNRred electrode. **Figure II.17C** shows that the separate components of a mixture comprising L-Tyr and UA could be identified using the GNRred electrode as well. The detection of individual target molecules in a mixture relies on the availability of distinct interactions between each nanomaterial and target molecule, and consequently, to the exceptional electrocatalytic properties exhibited.

The strength of the voltammetric studies was examined by measuring the technique repeatability and reproducibility. The repeatability (multiple experiments conducted on the same day) and the reproducibility (multiple experiments conducted on different days) of the oxidation peak positions was found to be excellent, with RSD <4 % (n=10). Good inter-electrode precision was achieved, with RSD values of <6 % (n=5, same day) and <9 % (n=5, different days), for the GNRred electrode. The precision was significantly better than the precision obtained from the GCE electrode (RSD <10%, n=4 electrodes, same day).

Finally using the GCE, real samples were also tested. **Figure II.18** illustrates the electrochemical detection of HQ and UA in cosmetic and urine samples, respectively. Interestingly, in both cases, the GNRs displayed better intensity currents than the GCE. The excellent results in complex matrix suggest that this technique is suitable for

the analysis of complex samples. Good precision was achieved for both samples. The cosmetic sample analysis was characterized by an RSD <0.5 % for the oxidation peaks and a RSD <2 % for the peak currents. The urine sample analysis showed a RSD <0.5% for the oxidation peaks and a RSD <10% for the peak currents.

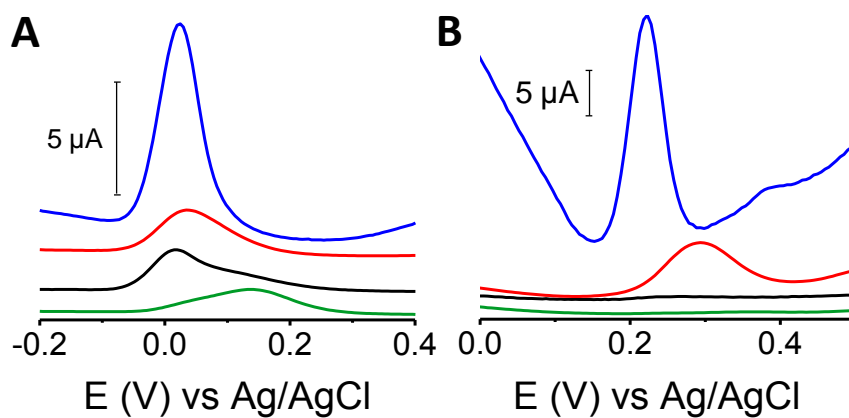


Figure II.18. Differential pulse voltammograms for the detection of (A) HQ in a cosmetic sample and (B) UA in a urine sample, on (—) bare GCE, (—) MWCNTs, (—) GNRox, and (—) GNRred electrodes. See experimental section in Figure II.15

II.2.4. Graphene nanoribbons-based electrochemical sensors on screen-printed platforms

The interesting features of screen printed platforms low sample consumption, disposability (one-use approach), fast response, easy to use by non-trained personnel, reliability, plus the excellent results found for GNRred/GCE in UA, AA, LD detection, were considered for the development of a new point of care device for UA determination in presence of AA and LD.

Therefore, firstly, the electrochemical behaviour of the three target molecules, AA, LD and UA was studied on non-modified CSPE as well as on MWCNT, GNROx and GNRred modified electrodes using DPV. **Figure II.19** shows the voltammograms obtained for AA, LD and UA using the four electrodic material surfaces. Interestingly, spectacular differences between all electrochemical sensors were observed. Indeed, GNRred exhibited a strong electrocatalytic effect toward the target molecules, which permitted their simultaneous detection while the other materials exhibited very poor electrochemical sensing. Indeed, the detection of AA, LD and UA was noticed at +0.08, +0.27 and +0.39 V, respectively, with a very good signal to noise characteristics.

These excellent results, in terms of electroanalytical performance, could be interpreted at the light of the characterization findings obtained on the GNRred surfaces (see **Characterization in II.2.2**). The higher content of defects and edge sites, showed by Raman spectroscopy, as well as the removal of the oxygen functionalities that significantly decreased, showed by XPS, resulted in drastically lowered the potential values for GNRred.

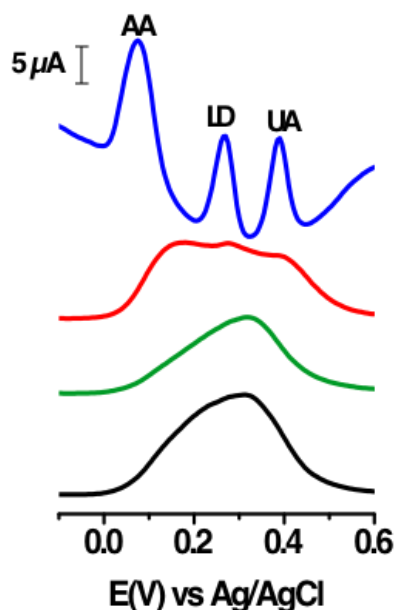


Figure II.19. Differential pulse voltammograms in CSPE (in black), MWCNT (in green), GNRox (in red) and GNRred (in blue) for the detection of 4.0 mM AA (peak AA); 0.05 mM LD (peak LD) and 0.05 mM UA (peak UA) in 0.10 M NaH_2PO_4/Na_2HPO_4 (pH 7.40). DPV at 25 mV pulse potential, 0.07 s pulse step and 5 mVs^{-1} scan rate, potentials versus Ag

The different easiness of the analyte to be oxidized and to donate the electrons to the electrodic surface could be explained because of the interaction between analyte and the carbon material. Indeed, it could be said that, carbon paste represented as graphite (CSPE) and MWCNT suffer from the same interactions (weak π - π adsorption) with the analytes and the capability of donating electrons could be understood to be similar. As for GNRox, the voltammograms obtained suggest that the interaction seems to be slightly bigger with AA, but the electron transference rate is not high enough to allow a clear differentiation between the electrons donated by AA from those ones donated by the other analytes. Remarkably, the GNRred

characterized by small layers, additionally present a structure with a low percentage of oxygen moieties in the edges capable of differently interacting with the analytes. Likewise, the higher content of sp² carbons compared to GNROx allowed the higher electron transference rate to get tight voltammograms peaks with satisfactory resolution to simultaneously detect the three molecules.

From the results obtained and discussed in the previous sections, one interesting application should be the construction of GNRred-based electrochemical sensor for fast and reliable determination of UA in urine samples.

To this end, firstly, precision and electrode stability was carefully studied. Intra-electrode repeatability was excellent with RSDs of 4.0, 2.0 and 1.0 % for detection potentials and 2.4, 4.5 and 5.7 % for faradaic amperometric currents (n=10) in AA, LD and UA, respectively. Moreover, the inter-electrode reproducibility was also estimated, with RSDs 5.0, 2.3 and 2.5 % for detection potentials and 5.1, 13.0 and 11.7 % for faradaic amperometric currents (n=5) for AA, LD and UA, respectively. These results demonstrated the good reproducibility of the graphene modified electrode. The stability of the electrode was further evaluated during 15 days and the modified electrode retained 93±3% of its initial response in terms of intensity current.

Figure II.20 shows the DPV of the simultaneous calibration of the three analytes. Analytical characteristics of the calibration graphs revealed a good linearity for the three analytes ($R^2 \geq 0.990$), intercepts statistically zero ($\alpha = 0.05$) and sensitivities of 2.2, 145.6 and 256.9 μAmM^{-1} for AA, LD and UA, respectively. Also, a good LOD of 5 μM for UA was obtained ($S/N=3$).

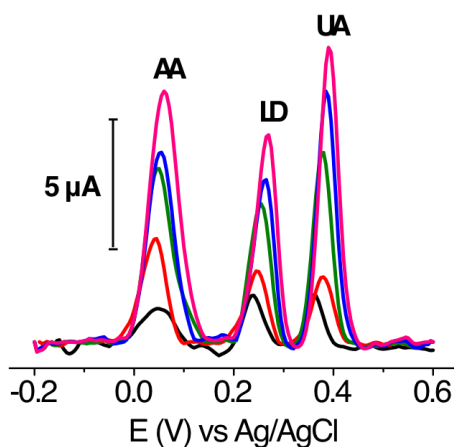


Figure II.20. Simultaneous calibration of AA, LD and UA (from 1 to 5 mM for AA and from 10 to 50 μM for LD and UA). (For experimental conditions, see Figure II.19)

Finally, urine samples were studied to evaluate the applicability of the proposed GNRred-based electrochemical sensor for UA sensing. **Figure II.21** illustrates the analysis of urine samples. A well-defined UA voltammetric peak at +0.39 V with very good S/N characteristics was clearly noticed allowing its identification in the samples in less than 100 s. Quantitatively, the levels of UA found in healthy individuals were 1.30 ± 0.03 mM with excellent precision, RSDs <5.2% during the analysis being these values in agreement with those expected for healthy individuals.

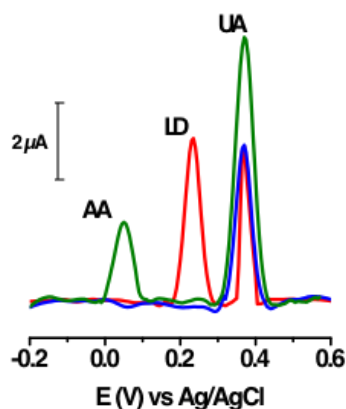


Figure II.21. Differential pulse voltammograms of 50-fold diluted urine samples. Urine sample (blue), spiked with 1.5 mM AA and 20 μM UA (green) and spiked with 20 μM LD (red). (For experimental conditions, see Figure II.19)

Additionally, in order to evaluate the capability of the method to determine UA in presence of AA and LD, urine samples were properly fortified in each analyte. Excellent recoveries ranging from 97 to 101% were also obtained as it is listed in **Table II.9**. These results indicated the accurate determination of the three target molecules in urine samples giving additional value to the proposal.

Table II.9. Determination of AA, LD and UA in urine samples (n=3)

Analyte	Found in sample (mM)	Added (mM)	Total (mM)	Recovery (%)
AA	ND	2.0	2.0 \pm 0.1	101 \pm 5
LD	ND	0.030	0.029 \pm 0.001	97 \pm 3
UA	0.026	0.020	0.046 \pm 0.001	100 \pm 4

ND Not detected

II.2.5. Conclusions

Both GNRs displayed excellent electrochemical behaviour in the detection of the target molecules, being this behaviour rigorously attributed to graphene and to other graphitic materials. The interactions between the target molecules and the GNR materials present new opportunities in the field of electrochemistry. A suitable graphene material may potentially be tailored for a particular detection application with consideration for the relevant degree of oxidation and sp^2 structure in the electrode that would be required to promote hydrogen bonding or π - π interactions between the electrode and the target molecule. GNRox appeared to be ideal for the detection of molecules having high oxidation potentials, whereas GNRred displayed a better response to aromatic molecules, such as the conjugated 1,2-diols, which interacted with the electrode predominantly through π - π interactions.

Although both graphenes exhibited excellent electrochemical performance, GNRred became an exceptional material. The completely opened GNRred lattices, which displayed an average thickness of 1.2 nm and a high percentage of sp^2 -carbon were obtained through the synthetic methods described here. GNRred exhibited a 10-fold higher electrochemical surface area and a better analytical performance in the context of electrochemical sensing in comparison with the GCE. These GNRred features allowed for improved electrochemical sensing and suggested that this material was suitable for the electrochemical detection of target molecules. The outstanding electrocatalytic effect performance relies on the presence of a restored sp^2 structure that includes oxygen groups in the GNRred lattice. These combined features yielded excellent electrocatalytic properties due to the effects of both the π - π and

hydrogen bonding interactions between the molecules and the GNRs. These interactions enhanced electrocatalysis at the primary catalytic sites at the oxidation centers. These studies demonstrate that GNRred is a promising material for use in molecular sensing, with very rich chemistry and electrochemistry properties. GNRred combines the advantages derived from both the high proportion of sp^2 -carbon atoms available within the surface layers (similar to the structure of exfoliated graphene, 0.4 nm corresponds to one layer) with the advantages derived from the remaining oxygen moieties present on the surface. Consequently, we anticipate, in this Thesis, the new opportunities opened for electrochemical sensing applications by guiding the process of tailoring a suitable graphene electrode material for use in a particular molecular detection application.

On the other hand, tailored electrochemical GNRred-based sensor showed an impress analytical performance for simultaneous electrochemical sensing of AA, LD and UA on disposable screen-printed platforms. These synthesized GNRred that contain remaining oxygen moieties and high content of carbons with sp^2 hybridization exhibited a marked electrocatalysis towards the simultaneously determination of these target molecules. The excellent electrocatalysis exhibited by this GNRred electrochemical sensor allowed a fast and reliable UA assessment in urine samples opening novel avenues for the construction of novel GNR-based electrochemical sensors for point of care testing applications.

II.2.6. Experimental section

II.2.6.1. Reagents

Synthesis of graphene nanoribbons

150 mg of MWCNTs were weighed and dispersed in 150 mL of H₂SO₄ for 30 minutes in US bath. Afterwards, the dispersion was stirred all the night. The obtained suspension was heated at 65 ° C, and 750 mg of KMnO₄ were added, letting react at that temperature for 2 hours. After those 2 hours, the product was cooled at room temperature.

Once the suspension was cold, it was dropped in a glass that contains 400 g of water ice and 10 mL of hydrogen peroxide, the suspension was let and was filtered with a 3 µm of pore polycarbonate filter. The filtered solution was redispersed with 150 mL of water in a ultrasound bath and flocculated with 15 mL of concentrated HCl and it was again filtered with the 3 µm polycarbonate filter.

Finally the filtered solution was redispersed with 150 mL of ethanol with a ultrasound bath and flocculated adding 150 mL of ether and 15 mL of hexane. Then, the solution was filtered with a 0.1 µm of pore diameter of polytetrafluoroethylene. The oxide graphene nanoribbon was a black powder after drying between 40 to 60 ° C.

For synthesizing the GNRred material, 50 mg of GNRox were weighted and dispersed in 250 mL of 1% SDS aqueous solution yielding a 0.2 mg/mL concentration, 1% of NH₃ was added to obtain a basic pH and then was heated to 95 ° C. Afterwards N₂H₄ was added until the reaction was completed.

Standards, reagents and samples

The sodium dihydrogen phosphate and disodium hydrogen phosphate used to prepare a phosphate buffered solution and the potassium hexacyanoferrate (III) were purchased from Panreac, (Badalona, Spain). LD, UA, RS, HQ and CT were purchased from Sigma-Aldrich (St. Louis, MO, USA). AA and L-Tyr were obtained from Fluka Chemika (Buchs, UK).

The cosmetic sample (Pigmentasa formulation containing 4% (w/w) HQ) was acquired in a local market. Urine samples were recollected from healthy patients.

Standard solutions were prepared in 1 mM in 0.1 M $\text{NaH}_2\text{PO}_4/\text{Na}_2\text{HPO}_4$ at 7.40 pH, adjusted using NaOH. All working solutions were protected from light and daily prepared. A 0.1 g (± 0.0001) sample of the Pigmentasa formulation was diluted in 10 mL $\text{NaH}_2\text{PO}_4/\text{Na}_2\text{HPO}_4$, sonicated in an ultrasonication bath for 10 min, filtered through a 0.2 μm Nylon filter, and diluted 4-fold prior to analysis. Urine samples were diluted 25-fold prior to analysis.

All solutions were prepared with Milli-Q water produced in a Milli-Q system (Millipore, Bedford, MA, USA).

II.2.6.2. Instruments

Atomic force microscopy images were recorded using a Nanoscope IIIa scanning probe microscope (Digital Instruments, USA) operated in the dynamic and contact modes. In both cases, silicon cantilevers (Veeco) with a force constant of ~ 40 N/m and a nominal radius of 8 nm were employed. The samples used for the measurements were prepared by drop-casting 0.5 μL of the graphene suspension (0.1

mg/mL) on the surface of a silicon wafer (in the case of the GNROx studies) or on a mica surface (in the case of the GNRred studies). The measurements were obtained in the surroundings of the wet drop where the concentration and aggregation of graphene sheets was lower. Transmission electron microscopy images were collected on a JEOL microscope model 2000 FXII at an acceleration potential of 200 kV, which yielded a maximum resolution of 0.28 nm. Raman spectra were obtained on a Micro-Raman confocal spectrophotometer model Horiba Jobin Yvon HR800 UV using a green laser at 532 nm, which yielded a resolution of 0.4 cm^{-1} . X-ray photoelectron spectroscopy was carried out on an ESCAPlus Omicron outfitted with a Mg anode and operated at 1253.6 eV with a power of 150 W (14 mA, 10 kV). X-ray diffraction measurements were obtained using an X-ray diffractometer Bruker D8 Advance Series. The oxygen content of the graphene samples was directly determined using a Flash 1112 analyzer from Thermo Fisher Scientific.

FE-SEM images were obtained on a JEOL Model JSM6335F equipment working at 5 kV. The aluminum mount stubs used for the FE-SEM analysis were obtained from Electron Microscopy Sciences (Hatfield, UK). The aluminum mount stubs used for the SEM analysis were obtained from Electron Microscopy Sciences (Hatfield, UK).

Electrochemical measurements (for optimization in GCE) were performed on an electrochemical station μ -AUTOLAB type II (Ecochemie, Utrecht, Holland) using a conventional three-electrode system comprising a platinum wire as an auxiliary electrode, a silver/silver chloride (Ag/AgCl) 3 M KCl reference electrode (CH Instrument, Austin, USA), and a GCE 3.0 mm in diameter (BAS

Instrumental, Warwickshire, UK) as the working electrode. Electrochemical experiments were performed at room temperature.

Electrochemical measurements (for applications in CSPEs) were performed, on an electrochemical station μ -Stat 100 potentiostat controlled by PSLite 1.6 software, by a CSPE which integrates a three-electrode system based on carbon counter and working electrodes of 4 mm diameter and silver (Ag) pseudo-reference electrodes (Dropsens, Oviedo, Spain), at room temperature.

II.2.6.3. Procedures

Modification of GCE electrodes

GNRox was dispersed in water by bath ultrasonication to form a 0.5 mg mL⁻¹ colloidal dispersion. GNRred was dispersed to obtain a 0.5 mg mL⁻¹ dispersion in water/NH₃ (1% v/v) by ultrasonication in a bath for 30 min, followed by tip sonication using a VCX130, (Sonics, Newtown, USA) for 2 minutes at 130 W. Interestingly, this last step was highly important for producing excellent dispersions of the GNRred (see **Figure II.S1**). The MWCNTs were dispersed in DMF by ultrasonication to form a 0.5 mg mL⁻¹ dispersion.

Prior to drop-casting deposition, the GCE was in turn polished using 0.1 and 0.05 μ M alumina powders and sequentially sonicated in Milli-Q water and anhydrous ethanol. The GNR and MWCNT-modified electrodes were prepared by casting 10 μ L of the GNR solutions (oxide or reduced) or MWCNTs dispersions on the GCE surface (see **Table II.8**).

Modification of CSPE electrodes

GNRred was dispersed to obtain a 0.5 mg mL⁻¹ dispersion in water/NH₃ (1% v/v) by ultrasonication in a bath for 30 min, followed by tip sonication using a VCX130, (Sonics, Newtown, USA) for 2 minutes and applying 130 W. Interestingly, this last step was important for producing a good dispersion of GNRred.

The GNRred/CSPE was prepared by casting 10 µL of the 0.5 mg mL⁻¹ dispersion of graphene nanoribbons on the CSPE surface.

GNRox was dispersed to obtain a 0.5 mg mL⁻¹ sample in water by ultrasonication in a bath for 30 min. The GNRox/CSPE was prepared by casting 10 µL of 0.5 mg mL⁻¹ graphene nanoribbons on the CSPE surface.

Electrochemical procedures

The electrochemical effective surface areas of the bare and modified GCE were estimated based on the slope of the plot of Q vs. t^{1/2} obtained by chronocoulometry based on Equation 1, as described by Anson,^{52,53} using 0.45 mM K₃[Fe(CN)₆] in 0.1 M PBS (pH=7.40) applying -0.30 V vs. Ag/AgCl (3 M KCl).

$$Q(t) = \frac{2nFAcD^{1/2}t^{1/2}}{\pi^{1/2}} + Q_{dl} + Q_{ads} \quad \text{(Equation II.1)}$$

In this equation, A is the effective electrochemical surface area of the working electrode (cm²), c is the concentration of the electroactive species (mol/cm³), n is the number of transfer electrons (that is, 1), F is the Faraday constant, and D is the diffusion coefficient, 7.6·10⁻⁶

cm^2s^{-1} ,⁵⁴ Q_{dl} is the double layer charge, which could be eliminated by background subtraction, and Q_{ads} is the Faradaic charge.

DPV (in GCE studies) was used for the voltammetry analysis with a pulse width of 0.05 V, a pulse frequency of 0.05 s, a pulse cycle of 0.2 s, a pulse interval of 0.004 V, and a standing time of 2 s.

On the other hand for CSPE, only 50 μL of the solution were necessary in the measurement to cover the three electrodes. After that, the DPV was scanned and was performed with a potential range between -0.20 to +0.60 V, 0.005 V step potential, 0.025 V pulse potential, 5 mV/s scan rate, 0.07 s pulse time and 3 s equilibration time.

II.2.7. Appendix

Voltammetry of the benzenediol isomers

Table II.S1. Oxidation potentials and peak intensities for HQ, CT, and RS. The brackets indicate the RSD values (% , n=3 electrodes)

Variable	Electrode material	HQ	CT	RS
E (V)	Bare GCE	0.178 (1.6)	0.137 (2.1)	0.530 (2.1)
	MWCNTs	0.107 (1.3)	0.228 (1.3)	0.495 (2.6)
	GNRox	0.027 (0)	0.243 (1.6)	0.505 (2.0)
	GNRred	0.032 (0)	0.142 (1.2)	0.369 (1.0)
I _p (μA)	Bare GCE	10.0 (2.9)	6.2 (3.9)	5.6 (6.0)
	MWCNTs	15.1 (2.3)	12.0 (3.6)	11.4 (6.7)
	GNRox	26.1 (0.7)	6.5 (4.6)	22.5 (8.4)
	GNRred	212.0 (1.1)	111.0 (5.8)	32.1 (5.7)

Voltammetry of AA, LD and UA

Table II.S2. Oxidation potentials and peak intensities for AA, LD, UA, and L-Tyr. The brackets indicate the RSD values (% , n=3 electrodes)

Variable	Electrode material	AA	LD	UA	L-Tyr
E (V)	Bare GCE	0.465 (0.7)	0.404 (2.0)	0.493 (1.2)	0.745 (1.0)
	MWCNTs	0.273 (1.2)	0.319 (0.5)	0.359 (1.5)	0.580 (0.4)
	GNRox	0.142 (1.1)	0.186 (3.0)	0.278 (1.6)	0.575 (0.7)
	GNRred	-0.054 (1.2)	0.130 (1.0)	0.257 (1.0)	0.535 (2.0)
I _p (μA)	Bare GCE	0.9 (9)	3.3 (10.1)	3.7 (4.1)	1.4 (1.4)
	MWCNTs	4.3 (3.7)	4.0 (1.3)	8.0 (3.4)	12.5 (8.0)
	GNRox	2.3 (5.0)	15.3 (8.6)	41.3 (6.5)	16.4 (6.1)
	GNRred	9.4 (4.0)	33.9 (2.4)	44.1 (4.0)	32.8 (1.5)

II.2.8. References

1. Novoselov, K. S.; Geim, A. K.; Morozov, S. V.; Jiang, D.; Zhang, Y.; Dubonos, S. V.; Grigorieva, I. V.; Firsov, A. A. Electric field effect in atomically thin carbon films. *Science* **2004**, *306*, 666-669.
2. Park, S.; Ruoff, R. S. Chemical methods for the production of graphenes. *Nature Nanotech.* **2009**, *4*, 217-224.
3. Lee, C.; Wei, X.; Kysar, J. W.; Hone, J. Measurement of the elastic properties and intrinsic strength of monolayer graphene. *Science* **2008**, *321*, 385-388.
4. Wong, C. H. A.; Chua, C. K.; Khezri, B.; Webster, R. D.; Pumera, M. Graphene Oxide Nanoribbons from the Oxidative Opening of Carbon Nanotubes Retain Electrochemically Active Metallic Impurities. *Angew. Chem. Int. Ed.* **2013**, *52*, 8685-8688.
5. Martín, A.; Escarpa, A. Graphene: The cutting-edge interaction between chemistry and electrochemistry. *Trends Anal. Chem.* **2014**, *56*, 13-26.
6. Chua, C. K.; Pumera, M. Chemical reduction of graphene oxide: a synthetic chemistry viewpoint. *Chem. Soc. Rev.* , 291.
7. Ambrosi, A.; Bonanni, A.; Sofer, Z.; Cross, J. S.; Pumera, M. Electrochemistry at Chemically Modified Graphenes. *Chem- Eur. J.* **2011**, *17*, 10763-10770.
8. Dreyer, D. R.; Park, S.; Bielawski, C. W.; Ruoff, R. S. The chemistry of graphene oxide. *Chem. Soc. Rev.* **2010**, *39*, 228-240.
9. Pumera, M.; Ambrosi, A.; Bonanni, A.; Chng, E. L. K.; Poh, H. L. Graphene for electrochemical sensing and biosensing. *Trends Anal. Chem.* **2010**, *29*, 954-965.
10. Brownson, D. A. C.; Banks, C. E. Graphene electrochemistry: an overview of potential applications. *Analyst* **2010**, *135*, 2768-2778.
11. Shao, Y.; Wang, J.; Wu, H.; Liu, J.; Aksay, I. A.; Lin, Y. Graphene Based Electrochemical Sensors and Biosensors: A Review. *Electroanalysis* **2010**, *22*, 1027-1036.
12. Kuila, T.; Bose, S.; Khanra, P.; Mishra, A. K.; Kim, N. H.; Lee, J. H. Recent advances in graphene-based biosensors. *Biosens. Bioelectron.* **2011**, *26*, 4637-4648.
13. Li, Z. J.; Xia, Q. F. Recent advances on synthesis and application of graphene as novel sensing materials in analytical chemistry. *Rev. Anal. Chem.* **2012**, *31*, 57-81.
14. Valentini, F.; Carbone, M.; Paleschi, G. Graphene oxide nanoribbons (GNO), reduced graphene nanoribbons (GNR), and multi-layers of oxidized graphene

- functionalized with ionic liquids (GO-IL) for assembly of miniaturized electrochemical devices. *Anal. Bioanal. Chem.* **2013**, *405*, 3449-3474.
15. Stankovich, S.; Dikin, D. A.; Dommett, G. H. B.; Kohlhaas, K. M.; Zimney, E. J.; Stach, E. A.; Piner, R. D.; Nguyen, S. T.; Ruoff, R. S. Graphene-based composite materials. *Nature* **2006**, *442*, 282-286.
 16. Kosynkin, D. V.; Higginbotham, A. L.; Sinitskii, A.; Lomeda, J. R.; Dimiev, A.; Price, B. K.; Tour, J. M. Longitudinal unzipping of carbon nanotubes to form graphene nanoribbons. *Nature* **2009**, *458*, 872-U5.
 17. Shinde, D. B.; Debgupta, J.; Kushwaha, A.; Aslam, M.; Pillai, V. K. Electrochemical Unzipping of Multi-walled Carbon Nanotubes for Facile Synthesis of High-Quality Graphene Nanoribbons. *J. Am. Chem. Soc.* **2011**, *133*, 4168-4171.
 18. Terrones, M.; Botello-Mendez, A. R.; Campos-Delgado, J.; Lopez-Urias, F.; Vega-Cantu, Y. I.; Rodriguez-Macias, F. J.; Elias, A. L.; Muñoz-Sandoval, E.; Cano-Marquez, A. G.; Charlier, J.; Terrones, H. Graphene and graphite nanoribbons: Morphology, properties, synthesis, defects and applications. *Nano Today* **2010**, *5*, 351-372.
 19. Zhang, S.; Tang, S.; Lei, J.; Dong, H.; Ju, H. Functionalization of graphene nanoribbons with porphyrin for electrocatalysis and amperometric biosensing. *J. Electroanal. Chem.* **2011**, *656*, 285-288.
 20. R. John, D.B. Shinde, L. Liu, F. Ding, Z. Xu, C. Vijayan, V. K. Pillai, T. Pradeep Sequential Electrochemical Unzipping of Single-Walled Carbon Nanotubes to Graphene Ribbons Revealed by in Situ Raman Spectroscopy and Imaging. *ACS Nano* , 234-242.
 21. Brownson, D. A. C.; Kampouris, D. K.; Banks, C. E. Graphene electrochemistry: fundamental concepts through to prominent applications. *Chem. Soc. Rev.* **2012**, *41*, 6944-6976.
 22. Martín, A.; Hernández, J.; Vázquez, L.; Martínez, M. T.; Escarpa, A. Controlled chemistry of tailored graphene nanoribbons for electrochemistry: a rational approach to optimizing molecule detection. *RSC Adv.* **2014**, *4*, 132-139.
 23. Guo, Y.; Guo, W.; Chen, C. Tuning field-induced energy gap of bilayer graphene via interlayer spacing. *Appl. Phys. Lett.* **2008**, *92*, 243101.
 24. Chng, C.; Pumera, M.; Bonanni, A. Electrochemically reduced graphene nanoribbons: Interference from inherent electrochemistry of the material in DPV studies. *Electrochem. Commun.* **2014**, *46*, 137-139.
 25. Valentini, F.; Romanazzo, D.; Carbone, M.; Palleschi, G. Modified Screen-Printed Electrodes Based on Oxidized Graphene Nanoribbons for the Selective Electrochemical Detection of Several Molecules. *Electroanalysis* **2012**, *24*, 872-881.

26. Dong, X.; Long, Q.; Wang, J.; Chan-Park, M. B.; Huang, Y.; Huang, W.; Chen, P. A graphene nanoribbon network and its biosensing application. *Nanoscale* **2011**, *3*, 5156-5160.
27. Yang, Y.; Zhou, J.; Zhang, H.; Gai, P.; Zhang, X.; Chen, J. Electrochemical evaluation of total antioxidant capacities in fruit juice based on the guanine/graphene nanoribbon/glassy carbon electrode. *Talanta* **2013**, *106*, 206-211.
28. Srivastava, R. K.; Srivastava, S.; Narayanan, T. N.; Mahlotra, B. D.; Vajtai, R.; Ajayan, P. M.; Srivastava, A. Functionalized Multilayered Graphene Platform for Urea Sensor. *Acs Nano* **2012**, *6*, 168-175.
29. Shen, X.; Cui, Y.; Pang, Y.; Qian, H. Graphene oxide nanoribbon and polyhedral oligomeric silsesquioxane assembled composite frameworks for pre-concentrating and electrochemical sensing of 1-hydroxypyrene. *Electrochim. Acta* **2012**, *59*, 91-99.
30. Wu, S.; Lan, X.; Huang, F.; Luo, Z.; Ju, H.; Meng, C.; Duan, C. Selective electrochemical detection of cysteine in complex serum by graphene nanoribbon. *Biosens. Bioelectron.* **2012**, *32*, 293-296.
31. Tang, J.; Hou, L.; Tang, D.; Zhou, J.; Wang, Z.; Li, J.; Chen, G. Magneto-controlled electrochemical immunoassay of brevetoxin B in seafood based on guanine-functionalized graphene nanoribbons. *Biosens. Bioelectron.* **2012**, *38*, 86-93.
32. Tan, S. M.; Chua, C. K.; Pumera, M. Graphenes prepared from multi-walled carbon nanotubes and stacked graphene nanofibers for detection of 2,4,6-trinitrotoluene (TNT) in seawater. *Analyst* **2013**, *138*, 1700-1704.
33. Goh, M. S.; Pumera, M. Graphene-based electrochemical sensor for detection of 2,4,6-trinitrotoluene (TNT) in seawater: the comparison of single-, few-, and multilayer graphene nanoribbons and graphite microparticles. *Anal. Bioanal. Chem.* **2011**, *399*, 127-131.
34. Sun, C.; Chang, C.; Lee, H.; Zhou, J.; Wang, J.; Sham, T.; Pong, W. Microwave-Assisted Synthesis of a Core-Shell MWCNT/GONR Heterostructure for the Electrochemical Detection of Ascorbic Acid, Dopamine, and Uric Acid. *Acs Nano* **2011**, *5*, 7788-7795.
35. Pumera, M.; Escarpa, A. Nanomaterials as electrochemical detectors in microfluidics and CE: Fundamentals, designs, and applications. *Electrophoresis* **2009**, *30*, 3315-3323.
36. Suresh, S.; Srivastava, V.; Mishra, I. M. Adsorption of catechol, resorcinol, hydroquinone, and their derivatives: a review. *IJEEE* **2012**, *3*, 32.
37. Salimi, A.; MamKhezri, H.; Hallaj, R. Simultaneous determination of ascorbic acid, uric acid and neurotransmitters with a carbon ceramic electrode prepared by sol-gel technique. *Talanta* **2006**, *70*, 823-832.

38. Zen, J. M.; Hsu, C. T.; Hsu, Y. L.; Sue, J. W.; Conte, E. D. Voltammetric peak separation of dopamine from uric acid in the presence of ascorbic acid at greater than ambient solution temperatures. *Anal. Chem.* **2004**, *76*, 4251-4255.
39. Reddaiah, K.; Reddy, T. M.; Raghu, P. Electrochemical investigation of L-dopa and simultaneous resolution in the presence of uric acid and ascorbic acid at a poly (methyl orange) film coated electrode: A voltammetric study. *J. Electroanal. Chem.* **2012**, *682*, 164-171.
40. O'Neill, R. D. Microvoltammetric Techniques and Sensors for Monitoring Neurochemical Dynamics In-Vivo - a Review. *Analyst* **1994**, *119*, 767-779.
41. Hu, G.; Chen, L.; Guo, Y.; Wang, X.; Shao, S. Selective determination of L-dopa in the presence of uric acid and ascorbic acid at a gold nanoparticle self-assembled carbon nanotube-modified pyrolytic graphite electrode. *Electrochim. Acta* **2010**, *55*, 4711-4716.
42. Antisari, M. V.; Marazzi, R.; Krsmanovic, R. Synthesis of multiwall carbon nanotubes by electric arc discharge in liquid environments. *Carbon* **2003**, *41*, 2393-2401.
43. Benito, A. M.; Maser, W. K.; Martinez, M. T. Carbon nanotubes: from production to functional composites. *Int. J. Nanotechnol.* **2005**, *2*, 71-89.
44. Gao, X.; Jang, J.; Nagase, S. Hydrazine and Thermal Reduction of Graphene Oxide: Reaction Mechanisms, Product Structures, and Reaction Design. *J. Phys. Chem. C* **2010**, *114*, 832-842.
45. Zhou, M.; Zhai, Y.; Dong, S. Electrochemical Sensing and Biosensing Platform Based on Chemically Reduced Graphene Oxide. *Anal. Chem.* **2009**, *81*, 5603-5613.
46. Jiao, L.; Zhang, L.; Wang, X.; Diankov, G.; Dai, H. Narrow graphene nanoribbons from carbon nanotubes. *Nature* **2009**, *458*, 877-880.
47. Barros, E. B.; Sato, K.; Samsonidze, G. G.; Souza Filho, A. G.; Dresselhaus, M. S.; Saito, R. D band Raman intensity calculation in armchair edged graphene nanoribbons. *Phys. Rev. B* **2011**, *83*, 245435.
48. Stankovich, S.; Dikin, D. A.; Piner, R. D.; Kohlhaas, K. A.; Kleinhammes, A.; Jia, Y.; Wu, Y.; Nguyen, S. T.; Ruoff, R. S. Synthesis of graphene-based nanosheets via chemical reduction of exfoliated graphite oxide. *Carbon* **2007**, *45*, 1558-1565.
49. Cheng, M.; Yang, R.; Zhang, L.; Shi, Z.; Yang, W.; Wang, D.; Xie, G.; Shi, D.; Zhang, G. Restoration of graphene from graphene oxide by defect repair. *Carbon* **2012**, *50*, 2581-2587.
50. Lerf, A.; He, H. Y.; Forster, M.; Klinowski, J. Structure of graphite oxide revisited. *J Phys Chem B* **1998**, *102*, 4477-4482.

51. He, H. Y.; Klinowski, J.; Forster, M.; Lerf, A. A new structural model for graphite oxide. *Chem. Phys. Lett.* **1998**, *287*, 53-56.
52. Anson, F. C.; Osteryoung, R. A. Chronocoulometry - a Convenient, Rapid and Reliable Technique for Detection and Determination of Adsorbed Reactants. *J. Chem. Educ.* **1983**, *60*, 293-296.
53. Anson, F. C. Application of Potentiostatic Current Integration to Study of Adsorption of Cobalt(3-)-Ethylenedinitrilo)tetraacetate on Mercury Electrodes. *Anal. Chem.* **1964**, *36*, 932-934.
54. Stevens, N. P. C.; Rooney, M. B.; Bond, A. M.; Feldberg, S. W. A comparison of simulated and experimental voltammograms obtained for the [Fe(CN)(6)](3-/4-) couple in the absence of added supporting electrolyte at a rotating disk electrode. *J. Phys. Chem. A* **2001**, *105*, 9085-9093.

II.3. Graphene nanoribbons for electrochemical biosensing



II.3.1. Introduction and objectives

The analysis of enantiomeric L/D-amino acids (L/D-AAAs) has been an incessant problem for scientists, because of their same physical and chemical properties. Although L-AAAs have been the most studied enantiomer, because they are involved in important physiological functions, D-AAAs have recently shown special interest in excellent literature. As selected and relevant example, Lam and collaborators described how in *Vibrio cholerae*, a racemase produces D-methionine (D-Met), whereas in *Bacillus subtilis* generates D-tyrosine (D-Tyr).¹ These unusual D-AAAs, which could be considered biomarkers of important diseases, appear to modulate the synthesis of peptidoglycan, a strong and elastic polymer that is a component of the bacterial cell wall.² Likewise, D-Tyr has been recognized as an important biomarker, because its excess in plasma and in urine indicates the presence of renal failures in humans.³

For the D,L-Tyr determination, there are several methods based on gas chromatography coupled with mass-spectrometry, HPLC or CE.⁴⁻⁶ However, the high cost of equipments and assays, the high time consumption and the use of derivatized amino acids have avoided its application to directly monitor *in situ* measurements as point of care testing tools. Other approaches such as microchip electrophoresis,⁷ molecular imprinted polymers⁸ or complex strategies based on inclusion complexes for the resolution of D,L-AAAs⁹ have also been explored with high sensitivity. However, these techniques still require specific expensive technology and qualified training.

Considering the clinical relevance of this issue, in this epigraph of this Doctoral Thesis, a fast, simple and reliable *in situ* approach for the simultaneous resolution and determination of the target D,L-AAAs

on disposable electrochemical (bio-)-sensors is studied. The strategy involves the simultaneous enantiomeric resolution and determination of both (i) the D-AA bio-sensing using a class-enzyme that selectively reacts with one of the enantiomers to yield hydrogen peroxide and, (ii) the direct electrochemical sensing of the L-enantiomer, taking advantage of its inherent electroactivity, using a suitable graphene-based transducer. This strategy was applied to the simultaneous analysis of D and L Tyr and Met, as relevant target clinical amino acids.

On the one hand, to assess the selectivity in the detection of the D-enantiomer biomarker and the complete quantitative reaction to hydrogen peroxide, we have used the enzyme D-amino acid oxidase (DAAO). This enzyme oxidatively deaminates D-AAs to the corresponding α -keto acids, without reacting with the corresponding L-AA.

On the other hand, the electrochemical sensing of the L-AAs needs to be selectively detected from the hydrogen peroxide, which is generated by the enzymatic reaction, with enough sensitivity and preventing the fouling. Therefore, GNRs were selected to enhance these analytical requirements for the direct, selective and *in situ* electrochemical detection of the L-AAs involved in the racemic solution.

As it has been already discussed in the previous sections, we hypothesizes that the very rich edge chemistry of GNRs and the features derived from their high specific surface area such as electro-catalysis, enhanced sensitivity and their resistance-to-fouling offer us a suitable electrochemistry in this (bio-)-sensing approach. Thus, we will describe in the following sections the appropriate combination of these advantages of GNRs plus the selectivity and sensitivity derived

from the DAAO for the fabrication of highly specific sensors for enantiomeric analysis as simplified valuable alternative to the well-established technology in the field.

Furthermore, despite the large number of applications employing DAAO to exclusively measure the generated H_2O_2 from the D-AAs by different electrochemical approaches,¹⁰⁻¹⁶ as far as we know, no examples of this enzyme coupled with graphene are found in the literature.

II.3.2. Strategy for the enantiomeric amino acid analysis

The proposed strategy involves both the simultaneous D-AA biosensing, using a class-enzyme that selectively reacts with D-enantiomer to yield hydrogen peroxide, and the direct electrochemical sensing of the L-enantiomer using GNR transducers. This strategy was applied to relevant AAs such as Tyr and Met, as it is illustrated in **Figure II.22**, on a disposable platform, just consuming 50 μ L of sample and avoiding any adsorption or covalent union of the enzyme. Under optimum bio-chemical conditions (10 mM NaH_2PO_4 pH 7.00), L,D-AA racemate was resolved under 360 s. Indeed, L-Tyr and L-Met were detected at +0.59 V and +1.25 V, respectively and the hydrogen peroxide was oxidized at +0.87 V on the GNRox. Suitable controls were also carefully checked. Background signal displayed by buffer and the blank of the enzyme without presence of D or L AA did not give any peak in the scanned window potential (see **Figure II.22**). No formation of hydrogen peroxide at the L-AA tested concentrations was either noticed.

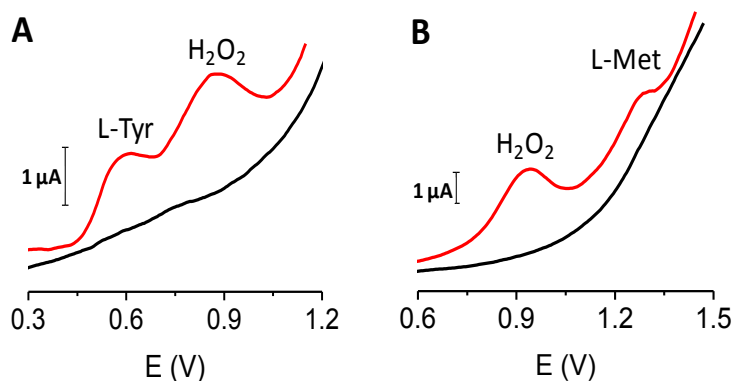


Figure II.22. Voltammograms for enantiomeric analysis of 1 mM L,D AAs: (A) Tyr, (B) Met in 10 mM NaH_2PO_4 , pH 7.00, and 0.50 mg/mL DAAO after 360 s. Background signal of NaH_2PO_4 with DAAO (black). DPV with 25 mV pulse potential and 0.07 s pulse time with 5 mVs^{-1} scan rate and potential versus Ag

II.3.3. Optimization of the enantiomeric amino acid analysis

Firstly, the optimization of the electrochemical sensing was performed, for that, two GNRs, GNRred and GNRox were explored in order to examine the suitability of these two nanomaterials for the determination of the target enantiomers. As it is shown in **Figure II.23**, GNRs exhibited an improved electrochemical performance in comparison with non-modified CSPE. Both GNRs presented much higher current intensity and lower oxidation potentials than the non-modified CSPE. The marked electrocatalytic effect exhibited by these two graphene materials could be explained considering the interactions between both graphene structures and Tyr. The interactions are caused by the adsorption of analytes via π - π stacking interaction with the non-oxidized benzene groups, as well as by

electrostatic or hydrogen bond-based interactions with functional moieties located at the edges. Considering the results obtained by XPS, GNRox showed high percentage of carboxyl and alcohol groups while the content of sp^2 carbons and defects in the structure were increased in GNRred.¹⁷

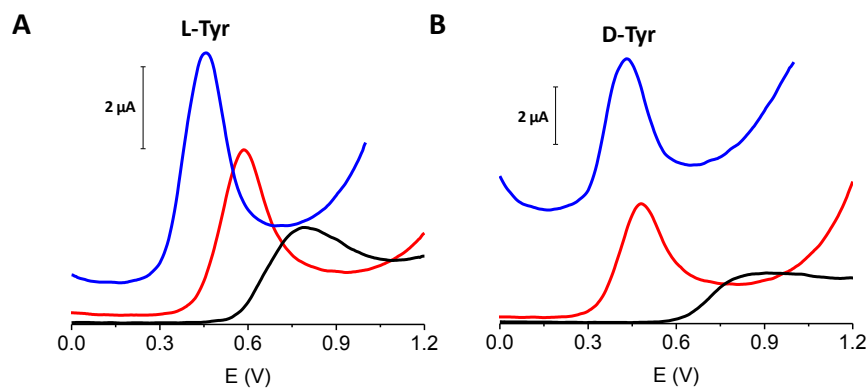


Figure II.23. Voltammograms for (A) L-Tyr and (B) D-Tyr, using GNRred (blue), GNRox (red) and non-modified CSPE (black) in 10 mM NaH_2PO_4 , pH 7.00. (For other conditions, see Figure II.22)

Remarkably, both L and D Tyr showed the highest intensity current and the lowest oxidation potentials with GNRred, however, at potentials over +0.50 V, in which analytes such as Met and H_2O_2 are oxidized, the background signal of GNRred makes difficult the detection of molecules of high oxidation potential. In this case, in GNRred, potentials over +0.50 V provokes the oxidation of the carbon material, avoiding the detection of H_2O_2 . However, this phenomenon does not appear in GNRox, becoming this transducer the most suitable for the detection of both H_2O_2 and Met with improved performance than CSPE. Hence, GNRox becomes as the most suitable electrochemical transducer for D-Tyr, D-Met and H_2O_2 detection. Furthermore, GNRox demonstrated to improve the

sensitivity as well as simultaneously detect and resolve the target enantiomers in comparison with non-modified CSPE that did not achieve so good results. **Table II.S3** (see Appendix II.3.7) lists the oxidation potentials and the amperometric currents obtained. Remarkably, as it is listed in this table, in comparison with CSPE, these GNRox dramatically improved the reproducibility of the electrochemical sensing of the L,D-enantiomers (up to 20-folds i.e. from RSDs of 19 % in CSPE to RSDs of 1% in GNRox, in amperometric currents, n=5). Overall, these results confirm our previous hypothesis regarding the electrocatalysis, high sensitivity and the anti-fouling effect expected from these carbon nanomaterials.

In order to elucidate how graphene is deposited on the electrode surface, FE-SEM images were obtained. In **Figure II.24**, clear differences were noticed in the surface of the electrode between the modified GNRox and non-modified CSPE (**inset**). Indeed, GNRox layers of several hundred of nm deposited on CSPE are randomly distributed along the electrode. They appear as thin GNRox curtains, creating a new surface.

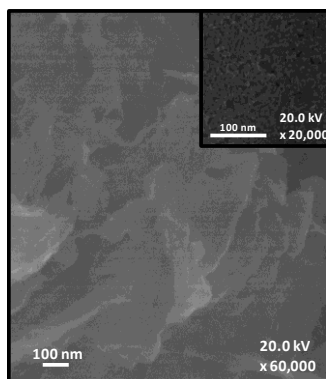


Figure II.24. Field-emission scanning microscopy images. Micrograph for modified GNRox and CSPE (**inset**) electrodic surfaces

Secondly, the optimization of the electrochemical biosensing was carried out. The enzymatic reaction was directly performed *in situ* on the electrode surface with a 50 μL drop mixture of the racemic amino acid and DAAO, behaving the electrode surface as the reaction cell. In this approach, the enzyme is not covalently immobilized onto the electrodic surface, therefore, the procedure is simpler than in the most classical covalent-based approaches.

On the one hand, **Table II.10** lists the enzymatic reaction progress. While the D-Tyr current intensity peak decreases, the H_2O_2 generated *in situ* increases. The optimal reaction time was 360 s. At that time, D-Tyr was quantitatively consumed and consequently, the signal obtained is only from the generated hydrogen peroxide. These results indicated the accurate resolution of the racemate.

We have also studied the buffer influence in the enzymatic reaction, varying both buffer concentration and pH values (results showed in **Tables II.S4** and **II.S5**, see Appendix II.3.7). The buffer optimal conditions were 10 mM and pH 7.00 for NaH_2PO_4 .

Table II.10. Optimization of the enzymatic reaction time

Time (s)	0	60	120	180	240	300	360	420	
Intensity	D-Tyr	0.614	0.598	0.890	0.481	0.360	0.017	ND	ND
(μA)	H_2O_2	0.574	0.636	0.733	0.780	0.848	0.855	0.927	0.932

1 mM D-Tyr and 0.50 mg mL^{-1} DAAO in 10 mM NaH_2PO_4 pH 7.00

On the other hand, enzyme and substrate concentrations are also important values to be optimized. While L-Tyr did not showed reaction with the enzyme, **Figure II.25A** shows the increase in the current intensity of the generated H_2O_2 and the decrease in the D-

enantiomer when the enzyme concentration increased. At concentrations of DAAO higher than 0.50 mg/mL, the D-AA completely reacted with the enzyme, the intensity of the hydrogen peroxide kept constant and the correspondent intensity of the D-AA was zero. Therefore, this value was considered the optimal enzyme concentration. Moreover, **Figure II.25B** suggests that at concentrations higher than 1.0 mM of substrate, the linearity in the H_2O_2 intensity is lost and the enzyme is saturated by the substrate. The good response of the enzyme and these results demonstrated that the enzymatic reaction carried out in the drop solution was perfectly working in the optimized conditions. Furthermore, the strategy could be developed in just 50 μL of sample without any covalent immobilization bond of the enzyme on the electrodic surface.

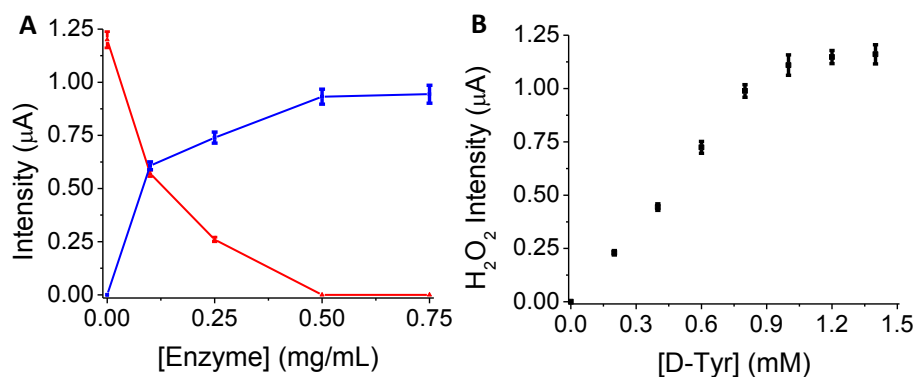


Figure II.25. (A) Plot of current intensities for extinction of D-Tyr (red) and apparition of enzymatic product, H_2O_2 (blue) versus enzyme concentration for 1 mM D-Tyr 10 mM NaH_2PO_4 , pH 7.00 after 360 s. (B) Plot representation of generated hydrogen peroxide current intensity versus D-Tyr concentration for 1 mM D-Tyr in 10 mM NaH_2PO_4 , pH 7.00 and 0.50 mg/mL DAAO after 360 s. Bar errors for RSDs (%), $n=3$)

Under these electrochemical and bio-sensing optimized conditions, a careful study of precision of the method was performed. The electrochemical graphene-based enantiomeric bio-sensor presented excellent intra-electrode repeatability ($RSD \leq 3\%$ for redox potentials and $RSD \leq 4\%$ for intensity currents, $n=5$) and inter-electrode reproducibility ($RSD \leq 5\%$ for redox potentials and $\leq 10\%$ for intensity currents, $n=5$). It indicated an excellent performance of the electrode to be used as a disposable platform.

II.3.4. Enantiomeric amino acid calibration and analysis

As we depict in the introduction section, the objective of this work was the development of an electrochemical point of care system capable of detecting and resolving the D-AA, in a similar concentration range than the one established by Lam et al.¹ Consequently, the simultaneous enantiomeric calibration was also another feature assayed during the evaluation of the sensor performances. Interestingly, **Figure II.26A** shows the DPV for different L,D Tyr concentrations, therefore, the two peaks increase with the AAs concentration, one of the peaks around +0.61 V corresponding to L-Tyr and the other around +0.92 V from H_2O_2 generated from D-Tyr at each assayed concentration. The calibration (see **Figure II.26B**) showed excellent linearity with ($R^2 \geq 0.990$) and low LODs of 100 and 60 μM for L and D Tyr, respectively.

In order to evaluate this strategy, we chose urine samples since D-Tyr is a renal biomarker.³ Furthermore, due to the health hazard of working with bacteria, urine samples become a suitable matrix to

assess future diagnosis using these samples as non-invasive and more accessible ones.

Figure II.26C shows the overall analysis carried out using healthy urine samples. Firstly, as expected, no detection of D-Tyr was noticed, however, UA was identified at +0.32 V in both non-spiked (voltammogram black) and spiked urine samples (voltammogram blue) releasing quantitative and reproducible recoveries of $100\pm 1\%$. Secondly, spiked urine samples in Tyr enantiomers were also assayed (voltammogram red) obtaining quantitative and reproducible recoveries of $95\pm 5\%$ and $99\pm 3\%$ ($n=3$) for L-Tyr (at +0.64 V) and generated H_2O_2 (at +0.99 V), respectively.

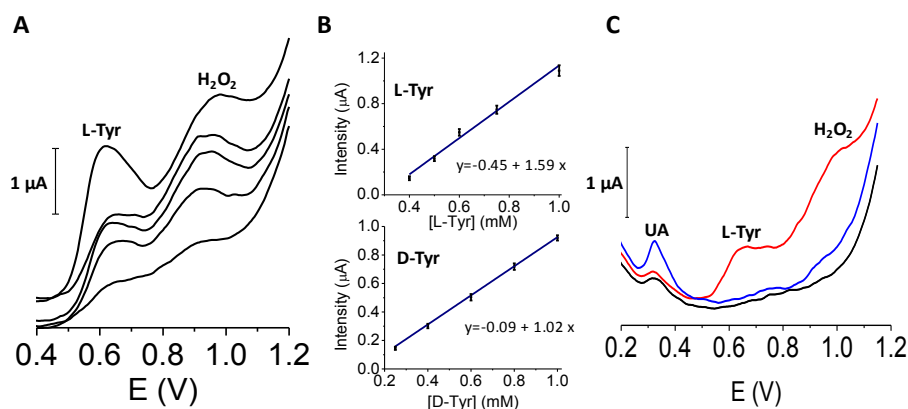


Figure II.26. (A) Voltammograms from 0.25 mM to 1.25 mM of D and L-Tyr. (B) Linear plot and linear equation for L (up) and D-Tyr (down), respectively. Bar errors for RSDs (%), $n=3$). (C) Voltammograms obtained for urine analysis. Diluted urine (black), fortified with 1 mM UA (blue) and fortified with 0.50 mM D-Tyr and L-Tyr (red). (For other conditions, see Figure II.22)

Overall, L and D Tyr enantiomers were determined with accuracy and precision in presence of UA, giving an additional value to the proposed approach. Even, under these conditions, the simultaneous detection of the two targeted D-AAs towards the confirmation of the detection of the L-AAs (Tyr and Met) could be possible.

The influence of other amino acids for the analysis of complex samples is expected, therefore, as well as L-Met, L-histidine was also considered as potential electroactive amino acid interference in biological fluids. This amino acid did not interfere in the Tyr analysis because its oxidation potential was found over the ones for tyrosine and hydrogen peroxide. Also, the presence of DAAO did not give any further signal, indicating the selectivity of the enzyme to D-enantiomers exclusively.

The determination of D-Tyr in urine samples was successfully performed in less time and with low cost, in comparison with other approaches found in the literature. The results obtained in this preliminary application are very valuable and promising. They have allowed the selective detection of the target D-AAs studied in this work (D-Met and D-Tyr), involved in important bacterial diseases (*Vibrio cholerae* and *Bacillus subtilis*), and they have also given a reliable and selective assessment of a D-AA index towards the electro-catalyzed detection of hydrogen peroxide. The successful exploration of these target D-AAs in non-invasive urine samples opens an exciting perspective for rapid *in-situ* diagnosis.

II.3.5. Conclusions

The strategically driven selectivity of the DAAO towards D-AAs and the inherent electrocatalysis exhibited by GNROx to L-AAs and hydrogen peroxide generated from D-AA have allowed to resolve the racemic mixture of L and D electroactive target AAs with clinical relevance such as Tyr and Met.

The disposable electrochemical graphene-based enantiomeric biosensor allows a fast, selective, accurate and reproducible determination of D-Tyr and D-Met biomarkers in urine samples in 360 s and using just 25 μ L of sample exploiting the advantages of the enzyme in solution.

From a technical point of view, the possibility of simultaneously detect these enantiomers and uric acid without any separation step is of chief interest for the clinical field since the equipment used is portable, adaptable in any electronic equipment and easy to use by any minimally trained personnel.

It is worth to notice that the possibility of using this strategy for new enantiomeric resolution of molecules is opened. Additionally, although this work has been merely focused on the resolution of L and D AAs, it opens new alternatives and the possibility of measuring total D AA content (D-AA index, even for non-electroactive amino acids). This new suggestion could be interesting to assure the presence of certain diseases or malfunctions in biological samples becoming a valuable screening tool for diagnosis. Even, this approach becomes highly promising as future point of care for fast *in situ* early diagnosis of these diseases related to the presence of D-AAs.

II.3.6. Experimental Section

II.3.6.1. Reagents, standards and samples

D-Tyr, L-Tyr and L-Met were purchased from Fluka Chemika (Buchs, UK) and hydrogen peroxide and D-Met was obtained in Sigma Aldrich (St. Louis, MO, USA). Sodium dihydrogen phosphate was purchased from Panreac, (Badalona, Spain). D-amino acid oxidase was purchased from Sigma Aldrich (St. Louis, MO, USA). Different concentrations and mixtures of D and L-Tyr were prepared in sodium dihydrogen phosphate buffer adjusted with NaOH. The enzyme was also diluted in the same buffer. Both pH value and buffer concentration were optimized, as well as the enzyme concentration.

All solutions were daily prepared using ultrapure water treated in a Milli-Q system (Millipore, Bedford, MA, USA). Urine samples 1:50 diluted were recollected from healthy individuals.

II.3.6.2. Apparatus and measurements

FE-SEM micrographs were obtained on a JEOL Model JSM6335F equipment working at 5 kV. Direct determination of oxygen was carried out with a Flash 1112 analyzer from Thermo Fisher Scientific.

All electrochemical measurements were performed, at room temperature, on an USB-based portable electrochemical station μ -Stat 100 potentiostat controlled by PSLite 1.6 software and on a CSPE, which integrates the three-electrode system, a carbon working electrode of 4 mm diameter as well as a carbon counter and silver reference electrodes (Dropsens, Oviedo, Spain).

II.3.6.3. Preparation of graphene modified electrode

Graphene detailed synthesis and characterization features have been previously reported (see **II.2.2**). In brief, graphene materials were

synthesized from MWCNTs via the longitudinal unzipping method.¹⁸ Using these oxidized nanoribbons (44 wt.% oxygen content, 0.8 nm height by AFM, 46% C=O, 26% C-O, 19% Csp³, 2% Csp² by XPS), reduced graphene oxide nanoribbons (14 wt. % oxygen content, 1.2 nm height by AFM, 15% C=O, 10% C-O, 47% Csp², 10% Csp³ by XPS) were obtained by chemical reduction with N₂H₄/NH₃.¹⁹

GNRox were dispersed to obtain a 0.5 mg mL⁻¹ sample in water by ultrasonication in a bath for 30 min. GNRred were dispersed to obtain a 0.5 mg mL⁻¹ dispersion in water/NH₃ (1% v/v) by ultrasonication in a bath for 30 min, followed by tip sonication using a VCX130, (Sonics, Newtown, USA) for 2 minutes at 130 W. The graphene nanoribbons modified electrodes were prepared by casting 10 μL of 0.5 mg mL⁻¹ graphene nanoribbons on the CSPE surface. This volume was previously optimized by modifying the CSPE with different volumes 5, 10, 15 and 20 μL of 0.5 mg mL⁻¹ and exploring its electrochemical behavior by cyclic voltammetry with 0.5 mM K₃Fe(CN)₆ in 1 M KCl on both graphene surfaces. The modified CSPEs will be named GNRox and GNRred along this work.

II.3.6.4. Analytical procedure

Following the optimal reaction conditions, 25 μL of a 0.50 mg mL⁻¹ DAAO in 10 mM NaH₂PO₄ pH 7.00 were placed on the electrode. Immediately, 25 μL of the amino acid solution in 10 mM NaH₂PO₄ pH 7.00 were added, considering this time reaction 0 s. These total 50 μL of the solution permitted to cover the three electrode electrochemical cell and to record the measurements.

After the optimized reaction time (360 s), DPV was performed with a potential range from +0.20 to +1.20 V and from +0.30 to + 1.50 V for Tyr and Met analysis, respectively, with 5 mV step potential, 25 mV pulse potential, 5 mVs⁻¹ scan rate, 0.07 s pulse time and 3 s equilibration time.

II.3.7. Appendix

II.3.7.1. Electrode selection

Table II.S3 shows both current intensity and oxidation potentials for 1 mM L,D-Tyr, L,D-Met and 1 mM H₂O₂ as well as buffer and enzyme background DPVs onto bare CSPE and modified with GNRox and GNRred electrodes using 10 mM NaH₂PO₄ (pH=7.00) and 0.50 mg/mL DAAO. The controls without analytes with the background electrolyte and enzyme were also carried out and they did not give any peak response. The measurements were repeated three times to establish repeatability conditions. (More information, see Experimental conditions in **II.3.6**).

Table II.S3. Electroanalytical features of the oxidation of aminoacid enantiomers in CSPE, GNRred/CSPE and GNRox/CSPE. (RSD (%), n=3)

Analyte	MATERIAL											
	CSPE				GNRred				GNRox			
	E (V)	RSD (%)	i (μ A)	RSD (%)	E (V)	RSD (%)	i (μ A)	RSD (%)	E (V)	RSD (%)	i (μ A)	RSD (%)
L-Tyr	0.81	3.5	1.32	19	0.46	7.2	5.00	4.6	0.54	8.0	3.55	1.0
D-Tyr	0.81	3.6	1.03	19	0.42	3.0	4.50	3.4	0.50	3.0	3.36	5.0
L-Met	1.30	4.0	2.56	17	1.27	4.0	2.10	4.0	1.19	3.0	1.80	6.5
D-Met	1.28	4.0	1.78	14	1.27	3.5	1.61	5.4	1.20	4.0	1.63	4.0
H ₂ O ₂	1.10	2.8	0.56	3.5	ND		ND		0.77	3.6	2.55	4.0

1 mM analyte; 10 mM NaH₂PO₄ (pH 7.00); 0.50 mg/mL DAAO

II.3.7.2. Buffer concentration and pH selection

Tables II.S4 and **II.S5** show the results obtained for the optimization of buffer concentration and pH of the proposed platform to resolve the enantiomeric L and D amino acids sample. DPV intensity currents of generated H_2O_2 , produced by the enzymatic reaction, depending on buffer concentration (**Table II.S4**) and pH (**Table II.S5**). Reaction conditions: 1 mM D-Tyr, 0.50 mg/mL DAAO in NaH_2PO_4 after 360 s.

Table II.S4. Optimization of detection buffer

[Buffer] (mM)	5	10	25	50
I (μA) H_2O_2	1.33	1.35	1.04	0.81

Reaction conditions: 1 mM D-Tyr, 0.5 mg/mL DAAO in NaH_2PO_4 pH 7.00

Table II.S5. Optimization of pH buffer

pH buffer	6.00	7.00	8.00	9.00
I (μA) H_2O_2	0.81	0.99	0.97	0.70

Reaction conditions: 1 mM D-Tyr, 0.50 mg/mL DAAO in 10 mM NaH_2PO_4

II.3.8. References

1. Lam, H.; Oh, D.; Cava, F.; Takacs, C. N.; Clardy, J.; de Pedro, M. A.; Waldor, M. K. D-Amino Acids Govern Stationary Phase Cell Wall Remodeling in Bacteria. *Science* **2009**, *325*, 1552-1555.
2. Siegrist, M. S.; Whiteside, S.; Jewett, J. C.; Aditham, A.; Cava, F.; Bertozzi, C. R. D-Amino Acid Chemical Reporters Reveal Peptidoglycan Dynamics of an Intracellular Pathogen. *ACS Chem. Biol.* **2013**, *8*, 500-505.
3. Young, G. A.; Kendall, S.; Brownjohn, A. M. D-Amino Acids in Chronic-Renal-Failure and the Effects of Dialysis and Urinary Losses. *Amino Acids* **1994**, *6*, 283-293.
4. Tojo, M.; Murakami, M.; Nagata, Y. Simple and Low-Cost High-Performance Liquid Chromatographic Method for Determination of D- and L-Amino Acids. *J. Chromatogr. Sci.* **2012**, *50*, 393-395.
5. Bruckner, H.; Schieber, A. Determination of amino acid enantiomers in human urine and blood serum by gas chromatography-mass spectrometry. *Biomed. Chromatogr.* **2001**, *15*, 166-172.
6. Kitagawa, F.; Otsuka, K. Recent progress in capillary electrophoretic analysis of amino acid enantiomers. *J. Chromatogr. B* **2011**, *879*, 3078-3095.
7. Huang, Y.; Shi, M.; Zhao, S.; Liang, H. Trace analysis of D-tyrosine in biological samples by microchip electrophoresis with laser induced fluorescence detection. *J. Chromatogr. B* **2011**, *879*, 3203-3207.
8. Liang, H. J.; Ling, T. R.; Rick, J. F.; Chou, T. C. Molecularly imprinted electrochemical sensor able to enantioselectively recognize D and L-tyrosine. *Anal. Chim. Acta* **2005**, *542*, 83-89.
9. Tao, Y.; Dai, J.; Kong, Y.; Sha, Y. Temperature-Sensitive Electrochemical Recognition of Tryptophan Enantiomers Based on β -Cyclodextrin Self-Assembled on Poly(L-Glutamic Acid). *Anal. Chem.* **2014**, *86*, 2633-2639.
10. Lata, S.; Batra, B.; Kumar, P.; Pundir, C. S. Construction of an amperometric D-amino acid biosensor based on D-amino acid oxidase/carboxylated multiwalled carbon nanotube/copper nanoparticles/polyaniline modified gold electrode. *Anal. Biochem.* **2013**, *437*, 1-9.
11. Lata, S.; Pundir, C. S. Fabrication of an amperometric d-amino acid biosensor based on nickel hexacyanoferrate polypyrrole hybrid film deposited on glassy carbon electrode. *Bioprocess Biosyst. Eng.* **2013**, *36*, 81-89.
12. Dominguez, R.; Serra, B.; Reviejo, A. J.; Pingarron, J. M. Chiral analysis of amino acids using electrochemical composite bienzyme biosensors. *Anal. Biochem.* **2001**, *298*, 275-282.

13. Nieh, C.; Kitazumi, Y.; Shirai, O.; Kano, K. Sensitive D-amino acid biosensor based on oxidase/oxidase system mediated by pentacyanoferrate-bound polymer. *Biosens. Bioelectron.* **2013**, *47*, 350-355.
14. Sacchi, S.; Rosini, E.; Caldinelli, L.; Pollegioni, L. Biosensors for D-Amino Acid Detection. *Unnatural Amino Acids: Methods and Protocols* **2012**, *794*, 313-324.
15. Wcislo, M.; Compagnone, D.; Trojanowicz, M. Enantio selective screen-printed amperometric biosensor for the determination of D-amino acids. *Bioelectroch.* **2007**, *71*, 91-98.
16. Wu, X. X.; Van Wie, B. J.; Kidwell, D. A. An enzyme electrode for amperometric measurement of D-amino acid. *Biosens. Bioelectron.* **2004**, *20*, 879-886.
17. Martin, A.; Hernandez-Ferrer, J.; Vazquez, L.; Martinez, M.; Escarpa, A. Controlled chemistry of tailored graphene nanoribbons for electrochemistry: a rational approach to optimizing molecule detection. *RSC Adv.* **2014**, *4*, 132-139.
18. Kosynkin, D. V.; Higginbotham, A. L.; Sinitskii, A.; Lomeda, J. R.; Dimiev, A.; Price, B. K.; Tour, J. M. Longitudinal unzipping of carbon nanotubes to form graphene nanoribbons. *Nature* **2009**, *458*, 872-U5.
19. Gao, X.; Jang, J.; Nagase, S. Hydrazine and Thermal Reduction of Graphene Oxide: Reaction Mechanisms, Product Structures, and Reaction Design. *J. Phys. Chem. C* **2010**, *114*, 832-842.

Chapter III

Graphene for electrochemical microfluidic (bio-)-sensing

From building materials and fossil fuels to pots, pans, space-age lasers and silicon chips we rely on the Earth's mineral wealth. From prospecting to production, understanding earth science is a key to our production. (Science Museum, London))



**III.1. Carbon nanomaterials for
electrochemical microfluidic (bio-)-
sensing: *State of the art***



III.1.1. Microfluidic chips coupled to electrochemical detection

The necessity of the scientific community to fabricate new analytical instruments and devices in the micro and nano-scales to adapt the older macro-scales, lead to Manz and other scientists to modify the concept of Total Analysis System to the new micro-total analysis system or “lab-on-a-chip”. In this latter concept, synthesis and analytical processes are performed in the miniaturized system.¹⁻³ Consequently, a total integration of sample injection, reaction, separation and detection would be possible in a simple, automatic device at the micro-scale.

The main reasons why the micro-scale presents more advantages in contrast to macro-scale are: (i) low sample volume and waste of reactive, (ii) possible integration of sample pre-treatment, derivation and calibration steps in the microfluidic system and the possibility of the automation of the analytical system, (iii) fast response because of the low dimensions, and (iv) easy coupling with nanomaterials such as graphene, CNTs, nanoparticles and other nanostructures.

As a result of the miniaturization in scale, afterwards, the concept of microfluidic was defined as the science and technology of systems that process or manipulate small amounts of fluids (nL-pL), using channels measuring from ten to hundreds of micrometers.^{2,4}

Capillary electrophoresis (CE) miniaturization has constituted one of the first examples of micro-total analysis system with the fabrication of microfluidic chips (MC).^{5,6} The fast development of microfabrication techniques and the low volumes in the range of (nL) has permitted the fast improvement of MC. Therefore the basics of

CE are implemented in these microsystems. From now on when referring to MC, we will refer to the electrophoresis miniaturization (microchip electrophoresis).

Briefly, as in traditional CE methods, in MC, analytes migrate through electrolyte solutions under the influence of an electric field. The velocity of migration of an analyte in the channel is based on the electrophoretic mobility of the molecule fundamentally dependent on its charge-mass ratio and the electroosmotic flow of the buffer solution. Therefore, these two variables permit the separation of the analytes along the microchip.

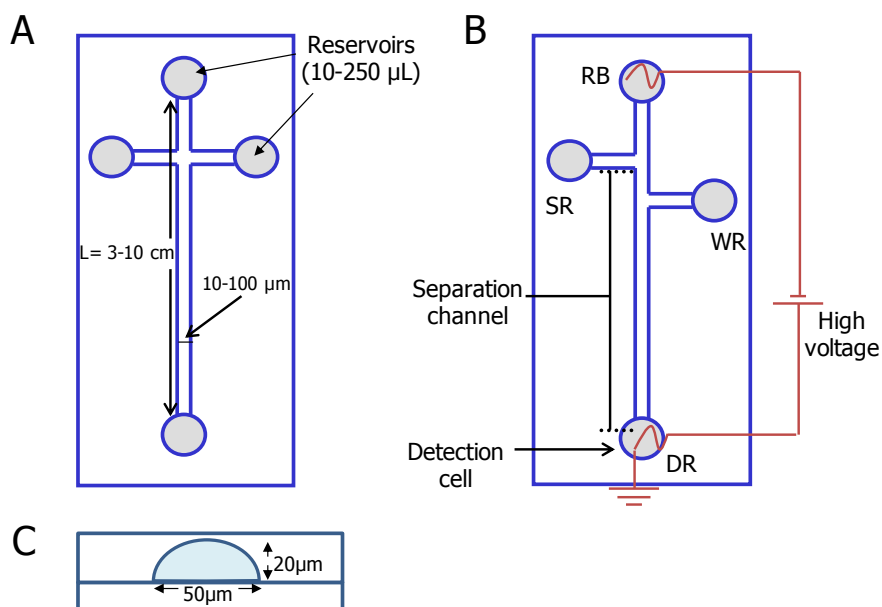


Figure III.1. MC layouts: (A) single cross-injector, (B) double-T injector and (C) cross section of the microchannel. Reservoirs: RB, running buffer reservoir. SR, sample reservoir. WR, waste reservoir. DR, detection reservoir

The MC layouts shown in **Figure III.1A-B** present a set-up of microchannels with a typical length between 3 to 10 cm and widths varying from 10 to 100 μm . The channels are only lithographed in one of the two wafers (see **Figure III.1C**), therefore, it consists in a semicircle of 50 μm diameter by 20 μm width, measured in our set-up. On the other hand, there are four main reservoirs to introduce the sample (SR), the running buffer (RB) and two other reservoirs for the waste (WR) and for the detection (DR), which volume varies from 50 to 200 μm .

In general, these MC are fabricated with glass and polymers such as polydimethylsiloxane (PDMS) or polymethyl methacrylate (PMMA) substrates. Glass is the most common material used because of the good optical properties, it allows optical detection and visual inspection, and it is chemically resistant. Likewise, its chemical structure permits a good electroosmotic flow and its dielectric properties allow working with high voltages, which are used in MC to move fluids in the microfluidic platform. Furthermore, it permits microfabrication to manufacture different template microchips. Therefore, either glass or certain polymers present good electroosmotic flow and dielectric properties to allow the use of electrokinetic approaches to move fluids in the microfluidic platforms. These approaches are based on the application of high electric fields between 1 to 5 kV between the extremes of the microchannel (generating an electrokinetic flow). With this used approach we avoid valves and pumps, which were highly used in conventional analytical systems such as HPLC, based on the pressure difference between the extremes of a capillary or a column (in this later case generating an hydrodynamic flow).^{7,8}

In MC, two basic injections are necessary, one for including the sample to the main channel and the second one to separate and drive the analytes to the detection reservoir. Especially, the injection of a well-defined reproducible sample plug into the separation channel is essential to obtain an efficient separation and enough sensitivity and reproducibility in the detection. The easiest injection procedure is the non-pinched approach.⁹ In this procedure, a high voltage is applied to the sample reservoir for few seconds with the detection reservoir held at ground (see **Figure III.2.A**). During this step, the sample is directly introduced in the separation channel by electrokinetic injection. Afterwards, the high voltage is switched to the buffer reservoir and applied for few minutes, taking place the separation of the analytes (see **Figure III.2.B**).

Figure III.2A presents the distribution of the sample injection using the double-T-form injection system. When the electric field is applied during the loading step, the sample flows from the injection channel (SR) to the waste channel (WR). Meanwhile, the potential distribution within the running buffer channel (RB) and the detection reservoir (DR) is kept motionless (float) in order to prevent sample leakage. Once the sample has filled the intersection in the double-T area, **Figure III.2B** shows the sample plug moving into the separation channel by establishing a linear potential distribution within the long channel. During this separation step, the sample fluid in SR and WR channels is kept floating.

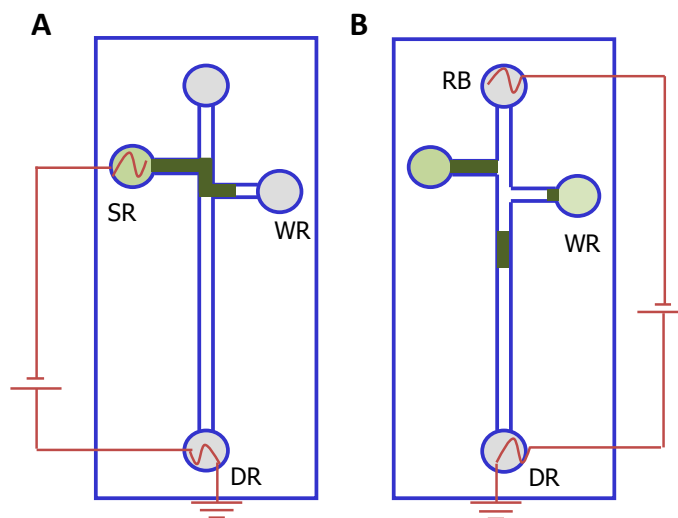


Figure III.2. Non-pinned electrokinetic protocol for (A) injection of the sample and (B) separation of the analytes

Additionally, the reduction in the system dimensions and the low volumes employed in MCs imply the extremely low quantity of analyte detected. For this reason, it is necessary a high sensitivity in the detection technique for analyzing the target molecules. Consequently, the most suitable detection techniques are, in general, electrochemical detection, mass spectrometry and optical techniques, such as fluorescence, not only for their high sensitivity but also for their non-invasive condition in the sample.^{4,10}

Regarding electrochemical detection, as we have already stated in **Chapter II**,¹¹⁻¹³ it is a powerful detection principle because its high sensitivity and selectivity, allowing to work with multiple electrodic materials and potentials. It is also very convenient due to its inherent facility for miniaturization without loss of performance, high sensitivity and extremely high compatibility with the micro and nanotechnologies, low cost, analytical response independent of optical path length and possible sample turbidity.^{14,15} However, in

MC-electrochemical detection coupling, the main disadvantage is the inherent problem of the coupling of potentials between the electric field from the separation in electrophoresis and the potential applied during the electrochemical detection. This latter inconvenient is highly reduced with a convenient coupling design between the microchip and the electrochemical cell, described below.

In the literature, three main coupling designs in MC with electrochemical detection¹² are found (see **Figure III.3**): *end-channel* detection, in which the electrode is placed just outside of the separation channel, with the working electrode on or off-chip; *in-channel* detection, in which the electrode is placed directly in the separation channel, and *off-channel* detection, which involves grounding the separation voltage with a decoupler before it reaches the detector.

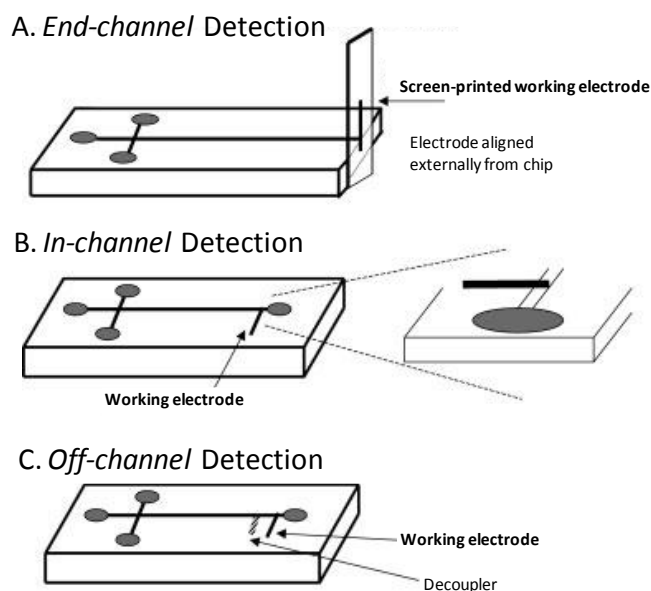


Figure III.3. Design configurations of the coupling between MC and electrochemical detection (A) *end-channel*, (B) *in-channel* and (C) *off-channel* detection. Reprinted with permission of reference 12

During this Thesis, the *end-channel* design, shown in **Figure III.3.A** has been used. In this design, the working electrode is externally located, existing a small distance (tens of micrometers) in between the channel (from which the sample leaks) and the detector. In this case, the separation voltage has a minimal influence on the potential applied in the electrochemical cell because most of the voltage is dropped across the channel. It does not require a decoupler and the system is simpler and more compatible with different working electrodes. On the other hand, the main disadvantage from this design is the loss of separation efficiency due to the distance between the end of the channel and the working electrode in comparison with the relatively short length of the channel, therefore, the control of this separation distance is crucial.

III.1.2. Carbon nanomaterials in microfluidic chips

The electrochemical detection has been proved as an ideal and valuable technique to be incorporated in miniaturized devices, as it was previously explained. More interestingly, the compatibility between electrochemical detection with microtechnologies and nanomaterials opened the way to significantly improve their analytical performance.^{14,16,17} In addition, as it was stated in **Chapter II**, the nanomaterials can offer high currents because of their large surface areas, thereby enabling large-scale redox conversion, which increases the analytical sensitivity, resists passivation, and yields very good reproducibility. Because of the extremely low sample volumes introduced into microfluidic systems, the MC sensitivity is often low being this feature a drawback of these systems. This problem can be overcome by exploiting the surface characteristics of nanomaterials, turning the microfluidic systems-carbon nanomaterials coupling into a very pertinent application for a novel generation of microfluidic systems. However, while carbon nanotubes have been previously coupled to these devices, graphene has been few times explored.¹⁵

The high electronic transference presented by the carbon nanomaterials permits to reduce the detection potentials and indeed, the noise. Thus, considering that high potentials are going to provoke higher coupling between the electric field of the MC and the detection potential, the inclusion of nanomaterials is also very convenient.

In the following sections of this chapter, it will be reviewed the coupling of carbon nanomaterials and MCs.

III.1.2.1. Carbon nanotubes in microfluidic chips

Briefly, before addressing the *state of the art* of MFCs-CNTs, we will explain the main features of CNTs. These nanomaterials have filled the first dimension of the carbon nanomaterials since their discovery in 1997.^{18,19} They are synthesized by rolling a sheet of graphene (already described in section II.1) into a cylinder. Their properties vary as a function of their chirality and diameter, so they can behave as metals or semiconductors with bands gaps that are relatively large or small, even with identical diameters.^{20,21}

CNT properties include high electrical ($\sigma = 10 \text{ mS cm}^{-1}$) and thermal conductivities ($k = \sim 6000 \text{ W m}^{-1} \text{ K}^{-1}$) and excellent mechanical properties (fracture strength 150 GPa),²² which have been exploited and have attracted an enormous interest in many fields such as energy conversion and storage, electrochemical actuators or chemical sensing, among others.^{22,23}

CNTs are usually classified into two categories, MWCNTs, which were the first ones discovered,¹⁸ being constituted by concentric cylinders which are placed around a common central hollow with an interlayer distance around 0.4 nm, correspondent to the interlayer distance in graphite. Remarkably, the layers are rotationally disordered one with respect to the others and their diameters range typically from 2 to 25 nm. SWCNTs are the other group of CNTs that are based on a unique rolled layer of graphene and present diameters of 1 to 2 nm.²⁴ The length of both materials varies in the micrometer range.

For electrochemical purposes, taking advantage of their high surface area ($\sim 1200 \text{ m}^2/\text{g}$ for SWCNT), the excellent electrical conductivity, among other properties, they have been exploited as electrodic

platforms in electrochemical applications. Thus, they have allowed increasing current intensities, improving the heterogeneous electron-transfer rates, decreasing the fouling of the electrodic surface, and provoking electrocatalysis on the redox potentials of a wide variety of analytes.²⁵

CNTs are commonly synthesized by laser ablation, electric arc discharge and CVD. The first two involve the condensation of carbon atoms generated from evaporation of solid carbon sources by employing high temperatures (3000-4000 °C). On the other hand, the CVD growth process involves flowing a hydrocarbon gas over a catalyst material based on a transition metal to get the carbon nanomaterial.

CNTs have been predominantly the most employed carbon materials for the last years coupled with microchips. The highly established knowledge of CNTs in electrochemistry and their excellent behavior in electrochemical detection have permitted CNTs to be the most developed materials as carbon surface materials coupled with microchips for the last ten years. Different approaches such as the ones described in CE have been explored for MC using CNTs, such as thin film CNTs-based electrodes, composite electrodes based on polymer/CNTs mixtures and a new strategy only published in CNTs-based electrodes coupled with microfluidic chips known as press-transfer approach, in which the nanomaterial is directly pressed on the surface of a inert polymer substrate.

The attraction of CNTs as carbon amperometric detectors in microfluidic chips have arisen since the first works of Wang and collaborators in 2004 using both thin film ²⁶ and composite-based electrode ²⁷ approaches. In both works the analytical advantages of using SWCNTs and MWCNTs as carbon-source detectors were

explored in the separation of molecules belonging to five groups, (a) hydrazine, dimethylhydrazine; (b) dopamine, catechol, ascorbic acid; (c) phenol, 2-chlorophenol, 2,4-dichlorophenol, 2,3-dichlorophenol; (d) guanine, xanthine, and (e) homocysteine, cysteine, glutathione, N-acetylcysteine. These two works demonstrated in the separation of these five groups of electroactive molecules the excellent features of CNTs in drop-casting and CNTs-paste electrodes, showing excellent sensitivity of the analysis, an impressive decrease in the operating potential in contrast to non-modified electrodes or graphite-paste electrodes because of the electrocatalytic activity of the CNT-modified detectors, and excellent repeatability and reproducibility with RSD values under 3% in contrast with the 15% for non-modified electrodes. These two works were the starting point of others using the approaches stated before to carry out different separations of analytes and their determination.

In order to more easily understand how SWCNT and MWCNT changed the analytical detection of common electrode surfaces, an interesting work, in which a comparison between graphite powder, SWCNT and MWCNTs films on GCE, gold and platinum electrode surfaces were modified, was explored.²⁸ To evaluate the electrocatalytic effect of these materials in comparison with non-modified electrodes, the hydrodynamic voltammograms (HDVs) were performed for dopamine and catechol separation in a MC. While MWCNT films on GCE showed a strong electrocatalytic effect, in the case of gold electrode as a substrate for deposition, graphite microparticle films were the carbon structures that showed the strongest electrocatalytic effect, both in comparison with non-modified surfaces. On the other hand, when Pt electrode was used as substrate, SWCNTs and differently synthesized MWCNTs showed this reduction in redox potentials. Although there is not a clear

explanation of these shift in potentials, authors suggest that the defects in CNT walls, open ends of CNTs, and edge plains of graphite microparticles resemble an edge plane pyrolytic graphite, that were considered as cause of this effect,²⁹ as well as the different contact resistance of carbon materials and GCE, Au and Pt surfaces.

The employment of CNT film electrodes in MC allowed not only low potentials of detection for dopamine and catechol, but also, high sensitivities for SWCNT film modified GCE in contrast to bare GCE and reproducible signals for all modified electrodes, with RSDs lower than 3% and 4% for dopamine and catechol, respectively, because of the high surface of CNTs that have a high number of electroactive sites, decreasing the capacity of the electrode to be fouled.

Another work explored the dramatic improved of SWCNTs deposited on gold detectors among the analytical response in the separation and determination of aminophenols and neurotransmitters.³⁰ Remarkably, SWCNTs showed an excellent electrocatalytic effect versus non-modified gold detector. The HDVs showed current intensities five times higher than the non-modified gold electrode for the two (ortho and para) aminophenols. Moreover, the electropherograms showed sharp and well-resolved peaks for this mixture of aminophenols, reflecting the fastest electron transfer of SWCNTs. This work also studied the separation and detection of two important catecholamines, dopamine and catechol, the excellent linearity ($R^2 \geq 0.998$) and good sensitivities found suggested that SWCNTs are excellent nanomaterials coupled with MC.

Although many works are focused on the improvements of using CNTs in the detection of different electroactive molecules, the role of the material in the detection of just separated molecules gives value to the synthesis and final preparation processes of the CNTs before

being used as electrochemical detectors. Consequently, different SWCNT materials with different purity index, dissolved in different dispersant agents and treatments have been employed to modify CSPE detectors in MC.³¹ The purity index was evaluated by measurements in near infrared as a ratio of the intensity bands for SWCNT content and the carbonaceous impurities in that material. Therefore, the near infrared-purity index value increased as the carbon impurity content decreased in the material explored.

In this work, two groups of SWCNTs, involving different purity indexes, dispersants (SDBS, pluronic F68 and DMF) and air oxidation and/or purification (centrifugation) treatments were carefully studied. All these SWCNTs with different near infrared-purity indexes were chosen to modify CSPEs and the analytical performance in MC was explored using a mixture of model electroactive analytes such as dopamine and catechol.³¹ All SWCNT-based electrodes demonstrated to better resolve the peaks and improve the signal-to-noise features and sensitivities, in contrast to the unresolved peaks in the case of CSPE. Remarkably, in terms of sensitivity, the highest near infrared-purity index SWCNT electrodic surfaces yielded the highest current intensities in the analyte detection. Further studies involved the influence of the dispersant, (SDBS, pluronic and DMF), showing the better analytical performance, the SWCNT dispersed with SDBS. This fundamental work demonstrates to the community of electrophoresis the significance of a complete and precise physical characterization of the nanomaterial before the integration in electrochemical detection coupled with MC as well as the value in the final analytical measurement of the solvent and nanomaterial selection.

Although the use of MC-CNTs have been studied with proof analytes and standards, the possibility of integration of real samples in the analysis has been actually very scarce as it has been previously reviewed.³²⁻³⁵ The technology seems to have jumped a gigantic leap improving the analytical performance, however, the complexity of real sample matrices has blocked the advances in real world analysis. Recently, the Lights and shadows on *Food microfluidics* have been discussed in a Frontier review.³⁵ This insight clearly invited to question the reader and attempt to answer why MC coupled with electrochemical detection should be used to solve analytical challenges in the food sector.

Initial studies including the detection of a variety of target molecules such as dietary antioxidants, water-soluble vitamins, vanilla flavors, and isoflavones found in representative food samples integrating CNTs and MC opened new opportunities in future routine analysis.^{5,36-39} MCs using both SWCNT and MWCNTs with different features were studied to explore the response in different groups of molecules and real samples. From the study of detection potential, HDVs were constructed for selected groups of analytes (polyphenols, vitamins, flavours and isoflavones). HDVs profiles showed lower oxidation potentials and enhancement of voltammetric currents with CNTs, being more remarked with MWCNT, with independence of the analyte under study. However, authors found a relationship between the surface area effect and the structures of the analytes, being decreased the oxidation potential on the analytes with enol and enediol as electroactive groups. On the contrary, this effect was not observed for carbonyl and hydroxymethyl as electroactive groups. Thus, it was demonstrated that the oxygen-containing species presented on the surface of CNTs and generated during acid treatment were responsible for an enhanced electron transfer

reaction for these structures, confirming their crucial role during the surface preparation process of this electrocatalysis.⁴⁰ Again, this work reinforces the idea of studying the inner structure of the nanomaterial to take advantage of the properties of carbon nanotubes to enhance the analytical performance.

CNT/polymer composites on MC platforms are also giving excellent results in the study of complex real samples. Cheng et al. reported a new CNT/polystyrene composite electrode for the determination of rutin and quercetin in a traditional Chinese medicine, *Flos Sophorae Immaturus*.⁴¹ The composite electrode was fabricated in a piece of fused silica capillary under polymerization of CNT and styrene. This composite electrode showed high anti-passivation capability, which was attributed to the electrocatalytic activity of CNT. At the optimum conditions, 50 mM borate buffer (pH 9.20) and a detection potential, +0.80 V vs. Ag/AgCl electrode, the herbal drug was evaluated showing good repeatability in the measurement of the target analytes with RSD < 3.7% (n=3).

This group also developed another composite electrode using PMMA with CNTs based on the same procedure as the one with polystyrene. The performance was evaluated by the separation and detection of eight phenolic pollutants, and purines (guanine and xanthine).⁴² The MC permitted an excellent reproducibility with RSD < 5% for the current peaks (n=20). Because of the good results found, a river water sample was evaluated and spiked with eight phenols, the excellent recoveries found from 93 to 101% and good RSDs $\leq 5\%$, n=3, showed the potential in environmental field of this MC coupled with CNT/PMMA detection.

A new cobalt hexacyanoferrate modified MWCNT/graphite composite electrode was electrochemically prepared and exploited as

an amperometric detector in MC for the rapid detection of hydrazine and isoniazid.⁴³ The excellent results were attributed to the synergetic electrocatalytic effect of cobalt hexacyanoferrate nanoparticles and MWCNTs, both metallic and carbon nanomaterials improved the analytical sensing of hydrazine and its derivative. The electrophoresis separation was carried out in a glass/PDMS hybrid chip using end-channel detection with engagement of the modified disk electrode, with 10 mM 2-(N-morpholino)ethanesulfonic acid (MES) at pH 6.10 as running buffer and a separation voltage of +1500 V at +0.70 V. The RSDs for peak current and migration time were 3.4% and 2.1%, respectively. These analytes were explored in river water sample and pharmaceutical tablets, and the recoveries found were between 92-105% in water and 95-98 % pharmaceutical tablets, respectively.

A new CNT/copper composite electrode was developed for the detection of carbohydrates and amino acids which were separated using a MC.⁴⁴ The marked catalytic action of the CNT/Cu material permitted a low amperometric potential detection.

In addition, a mineral oil was used to obtain the CNT-Cu paste where the 1:1:2 oil/MWCNT/Cu composition exhibited the lowest noise level and higher sensitivity yielding sharper peaks and improved resolution. A well-defined separation of mixture containing glucitol, glucose, gluconic acid and glucuronic acid was obtained. For this separation, it was required a strongly alkaline running buffer 35 mM NaOH and separation and injection voltages of +1000 V and injection time of 2 s.

The favorable signal-to-noise characteristics of a mixture containing 50 μ M glucose and gluconic acid indicated low detection limits of 20 μ M for glucose and 25 μ M gluconic acid (based on S/N= 3). The high

sensitivity and speed of the MC was coupled with a good reproducibility ($RSD \leq 5\%$).

Apart from the classical casting and composite approaches, recently, a novel technology to fabricate CNT-based detectors in which the nanomaterial is the exclusive transducer has been proposed.⁴⁵ This new approach directly exploits the inherent advantages of CNTs.

These novel electrodes termed as press-transfer electrodes have been recently coupled with MC.⁴⁵ In this approach, CNTs are press-transferred on PMMA substrates acting as the exclusive transducer in the detection of the target molecules.

The fabrication reproducibility showed RSD values of $<3\%$ and $<9\%$ ($n = 5$) for dopamine and catechol currents, respectively. After carefully studying the detection and separation performances and HDVs to assess the suitability of the channel coupling of the novel single-walled press-transfer electrodes with microfluidic devices, the oxidation potential of $+0.70$ V applied on single-walled press-transfer electrode working electrodes, in connection with a separation voltage of $+1500$ V were chosen as optimized conditions to carry out the studies of analytical performance evaluation because they resulted in a well-defined, sharp, and resolved peaks, a flat baseline, and favorable signal-to-noise characteristics. Indeed, for all the electrodes, the signal-to-noise characteristics were excellent. Authors explained that these improvements could be provoked by the CNT rigid films obtained on the PMMA substrate, in contrast to the vibrate film often obtained in casting approaches.

Finally, the resistance to the fouling was also evaluated through consecutive measurements during one hour obtaining RSD values of

$\leq 4\%$ and $\leq 9\%$ ($n = 15$) for migration times and peak heights, respectively.

Press-transfer technology has been also recently reported in the separation of class-selective isoflavones (total glycosides and total aglycones) in less than 250 s in soy extracts and dietary products.⁴⁶ In order to demonstrate this concept, different mixtures of targets aglycone (daidzin, genistin) and glycoside (genistein, daidzein) isoflavone-classes were examined. Good intra-electrode repeatability ($RSD \leq 8\%$, $n=5$) and inter-reproducibility ($RSD \leq 9\%$, $n=3$) were found. Under the optimized separation (borate 25 mM, pH 9.00 at +1500 V) and detection ($E = +1.00$ V in 0.1 M nitric acid) conditions, the analysis of real samples was in agreement between the values declared by the manufacturer and the ones obtained with single-walled press-transfer electrodes.

Press-transfer electrodes have demonstrated to be highly compatible with microfluidic technologies and this coupling opens a new idea of using new nanomaterial-based electrodes as unique transducers to enhance the sensing and biosensing.

The summary of the target analytes studied, real samples explored and the electrophoretic and detection conditions using CNTs have been listed in **Table III.1** (see page 153) for MC-CNTs works.

III.1.2.2. Graphene in microfluidic chips

Graphene materials have been received important attention in the last years (see **Chapter II.1**); as a result, it has been used as the new carbonaceous nanomaterial for electrochemistry.⁴⁷⁻⁵⁰ Although this detection has been highly employed in MC, as we could understand from the discussion about CNTs-based detectors, graphene material is still in its beginning in both electrochemical applications and in its coupling with MC. Graphene isolation and superior properties from those of CNTs rapidly opened new alternatives in electrochemical sensing,⁵¹⁻⁵⁴ however, the coupling with MC has been less studied and the first examples were introduced only some years ago. Indeed, there are only few examples showing this coupling. Thus, the foreseeable future is expected to present an increment in the study of interest analytes with MC coupled with graphene as electrochemical detector in the detection step.

In the bibliography, it is possible to find two papers using MC and graphene as detector nanomaterial. In the first published article, Pumera et al. shows an evaluation about the advantages of using GO as detector in MC with *end-channel* amperometric detection. They compared GO and graphite microparticles as modifiers in GCE and the bare GCE.⁵⁵ In order to evaluate the electrochemical performance of these three materials, two different kinds of analytes were studied. Firstly, important catecholamines such as dopamine and catechol were separated using MES buffer (25 mM, pH=6.50) and detected at +0.60 V. Furthermore, nitroaromatic explosives such as, 2,4-dinitrotoluene, 1,3-dinitrobenzene and 2,4-dinitrotoluene were separated using borate buffer (15 mM, pH=9.20) with addition of 20 mM SDS and detected at -0.50 V. They conclude in a preliminary study that there were no differences in terms of sensitivity and

selectivity for the detection of these analytes using GO as electrochemical detector in MC over that obtained with graphite microparticles, attributing the results to the low electrical conductivity of GO.

On the other hand, it was demonstrated that conductive graphene showed strong electrocatalytic activity when it was employed to improve the electrochemical response of some bioactive substances.⁵⁶⁻⁵⁸

The performance of various graphene materials (GO, chemically, electrochemically and thermally rGO), graphite and graphite oxide was compared to GCE as control using dopamine and catechol.⁵⁹ Graphite-oxide modified electrode achieved the highest currents for the detection of dopamine while graphite modified electrode produced the highest current peaks for catechol detection. The lowest currents for both dopamine and catechol were observed on the thermally reduced graphene oxide modified electrode in comparison to the bare GCE. The poor performance exhibited by graphenes coupled with MC is due to the large capacitive behavior of all graphene materials, which leads to high background currents in MC coupled to electrochemical detection systems.

The electrochemically reduced graphene oxide yielded the highest resolution, with almost a two-fold increment as compared to the bare GCE. On the other hand, the thermally reduced graphene oxide provided the lowest resolution among all the modified electrodes. At the light of these findings, the performances of the chemically modified graphene materials on these MC devices greatly differ compared to the well-studied three-electrode electrochemical cell set up analyses. Therefore, it must be emphasized that graphene materials prepared from various routes must be tested for detection

on MC devices before making conclusion of beneficial/detrimental performance of the graphene materials on these devices and their practical applications.

Indeed, graphene has demonstrated to be an excellent nanomaterial in electrochemistry with excellent properties in sensing. Remarkably, this enhancement in the electrochemical properties depends on the graphene material and its synthesis. Recently, it has been published the possibility of new tailored graphene electrodes that have brought light about the use of different graphene nanoribbons with different oxygen content and oxygen functionalities in its structures to improve the electrochemical sensing.⁶⁰ Consequently, from these ideas as well as from the good results already found in CE with electrochemical detectors based on graphene,¹⁵ we foresee that MC coupled with graphene will catch up with the CNT coupling and would be more and more exploited in the resolution of analytical problems because of the significantly enhancement in the final detection analysis.

Analytical relevant remarks of graphene electrodic surfaces as detectors coupled with MC have been listed in **Table III.2** (see page 154). In this table, graphene material, analyte and real samples tested as well as separation and buffer electrophoretic conditions have been detailed.

III.1.3. Outlook and perspectives

The *state of the art* of MC coupled with electrochemical detection using the carbon allotropes has shown the improvement reached in analytical chemistry. From this overview, it is clear the strong role of carbon nanomaterials in electrochemical detection and, more remarkably, the importance in the last years of CNTs materials coupled with MC. Additionally, the newest nanomaterial in the multidimensional carbon family, graphene, is catching up with the rest of the carbon materials in the applications of electrochemistry and in the coupling with MC. Therefore, graphene and its new derivatives are waiting to improve the analytical performance in the separation (resolution and width of the peaks) and in the detection (increasing current intensities, decreasing redox detection potentials) because of the higher surface areas and rich chemistry of these novel carbon nanomaterials.

Table III.1. Analytical remarks of the coupling MC-CNTs

ANALYTE	SAMPLE	ELECTROPHORETIC CONDITIONS			DETECTION			Ref
		Channel features (length, i.d.)	Separation media	Injection/separation	Electrode substrate	E(V) (vs. Ag/AgCl)	LOD (μ M)	
Flavonoids, antioxidants	Fruits	74 cm, 20 μ m	50 mM borate (pH 9.00)	+2 kV, 5s/ +2 kV	SW and MWCNTs/CSPE	+1.00	12	5
Antioxidants	Drug	74 cm, 20 μ m	10 mM borate (pH 7.00)	+2 kV, 3s/ +2 kV	SWCNTs/ CSPE, GCE	+1.20	8	37
Antioxidants	Fruits	74 cm, 20 μ m	50 mM borate (pH 9.00)	+2 kV, 3s/ +2 kV	MWCNTs/ CSPE	+1.00	7.1	36
Flavonoids	ND	74 cm, 20 μ m	10 mM borate (pH 8.00)	+2 kV, 3s/ +2 kV	MWCNTs / CSPE	+1.20	4	36
Antioxidants	Herbs	74 cm, 20 μ m	50 mM borate (pH 9.20)	+2 kV, 3s/ +2 kV	MWCNT/ polystyrene	+0.80	0.7	41
Phenols	River water	74 cm, 20 μ m	40 mM borate (pH 9.80)	+2.5 kV, 3s/ +2.5 kV	MWCNT/PMMA	+0.80	12 nM	42
Nitrogenous bases	ND	74 cm, 20 μ m	10 mM borate/ 20 mM phosphate (pH 8.00)	+1.5 kV, 3s/ +1.5 kV	MWCNT/PMMA	+0.80	ND	42
Hydrazines	River water, drug	43 mm, 250 μ m	10 mM MES (pH 6.10)	+0.5 kV, 10s/+1.5kV	CoNP/MWCNT/ graphite	+0.70	1.3	43
Sugars	ND	75 cm, 20 μ m	25 mM NaOH	+1 kV, 2 s/ +1 kV	MWCNT/Cu	+0.50	25	44
Amino acids	ND	75 cm, 20 μ m	10 mM NaOH	+1 kV, 2 s/ +1 kV	MWCNT/Cu	+0.55	ND	44

Table III.2. Analytical remarks of the coupling MC-graphene

ANALYTE	SAMPLE	ELECTROPHORETIC CONDITIONS			DETECTION			Ref
		Capillary features (length, i.d.)	Separation media	Injection/ separation	Electrode substrate	E(V) (vs.Ag/AgCl)	LOD (μ M)	
Catecholamines	ND	75 mm, 50 μ m	25 mM MES (pH=6.50)	+1.5 kV, 5 s/ +1.5kV	GO/GCE	+0.60	ND	55
Explosives	ND	75 mm, 50 μ m	15 mM borate 20 mM SDS (pH 9.20)	+2 kV, 3 s/ +2 kV	GO/GCE	-0.50	ND	55
Catecholamines	ND	75 mm, 50 μ m	25 mM MES (pH=6.50)	+2 kV, 3 s. +2 kV	GO and rGO/GCE	+0.50	ND	59

ND. Not detected

III.1.4. References

1. Manz, A.; Graber, N.; Widmer, H. M. Miniaturized total chemical analysis systems: A novel concept for chemical sensing. *Sens. Actuators B: Chem.* **1990**, *1*, 244-248.
2. Janasek, D.; Franzke, J.; Manz, A. Scaling and the design of miniaturized chemical-analysis systems. *Nature* **2006**, *442*, 374-380.
3. Whitesides, G. M. The origins and the future of microfluidics. *Nature* **2006**, *442*, 368-373.
4. Kitamori, T., Tokeshi, M., Hibara, A., Sato, K. Thermal Lens Microscopy and Microchip Chemistry. *Anal. Chem.* **2004**, *76*, 52 A-60A.
5. Crevillen, A. G.; Avila, M.; Pumera, M.; Gonzalez, M. C.; Escarpa, A. Food analysis on microfluidic devices using ultrasensitive carbon nanotubes detectors. *Anal. Chem.* **2007**, *79*, 7408-7415.
6. Ríos, A.; Escarpa, A.; González, M. C.; Crevillén, A. G. Challenges of analytical microsystems. *Trends Anal. Chem.* **2006**, *25*, 467-479.
7. Szekely, L.; Freitag, R. Study of the electroosmotic flow as a means to propel the mobile phase in capillary electrochromatography in view of further miniaturization of capillary electrochromatography systems. *Electrophoresis* **2005**, *26*, 1928-1939.
8. Blasco, A. J.; Escarpa, A. *Electrochemical detection in capillary electrophoresis on microchips*. Comprehensive Analytical Chemistry. Elsevier. **2005**. Vol. 45, pp. 703-758.
9. Fu, L.-M.; Yang, R.-J.; Lee, G.-B.; Liu, H.-H. Electrokinetic Injection Techniques in Microfluidic Chips. *Anal. Chem.* **2002**, *74*, 5084-5091.
10. Dittrich, P. S.; Manz, A. Single-molecule fluorescence detection in microfluidic channels—the Holy Grail in μ TAS? *Anal. Bioanal. Chem.* **2005**, *382*, 1771-1782.
11. Wang, J. Electrochemical detection for microscale analytical systems: a review. *Talanta* **2002**, *56*, 223-231.
12. Vandaveer, W. R.; Pasas, S. A.; Martin, R. S.; Lunte, S. M. Recent developments in amperometric detection for microchip capillary electrophoresis. *Electrophoresis* **2002**, *23*, 3667-3677.
13. Tanyanyiwa, J.; Leuthardt, S.; Hauser, P. C. Conductimetric and potentiometric detection in conventional and microchip capillary electrophoresis. *Electrophoresis* **2002**, *23*, 3659-3666.
14. Pumera, M.; Escarpa, A. Nanomaterials as electrochemical detectors in microfluidics and CE: Fundamentals, designs, and applications. *Electrophoresis* **2009**, *30*, 3315-3323.

15. Martín, A.; López, M. Á.; González, M. C.; Escarpa, A. Multidimensional carbon allotropes as electrochemical detectors in capillary and microchip electrophoresis. *Electrophoresis* **2015**, *36*, 179-194.
16. Escarpa, A. Food electroanalysis: sense and simplicity. *Chem. Rec.* **2012**, *12*, 72-91.
17. Pumera, M. Nanomaterials meet microfluidics. *Chem. Commun.* **2011**, *47*, 5671-5680.
18. Iijima, S. Helical Microtubules of Graphitic Carbon. *Nature* **1991**, *354*, 56-58.
19. Iijima, S.; Ichihashi, T. Single-Shell Carbon Nanotubes of 1-nm Diameter. *Nature* **1993**, *363*, 603-605.
20. Dumitrescu, I.; Unwin, P. R.; Macpherson, J. V. Electrochemistry at carbon nanotubes: perspective and issues. *Chem. Commun.* **2009**, 6886-6901.
21. Dai, H. J. Carbon nanotubes: Synthesis, integration, and properties. *Acc. Chem. Res.* **2002**, *35*, 1035-1044.
22. Burghard, M. Electronic and vibrational properties of chemically modified single-wall carbon nanotubes. *Surf. Sci. Rep.* **2005**, *58*, 1-109.
23. Gong, K. P.; Yan, Y. M.; Zhang, M. N.; Su, L.; Xiong, S. X.; Mao, L. Q. Electrochemistry and electroanalytical applications of carbon nanotubes: A review. *Anal. Sci.* **2005**, *21*, 1383-1393.
24. Ajayan, P. M. Nanotubes from carbon. *Chem. Rev.* **1999**, *99*, 1787-1799.
25. Pumera, M. The Electrochemistry of Carbon Nanotubes: Fundamentals and Applications. *Chem.-Eur. J.* **2009**, *15*, 4970-4978.
26. Wang, J.; Chen, G.; Chatrathi, M. P.; Musameh, M. Capillary electrophoresis microchip with a carbon nanotube-modified electrochemical detector. *Anal. Chem.* **2004**, *76*, 298-302.
27. Chen, G.; Zhang, L. Y.; Wang, J. Miniaturized capillary electrophoresis system with a carbon nanotube microelectrode for rapid separation and detection of thiols. *Talanta* **2004**, *64*, 1018-1023.
28. Pumera, M.; Merkoci, A.; Alegret, S. Carbon nanotube detectors for microchip CE: Comparative study of single-wall and multiwall carbon nanotube, and graphite powder films on glassy carbon, gold, and platinum electrode surfaces. *Electrophoresis* **2007**, *28*, 1274-1280.
29. Moore, R. R.; Banks, C. E.; Compton, R. G. Basal plane pyrolytic graphite modified electrodes: Comparison of carbon nanotubes and graphite powder as electrocatalysts. *Anal. Chem.* **2004**, *76*, 2677-2682.

30. Pumera, M.; Llopis, X.; Merkoci, A.; Alegret, S. Microchip capillary electrophoresis with a single-wall carbon nanotube/gold electrochemical detector for determination of aminophenols and neurotransmitters. *Microchim. Acta* **2006**, *152*, 261-265.
31. Vilela, D.; Anson-Casaos, A.; Teresa Martinez, M.; Cristina Gonzalez, M.; Escarpa, A. High NIR-purity index single-walled carbon nanotubes for electrochemical sensing in microfluidic chips. *Lab Chip* **2012**, *12*, 2006-2014.
32. Blasco, A. J.; Crevillen, A. G.; Gonzalez, M. C.; Escarpa, A. Direct electrochemical sensing and detection of natural antioxidants and antioxidant capacity in vitro systems. *Electroanalysis* **2007**, *19*, 2275-2286.
33. Escarpa, A.; Cristina Gonzalez, M.; Lopez Gil, M. A.; Crevillen, A. G.; Hervas, M.; Garcia, M. Microchips for CE: Breakthroughs in real-world food analysis. *Electrophoresis* **2008**, *29*, 4852-4861.
34. Martín, A.; Vilela, D.; Escarpa, A. Food analysis on microchip electrophoresis: An updated review. *Electrophoresis* **2012**, *33*, 2212-2227.
35. Escarpa, A. Lights and shadows on Food microfluidics. *Lab Chip* **2014**, *14*, 3213-3224.
36. Crevillen, A. G.; Pumera, M.; Gonzalez, M. C.; Escarpa, A. Towards lab-on-a-chip approaches in real analytical domains based on microfluidic chips/electrochemical multi-walled carbon nanotube platforms. *Lab Chip* **2009**, *9*, 346-353.
37. Crevillen, A. G.; Pumera, M.; Gonzalez, M. C.; Escarpa, A. Carbon nanotube disposable detectors in microchip capillary electrophoresis for water-soluble vitamin determination: Analytical possibilities in pharmaceutical quality control. *Electrophoresis* **2008**, *29*, 2997-3004.
38. Avila, M.; Zougagh, M.; Escarpa, A.; Rios, A. Fast single run of vanilla fingerprint markers on microfluidic-electrochemistry chip for confirmation of common frauds. *Electrophoresis* **2009**, *30*, 3413-3418.
39. Kovachev, N.; Canals, A.; Escarpa, A. Fast and Selective Microfluidic Chips for Electrochemical Antioxidant Sensing in Complex Samples. *Anal. Chem.* **2010**, *82*, 2925-2931.
40. Crevillen, A. G.; Pumera, M.; Gonzalez, M. C.; Escarpa, A. The preferential electrocatalytic behaviour of graphite and multiwalled carbon nanotubes on enediol groups and their analytical implications in real domains. *Analyst* **2009**, 657-662.
41. Xu, J.; Zhang, H.; Chen, G. Carbon nanotube/polystyrene composite electrode for microchip electrophoretic determination of rutin and quercetin in *Flos Sophorae Immaturus*. *Talanta* **2007**, *73*, 932-937.
42. Yao, X.; Wu, H.; Wang, J.; Qu, S.; Chen, G. Carbon nanotube/poly(methyl methacrylate) (CNT/PMMA) composite electrode fabricated by in situ

- polymerization for microchip capillary electrophoresis. *Chem.- Eur. J.* **2007**, *13*, 846-853.
43. Li, X.; Chen, Z.; Zhong, Y.; Yang, F.; Pan, J.; Liang, Y. Cobalt hexacyanoferrate modified multi-walled carbon nanotubes/graphite composite electrode as electrochemical sensor on microfluidic chip. *Anal. Chim. Acta* **2012**, *710*, 118-124.
 44. Wang, J.; Chen, G.; Wang, M.; Chatrathi, M. P. Carbon-nanotube/copper composite electrodes for capillary electrophoresis microchip detection of carbohydrates. *Analyst* **2004**, *129*, 512-515.
 45. Vilela, D.; Garoz, J.; Colina, A.; Cristina Gonzalez, M.; Escarpa, A. Carbon Nanotubes Press-Transferred on PMMA Substrates as Exclusive Transducers for Electrochemical Microfluidic Sensing. *Anal. Chem.* **2012**, *84*, 10838-10844.
 46. Vilela, D.; Martin, A.; Gonzalez, M. C.; Escarpa, A. Fast and reliable class-selective isoflavone index determination on carbon nanotube press-transferred electrodes using microfluidic chips. *Analyst* **2014**, *139*, 2342-2347.
 47. Pumera, M. Graphene-based nanomaterials and their electrochemistry. *Chem. Soc. Rev.* **2010**, *39*, 4146-4157.
 48. Shao, Y.; Wang, J.; Wu, H.; Liu, J.; Aksay, I. A.; Lin, Y. Graphene Based Electrochemical Sensors and Biosensors: A Review. *Electroanalysis* **2010**, *22*, 1027-1036.
 49. Ratinac, K. R.; Yang, W.; Gooding, J. J.; Thordarson, P.; Braet, F. Graphene and Related Materials in Electrochemical Sensing. *Electroanalysis* **2011**, *23*, 803-826.
 50. Brownson, D. A. C.; Banks, C. E. Graphene electrochemistry: an overview of potential applications. *Analyst* **2010**, *135*, 2768-2778.
 51. Kuila, T.; Bose, S.; Khanra, P.; Mishra, A. K.; Kim, N. H.; Lee, J. H. Recent advances in graphene-based biosensors. *Biosens. Bioelectron.* **2011**, *26*, 4637-4648.
 52. Brownson, D. A. C.; Banks, C. E. Graphene electrochemistry: an overview of potential applications. *Analyst* **2010**, *135*, 2768-2778.
 53. Li, J.; Kuang, D.; Feng, Y.; Zhang, F.; Xu, Z.; Liu, M. A graphene oxide-based electrochemical sensor for sensitive determination of 4-nitrophenol. *J. Hazard. Mater.* **2012**, *201*, 250-259.
 54. Valentini, F.; Carbone, M.; Paleschi, G. Graphene oxide nanoribbons (GNO), reduced graphene nanoribbons (GNR), and multi-layers of oxidized graphene functionalized with ionic liquids (GO-IL) for assembly of miniaturized electrochemical devices. *Anal. Bioanal. Chem.* **2013**, *405*, 3449-3474.

55. Chua, C. K.; Ambrosi, A.; Pumera, M. Graphene based nanomaterials as electrochemical detectors in Lab-on-a-chip devices. *Electrochem. Commun.* **2011**, *13*, 517-519.
56. Chen, L.; Tang, Y.; Wang, K.; Liu, C.; Luo, S. Direct electrodeposition of reduced graphene oxide on glassy carbon electrode and its electrochemical application. *Electrochem. Commun.* **2011**, *13*, 133-137.
57. Du, H.; Ye, J.; Zhang, J.; Huang, X.; Yu, C. A voltammetric sensor based on graphene-modified electrode for simultaneous determination of catechol and hydroquinone. *J Electroanal Chem* **2011**, *650*, 209-213.
58. Ping, J.; Wu, J.; Wang, Y.; Ying, Y. Simultaneous determination of ascorbic acid, dopamine and uric acid using high-performance screen-printed graphene electrode. *Biosens. Bioelectron.* **2012**, *34*, 70-76.
59. Chua, C. K.; Pumera, M. Chemically Modified Graphenes as Detectors in Lab-on-Chip Device. *Electroanalysis* **2013**, *25*, 945-950.
60. Martín, A.; Hernández, J.; Vázquez, L.; Martínez, M. T.; Escarpa, A. Controlled chemistry of tailored graphene nanoribbons for electrochemistry: a rational approach to optimizing molecule detection. *RSC Adv.* **2014**, *4*, 132-139.

III.2. Graphene-based materials in electrochemical microfluidic biosensing



III.2.1. Introduction and objectives

D-enantiomers of amino acids (D-AAAs) have been thought to have a minor role in the regulation of biological processes, being L-AAAs the ones that predominate in nature. However, it was reviewed that D-AAAs can appear naturally in antibiotics, immunosuppressive drugs and antitumor agents.¹ As selected significant examples, they prevent biofilm formation and can break down the already formed,² may regulate adult neurogenesis³ (i.e. D-aspartate) and present a role as neurotransmitters⁴ (D-serine) becoming its availability altered in the nervous system of schizophrenic patients.⁵

As we have stated in epigraph **II.3.1**, recently, relevant publications highlight that some bacteria produce types of D-AAAs, which were not previously known to be synthesized but are present in the supernatants of the stationary phase cultures.^{6,7} These works have revealed that different bacteria produce diverse D-AAAs: *Vibrio cholerae* generates mainly D-Met and D-leucine (D-Leu); whereas *Bacillus subtilis* produces principally D-phenylalanine and D-Tyr, among others. The particular D-AAAs identified in stationary phase supernatants varied among bacterial species,⁶ being the proportion and amount of D-AAAs characteristic of each bacteria. Consequently, these D-AAAs biomarkers might become a molecular fingerprint. Some of these bacteria present clinical importance, for example *V. cholerae* is the etiologic agent of the pandemic cholera disease. Hence, this information based on the identification and detection of D-AAAs is highly important and is expected to be extremely relevant in a foreseeable future.

Due to these biological and clinical relevancies, the development of screening methods for detecting different D-AAAs in a biological

sample has become a must. Since enantiomers present the same physical and chemical properties but react very differently, scientists have attempted for many years to find a simple and efficient method to identify and separate the enantiomers present in a mixture. Several methodologies have been reported to achieve this purpose. One of the most common methods is the chiral derivatization in combination with reversed-phase HPLC methods, using different reagents for the derivatization,^{8,9} however, this methodology presents several disadvantages derived from the derivatization step. Hence, other HPLC strategies as chiral stationary phase and 2D-HPLC systems have been reported.^{10,11} CE has been another technique used in the chiral separation of AAs using both direct and indirect approaches, with different chiral selectors and chiral reagents for diastereomers formation, respectively.¹²

MCs offer excellent opportunities to carry out novel and creative analytical works. One of the most important applications of MCs is their role as point of care devices for clinical diagnosis as analytical screening tools because of inherent miniaturization, portability and extremely low biological sample required.¹³ Some related works for detecting (L,D)-AAs have employed fluorescence detection,^{14,15} however, this detection is a little expensive, making difficult design a portable device for *in situ* monitoring of D-AAs. In this way, as it was already detailed in this Thesis (section **III.1**) the electrochemical detection in MC has been proved as an ideal and valuable analytical technique highly compatibility with the micro and nanotechnologies,^{16,17} and with carbon nanomaterials,¹⁸⁻²² however, only a few examples are found with graphene.^{18,23}

Another valuable merit of MC is its high compatibility with biological molecules for selective and sensitive bio-sensing.²⁴⁻²⁶ In this sense,

DAAO, which oxidatively deaminates D-AAs to the corresponding alpha-keto acid, generating one mol of H_2O_2 per mol of deaminated D-AA, has been previously used for D-AA detection using a post-column approach.²⁷

Therefore it, the main objective has been the development of an electrochemical microfluidic strategy on a single and simple MC capable of separating and detecting D-Met and D-Leu biomarkers of *V. cholerae* as future point of care for bacterial screening, where miniaturization and extremely low biological sample consumption are highly required. Furthermore, the presented strategy allows the controlled microfluidic manipulation of the D-AAs and the class-enzyme DAAO to govern both the D-AA separation and the specific reaction between DAAO and each D-AA biomarker avoiding any covalent immobilization of the enzyme into the wall channels or on the electrode surface such as in the biosensor-based approaches.²⁸

III.2.2. Enzyme-based microfluidic chip for D- amino acid enantiomer biomarkers detection

The optimized electrokinetic microfluidic protocol proposed in **Figure III.4** consists in (i) the simultaneous electrokinetic injection of DAAO (from enzymatic reservoir, ER) and amino acids (from amino acid reservoir, AA) (**4A**), (ii) the electro-focusing of the DAAO and AAs (in downstream and in the upstream of the micro-channel, respectively) (**4B**), and (iii) the AAs separation, the selective in-channel reaction and the hydrogen peroxide detection produced from each D-AA enantiomer after enzymatic reaction (in detection reservoir DR) (**4C**).

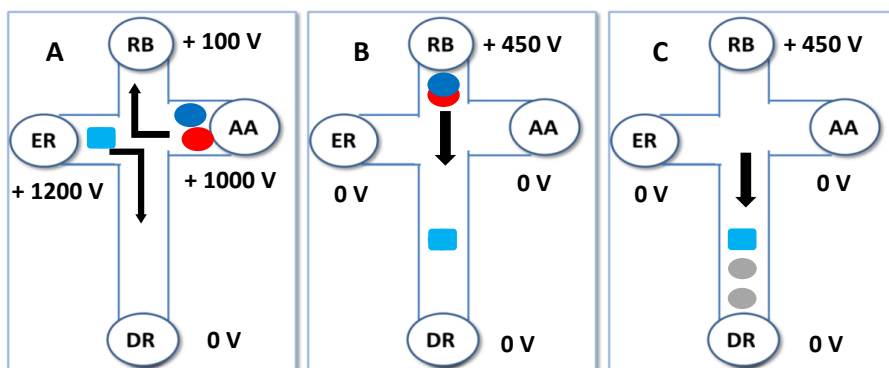


Figure III.4. Electrochemical microfluidic strategy: (A) enzyme and D-AAs electrokinetic co-injection for 5 s, (B) enzyme and D-AAs electro-focusing and (C) D-AAs separation and in-channel enzymatic reaction and hydrogen peroxide detection. RB: running buffer reservoir; ER: enzymatic buffer reservoir, AA: amino acid reservoir, DR: detection reservoir. Color symbols: DAAO (blue square); D-Met (dark blue); D-Leu (red); H_2O_2 (grey). Conditions: (RB) 20 mM borate buffer pH 10.0; (ER) $0.50 \text{ mg}\cdot\text{mL}^{-1}$ DAAO 5 mM NaH_2PO_4 ; (AA) 0.50 mM D-Leu and 0.30 mM D-Met in 20 mM borate buffer pH 10.0. Detection conditions: +0.70 V vs. Ag/AgCl

A simultaneous injection of the enzyme (from ER) and the AAs (**4A**) was developed by applying +1200 V in ER, +1000 V in AA and +100 V in RB (running buffer reservoir) during 5 s with the DR grounded at 0 V. Then, for the AAs separation and selective *in-channel* reaction, RB was pumped at +450 V with all reservoirs grounded at 0 V (**4B-C**), until complete detection of hydrogen peroxide from each enantiomer was achieved.

The difference between the high voltages applied between ER (+1200 V) and DR (0 V) and between AA (+1000 V) and RB (+450 V) reservoirs was essential in order to electro-focus the amino acid in the upstream and the DAAO in the downstream of the channel. Indeed, applying the same high voltages (+1200 V) from both ER and AA did not give satisfactory results. In addition, the separation voltage applied from RB was optimized to +450 V for achieving the AA separation.

Secondly, enzyme concentration and in channel enzymatic reaction between DAAO and the target D-AA were carefully assayed in phosphate buffer at pH 8.00 since at this target pH the enzymatic reaction is favored.²⁹ From the **Figure III.5A** can be noticed that enzymatic activity increased with the enzyme concentration, revealing 0.50 mg·mL⁻¹ as optimum value. The amount of DAAO injected was controlled towards injection time and potential with reproducibility. **Figure III.5B** illustrates the influence of the injection time of the D-Met as selected example on the hydrogen peroxide production. It was observed that increasing injection time, the hydrogen peroxide also increases revealing the suitability of the strategy. An optimum time of 5 s was chosen, since with longer injection times, sensitivity was not much enhanced and not well-defined peak shape was either obtained.

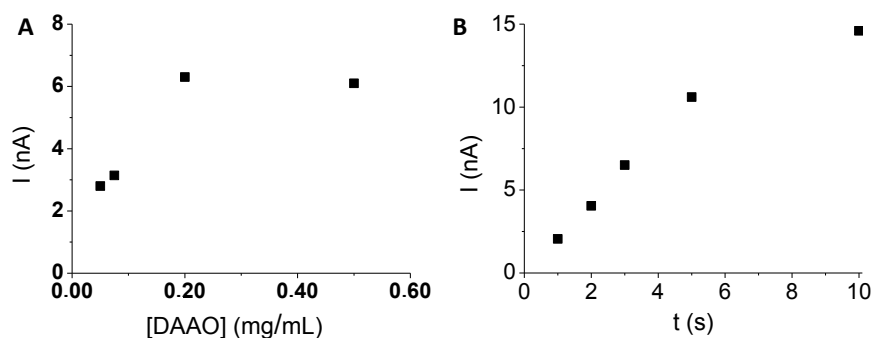


Figure III.5. (A) Effect of DAAO concentration on 1 mM D-Met amperometric signal. (B) Effect of injection time on 0.50 mM D-Met amperometric signal. Conditions as in Figure III.4

Thirdly, electrochemical detection of hydrogen peroxide, as product of the in-channel enzymatic reaction, was also carefully evaluated. In order to improve the signal obtained with bare CSPE, this electrode was modified with nanomaterials. GNRred previously characterized³⁰ (see epigraph **II.2.2**), briefly (1.2 nm height, 3-4 layers, 120 nm x 50 nm, 47 % Csp², 10 % Csp³ functionalities and 14 % total oxygen content) were evaluated following an off-chip approach drop-casting the CSPEs. The edge chemistry is an important characteristic of these GNRred, because the edges present chemical functionalities such as carboxylic acid or carbonyl, among others. Different volumes of GNRred were deposited onto the CSPE for setting the optimal volume of graphene, detecting an improvement in the signal when the amount of GNRred increased. The optimal GNRred volume was fixed as 3 μ L because higher amounts raised the background signal.

Since the GNRred edge chemistry facilitates the interaction of the negatively charged carboxylic acid moieties of the GNRred with cationic amine groups of some polymers such as polyallylamine

(PAA) and polyethyleneimine (PEI), the influence of these polymers was also assayed. Indeed, the presence of the polymer points out an increase in the electrode effective electrochemical area³¹ and provides the conducting bridges for the electron-transfer process. The modification with PEI always showed more electrochemical effective area than the ones modified with PAA (data not shown). So, the chosen electrode for the *end-channel* microchip detection was the CSPE modified with GNRred and PEI, which henceforth will be named as GNRred/PEI electrode. **Figure III.6** shows the impressive enhancement of the electrochemical area of this electrode more than 30 times bigger than the area of the bare CSPE when GNRred/PEI was used as electrode modifiers. Indeed, the inclusion of hybrid polymer/graphene-based electrodes end-channel coupled to the microfluidic system notably improved the analytical performance.

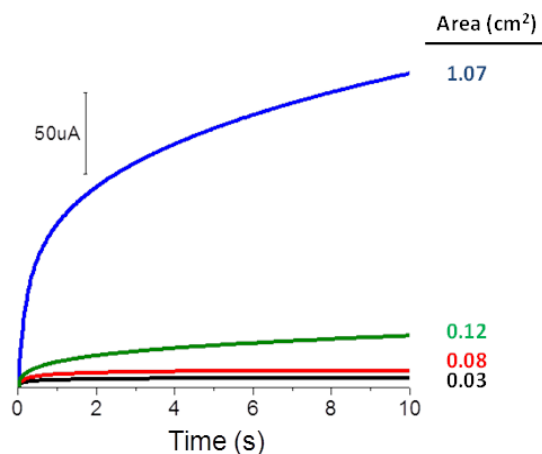


Figure III.6. Estimation of electrochemical surface area of the different electrodes (0.30 x 2.50 mm): black (CSPE), red (GNRred), green (CSPE/PEI), blue (GNRred/PEI). Conditions: 3 μL of a dispersion of 0.50 $\text{mg}\cdot\text{mL}^{-1}$ GNRred plus 3 μL of a 100 $\text{mg}\cdot\text{mL}^{-1}$ polymer preparation

Under optimized electrokinetic conditions, the detection potential was also carefully studied. **Figure III.7** shows the hydrodynamic voltammograms for the involved molecules: H_2O_2 , DAAO and the moderate electroactive D,L-Met.³² The optimal detection potential was found to be +0.70 V where H_2O_2 detection showed the best analytical sensitivity on the GNRred/PEI electrode in comparison with bare electrode (as control), while D,L-Met did not exhibit electroactivity. Under these conditions, a complete isolation of the detection potential from the electrokinetic protocol was also noticed, exhibiting H_2O_2 detection excellent S/N characteristics. Also, as expected, DAAO did not exhibit electroactivity at any assayed potential.

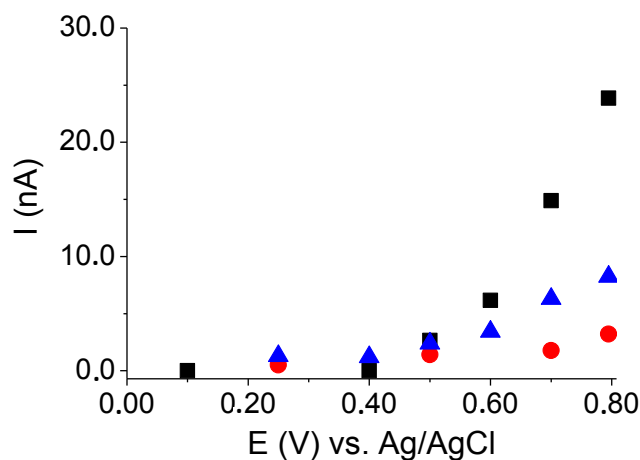


Figure III.7. HDVs for 1 mM H_2O_2 on GNRred/PEI (black) and CSPE (blue). 2 mM D,L-Met on GNRred/PEI (red). Conditions as in Figure III.4

Finally, separation of both AAs was carefully optimized using a 20 mM borate buffer at pH 10.0. **Figure III.8** illustrates the separation and D-enantiomeric detection of Met and Leu at +0.70 V accordingly to a capillary zone electrophoresis mechanism where both D-AAs

remains negatively charged. The detection of D-Leu ($pK_{a2}=9.58$; $M_r=131.17 \text{ g mol}^{-1}$) was achieved through the detection of H_2O_2 with a well-defined peak that migrated at $568.5 \pm 6.8 \text{ s}$. The H_2O_2 peak corresponding to D-Met ($pK_{a2}=9.08$; $M_r=149.21 \text{ g mol}^{-1}$) presented higher migration time of $727.8 \pm 9.8 \text{ s}$. The sensitivity of the system allowed to detect the D-AAs concentration indicated in the relevant literature (1 mM).⁶ An excellent precision in migration times ($RSD \leq 2 \%$, $n=5$) and in peak heights ($RSD \leq 10 \%$, $n=5$) were also achieved indicating a very good precision and a very good electroosmotic flow stability. In contrast, when only L-amino acids (L-Met and L-Leu) were injected, no peaks were detected; as the enzyme does not react with L-enantiomers (**Figure III.8**, control).

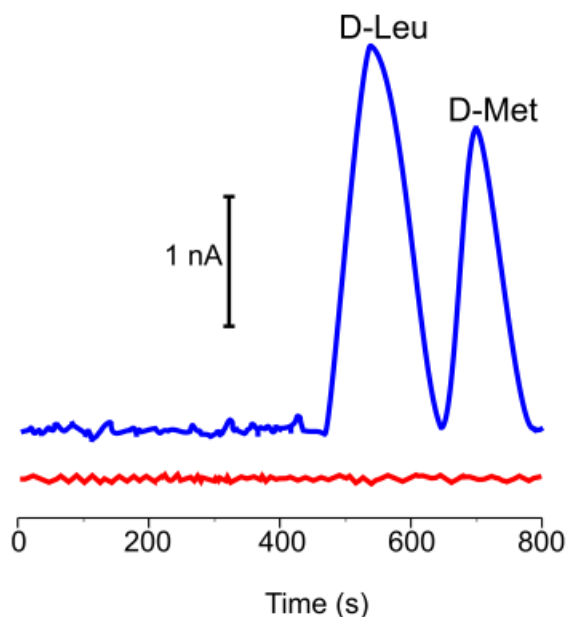


Figure III.8. Microchip electropherograms corresponding to the reaction of: $0.50 \text{ mg} \cdot \text{mL}^{-1}$ DAAO with a mixture of 0.50 mM D-Leu and 0.30 mM D-Met (blue) and $0.50 \text{ mg} \cdot \text{mL}^{-1}$ DAAO with a mixture of 0.50 mM L-Leu and 0.30 mM L-Met (red). Conditions as in Figure III.4

III.2.3. Conclusions

This work demonstrated a simple and creative strategy which allows both the racemic resolution and detection of D-AAs involved in high significance diseases, such as those produced by *V. cholerae*, on a single layout MC, highly compatible with extremely low biological sample consumption. This approach improves previous literature since it uses a simpler and commercial MC layout and geometry, extremely low amount of enzyme and offers a high versatility allowing the electro-focus of the enzyme along the main channel avoiding the use of additives (i.e. cyclodextrins) for enantiomeric separation as well as it does not require any covalent immobilization of the enzyme into the wall channels or on the electrode surface such as in the biosensor-based approaches.

This proof of the concept approach opens novel avenues for the detection of amino acidic enantiomers on microfluidic systems, not only for clinical but also for agro-food relevant applications using commercial and available micro-technology, becoming a breakthrough for future development of point of care devices applied to the detection of bacteria.

III.2.4. Experimental section

III.2.4.1. Reagents

L-methionine, D,L-methionine, D-leucine, L-leucine were purchased from Fluka Chemika (Buchs, UK) and hydrogen peroxide, D-methionine and sodium tetraborate decahydrate were obtained in Sigma Aldrich (St. Louis, MO, USA). Sodium dihydrogen phosphate was purchased from Panreac, (Badalona, Spain). D-amino acid oxidase (DAAO) was purchased from Sigma Aldrich (St. Louis, MO, USA). All solutions were daily prepared using ultrapure water treated in a Milli-Q system (Millipore, Bedford, MA, USA).

III.2.4.2. Apparatus and measurements

All electrochemical measurements were performed at room temperature, using a Potentiostat Autolab PGSTAT101 from Eco Chemie. The high-voltage source was a LabSmith Model HVS448 high-voltage sequencer with eight independent high-voltage channels and programmable sequencing (LabSmith, Livermore, CA).

The used analytical microchip was previously reported³³ and some design adaptations were performed.³⁴ The microchip fabricated by Micralyne (Model MC-BF4-001, Edmond, Canada) consisted of a glass plate (88 mm x 16 mm) with a four-way injection cross, a 74 mm long separation channel with a semicircular section of 50 μm width and 20 μm depth. The side arms, measuring 5 mm long, and separation channels have a double-T shaped. The amperometric detector (end-channel detection) consisted of an Ag/AgCl wire as a reference electrode, a platinum wire as a counter electrode, and a CSPE as a working electrode of 0.3 x 2.5 mm (Dropsens, Oviedo,

Spain). A spacer (easily removable adhesive tape, 60 μm thick) was placed between the surface of the electrode and the channel outlet to reproducibly control the distance between the electrode and the separation channel and to avoid interference from the electrical field applied for the separation in the detector.

III.2.4.3. Preparation of graphene modified electrode

CSPE for MC coupling (0.30 x 2.50 mm) was modified following a two-step drop-casting protocol. Firstly, 3 μL of a 0.50 $\text{mg}\cdot\text{mL}^{-1}$ GNRred dispersion in $\text{H}_2\text{O}/\text{NH}_3$ (1%) were deposited (previously optimized, results are not shown) along the electrode. Secondly, a solution of 100 $\text{mg}\cdot\text{mL}^{-1}$ PEI or PAA was prepared in 5 mM sodium phosphate buffer pH 8.00. After 1 hour, when the GNRred modified electrode was totally dried, the second step of the deposition procedure took place. Then, 3 μL of the polymer preparation were deposited onto the electrode, covering all the length of the electrode with the solution. The modified electrode rested during 1 hour until all the electrode was dried, before using it.

III.2.4.4. Estimation of the electrochemical effective surface area

To characterize the electrodes and in order to find the electrochemical effective surface area, the slope of the plot of Q vs. $t^{1/2}$ obtained by chronocoulometry using 0.50 mM $\text{K}_3[\text{Fe}(\text{CN})_6]$ in 0.1 M KCl have been calculated. This methodology is based on **Equation III.1**, given by Anson:³⁵

$$Q(t) = \frac{2nFAcD^{1/2}t^{1/2}}{\pi^{1/2}} + Q_{dl} + Q_{ads} \quad (\text{Equation III.1})$$

The different parameters of this equation are the following ones: A is the effective electrochemical surface area of the working electrode (cm^2), c is the concentration of the electroactive species (mol/cm^3), n is the number of transfer electron that is 1, and D is the diffusion coefficient, $7.6 \times 10^{-6} \text{ cm}^2 \cdot \text{s}^{-1}$,³⁶ Q_{dl} is the double layer charge which could be eliminated by background subtraction and Q_{ads} is Faradaic charge.

III.2.4.5. Electrophoretic procedure and amperometric detection

Before the application of the microfluidic voltages as it will be described in the results and discussion section, the channels of the glass microchip were treated before their use with 0.50 M NaOH for 40 min, being rinsed afterwards with deionized water for 10 min. The running buffer, the enzymatic, the amino acid and the detection reservoirs were suitably fill accordingly with the buffer media.

A detection potential of +0.70 V was applied to the working electrode placed in the detection reservoir, to analyze the hydrogen peroxide generated in the enzymatic reaction. All experiments were performed at room temperature.

II.2.5. References

1. Blanke, S.R. Cell biology. Expanding functionality within the looking-glass universe. *Science* **2009**, *325*, 1505-1506.
2. Kolodkin-Gal, I.; Romero, D.; Cao, S.; Clardy, J.; Kolter, R.; Losick, R. D-Amino Acids Trigger Biofilm Disassembly. *Science* **2010**, *328*, 627-629.
3. Kim, P. M.; Duan, X.; Huang, A. S.; Liu, C. Y.; Ming, G.; Song, H.; Snyder, S. H. Aspartate racemase, generating neuronal D-aspartate, regulates adult neurogenesis. *P. Natl A Sci* **2010**, *107*, 3175-3179.
4. Wolosker, H.; Dumin, E.; Balan, L.; Foltyn, V. N. d-Amino acids in the brain: d-serine in neurotransmission and neurodegeneration. *FEBS J* **2008**, *275*, 3514-3526.
5. Madeira, C.; Freitas, M. E.; Vargas-Lopes, C.; Wolosker, H.; Panizzutti, R. Increased brain d-amino acid oxidase (DAAO) activity in schizophrenia. *Schizophr. Res.* **2008**, *101*, 76-83.
6. Lam, H.; Oh, D.; Cava, F.; Takacs, C. N.; Clardy, J.; de Pedro, M. A.; Waldor, M. K. D-Amino Acids Govern Stationary Phase Cell Wall Remodeling in Bacteria. *Science* **2009**, *325*, 1552-1555.
7. Cava, F.; Lam, H.; de Pedro, M. A.; Waldor, M. K. Emerging knowledge of regulatory roles of d- amino acids in bacteria. *Cell. Mol. Life Sci.* **2011**, *68*, 817-831.
8. Visser, W. F.; Verhoeven-Duif, N. M.; Ophoff, R.; Bakker, S.; Klomp, L. W.; Berger, R.; de Koning, T. J. A sensitive and simple ultra-high-performance-liquid chromatography–tandem mass spectrometry based method for the quantification of d-amino acids in body fluids. *J. Chromatogr. A* **2011**, *1218*, 7130-7136.
9. Grant, S. L.; Shulman, Y.; Tibbo, P.; Hampson, D. R.; Baker, G. B. Determination of d-serine and related neuroactive amino acids in human plasma by high-performance liquid chromatography with fluorimetric detection. *J. Chromatogr. B* **2006**, *844*, 278-282.
10. Waldhier, M. C.; Almstetter, M. F.; Nürnberger, N.; Gruber, M. A.; Dettmer, K.; Oefner, P. J. Improved enantiomer resolution and quantification of free d-amino acids in serum and urine by comprehensive two-dimensional gas chromatography–time-of-flight mass spectrometry. *J. Chromatogr. A* **2011**, *1218*, 4537-4544.
11. Miyoshi, Y.; Koga, R.; Oyama, T.; Han, H.; Ueno, K.; Masuyama, K.; Itoh, Y.; Hamase, K. HPLC analysis of naturally occurring free d-amino acids in mammals. *J. Pharm. Biomed. Anal.* **2012**, *69*, 42-49.

12. Wan H., B. L. G. Chiral separation of amino acids and peptides by capillary electrophoresis. *J. Chromatogr. A* **2000**, *875*, 43-88.
13. Garcia, M.; Escarpa, A. Microchip electrophoresis-copper nanowires for fast and reliable determination of monosaccharides in honey samples. *Electrophoresis* **2014**, *35*, 425-432.
14. Munro, N.J., Huang, Z., Finegold, D.N., Landers, J.P. Indirect fluorescence detection of amino acids on electrophoretic microchips. *Anal. Chem.* **2000**, *72*, 2765-2773.
15. Huang, Y.; Shi, M.; Zhao, S.; Liang, H. Trace analysis of D-tyrosine in biological samples by microchip electrophoresis with laser induced fluorescence detection. *J. Chromatogr. B* **2011**, *879*, 3203-3207.
16. Pumera, M.; Escarpa, A. Nanomaterials as electrochemical detectors in microfluidics and CE: Fundamentals, designs, and applications. *Electrophoresis* **2009**, *30*, 3315-3323.
17. Martín, A.; López, M. Á.; González, M. C.; Escarpa, A. Multidimensional carbon allotropes as electrochemical detectors in capillary and microchip electrophoresis. *Electrophoresis* **2015**, *36*, 179-194.
18. Crevillen, A. G.; Avila, M.; Pumera, M.; Gonzalez, M. C.; Escarpa, A. Food analysis on microfluidic devices using ultrasensitive carbon nanotubes detectors. *Anal. Chem.* **2007**, *79*, 7408-7415.
19. Crevillen, A. G.; Pumera, M.; Cristina Gonzalez, M.; Escarpa, A. Towards lab-on-a-chip approaches in real analytical domains based on microfluidic chips/electrochemical multi-walled carbon nanotube platforms. *Lab Chip* **2009**, *9*, 346-353.
20. Vilela, D.; Anson-Casaos, A.; Teresa Martinez, M.; Cristina Gonzalez, M.; Escarpa, A. High NIR-purity index single-walled carbon nanotubes for electrochemical sensing in microfluidic chips. *Lab Chip* **2012**, *12*, 2006-2014.
21. Vilela, D.; Garoz, J.; Colina, A.; Cristina Gonzalez, M.; Escarpa, A. Carbon Nanotubes Press-Transferred on PMMA Substrates as Exclusive Transducers for Electrochemical Microfluidic Sensing. *Anal. Chem.* **2012**, *84*, 10838-10844.
22. Ambrosi, A.; Chua, C. K.; Bonanni, A.; Pumera, M. Electrochemistry of Graphene and Related Materials. *Chem. Rev.* **2014**, *114*, 7150-7188.
23. Chua, C. K.; Ambrosi, A.; Pumera, M. Graphene based nanomaterials as electrochemical detectors in Lab-on-a-chip devices. *Electrochem. Commun.* **2011**, *13*.
24. Hervás, M.; López, M. A.; Escarpa, A. Electrochemical immunosensing on board microfluidic chip platforms. *Trends Anal Chem* **2012**, *31*, 109-128.

25. Iqbal, J.; Iqbal, S.; Muller, C. E. Advances in immobilized enzyme microreactors in capillary electrophoresis. *Analyst* **2013**, *138*, 3104-3116.
26. Blanes, L.; Mora, M., F.; do Lago, C. L.; Ayon, A.; García, C. D. Lab-on-a-Chip Biosensor for Glucose Based on a Packed Immobilized Enzyme Reactor. *Electroanalysis* **2007**, *19*, 2451-2456.
27. Wang, J. Electrochemical detection for microscale analytical systems: a review. *Talanta* **2002**, *56*, 223-231.
28. Mora, M.F.; Giacomelli, C.E.; Garcia, C.D. Interaction of d-Amino Acid Oxidase with Carbon Nanotubes: Implications in the Design of Biosensors. *Anal. Chem.* **2009**, *81*, 1016-1022.
29. Lopez-Gallego, F.; Betancor, L.; Hidalgo, A.; Alonso, N.; Fernandez-Lorente, G.; Guisan, J. M.; Fernandez-Lafuente, R. Preparation of a robust biocatalyst of D-amino acid oxidase on sepabeads supports using the glutaraldehyde crosslinking method. *Enzyme Microb. Technol.* **2005**, *37*, 750-756.
30. Martín, A.; Hernández, J.; Vázquez, L.; Martínez, M. T.; Escarpa, A. Controlled chemistry of tailored graphene nanoribbons for electrochemistry: a rational approach to optimizing molecule detection. *RSC Adv.* **2014**, *4*, 132-139.
31. Song, M.; Xu, J. Preparation of Polyethylenimine-Functionalized Graphene Oxide Composite and Its Application in Electrochemical Ammonia Sensors. *Electroanalysis* **2013**, *25*, 523-530.
32. Martín, A.; Batalla, P.; Hernández-Ferrer, J.; Martínez, M. T.; Escarpa, A. Graphene oxide nanoribbon-based sensors for the simultaneous bio-electrochemical enantiomeric resolution and analysis of amino acid biomarkers. *Biosens Bioelectron* **2015**, *68*, 163-167.
33. Wang, J.; Tian, B. M.; Sahlin, E. Micromachined electrophoresis chips with thick-film electrochemical detectors. *Anal. Chem.* **1999**, *71*, 5436-5440.
34. Blasco, A.; Escarpa, A. *Electrochemical detection in capillary electrophoresis on microchips*. Elsevier, Amsterdam, 2005; Vol. 45, pp 703-758.
35. Anson, F. C. Application of Potentiostatic Current Integration to Study of Adsorption of Cobalt(3-)-Ethylenedinitrilo)tetraacetate on Mercury Electrodes. *Anal. Chem.* **1964**, *36*, 932-934.
36. Stevens, N. P. C.; Rooney, M. B.; Bond, A. M.; Feldberg, S. W. A comparison of simulated and experimental voltammograms obtained for the [Fe(CN)(6)](3-/4-) couple in the absence of added supporting electrolyte at a rotating disk electrode. *J. Phys. Chem. A* **2001**, *105*, 9085-9093.

III.3. Novel carbon nanomaterial-based electrodes for electrochemical microfluidic sensing



III.3.1. Introduction and objectives

The design of nanomaterial-based electrodic surfaces has fundamentally consisted of casting a drop of a carbon nanomaterial on a solid commercial electrode surfaces. Despite this approach has given excellent results (see epigraph **II.1**) the use of two transducers, the carbon nanomaterial and the carbon electrode itself, make the displayed signal be dependable on two carbon sources. Therefore, new alternative strategies relying on exclusive carbon nanomaterial-based electrodes could improve the analytical response and permit reliable studies of the pure nanomaterial.

Recently, free-standing electrodes fabricated by filtering CNTs (buckypapers)^{1,2} and graphene papers³⁻⁶ have been described in the literature with high applicability as electrode materials for batteries and supercapacitors. This approach has been explored off-chip stuck on solid electrodes⁷ and as unique working electrode in the electrochemical cell,⁸⁻¹⁰ but never coupled to microfluidic devices. Another electrode technology, namely press-transfer, opened a new idea of using directly SWCNTs for electrochemical on-chip applications¹¹⁻¹³ and for spectroelectrochemistry using other transfer strategies.¹⁴ This technology relies on SWCNT embedded in a PMMA piece, inert wafer, not being necessary the deposit on other electric surface or a mixture of polymer or mineral oil as in the majority of strategies.

Besides, as it was concluded in section **III.1**, for the suitable coupling of MCs and electrochemical detection, CNTs were the most exploited carbon nanomaterials while graphene (GP) was few times explored.

Consequently, the first objective was the tailored design of novel electrodes based on carbon nanomaterials (SW, MWCNTs and GP) as

a unique conductive material. These electrodes named as teflon filtered electrodes (TFEs) rely on the filtration of conductor carbon nanomaterials on a teflon filter using tailor-designed templates. The filter becomes the main assembly of the nanomaterial not involving chemical reactions or high external forces or energies. Two different designs a three-electrode and one-electrode configurations for off-chip and on-chip detection, respectively, have been proposed.

The second objective was to couple these TFEs to MC for the separation of quality phenolic markers, tyrosol (TY), hydroxytyrosol (HTY) and oleuropein (OL), presented in olive oil as selected application with food significance.

III.3.2. Graphene and carbon nanotubes teflon-filtered electrodes for electrochemical microfluidic sensing

Two designs a three-electrode and a line-electrode configuration were proposed as it is shown in **Figure III.9**. The filtration of these nanomaterials in a porous Teflon membrane allows the accumulation of the carbon nanomaterial on the filter. **Figure III.9A** shows the three electrode configuration, in which working electrode (WE) and auxiliary electrode (AE) consist of the same filtered carbon nanomaterial. The desired shape of the WE and AE are previously cut in two polyethylene terephthalate (PET) wafers, which are located in between the filter and act as templates during the filtration process. For enhancing the mechanical resistance of the filter, and to demonstrate the possibilities of using different substrates, the filtered nanomaterial was stuck using a double-sided tape on a PET substrate (3.5 x 1.5 x 0.05 cm³). The silver reference electrode (RE) was also integrated in the PET substrate. **Figure III.9B** shows the line electrode configuration to be coupled to MC. This design only contained the WE, because RE and AE are integrated in the MC electrochemical cell (see experimental). The detector design consisted of a line-sized (1 x 10 mm) filter of nanomaterial centered and stuck on the PMMA wafer (3.5 x 1.0 x 0.2 cm³). PMMA offers a mechanical extra-support for suitable *end-channel* coupling to the MC.

Both three-electrode and line-configuration TFEs were explored using SW, MW and GP-TFEs and DA and CT as model analytes.

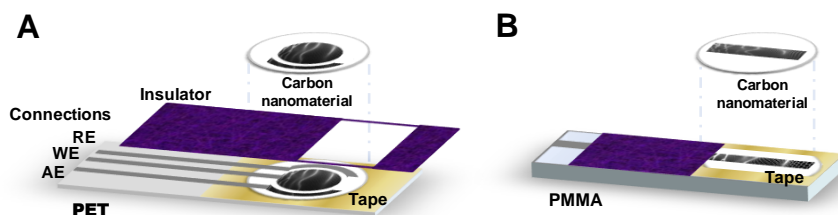


Figure III.9. Design of the carbon nanomaterial-based TFEs: **(A)** three electrode configuration for off-chip and **(B)** line electrode configuration for on-chip detection

Firstly, a three-electrode configuration was evaluated by CV and DPV. On the one hand, the carbon nanomaterial based TFEs were characterized by CV. The electrochemical behaviour of the three SW, MW and GP TFEs was very similar as it is shown in **Figure III.10A**.

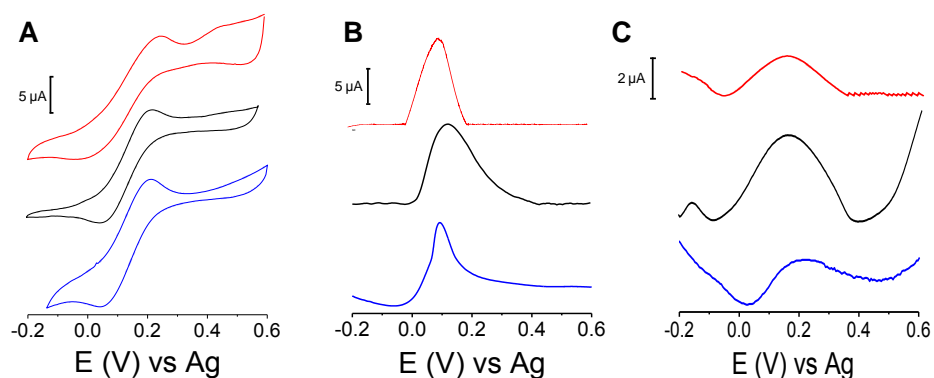


Figure III.10. **(A)** CV of 0.5 mM $\text{Fe}(\text{CN})_6^{3-/4-}$ in 0.10 M KCl **(B)** DPV for 1 mM DA in 25 mM MES and **(C)** DPV for 1 mM CT in 25 mM MES using SW (red), MW (black) and GP (blue) TFEs. Filtered volumes: 2.5 mL for GP and 15 mL for SW and MW, respectively

Particularly, GP and MW-TFEs showed the lowest potential difference between anodic and cathodic peaks (~ 160 mV), being in the three cases the peak current ratios close to 1.

On the other hand, **Figure III.10** shows the electrochemical sensing of DA (**B**) and CT (**C**) using DPV. **Table III.3** lists the oxidation potentials and the amperometric currents obtained during the electrochemical sensing of the analytes. While for DA sensing, the three materials showed similar intensity currents, MW-TFEs showed the highest current intensities for CT sensing. Interestingly, the DA peak oxidation was narrower for GP-TFE. RSDs $\leq 4\%$ (n=3) for intra-electrode repeatability and RSD $\leq 7\%$ (n=3) for inter-electrode reproducibility were obtained revealing a very good precision for these electrodes.

Both CV and DPV electrochemical techniques suggested the good performance and capabilities of these tailored-design TFEs and the good response of even GP-TFEs with 6 times less quantity of material than in the case of CNTs.

Table III.3. Electrochemical sensing of dopamine and catechol using three-electrode configuration

Carbon nanomaterial	E, mV		Intensity, μA	
	DA	CT	DA	CT
SW	96.0 \pm 0.4	179 \pm 1	10.10 \pm 0.03	3.80 \pm 0.01
MW	117.0 \pm 0.5	190 \pm 1	10.80 \pm 0.05	5.60 \pm 0.03
GP	95.0 \pm 0.3	203 \pm 2	9.30 \pm 0.02	2.80 \pm 0.01

Values are expressed as mean values \pm standard deviation for n=3

Secondly, the line electrode configuration coupled with the MCs was also evaluated using DA and CT. Thus, different dispersion volumes (1, 2.5, 5, 10, 15 and 20 mL) were explored during the development of the SW, MW and GP TFEs. **Table III.4** lists the migration times and

amperometric currents for the DA and CT electrochemical microfluidic sensing. It is worth it to mention that 15 mL were chosen for SW and MW and 2.5 mL was chosen for GP. This fact suggested the good conductivity of GP and the excellent results obtained with 6 times lower content of material than in the case of CNTs.

Table III.4. Analytical evaluation of the TFEs

Electrode	Filtered volume (mL)	R (k Ω)	Dopamine		Catechol	
			t \pm s (s)	i \pm s (nA)	t \pm s (s)	i \pm s (nA)
SW-TFE	5.0	216	76.2 \pm 0.3	10.8 \pm 0.4	119.8 \pm 0.4	2.2 \pm 0.1
	10.0	72	76.0 \pm 0.2	16.2 \pm 0.1	121.8 \pm 0.3	4.3 \pm 0.1
	15.0	58	76.8 \pm 0.2	17.0 \pm 0.1	123.9 \pm 0.2	7.4 \pm 0.2
MW-TFE	5.0	2120	80.3 \pm 0.8	16.1 \pm 0.5	128.8 \pm 1.0	4.2 \pm 0.7
	10.0	150	76.5 \pm 0.4	18.8 \pm 0.7	121.0 \pm 0.7	4.4 \pm 0.7
	15.0	10.8	75.6 \pm 0.9	20.9 \pm 0.5	122.5 \pm 0.8	5.9 \pm 0.1
GP-TFE	2.5	110	80.2 \pm 0.1	16.3 \pm 0.3	121.7 \pm 0.7	5.5 \pm 0.6
	5.0	54	76.4 \pm 0.3	14.4 \pm 0.3	125.0 \pm 0.5	1.9 \pm 0.2
	10.0	16	82.1 \pm 0.2	13.9 \pm 0.6	125.4 \pm 0.4	4.6 \pm 0.6
	15.0	10	76.1 \pm 0.5	8.7 \pm 0.1	120.0 \pm 0.2	2.8 \pm 0.3

Values are expressed as mean values \pm standard deviation (n=5)

The precision obtained was good whichever the electrode used, showing RSD values $\leq 1\%$ and $\leq 4\%$ in DA and $\leq 1\%$ and $\leq 15\%$ (n = 5) in CT, for migration times and amperometric currents, respectively.

Furthermore, these electrodes exhibited a good electroanalytical performance and low resistance (see **Table III.4**) involving very low

quantity of carbon nanomaterial accumulated in the electrode surface (0.25 g/m^2 and 1.5 g/m^2 for CNTs).

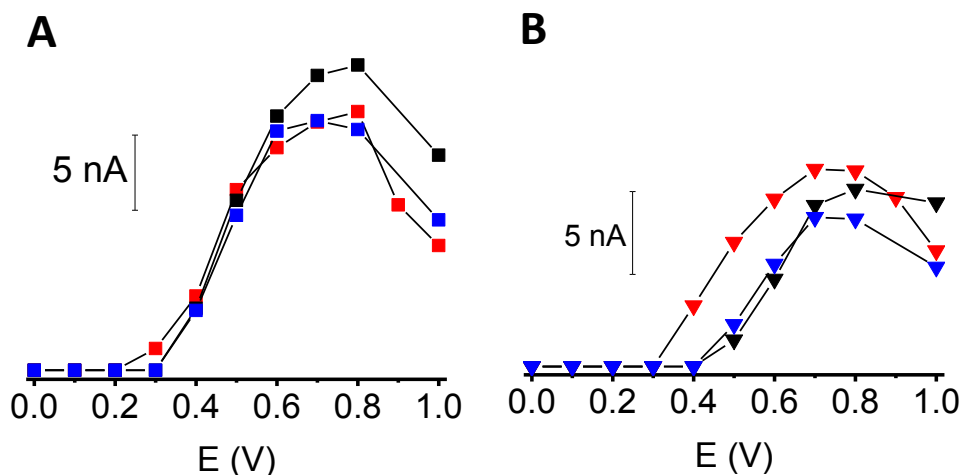


Figure III.11. Hydrodynamic voltamograms for $100 \mu\text{M}$ DA (**A**) and $100 \mu\text{M}$ CT (**B**) in SW (red), MW (black) and GP (blue) TFEs. Conditions: 5 s injection time, +1500 V injection and separation voltage, 25 mM MES (pH 6.50). Detection voltage +0.70 V vs. Ag/AgCl

Under optimized electrokinetic conditions (5 s injection time at +1500 V for injection and separation voltage), **Figure III.11** illustrates the HDVs at the three carbon nanomaterial based TFEs. The response between the three materials slightly differs from one to the others, suggesting the good behavior of all the nanomaterials employed. While, for DA (**Figure III.11A**), GP-TFE reached the highest sensitivity at +0.60 V, both CNT-TFEs, reached higher values at +0.80 V. For CT (**Figure III.11B**), SW-TFEs showed the better response and started at lower potentials of +0.40 V. The optimal detection potential was chosen at +0.70 V because it offered the best signal-to-noise characteristics.

Figure III.12 illustrates the electrochemical microfluidic sensing of DA and CT using SW, MW and GP-based TFEs. The oxidation potential of +0.70 V applied on TFE working electrodes, in connection with a separation voltage of +1500 V, resulted in a well-defined, sharp, and resolved peaks, a flat baseline, and favorable signal-to-noise characteristics. A very good intra-electrode repeatability with RSD values found were $\leq 1\%$ and $\leq 3\%$ for DA and $\leq 1\%$ and $\leq 10\%$ for CT (n=10), in migration time and current intensities, respectively. These results suggested the inherent resistance of the electrode to be fouled by the analytes with independence of the carbon nanomaterial assayed, which is one of the most valuable advantages derived from the large surface area of carbon nanomaterials to be exploited with analytical purposes. In addition, these results indicated a good stability of the electrode.

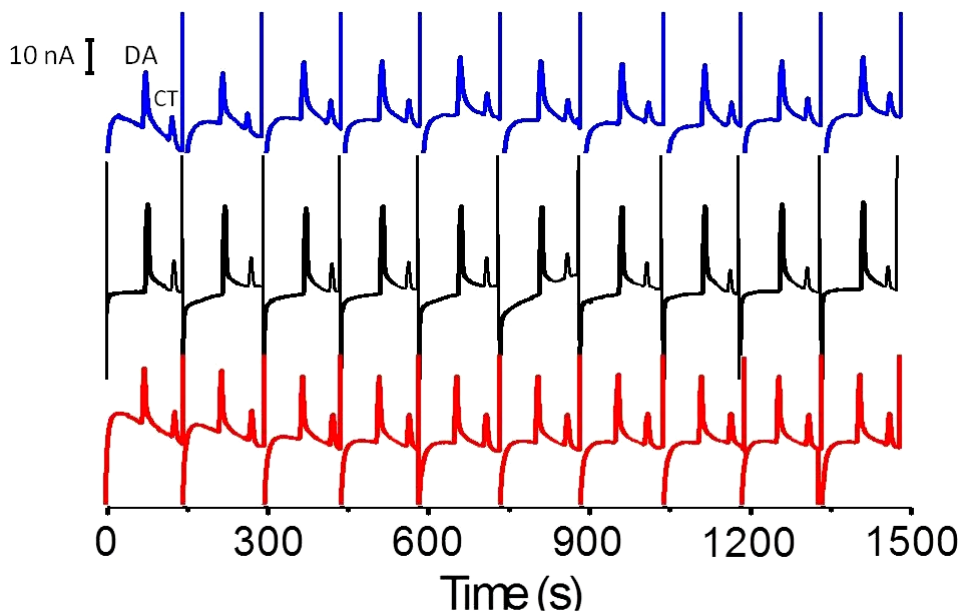


Figure III.12. Sensing capabilities on electrochemical microfluidic sensing of 100 μM of DA and CT (n=10) in SW (red), MW (black) and GP (blue). Conditions as in Figure III.11

To prove the reliability of the fabrication process, various electrodes with different filters were fabricated and evaluated. Non significant differences were found in terms of current intensities for DA and CT with the three carbon nanomaterials, indicating optimal inter-electrode reproducibility with RSD values of 5, 8 and 6 % in DA and 14, 12 and 19% in CT currents (n=5 electrodes) in SW, MW and GP-TFEs, respectively.

Also, TFEs displayed well-defined concentration dependence for DA and CT. The resulting calibration plots were highly linear ($R^2 \geq 0.990$) in the assayed concentration ranges (from 10 to 125 μM for DA and from 20 to 250 μM for CT), with intercepts statistically zero and with high sensitivities for all the electrodes explored. Optimal precision was also obtained with independence of the concentration assayed (RSDs<6%, n=3).

Combining the high sensitivity of the TFEs with its low noise level resulted in suitable LODs calculated as $3 S_a/b$, (~ 8 and ~ 15 μM for DP and CT, respectively) ($S/N = 3$) as it is appreciate in **Table III.5**.

Table III.5. Calibration analytical features ($\alpha= 0.05$, n=5)

Analyte	Material	$a \pm ts_a$ (nA)	$b \pm ts_b$ (nA μM^{-1})	R^2	LOD (μM)
DA	SW	2.72 ± 2.73	0.15 ± 0.04	0.990	10
	MW	-0.48 ± 1.89	0.21 ± 0.04	0.994	6
	GP	-1.78 ± 3.76	0.30 ± 0.07	0.990	8
CT	SW	0.20 ± 0.82	0.046 ± 0.006	0.995	12
	MW	-2.01 ± 2.75	0.097 ± 0.030	0.990	18
	GP	-2.25 ± 2.29	0.092 ± 0.017	0.994	15

III.3.3. Characterization of the carbon nanomaterial-based teflon filter electrodes

The TFEs were characterized by microscopy techniques. In a first approach, **Figure III.13** shows the FE-SEM micrographs for the nanomaterial and the control teflon filter. The surface of the SW-TFE indicates a compact deposit of nanomaterial largely incrustated within the filter pores leading to a homogeneous morphology with low contrast by FE-SEM. MW-TFE seems to present a highly porous surface with clear protrusions. Many MWCNTs are observed with different tilts some quite horizontally disposed. This MW-TFE presents holes and high roughness (darker areas in the image). In GP-TFE, the graphene sheets are extended as thin layers on the teflon filter covering the whole filter pores, generating a thin film of stacked graphene layers. The control teflon filter structure is a net of polymer with pores down to 1 μm .

In a second approach, the TFEs were carefully evaluated by current sensing AFM to assess the roughness, level of porosity and the electric resistance of these electrodes. On the one hand, **Figure III.14A** illustrates the topography micrographs of the nanomaterials and informs about the roughness of each nanomaterial on the teflon filter. Thus, the roughness values found were 88, 220, 113, 140 nm for SW-TFE, MW-TFE, GP-TFE and teflon (control), respectively. SW-TFE shows the lowest roughness values, suggesting that all the material may be filling the pores of the teflon filter during the filtration process. GP-TFE consists in stacked graphene layers constructing a thin film with average roughness of 113 nm.

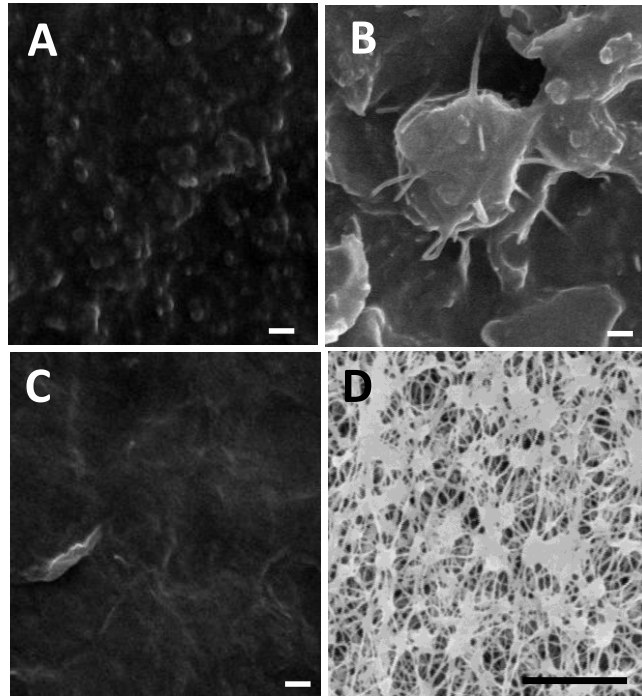


Figure III.13. Morphological characterization. FE-SEM micrographs for (A) SW-TFE, (B) MW-TFE, (C) GP-TFE and (D) teflon (control). Scale bar 200 nm except in teflon 5 μm

Interestingly, MW-TFE presents the highest roughness value even higher than the teflon (control). These roughness values are in agreement with the micrographs found in FE-SEM and suggest the high porosity of MW-TFEs in comparison with the other teflon filtered carbon materials. Moreover, clear protrusions are observed. Some of them appear blurred to some extent, which can correspond to the fact of imaging dangling nanotubes. On the other hand, as it is shown in **Figure III.14B**, the teflon surface shows high resistance on its entire surface around 500 G Ω compared to the M Ω found for the nanomaterials on the nanomaterial-TFEs. These data demonstrate that the nanomaterials are the exclusive responsible for the decrease of resistance and indicate that they are the unique transducers for the electrical signal. The average resistances found

for the nanomaterial surface- arrangements were 50, 10 and 14 M Ω , for SW-TFE, MW-TFE and GP-TFE, respectively. These results revealed the highest resistance in SW-TFE and the lowest resistance for MW-TFE, suggesting that these data may be related with the arrangement of the nanomaterials on the filter. Interestingly, for these fabricated electrodes, the final disposition of the nanomaterials on the filter seems to be crucial for the final device performance. As a result, the distribution of the MWCNTs on the teflon filter suggests the best performance.

We have further characterized the, previously shown in **Figure III.9B**, line configuration TFEs by electrochemical impedance spectroscopy. **Figure III.15** illustrates the Nyquist plot for the three carbon nanomaterial based electrodes. The plots at high frequencies, in the frequency range between 10^5 to 0.1 Hz, except in MW until 1 Hz (see **Figure III.15A**) present a linear tendency, demonstrating the low resistance of the nanomaterials to the electronic transference. However, when the range of the frequencies studied is widen to 0.01 Hz, (see **Figure 15B**) the Nyquist plot ends with a semicircle, showing high resistance values reaching 60, 180 and 360 k Ω for MW, SW and GP, respectively. This behavior suggests the behavior of a porous electrode,^{18,19} where the electrode consists of two differentiated parts. The bottom part is an insulator and non-conductive material, (teflon filter) and the top part is the conductive material (the carbon nanomaterials embedded on the filter). The electrochemical impedance spectroscopy results found in these porous surfaces are more complex than in conventional electrodic surfaces or commercial modified surfaces due to the interfacial impedance throughout the pore.¹⁹ MW-TFE displays again the lowest resistance demonstrating a high agreement with the current sensing AFM results.

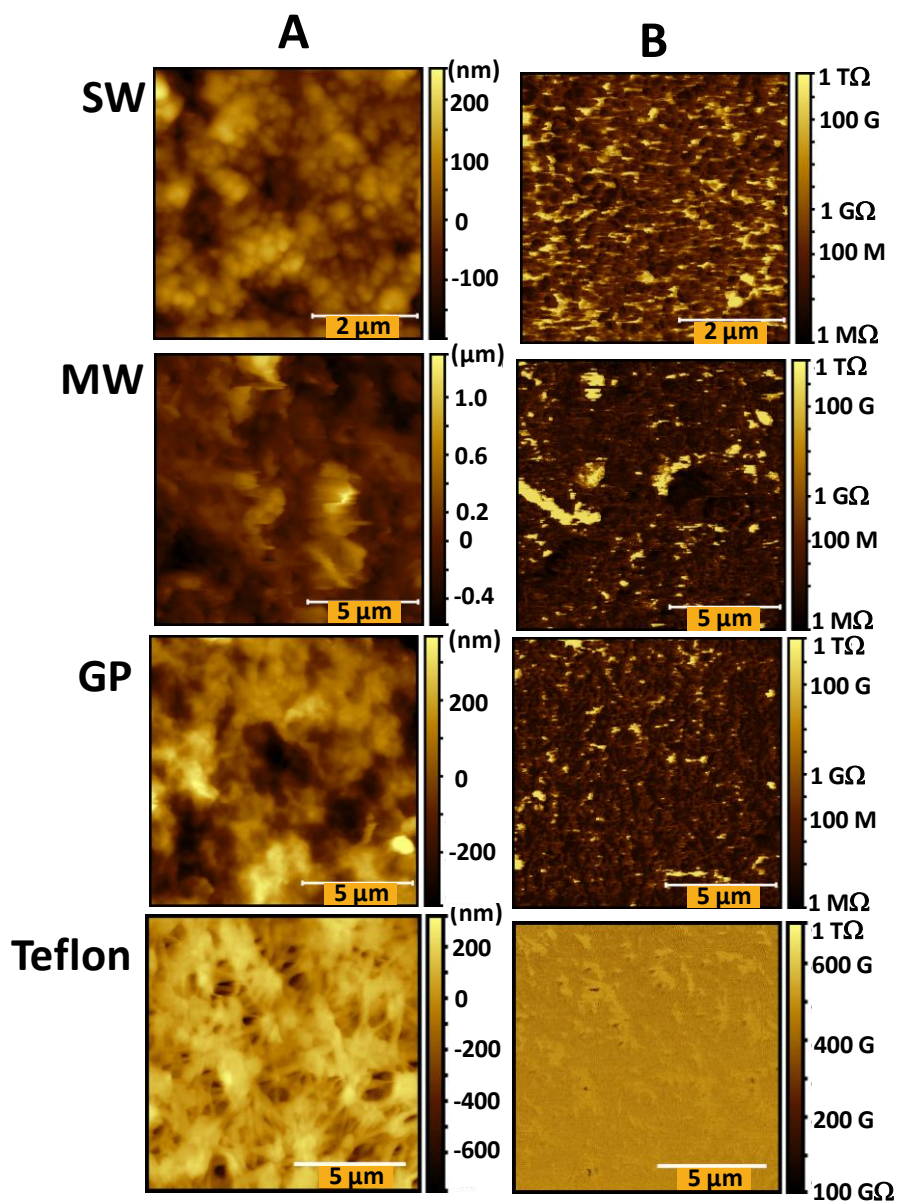


Figure III.14. Current sensing AFM characterization: (A) topographical and (B) resistance data

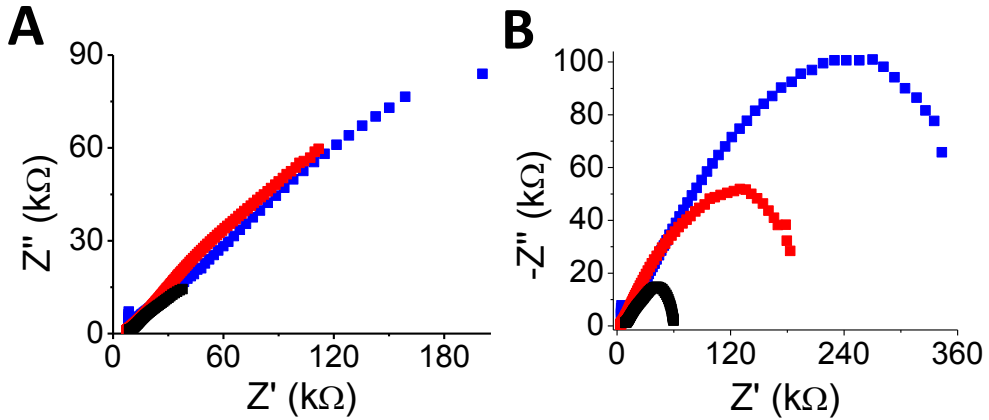


Figure 15. Nyquist impedance plots of GP-TFE (blue), SW-TFE (red) and MW-TFE (black) for 5 mM $\text{Fe}(\text{CN})_6^{4-/3-}$ in 0.01 M PBS (pH=7.4) and 5 mV amplitude in the range of (A) 10^5 to 0.1 Hz (except MW to 1 Hz) and (B) 105 to 0.01 Hz (except MW to 0.1 Hz) frequencies

The characterization of the surface-arrangements suggests that each material is filtered adopting a particular arrangement on the filter and the final disposition of the material in the filter is key for achieving the lower resistance. **Figure III.16** illustrates an interpretation of the final disposition of the materials on the filter.

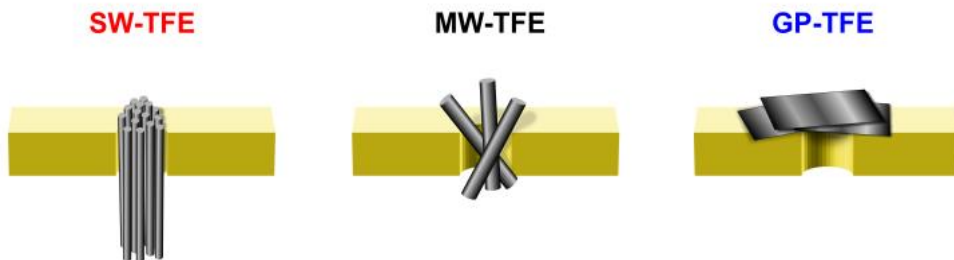


Figure III.16. Interpretation of the disposition of the nanomaterials on the filter pores of the SW, MW and GP-TFE

III.3.4. Application of the carbon nanomaterial-based teflon filter electrodes for phenolic detection in olive oil

Due to the distribution of the MW on the teflon filter suggested the best performance, these electrodes were chosen as the optimal to be coupled as electrochemical transducer with MC.

The nowadays challenging food sector is demanding fast, simple, cheap and reliable responses.^{15,16} The valuable inherent features, the enormous analytical potential and the drawbacks of lab-on-a-chip for food safety and quality assurance have recently been discussed under the term *Food Microfluidics*.¹⁷ Some of the identified drawbacks in *Food Microfluidics* are the sensitivity, selectivity and reproducibility during the analysis of food complex samples. The exploration of these novel materials and technologies, without the need of expensive and sophisticated facilities (i.e. clean room facilities) could improve food microfluidic performances.

As a result, MW-TFEs were explored for the fast assessment of relevant phenolic compounds, TY, OL and HT as quality markers in olive oil. On chip detection performance was carefully assayed for the target analytes. **Figure III.17** shows the chemical structure and HDV plots at the MW-TFEs for TY, OL and HTY. The response suggests the good behavior of MW-TFE and the optimal detection potential at +0.70 V because it offered the best signal-to-noise characteristics. In addition, these electrodes were compared with drop-casting modified MW-CSPEs and further with commercial non-modified CSPEs. Furthermore, as it is shown in **Figure III.17** in the detection of TY using the non-modified CSPEs, the potential for the detection of the molecule with a good signal to noise features starts at +1.20 V, while for MW-CSPE it is +1.00 V. In contrast, as MW-TFE

provokes a strong electrocatalysis on this oxidation, it only requires +0.70 V. Furthermore, TY and HTY showed lower potential with oxidation starting at +0.50 and +0.30 V for TY and HTY, respectively using MW-TFE than with CSPE modified and non-modified.

The microfluidic separation media was optimized to be 10 mM borate at pH 9.50 with 5% MeOH as additive to improve the resolution (data not shown). The influence of separation voltage on electrochemical microfluidic sensing of TY, OL and HTY when separation voltages were increased from +750 to +2750 V was initially evaluated. As expected, the increment of separation voltages from +750 V to +2750 V caused a dramatic decrease in the migration times, with a clear decrease in the analyte resolution (the peak resolutions were 0.85 and 0.79 at +2750 V, 1.6 and 2.1 at +1700 V and increased until 3.7 and 4.6 in the case of +750 V, between the couples TY-OL and OL-HTY, respectively). Also, initial rise in charging-current baseline indicates incomplete isolation of the electrochemical detector from separation voltages higher than +2000 V. Thus, +1700 V became the most favorable separation voltage for the phenolic compounds detection.

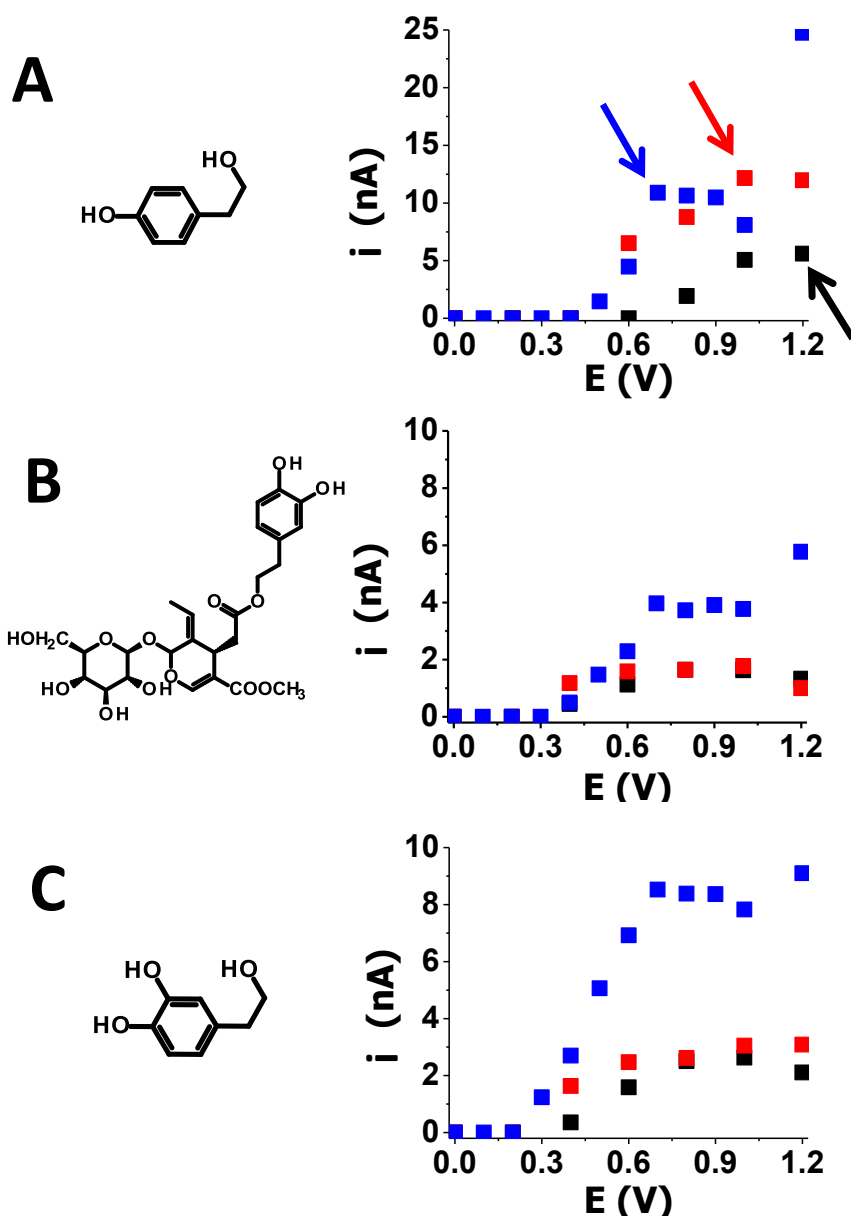


Figure III.17. Chemical structures and hydrodynamic voltamograms using (A) 100 μM TY (arrows highlight the optimal oxidation potential), (B) 100 μM OL and (C) 200 μM HTY at MW-TFE (blue), non-modified CSPE (black) and MW-CSPE (red). Other conditions: running buffer 10 mM borate and 5% MeOH, 5 s at +1700 V injection voltage, +1700 V separation voltage and detection buffer 0.1 HNO_3 and 5% MeOH

Under optimized separation (borate 25 mM, pH 9.50 and 5% MeOH, + 1700 V) and detection (+0.70 V in 0.1 M nitric acid + 5% MeOH) conditions, the separation of phenolic markers was successfully achieved. **Figure III.18A** shows the microchip electropherograms for the separation of the quality phenolic markers TY, OL and HTY using MW-TFEs compared to drop casting modified MW-CSPE as well as non-modified CSPE. MW-TFEs showed the best sensitivity (5 times higher peak height than non-modified CSPE) and improved from the drop casted MW-CSPEs. Furthermore, as illustrated in this figure, the separation with MW-TFEs showed narrower peak widths, which is probably due to the exclusive presence of nanomaterial and the faster electron transfer using this TFE approach.

Table III.6 quantitatively indicates that MW-TFE improves the electrochemical detection towards a decrease in the oxidation potentials and an enhancement of the amperometric currents with improved precision.

Table III.6. Analytical evaluation of the MW-TFEs

Electrode	Analyte	E_{opt} (V)	$t_m \pm s$ (s)	RSD(%)	$i \pm s$ (nA)	RSD(%)
MW-TFE	TY	+ 0.70	112.6±0.6	0.5	10.0±0.6	6
	OL	+ 0.70	152.9±0.8	0.5	5.9±0.3	4
	HTY	+ 0.70	205.7±0.8	0.4	7.9±0.4	4
MW-CSPE	TY	+ 1.00	113.1±0.6	0.5	4.4±0.2	5
	OL	+ 0.70	153.4±0.4	0.3	4.1±0.1	2
	HTY	+ 0.80	209.4±0.6	0.3	6.8±0.2	3
CSPE	TY	+ 1.20	112.2±1.8	1.6	2.0±0.2	10
	OL	+ 0.80	153.0±3.8	2.5	1.3±0.1	7
	HTY	+ 1.00	210.1±8.0	3.8	1.9±0.2	9

Values are expressed as mean values \pm standard deviation (n=5)

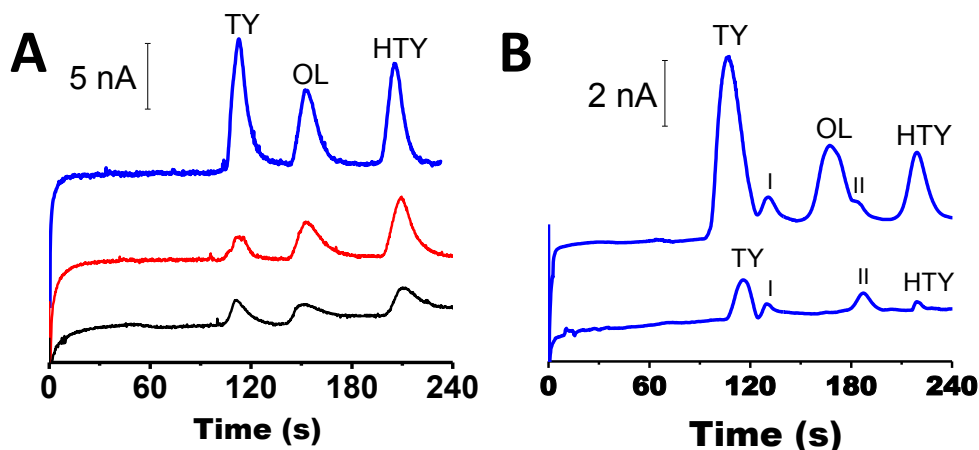


Figure III.18. (A) Microchip electropherograms for the separation of 100 μM TY, 100 μM OL and 200 μM HTY at MW-TFE (blue), MW-CSPE (red) and non-modified CSPE (black). (B) Microchip electropherograms corresponding to a virgin olive oil sample (down) and virgin olive oil spiked with 25 μM of TY, 100 μM of OL and 50 μM of HTY (up) at MW-TFE. Other conditions: running buffer 10 mM borate and 5% MeOH, injection voltage 5 s +1700 V, +1700 V separation voltage and detection buffer 0.1 HNO_3 and 5% MeOH, +0.70 V detection potential

The selected MW-TFEs displayed well-defined concentration dependence for TY, OL and HTY. **Table III.7** lists the data from the resulting calibration plots, which were highly linear ($R^2 \geq 0.990$) in the assayed concentration ranges (from 25 to 125 μM for TY, 50 to 250 μM for OL and from 100 to 500 μM for HTY), with intercepts statistically zero and with high sensitivities for all the electrodes explored. Precision was also carefully evaluated with excellent values for intra-electrode repeatability (RSDs <7%, $n=10$) and inter-electrode reproducibility (RSDs <8%, $n=5$).

Combining the high sensitivity of the MW-TFEs with its low noise level resulted in suitable LODs, calculated as $3 S_a/b$, ($\sim 10 \mu\text{M}$ for TY, OL and HTY) as it is appreciated in **Table III.7**. These TFEs showed better analytical response than the other previous work using MC coupled with gold electrodes,²⁰ showing MW-TFEs much better sensitivity for TY and lower LODs for the analytes under study.

Table III.7. Calibration analytical features ($\alpha = 0.05$, $n=5$)

Analyte	$a \pm tS_a$ (nA)	$b \pm tS_b$ (nA μM^{-1})	R^2	LOD (μM)
TY	0.58 ± 0.92	0.094 ± 0.011	0.990	7
OL	0.15 ± 0.53	0.021 ± 0.003	0.990	10
HTY	0.37 ± 0.58	0.029 ± 0.002	0.997	13

Figure III.18B illustrates the analysis of virgin olive oil samples. TY at 113 s and HTY at 212 s were identified in less than 240 s. As expected, OL was not detected since it is a minority phenolic compound²¹ and also its concentration highly vary in virgin olive oil depending on agronomical and technological factors.²² Two unidentified compounds (peaks *I* and *II*) were also detected. A good precision was also obtained during the analysis of virgin olive oil samples with values of $\text{RSD} < 6\%$ ($n=5$) indicating the good performance and stability of the TFEs when they are operating with these complex matrices.

In order to evaluate the accuracy and capability of the approach for the simultaneous determination of TY, OL and HTY, VOO samples were properly fortified in each analyte. Quantitative recoveries ranging from 97-101% were also obtained with excellent precision

(RSDs \leq 5 %, n=3). These results indicated the accurate determination of the three target molecules in virgin olive oil samples, showing the reliability of these electrodes for quantitative analysis of these target quality markers in complex matrix, which gives additional value to the presented electrodes.

III.3.5. Conclusions

A straightforward and direct use of the excellent properties of carbon nanomaterials using two different TFEs designs: the three-electrode configuration for off-chip detection and line configuration for on-chip detection was demonstrated. The exclusive electronic transduction allowed unique analytical response with good sensitivity and excellent precision due to the extremely low fouling of the nanomaterial-based electrodic surface.

The TFEs demonstrated their electrochemical applicability for different carbon nanomaterials off chip and coupled with microfluidics, in which graphene has been rarely explored. This is a clear example of the first coupling of all the carbon nanomaterials as a unique electrochemical transducer with MC.

These TFEs have demonstrated to be a very useful approach for all conductive carbon nanomaterials and for any supporting non-conductive wafer (PET and PMMA). Thus, the filter becomes the main assembly of the nanomaterial not involving any chemical reaction or high external energy.

These electrodes exhibited a porous surface-arrangement, being the nanomaterial the only responsible for the electrochemical transduction. The nanomaterial disposition plays a relevant role in the final performance, opening novel avenues for designed and tailored nanomaterial-based electrodes. MW-TFEs showed a very good analytical performance during the fast determination of quality phenolic markers in olive oil.

This approach opens the field to other porous films based on nanomaterials for electrochemical detection as a clear alternative to

other traditional transducers. The valuable properties of the TFEs such as excellent analytical performance, high versatility, potential disposability and easy fabrication suggest a tailored electrode manufacturing for many other nanomaterials or composites such as hybrid carbon nanomaterials and metallic nanoparticles or related microstructures. Hence, these electrodes pave the way to a broad field of opportunities in electrochemistry for the exclusive use of nanomaterial transducers and suggest the interest of their coupling with microfluidic devices for analysis in real domains and pave the way for new applications not only in the food but also in other relevant fields.

III.3.6. Experimental section

III.3.6.1. Reagents and materials

The used carbon nanomaterials were reduced graphene oxide (Graphenea, Spain), single-walled carbon nanotubes (Sigma-Aldrich, 704121) and multi-walled carbon nanotubes (Sigma-Aldrich, 659258). Other employed materials for the development of the TFEs were 35 x 10 x 2 mm³ piece of PMMA (Maniplastic, Spain) as the support structure, a teflon filter with a pore size of 0.1 μm (JVWPO1300, Millipore Omnipore), double-sided cello tape, silver conductive paint (Electrolube, UK) for the electrical contacts and epoxy protective overcoat (242-SB, ESL Europe) for the isolation.

DA, CT and MES were purchased from Sigma Chemical Co. (St. Louis, MO, USA). Potassium hexacyanoferrate (III) and potassium chloride were purchased in Panreac (Badalona, Spain). All standard solutions were daily prepared by diluting the reagents in the buffer before the measurement and were well-protected from the light. OL and HTY were obtained from Sigma (St. Louis, Missouri, USA). TY was purchased from Fluka Chemika (Buchs, UK), methanol from Scharlab S. L. (Barcelona, Spain). Sodium tetraborate decahydrate from Merck (Germany) and sodium hydroxide and nitric acid from Panreac (Badalona, Spain). Stock solutions of 0.01 M of the phenolic compounds in methanol were stored in amber vials, at -20 °C, avoiding exposure to direct light. Thus, fresh solutions of determined concentrations were daily prepared by appropriate dilution of the stock solution with the selected solvent. Buffer solutions of sodium tetraborate were prepared by dissolving the amount of the salt in water and adjusted to pH 9.50 with NaOH. Ultrapure water (18 MΩ

cm) was used for the experiments and obtained from Milli-Q system (Millipore, Bedford, MA, USA).

III.3.6.2. Carbon nanomaterial-based electrode fabrication

Carbon nanomaterials were dispersed with a 0.50 mg/100 mL concentration in DMF. The dispersion protocol was as follows: (a) ultrasound bath for 1 hour to provoke the strongest dispersion. (b) tip sonication for 15 minutes at 130 W, to assure the maximum dispersion of the carbon materials in the DMF. Before each filtration, the nanomaterial is sonicated for 15 minutes with a US bath and for 5 minutes with a tip-sonicator at 130 W.

The carbon nanomaterial dispersions were gently filtered in soft vacuum conditions using a steel funnel on a 0.1 μm teflon filter in between two PET layers cut with the desired tailored size and shape. The two PET wafers with an external size equal to the filter and cut in the inner with the selected design of the electrode are used as a template for further filtrations, conferring inherent reproducibility in the final fabrication process. Each filter is used for one electrode and afterwards, the filter is dried at room temperature overnight.

Silver conductive paint was employed. This silver paint was also used as the reference electrode for the three-electrode configuration. An overcoat paint to isolate the silver paint was used to avoid possible interferences of silver conductive paint in the measurement and short-circuit and for confining the volume of sample in the three-electrode configuration.

III.3.6.3. Carbon nanomaterial-based teflon filter electrodes characterization

In order to characterize the TFE surface, the electrodes were firstly metalized with a layer of gold to improve the conductivity of the surface and afterwards characterized by FE-SEM on a JEOL Model JSM6335F equipment working at 20 kV.

AFM images were recorded using an Agilent 550 Pico Plus equipped with an environmental chamber. Current sensing AFM measurements were performed under nitrogen ambient to minimize humidity interferences. Diamond coated cantilevers (DCP11 from Nt-MDT) were used. A resiscope module (from CSInstruments, France), which allows accurate current and resistance measurements over a large current range, was employed. A bias of 5 V was applied between the tip and the TFE sample (the electrical contact, for this purpose, was made on the sample on the silver paint spot). Three signals: topographical, current flowing from the tip to the sample and the sample resistance were simultaneously recorded with this set-up.

Electrochemical impedance spectroscopy measurements were carried out starting at open circuit potential using AC signals of amplitude 5 mV peak to peak in the frequency range of 10^5 Hz to 0.01 Hz, at room temperature, in an electrochemical station PGSTAT-204 (Autolab, Utrecht, Holland) using a conventional three-electrode system comprising a platinum wire as an auxiliary electrode, a silver/silver chloride (Ag/AgCl), 3 M KCl as a reference electrode (CH Instrument, Austin, USA), and the explored TFEs as working electrodes. A concentration of 5 mM of potassium hexacyanoferrate (III), purchased from Panreac (Badalona, Spain), and potassium hexacyanoferrate (II), purchased from Sigma Aldrich (St. Louis, MO,

USA), were dissolved in 0.01 M $\text{Na}_2\text{HPO}_4/\text{NaH}_2\text{PO}_4$ (pH 7.40) adjusted with NaOH, purchased from Panreac, (Badalona, Spain).

III.3.6.4. Drop-casting modified electrodes

CSPE for microchip coupling ($34 \times 10 \times 0.5 \text{ mm}^3$) were modified following a drop-casting protocol. For that, 3 μL of a 0.50 mg mL^{-1} MWCNTs dispersion in DMF were deposited along the electrode and let dry for 1 h before using it.

III.3.6.5. Olive oil sample extraction

Extra virgin olive oil sample was obtained from different batches of mixed varieties including Dritta, Coratina, Leccino and Tortiglione cultivars in an industrial olive mill. Sampling was carried out in the year 2013 and a representative sample was selected in order to carry out the analyses. Samples were stored at room temperature in amber glass bottles. Commercially available octadecyl C18 cartridges (1 g, 6 mL) (International Sorbent Technology, UK) were used for the extraction of the phenolic fraction according to the following protocol: 1 g of olive oil was dissolved in 5 mL of hexane, and the solution was loaded onto a column, previously conditioned with 2 x 5 mL of methanol and 2 x 5 mL of hexane. The column was eluted with 2 x 5 mL of hexane to eliminate the entire lipophilic fraction; the retained polar compounds were recovered by eluting with 2 x 10 mL of methanol. The elute was evaporated to dryness at room temperature (30 °C, 150 rpm) in a rotary evaporator. The extract was recovered with 0.5 mL of methanol and stored in amber glass at -20 °C.

III.3.6.6. Microfluidic chip system and electrochemical procedures

The used microfluidic set-up was identical to the described in the Experimental section in epigraph **III.2.4.1**.

For DA and CT determination, the optimized injection was 5 s at +1500 V and the optimized separation voltage was +1500 V. A detection voltage of +0.70 V was applied in the detection cell to the nanomaterial-based lab-manufactured working electrode for the DA and CT detection. All experiments were performed at room temperature.

For quality phenolic markers determination, the running buffer consisted in 10 mM borax buffer (pH 9.50) and 5% MeOH, while the detection buffer was 0.1 M HNO₃ and 5% MeOH. The sample solution consisted of selected concentrations of the phenolic compounds dissolved in the running buffer. The running buffer, sample and detection reservoirs were filled with their respective solutions. A voltage of +1700 V was applied for 5 min to the buffer reservoir to fill the separation channel, while the detection reservoir was grounded and the others were floating. This process was performed on each sample reservoir for 20 s to facilitate filling the injection channel (between the separation channel and the sample reservoir), and then the voltage was applied for 5 min to the running buffer reservoir to eliminate the residues of the previously introduced samples from the separation channel.

The optimized injection was 5 s at +1700 V and the separation voltage of +1700 V. The optimized detection voltage of +0.70 V was applied in the detection cell to the carbon nanomaterial-based

working electrode against the Ag/AgCl reference electrode. All experiments were performed at room temperature.

All electrochemical measurements were performed, at room temperature, using a Potentiostat Autolab PGSTAT12 from Eco Chemie. A total volume of 100 μL is dropped on the three-electrode TFE electrochemical cell consisting of carbon nanomaterial as a working and counter electrodes and Ag as pseudo-reference electrode.

II.3.7. References

1. Chen, A.; Chatterjee, S. Nanomaterials based electrochemical sensors for biomedical applications. *Chem. Soc. Rev.* **2013**, *42*, 5425-5438.
2. Fagan-Murphy, A.; Whitby, R. L. D.; Patel, B. A. Buckycolumn electrodes: a practical and improved alternative to conventional materials utilised for biological electrochemical monitoring. *J. Mater. Chem. B* **2013**, *1*, 4359-4363.
3. Dikin, D. A.; Stankovich, S.; Zimney, E. J.; Piner, R. D.; Dommett, G. H. B.; Evmenenko, G.; Nguyen, S. T.; Ruoff, R. S. Preparation and characterization of graphene oxide paper. *Nature* **2007**, *448*, 457-460.
4. Chen, H.; Müller, M. B.; Gilmore, K. J.; Wallace, G. G.; Li, D. Mechanically Strong, Electrically Conductive, and Biocompatible Graphene Paper. *Adv Mater* **2008**, *20*, 3557-3561.
5. Xu, H.; Song, Y.; Kunz, H. R.; Fenton, J. M. Operation of PEM fuel cells at 120–150 °C to improve CO tolerance. *J. Power Sources* **2006**, *159*, 979-986.
6. Wang, D.; Li, F.; Zhao, J.; Ren, W.; Chen, Z.; Tan, J.; Wu, Z.; Gentle, I.; Lu, G. Q.; Cheng, H. Fabrication of Graphene/Polyaniline Composite Paper via In Situ Anodic Electropolymerization for High-Performance Flexible Electrode. *ACS Nano* **2009**, *3*, 1745-1752.
7. Sieben, J. M.; Ansón-Casaos, A.; Montilla, F.; Martínez, M. T.; Morallón, E. Electrochemical behaviour of different redox probes on single wall carbon nanotube buckypaper-modified electrodes. *Electrochim. Acta* **2014**, *135*, 404-411.
8. Xiao, F.; Song, J.; Gao, H.; Zan, X.; Xu, R.; Duan, H. Coating Graphene Paper with 2D-Assembly of Electrocatalytic Nanoparticles: A Modular Approach toward High-Performance Flexible Electrodes. *ACS Nano* **2012**, *6*, 100-110.
9. Dong, S.; Xi, J.; Wu, Y.; Liu, H.; Fu, C.; Liu, H.; Xiao, F. High loading MnO₂ nanowires on graphene paper: Facile electrochemical synthesis and use as flexible electrode for tracking hydrogen peroxide secretion in live cells. *Anal. Chim. Acta* **2015**, *853*, 200-206.
10. Wang, Y.; Ping, J.; Ye, Z.; Wu, J.; Ying, Y. Impedimetric immunosensor based on gold nanoparticles modified graphene paper for label-free detection of *Escherichia coli* O157:H7. *Biosens. Bioelectron.* **2013**, *49*, 492-498.
11. Vilela, D.; Garoz, J.; Colina, A.; Cristina Gonzalez, M.; Escarpa, A. Carbon Nanotubes Press-Transferred on PMMA Substrates as Exclusive Transducers for Electrochemical Microfluidic Sensing. *Anal. Chem.* **2012**, *84*, 10838-10844.
12. Vilela, D.; Martin, A.; Gonzalez, M. C.; Escarpa, A. Fast and reliable class-selective isoflavone index determination on carbon nanotube press-transferred electrodes using microfluidic chips. *Analyst* **2014**, *139*, 2342-2347.

13. Gomez, F. J. V.; Martín, A.; Silva, M. F.; Escarpa, A. Microchip electrophoresis-single wall carbon nanotube press-transferred electrodes for fast and reliable electrochemical sensing of melatonin and its precursors. *Electrophoresis* **2015**, *36*, 1880-1885.
14. Garoz-Ruiz, J.; Heras, A.; Palmero, S.; Colina, A. Development of a Novel Bidimensional Spectroelectrochemistry Cell Using Transfer Single-Walled Carbon Nanotubes Films as Optically Transparent Electrodes. *Anal. Chem.* **2015**, *87*, 6233-6239.
15. Hamburg, M. A. Advancing Regulatory Science. *Science* **2011**, *331*, 987-987.
16. García-Cañas, V.; Simó, C.; Herrero, M.; Ibáñez, E.; Cifuentes, A. Present and Future Challenges in Food Analysis: Foodomics. *Anal. Chem.* **2012**, *84*, 10150-10159.
17. Escarpa, A. Lights and shadows on Food microfluidics. *Lab Chip* **2014**, *14*, 3213-3224.
18. Candy, J.; Fouilloux, P.; Keddami, M.; Takenouti, H. The characterization of porous electrodes by impedance measurements. *Electrochim. Acta* **1981**, *26*, 1029-1034.
19. Lasia, A. *Electrochemical Impedance Spectroscopy and its Applications; Modern Aspects of Electrochemistry*; Springer US: New York, **2014** pp 143-248.
20. Godoy-Caballero, M. d. P.; Acedo-Valenzuela, M. I.; Galeano-Diaz, T.; Costa-García, A.; Fernandez-Abedul, M. T. Microchip electrophoresis with amperometric detection for a novel determination of phenolic compounds in olive oil. *Analyst* **2012**, *137*, 5153-5160.
21. Servili, M.; Selvaggini, R.; Esposto, S.; Taticchi, A.; Montedoro, G.; Morozzi, G. Health and sensory properties of virgin olive oil hydrophilic phenols: agronomic and technological aspects of production that affect their occurrence in the oil. *J. Chromatogr. A* **2004**, *1054*, 113-127.
22. Lerma-García, M. J.; Lantano, C.; Chiavaro, E.; Cerretani, L.; Herrero-Martínez, J. M.; Simó-Alfonso, E. F. Classification of extra virgin olive oils according to their geographical origin using phenolic compound profiles obtained by capillary electrochromatography. *Food Res. Int.* **2009**, *42*, 1446-1452.

Chapter IV

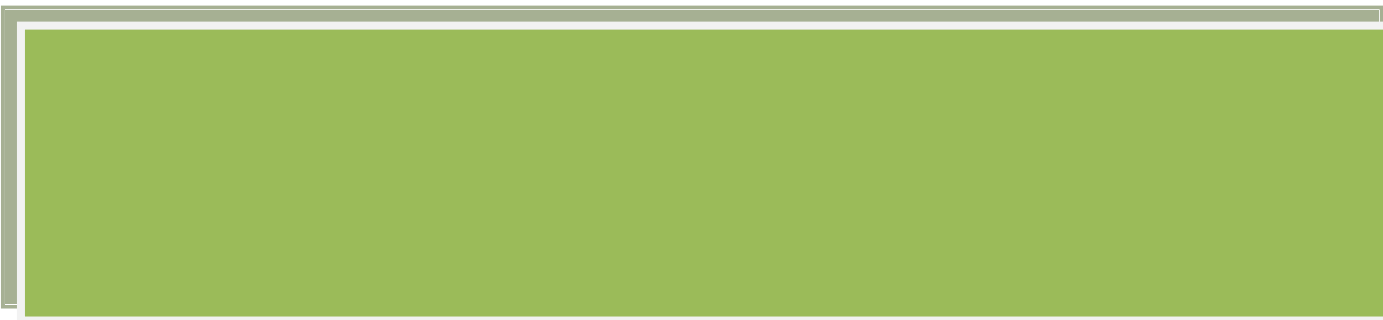
Graphene-based micromotors: electrosynthesis, characterization and applications

Un científico es el que sabe o se interesa no solo por su especialidad.

(J.M. Sánchez Ron)



IV.1. Micromotors: *state of the art*



IV. 1.1. Micromotors: novel analytical tools

Human being has been developed many devices for improving the chemical sensing and facilitate the daily life. The development of autonomous machines or artificial smart devices had been the dreamt illusion in our lives.¹ Inspired by the biological machines in nature and imitating their behavior, scientists started in 2004 to create analogous artificial machines in the nano and micro scales.² The micromotors has resulted, during the last years, to be a fascinating challenge in nanotechnology and a new tool for enhancing the (bio-)-sensing.³⁻⁷

It is worth to mention that in the literature many terms are used for describing this device such as micromotor, microengine, microrocket, microjet, microbot, micromachine, among others. A motor or engine could be define as a device capable of transforming any kind of energy into movement and forces, thus micromotors are, in the same way, devices able to move autonomously in fluids by converting different sources of energy into mechanical work at the microscales. Commonly, these micromotors are particles with a few microns dimensions and their shapes and composition are creatively designed with certain asymmetry. Therefore, the application of certain energy in the system permits a local gradient and the uneven distribution of the forces in the micromotor, permitting the expected movement. These motors can move autonomously in fluids at speeds up to millimeters per second and even generate sufficient force to penetrate cell membranes.⁸

At the microscale, as it happens in microfluidics, fluids and particles do not behave as in the macroscale. When the particle size decrease the inertia force is insignificant compared to the viscous forces, thus

the Reynolds number, ratio of inertia and viscous forces, is very low. The main consequences of this low Reynolds number and the negligible inertia suppose that there can only be instantaneous motion caused by the instant forces applied on the micromotor, and the motion ends when the energy is finished. Also, as we have anticipated, for inducing motion, the motors have to be asymmetrical in the particle composition, the shape, or this asymmetry has to be forced by the reactions suffered on their surface. Therefore, the broken asymmetry in one axis dictates the direction of the final motion. Additionally, the mechanism responsible for propulsion is usually ineffective when decreasing the motor size under 1 μm .

In general, the movement of these synthesized motors is autonomous, as it will be discussed during the explanation of the propulsion mechanisms, however, external fields such as magnetic and electric fields may be used to direct and control the propulsion of the motors at nano and microscales,⁹ allowing a directed and non-autonomous motion.

Fabrication is a key step towards successful realization of the applications of micromotors. The ultimate goal of fabrication is to make micromotors that are suitable for application in an easy and cost-effective way. The rapid development of nanotechnology has resulted in diverse strategies and techniques for the fabrication of micro- and even nanoscale motors. Micromotors could be classified considering many features, such as the fabrication method, the method of propulsion or the final application. In this Thesis, the classification has been proposed according to the propulsion methods.

IV.1.2. Micromotors: propulsion methods

As we stated before, micromotors are devices capable of converting energy into movement. Thus, the propulsion methods will depend on the source of energy. If the energy comes from a chemical reaction, we will have chemically-driven micromotors, in which we could find several propulsion methods, self-electrophoresis (see **Figure IV.1.A**), self-diffusiophoresis and bubble-propulsion (see **Figure IV.1.B**). When using acoustic energy, ultrasound propulsion motors are found (see **Figure IV.1.C**). Other propulsion methods are based on other external fields such as, magnetic or electric fields or external stimuli such as light, pH or temperature yielding the respective propulsion methods (see **Figure IV.1.D**). A scheme of these motions is shown in **Figure IV.1**. Briefly, the most used propulsion mechanism will be discussed in the following sections.

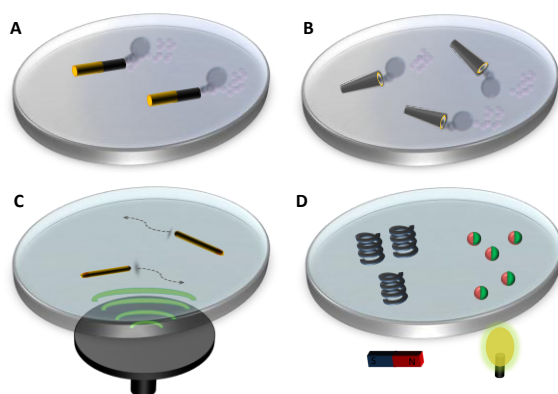


Figure IV.1. Micromotors classification attending to the propulsion mechanism: **(A)** self-electrophoresis, **(B)** bubble-propulsion, **(C)** Ultrasound propulsion, and **(D)** other propulsion methods: magnetically and light-induced

Self-electrophoresis propulsion

In general terms, as we have already seen for microfluidic chips in **Chapter III**, electrophoresis is based on the migration of charged particles under the application of an electric field. However, these autonomous motors do not respond to the application of an external field. The self-electrophoresis propulsion of these motors relies on the generation of chemical gradients along the motor and the movement in response to the self-generation of a local electric field due to these chemical gradients.

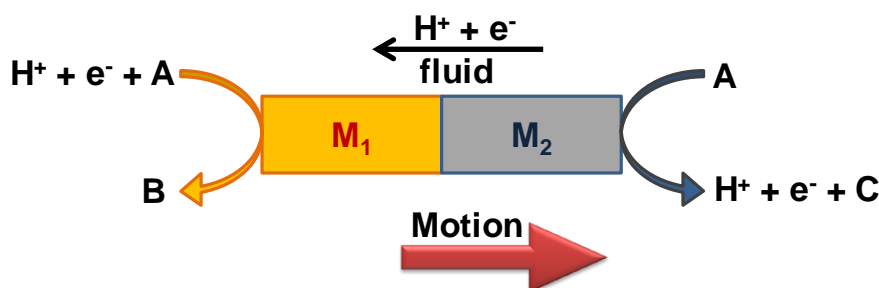


Figure IV.2. Self-electrophoresis propulsion of bimetallic structures. The motion is against the protons (H^+) and electrons (e^-) flow. M_1 and M_2 are two different catalytic metals. A, B and C are the chemical reagents and products yielded from the redox reactions

Figure IV.2 shows the scheme of these micromotors. In the literature, the most common structures found are the bimetallic rods-wires (cylinders)² or the Janus particles (spheres)¹⁰ with the characteristic of having both two different segments or parts based on two different materials, which confer the motor of asymmetry. In self-electrophoresis, the micromotor moves in a self-generated

electric field as a result of an asymmetric distribution of ions. In the case of bimetallic motors, as in **Figure IV.2**, the oxidation of A preferentially occurs at the anode (M_1) end and the reduction of A at the cathode (M_2) end. This bipolar electrochemical reaction leads to a higher concentration of protons near the M_2 end and a lower concentration near the M_1 end. Since the protons are positively charged, the asymmetric distribution results in an electric field pointing from the M_2 end to the M_1 end. The negatively charged motor therefore moves in the self-generated electric field, an effect similar to electrophoresis. In this example a proton gradient is responsible for the motion of bimetallic motors as it happens when A is H_2O_2 solution, M_1 is Au and M_2 is Pt.^{2,11,12} however other ions gradient can also be used for the same propose.¹³

Although there has been much progress on self-electrophoresis propelled micromotors, there are few disadvantages that slow down the progress on these micromotors. One of them is the use of toxic fuels such as H_2O_2 , hydrazine, although some biocompatible motors have been explored such as glucose-propelled. Another main problem of self-electrophoresis is that it does not work at high ionic strength,¹⁴ so the use in biological media is not viable. Furthermore, these motors have low energy efficiency, thus the research has been more focused on new designs and propulsion methods.

In terms of fabrication, the bimetallic nanowire motors are commonly prepared by template-directed electrodeposition as other nanowires.^{2,12} This method employs the pores of the membrane to synthesize the desired tubes and wires composed of different materials such as polymers, metals, semiconductors, and carbons. Because of the monodisperse diameters and large pore densities in

the membrane, similar nanostructures can be mass produced. The final shape of the wire relies on the pore diameter (diameter of the wire) and the charge deposited (proportional to the length of the wire). An alumina membrane with the desired nanosized pores is used and sequentially, different metals are deposited to form striped rod structures. **Figure IV.3** shows the electrochemical template based method for wires fabrication. Firstly, a layer of silver or gold is deposited on one side of the membrane to serve as the working electrode. The membrane is assembled in a teflon plating cell with flat aluminum foil against the metal layer to serve as a conductive contact for subsequent electrodeposition. Usually, a sacrificial layer of copper or silver is first deposited, followed by sequential electrodeposition of the desired materials. The silver or gold working surface and the sacrificial layers are removed by mechanical polishing or chemical etching. Finally, the alumina membrane is dissolved in NaOH solution and the nanowire motors can be obtained after rinsing steps.

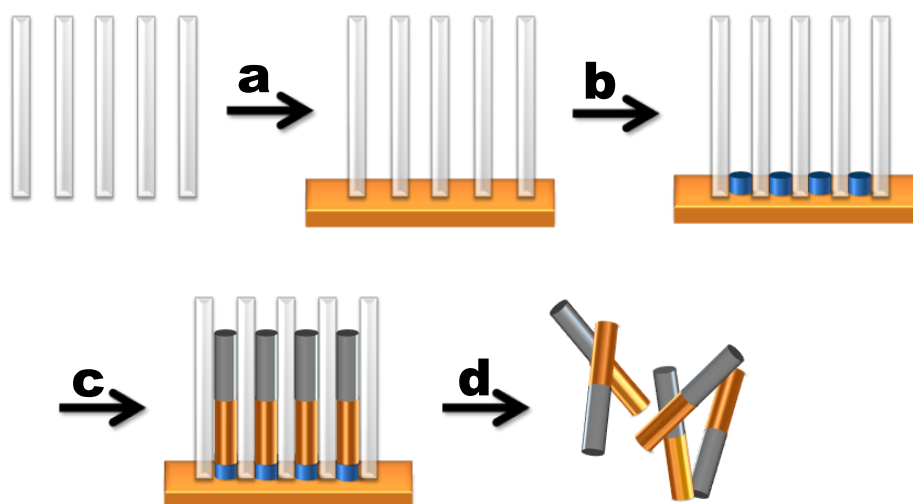


Figure IV.3. Synthesis of nanowire motors. **(a)** Sputtering of a gold or silver layer on the membrane template. **(b)** Electrodeposition of a sacrificial layer. **(c)** Sequential electrodeposition of the desired materials. **(d)** Removal of the working surface and sacrificial layers and dissolution of the membrane

The main application of these micromotors has been the cargo-towing and delivery.^{15,16} In applications in chemical sensing, only few works have been reported. The Ag (I) ion determination in water in the range between 0.5 to 100 μM ¹¹ and the detection of DNA and bacterial ribosomal RNA down to the 40 attomol level.¹⁷

Bubble propulsion

Bubble propulsion was the first reported mechanism of locomotion for micromotors. This propulsion mechanism is based on the generation of a gas by a chemical reaction, which allows the motion of the motor. The more used strategy has been the bubbling upon rapid breakdown of hydrogen peroxide into water and oxygen by the motor itself in the presence of one or more transition metals (e.g., platinum, silver, manganese...). However, more environmental-free strategies are starting to be used suggesting the use of water as fuel in presence of magnesium¹⁸ or gallium/aluminum as catalyst in the motor¹⁸. Another fuel employed is hydrochloric acid for its use for future *in-vivo* applications in the acid media of the stomach¹⁹ in presence of zinc-based motors²⁰ to generate in both cases hydrogen bubbling.

In the literature, tubular micromotors^{21,22} and Janus particles⁶ are the main motors found using these propulsion methods. Furthermore, the tubular micromotors are usually fabricated by template electrodeposition or rolled-up strategies.

In this Thesis, we are going to focus on tubular micromotors. Such microengines rely on the propulsion of oxygen bubbles generated on the inner surface by catalytic decomposition of H_2O_2 . The bubble recoiling mechanism provides these micromotors with higher speed^{23,24} and lower problem using biological media or higher ionic strength^{25,26} than self-electrophoresis wire-based motors as well as greater towing ability,^{9,27} thus they have been highly applied in practical biomedical and environmental applications.²⁸⁻³⁰

Figure IV.4 shows the electrodeposition method for fabricating microtube engines. Cyclopore polycarbonate (PC) membrane, which consists in a symmetrical double-cone pore structure, is used to electrodeposit the asymmetric microtubes. The procedure is the same as that for preparing nanowires, first a gold layer is sputtered for acting as working electrode. Afterwards a monomer such as aniline, 3,4-ethylenedioxythiophene, pyrrol, or other conductive electroactive monomers are electropolymerized.²¹ They are deposited on the walls of the PC membrane, creating a hollow truncated cone. Then, a layer of platinum is subsequently deposited, and bilayer polyaniline (PANI)/Pt, polypyrrol (PPy)/Pt, poly-3,4-ethylenedioxythiophene (PEDOT)/Pt microtubes is formed. The resulting microtubes are conical in shape with lengths of several micrometers and diameters depending on the pore size of the membrane template (1, 2, 5 μm).³¹ The microtube engines fabricated by this method exhibit ultrafast speed and require a very low concentration of hydrogen peroxide fuel.

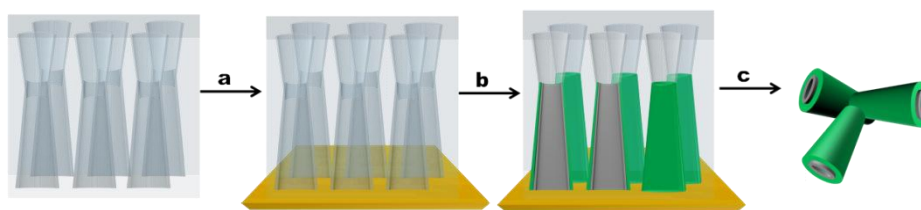


Figure IV.4. Synthesis of tubular conical motors. **(a)** Sputtering of a gold or silver layer on the membrane template. **(b)** Sequential electrodeposition of an outer polymer layer (green) and an inner platinum layer (grey). **(c)** Removal of the sputter layer and dissolution of the membrane

The other fabrication strategy, rolled-up nanotechnology, pioneered by Schmidt employs strain engineering to prepare microtube motors from deposited films.^{22,32} Its nature is more complex and more expensive than the electrochemical fabrication but considerable efforts have been devoted to simplify the rolled-up process and reducing its cost. The technique relies on the deposition on a photoresist sacrificial layer patterned by photolithography of a prestressed nanomembrane. Different layers of materials are deposited by a tilted physical vapor deposition process controlling temperature and deposition rate, together with the stress evolution during deposition, to create the strain gradient needed for the rolling process. By removal of the sacrificial layer, the deposited nanomembrane rolls into a microtube. Microtubes with different opening diameters ranging from 1 to 30 μm can be obtained by changing the thickness and the built-in strain of the nanomembranes.³³ The lengths of the microtube engines are in the range of hundred micrometers. The order of the layers in the final microtube is, therefore, controlled by simply depositing from the outer to the inner the layers on top of the nanomembrane.

The mechanism of propulsion in the tubular micromotors is based on the detachment of the bubbles generated on the inner surface of the tube, propelling the motors through a recoil force, see **Figure IV.5**. The fuel, peroxide, enters the microtubes through the small opening, then the bubble generation results from the catalytic decomposition of H_2O_2 into O_2 along the inner wall of micromotors. The produced oxygen coalesces into bubbles which grow and expand into the cavity of the tube, and then diffuses and migrates toward the larger opening of the micromotor (due to the pressure differential caused by the asymmetry of the conical tube). The conical shape of the microtube

assists the unidirectional bubble expansion and the expelled bubbles produce a force in the opposite direction resulting in the movement of the microtube.^{34,35} Due to the hydrophobic character of the platinum surface cationic (sodium cholate) or anionic (sodium dodecyl sulfate) surfactants are used to facilitate the fuel filling. Also, they reduce the surface tension, stabilize the bubbles and reduce their size.^{7,36}

Since each micromotor is itself an engine that converts chemical energy into movement, they exhibit autonomous and uncontrolled trajectories (linear, circular, spiral...). However, it is possible to impart directionality via magnetically guided movement of the micromotors. Thus, a short of ferromagnetic material (nickel) layer is incorporated in the structure. The new design can be magnetized transversely in a direction perpendicular to the motor axis by an external magnetic field. Then, the direction of the motors may be remotely controlled using a magnet or a magnetic field.³⁷ It is worth mentioning that the magnetic field is exclusively employed for controlling the direction of the motion and does not influence the speed of the motors.

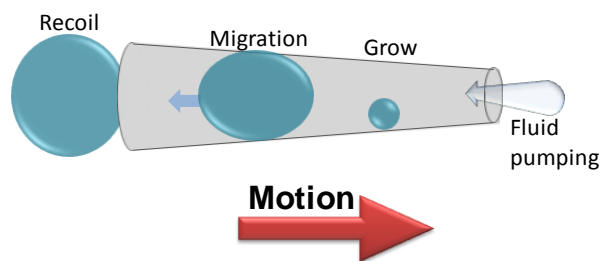


Figure IV. 5. Schematic of bubbling principle. From right to left, grow of oxygen bubble, migration to the large opening and recoiling. Motion is against the bubble flow

This group of micromotors has been not only used in cargo-release approaches, but also they have been highly developed in both clinical and environmental applications as stated before.

Furthermore, in the framework of this Thesis, as analytical tools in (bio-)-sensing, the use of micromotors is still in its beginning. Micromotors may have some advantages over conventional electrochemical or optical sensors, such as no electrical interferences, and operation in a wireless manner, using low amount of sample. However, among its drawbacks, they still present poor reproducibility.

Indeed, these motors have been mostly used for detection of heavy metals,^{38,39} inorganic electrolytes present in blood,⁴⁰ organic compounds such as dimethyl sulfoxide,⁴¹ uric acid,⁴² blood proteins such as bovine serum albumin, γ -globulin, and glucose oxidase enzymes,⁴³ amino acids containing thiol groups, for example, cysteine, serine, and methionine, peptides such as glutathione,⁴¹ protein⁴⁴ and DNA.⁴⁵

Ultrasound propulsion

The disadvantages of bubble-propelled micromotors such as the generation of bubbles sometimes not desirable, the high use of toxic fuels, and the necessity of new micromotors for *in-vivo* applications with motion in biocompatible media, with high viscosity or high ionic strength, brought to the scientist the necessity of new biocompatible energy and externally driven micromotors. Among the ways of achieving this motion, acoustic energy is an interesting candidate for moving micromotors in fluids because this acoustic high frequency sound waves present minimal deleterious effects on biological systems.

The first autonomous micromotors propelled by ultrasound (US) frequency were based on metallic nanowires (synthesis described before, see **Figure IV.3**) which showed speeds around $200 \mu\text{m s}^{-1}$. The template-assisted electrodeposited micromotors are autonomously propelled in water using a home-made cell, which consists in a transducer connected to the generator of acoustic waves.⁴⁶ Mallouk's group demonstrated that by applying a MHz constant frequency to the cell, all the particles in solution levitates in a unique nodal plane (in axis z) where the pressure is minimum, so the particles are trapped in that z plane and are only allowed to move in x-y plane (see **Figure IV.6.A**). In that plane, the micromotors form patterns in the levitation plane as a result of nodes and anti-nodes within the plane. Consequently, when turning off the acoustic energy results in sinking the motors to the bottom of the cell.⁴⁷

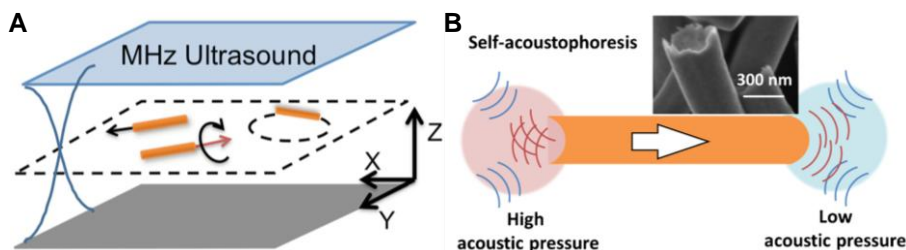


Figure IV.6. US propelled micromotors. **(A)** Microwires are propelled by an ultrasonic standing wave generating a levitation plane where the microwires move. **(B)** Scheme of explanation of the acoustophoresis mechanism on the asymmetrically shaped metallic microwires⁴⁶

Interestingly, depending on the material composition, size, shape and compressibility of the particle, the behavior under acoustic field dramatically change. Therefore, only some materials can be autonomously propelled under ultrasound:

- Microparticles with sizes bigger than 1 μm . Sizes smaller than the wavelength of the soundwaves can hardly be manipulated.⁴⁷
- Particles with densities bigger than the medium and low compressibility, rigid, such as metallic structures, polymers or cells only levitate and aggregate in the levitation plane.^{46,48}
- The microparticles should present certain asymmetry.^{46,49}

This last characteristic is of great importance because it allows the uneven distribution of the acoustic pressures in the fluid that is going to permit the autonomous motion. **Figure IV.6B** shows metallic microwires fabricated by template-assisted electrodeposition. Regardless of the metal deposited, the end grown immediately after deposition of the sacrificial layer, the first step in the electrodeposition of nanowires present a concave shape while the

other end is slightly convex. Thus, this asymmetric structure of the motors leads to an asymmetric distribution of the acoustic pressure (pressure gradient) from the dispersion of the incident acoustic waves at the motor surface, high at the concave end and low at the convex end.

The main disadvantages of these micromotors are that the propulsion mechanism is not well understood and the set up is still home-made and has not been completely optimized; besides the motion behavior is still difficult to predict.

The main applications of these ultrasound-based motors are in biological or clinical fields, in cargo-towing and release of drugs⁵⁰ or bacteria *E. Coli* and *S. Aureus*.⁴⁹ From this later work, nanomotors coupling the antibacterial activity of lysozyme with rapid movement were proved toward efficient bacteria killing.⁵¹

Recently, acoustically powered gold nanorods were propelled inside cells showing the possibilities of these motors in biomedical research.⁵² In terms of chemical sensing, and incorporating the capability of nanowires to penetrate the cell, a microRNA-21 detector based on the quenching of fluorescence by graphene (on/off fluorescence signal) into living cells have been performed.⁸

Interestingly, Wang's group developed a novel biocompatible red blood cell-based motors. The magnetic iron oxide nanoparticles were internalized in the red blood cells and they were aggregated within the cells. The aggregated magnetic nanoparticles within the red blood cell provided the required density necessary to achieve an acoustic response after applying the US field. The red blood cell membrane serves as an intrinsic shield to protect the magnetic nanoparticles

from etching by coexisting ions (e.g., chlorides, phosphates) in the blood and prevent uptake by immune cells such as macrophages. Thus, they display remarkable biocompatibility essential for practical biomedical uses.⁵³

Furthermore, in another work, these red blood cell motors, which were able to convert acoustic energy into motion due to the uneven distribution of the magnetic nanoparticles within the red blood cell, incorporated imaging fluorescence particles, quantum dots and chemotherapy drug within the cell, towards theranostic applications. They were also explored as the first example of US motors in microfluidic channels for mimetizing the blood vessels. Thus, the performance of the theranostic red blood cell motors was proved applying US for the autonomous movement and controlling the direction of the multicargo-loaded red blood cell micromotor in different microfluidic chip by changing the orientation of a magnet.⁵⁴

Another ultrasound-based motor is the one based on the vaporization of perfluorocarbon (PFC) loaded emulsions. PFC emulsion are stable under physiological conditions, however, the US pressure wave break the emulsion and vaporize the molecule, which presents a low boiling point. By applying focalized short pulses (4.4 ms) of high pressure (3.8 MPa) to the emulsion, the gas expands firing the micromotor. Kagan et al. developed a conically shaped rolled-up microtube loaded with PFCs with potential use in drug delivery and penetration into tissues. The propulsion is ultimately provided by the ejection of gas bubbles of the vaporized PFC, therefore, its mechanism is the same than other bubble-propelled micromotors.⁵⁵

Other propulsion methods

Other propulsion methods are based on external fields such as, magnetic or electric fields or external stimuli such as light, pH or temperature yielding the respective propulsion methods.

As an example, magnetically driven micromotors are a group of highly explored motors. The propulsion mechanism is based on magnetic forces and torques, therefore, helical-shape micromotors have been explored by this propulsion mechanism.^{56,57} Furthermore, the use of stimuli responsive mechanisms offers the possibility for smart behaviors such as autonomous responses in specific environments. In this sense, hydrogels are some of the most employed materials in these devices since they are able to swell significantly in response to some of these stimuli generating the energy and force to perform the expected mechanical tasks.⁵⁸

IV.1.3. Nanomaterials in micromotors

We have presented during this Thesis the importance of the nanomaterials being part of electrochemical (bio-)-sensors (**Chapter II**) and electrochemical microfluidic chips (**Chapter III**). The main question is if it is possible to include these nanomaterials in the micromotors. The similarities in the scale between the nanomaterials and the micromotors make the fabrication of these machines with nanomaterials or nanostructures an easy coupling, due to the similarities in the scale, so the immediate answer would be yes.

Nanomaterials, as we have described in **Chapter II**, present a large surface area, this feature would improve the final characteristics of the tubular bubble-propelled micromotors whether they comprise outer or inner layers. In the case of tubular micromotors, the nanomaterials in the outer layer will enhance the contact points for generating more interaction with cargos improving the interaction between the surface of the motor and the target cargo to be towed. On the other hand, being part of the inner layer, they will enhance the probable chemical reaction with the fuel, improving the motor speed.

More interesting features of some nanomaterials such as carbon or metallic nanomaterials is the high electrical and thermal conductivities, the former one is going to let an easy fabrication using electrodeposition techniques, as discussed before in the template-based electrochemical manufacturing of tubular micromotors or nanowires.

Furthermore, the excellent physical features of nanomaterials as discussed in the case of graphene, extraordinary elasticity and

mechanical strength will provide the final motor of the inherent properties of the nanomaterial.

Consequently, nanomaterials are excellent candidates for developing new applications using nanomaterial-based micromotors.

Focused on carbon nanomaterials in micromotors, in the literature, these previous ideas have been started to be exploited.

The first example was the use of CNT in the Pt catalytic segment of a Au/Pt nanowire, which highly improved the speed of the self-electrophoresis propelled motor.¹² Then, CNTs were included in Pt nanoparticles for improving the speed of tubular micromotors.⁵⁹

On the other hand, in the case of graphene, the literature presents different examples of fabrication of tubular micromotors using this material as the outer layer. Thus, a complex synthesis of multilayered GO/Ti/Pt tubular microengine, by roll-up approach was fabricated with 1-2 μm diameter and 10-20 μm length.⁶⁰ The hydrothermal reduction of GO on a Cu wire contained in a glass pipeline and the posterior functionalization with metals in the outer of inner walls of the previously synthesized graphene tube was described.⁶¹ A different micromotor synthesis based on a Janus particle micromotor based on graphene-iridium,⁶² an hydrothermal synthesis of MnO_2 /graphene⁶³ and a balloon-like MnOx -graphene crumples synthesized via an ultrasonic spray pyrolysis method are found to move under hydrogen peroxide.⁶⁴

IV.1.4. Outlook and future perspectives

Artificial micromotors have appeared in the chemical sensing scene as a new tool for diverse medical and environmental applications, among other fields. These smart devices are capable to cooperate and communicate for achieving a demanded task. Particularly attractive is the impressive progress in the great diversity of propulsion methods, which still requires further improvement due to the disadvantages needed to be enhanced.

Indeed, for future development of fabrication methods the tendency should be the development of easy and cost-effective approaches to produce large quantities of motors in order to improve the reproducibility in the sensing and the uniformity of the structure. Thus, the morphology and final structure of the motor is going to determine the movement.

The main limitation currently is the few fuels used in the proof-of-concept applications (mainly H_2O_2 , with certain toxicity) and thus, the low compatibility with living systems. Although some attempts are reported in the literature, mainly using US propulsion mechanisms, they are still in its infancy.

The inspiration and creativity in the design of new micromachines is, consequently, key for enhancing the motion of the future motors as well as the materials used. Nanomaterials are then starting to appear for improving the physical properties (mechanical strength, resistance) and chemical properties for posterior functionalization or interaction with target molecules or particles and of course, enhancing the speed of the micromotor. Therefore, artificial micromotors are expected to advance in material composition and into more practical and sophisticated applications.

The inspiration in the real macroscopic world full of interesting engines could launch the emerging and exciting future technological breakthroughs of micromotors.

IV. 1.5. References

1. Ozin, G.A.; Manners, I.; Fournier-Bidoz, S.; Arsenault, A. Dream Nanomachines. *Adv. Mater.* **2005**, *17*, 3011-3018.
2. Paxton, W. F.; Kistler, K. C.; Olmeda, C. C.; Sen, A.; St. Angelo, S. K.; Cao, Y.; Mallouk, T. E.; Lammert, P. E.; Crespi, V. H. Catalytic Nanomotors: Autonomous Movement of Striped Nanorods. *J Am Chem Soc* **2004**, *126*, 13424-13431.
3. Hänggi, P.; Marchesoni, F. Artificial Brownian motors: Controlling transport on the nanoscale. *Rev. Mod. Phys.* **2009**, *81*, 387.
4. Wang, W.; Duan, W.; Ahmed, S.; Mallouk, T. E.; Sen, A. Small power: Autonomous nano- and micromotors propelled by self-generated gradients. *Nano Today* **2013**, *8*, 531-554.
5. Guix, M.; Mayorga-Martinez, C.C.; Merkoçi, A. Nano/Micromotors in (Bio)chemical Science Applications. *Chem. Rev.* **2014**, *114*, 6285-6322.
6. Sánchez, S.; Soler, L.; Katuri, J. Chemically Powered Micro- and Nanomotors. *Angew. Chem. Int. Ed.* **2015**, *54*, 1414-1444.
7. Wang, J. *Nanomachines: Fundamentals and Applications*; Wiley- VCH: Weinheim, Germany, 2013.
8. Esteban-Fernandez de Avila, B.; Martin, A.; Soto, F.; Lopez-Ramirez, M. A.; Campuzano, S.; Vasquez-Machado, G. M.; Gao, W.; Zhang, L.; Wang, J. Single Cell Real-Time miRNAs Sensing Based on Nanomotors. *Acs Nano* **2015**, *9*, 6756-6764.
9. García, M.; Orozco, J.; Guix, M.; Gao, W.; Sattayasamitsathit, S.; Escarpa, A.; Merkoçi, A.; Wang, J. Micromotor-based lab-on-chip immunoassays. *Nanoscale* **2013**, *5*, 1325-1331.
10. Yoshizumi, Y.; Date, Y.; Ohkubo, K.; Yokokawa, M.; Suzuki, H. In *In Bimetallic micromotor autonomously movable in biofuels*; Micro Electro Mechanical Systems (MEMS), IEEE 26th International Conference. **2013**, pp 540-543.
11. Kagan, D.; Calvo-Marzal, P.; Balasubramanian, S.; Sattayasamitsathit, S.; Manesh, K. M.; Flechsig, G.; Wang, J. Chemical Sensing Based on Catalytic Nanomotors: Motion-Based Detection of Trace Silver. *J. Am. Chem. Soc* **2009**, *131*, 12082-12083.
12. Laocharoensuk, R.; Burdick, J.; Wang, J. Carbon-Nanotube-Induced Acceleration of Catalytic Nanomotors. *Acs Nano* **2008**, *2*, 1069-1075.

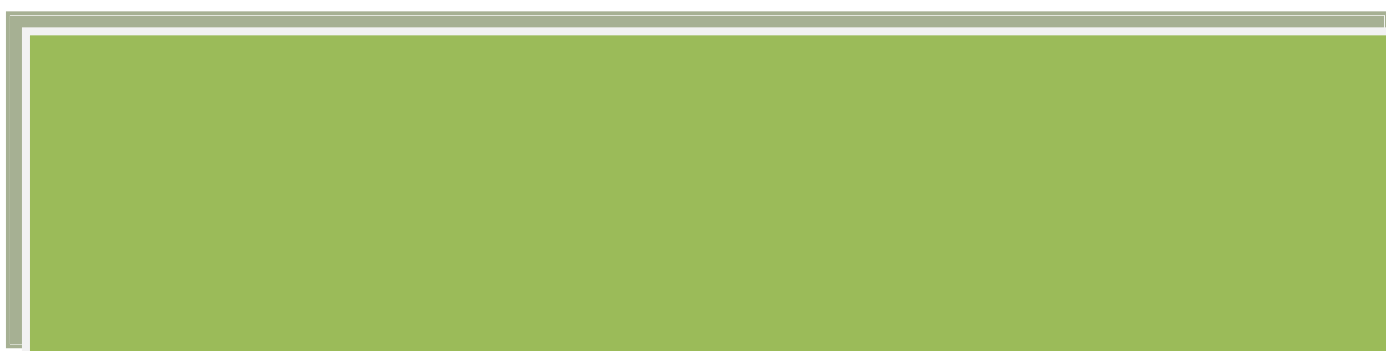
13. Ibele, M.E.; Wang, Y.; Kline, T.R.; Mallouk, T.E.; Sen, A. Hydrazine Fuels for Bimetallic Catalytic Microfluidic Pumping. *J. Am. Chem. Soc.* **2007**, *129*, 7762-7763.
14. Paxton, W. F.; Baker, P. T.; Kline, T. R.; Wang, Y.; Mallouk, T. E.; Sen, A. Catalytically Induced Electrokinetics for Motors and Micropumps. *J. Am. Chem. Soc.* **2006**, *128*, 14881–14888.
15. Kagan, D.; Laocharoensuk, R.; Zimmerman, M.; Clawson, C.; Balasubramanian, S.; Kang, D.; Bishop, D.; Sattayasamitsathit, S.; Zhang, L.; Wang, J. Rapid Delivery of Drug Carriers Propelled and Navigated by Catalytic Nanoshuttles. *Small* **2010**, *6*, 2741-2747.
16. Sundararajan, S. P.; Lammert, E.; Zudans, A. W.; Crespi, V. H.; Sen, A. Catalytic Motors for Transport of Colloidal Cargo. *Nano Lett.* **2008**, *8*, 1271–1276.
17. Wu, J.; Balasubramanian, S.; Kagan, D.; Manesh, K.M.; Campuzano, S.; Wang, J. Motion-based DNA detection using catalytic nanomotors. *Nat. Commun.* **2010**, *1*, 36.
18. Gao, W.; Pei, A.; Wang, J. Water-driven micromotors. *ACS Nano* **2012**, *6*, 8432-8438.
19. Gao, W.; Feng, X.; Pei, A.; Gu, Y.; Li, J.; Wang, J. Seawater-driven magnesium based Janus micromotors for environmental remediation. *Nanoscale* **2013**, *5*, 4696–4700.
20. Gao, W.; Dong, R.; Thamphiwatana, S.; Li, J.; Gao, W.; Zhang, L.; Wang, J. Artificial Micromotors in the Mouse's Stomach: A Step toward *in Vivo* Use of Synthetic Motors. *ACS Nano* **2015**, *9*, 117–123.
21. Gao, W.; Sattayasamitsathit, S.; Orozco, J.; Wang, J. Highly Efficient Catalytic Microengines: Template Electrosynthesis of Polyaniline/Platinum Microtubes. *J. Am. Chem. Soc.* **2011**, *133*, 11862-11864.
22. Mei, Y.; Solovev, A. A.; Sanchez, S.; Schmidt, O. G. Rolled-up nanotech on polymers: from basic perception to self-propelled catalytic microengines. *Chem. Soc. Rev.* **2011**, *40*, 2109-2119.
23. Sanchez, S.; Ananth, A. N.; Fomin, V. M.; Viehrig, M.; Schmidt, O.G. Superfast Motion of Catalytic Microjet Engines at Physiological Temperature. *J. Am. Chem. Soc.* **2011**, *133*, 14860–14863.
24. Gao, W.; Sattayasamitsathit, S.; Wang, J. Catalytically Propelled Micro-/Nanomotors: How Fast Can They Move? *Chem. Rec.* **2012**, *12*, 224-231.
25. Zhao, G.; Viehrig, M.; Pumera, M. Challenges of the movement of catalytic micromotors in blood. *Lab Chip* **2013**, *13*, 1930–1936.

26. Gao, W.; Sattayasamitsathit, S.; Orozco, J.; Wang, J. Efficient bubble propulsion of polymer-based microengines in real-life environments. *Nanoscale* **2013**, *5*, 8909-8914.
27. Wang, J. Cargo-Towing Synthetic Nanomachines: Towards Active Transport in Microchip Devices. *Lab Chip* **2012**, *12*, 1944-1950.
28. Gao, W.; Wang, J. The Environmental Impact of Micro/Nanomachines: A Review. *Acs Nano* **2014**, *8*, 3170-3180.
29. Wang, J.; Gao, W. Nano/Microscale Motors: Biomedical Opportunities and Challenges. *Acs Nano* **2012**, *6*, 5745-5751.
30. Soler, L.; Magdanz, V.; Fomin, V. M.; Sanchez, S.; Schmidt, O. G. Self-Propelled Micromotors for Cleaning Polluted Water. *Acs Nano* **2013**, *7*, 9611-9620.
31. Gao, W.; Sattayasamitsathit, S.; Uygum, A.; Pei, A.; Ponedal, A.; Wang, J. Polymer-based tubular microbotos: role of composition and preparation. *Nanoscale* **2012**, *4*, 2447-2453.
32. Solovev, A. A.; Mei, Y.; Bermudez Urena, E.; Huang, G.; Schmidt, O. G. Catalytic Microtubular Jet Engines Self-Propelled by Accumulated Gas Bubbles. *Small* **2009**, *5*, 1688-1692.
33. Harazim, S. M.; Wang, X.; Schmidt, C. K.; Sanchez, S.; Schmidt, O. G. Fabrication and applications of large arrays of multifunctional rolled-up SiO/SiO₂ microtubes. *J. Mater. Chem.* **2012**, *22*, 2878-2884.
34. Li, J.; Huang, G.; Ye, M.; Li, M.; Liu, R.; Mei, Y. Dynamics of catalytic tubular microjet engines: Dependence on geometry and chemical environment. *Nanoscale* **2011**, *3*, 5083-5089.
35. Li, L.; Wang, J.; Li, T.; Songa, W.; Zhanga, G. Hydrodynamics and propulsion mechanism of self-propelled catalytic micromotors: model and experiment. *Soft Matter* **2014**, *10*, 7511-7518.
36. Mohammadi, R.; Wassink, J.; Amirfazli, A. Effect of Surfactants on Wetting of Super-Hydrophobic Surfaces. *Langmuir* **2004**, *20*, 9657-9662.
37. Kline, T.R.; Paxton, W. F.; Mallouk, T.E.; Sen, A. Catalytic Nanomotors: Remote-Controlled Autonomous Movement of Striped Metallic Nanorods. *Angew. Chem. Int. Ed.* **2005**, *44*, 744-746.
38. Moo, J.G.S.; Wang, H.; Zhao, G.; Pumera, M. Biomimetic Artificial Inorganic Enzyme-Free Self-Propelled Microfish Robot for Selective Detection of Pb²⁺ in Water. *Chem-Eur. J.* **2014**, *20*, 4292-4296.
39. Orozco, J.; Garcia-Gradilla, V.; D'Agostino, M.; Gao, W.; Cortes, A.; Wang, J. Artificial Enzyme-Powered Microfish for Water-Quality Testing. *Acs Nano* **2013**, *7*, 818-824.

40. Wang, H.; Zhao, G.; Pumera, M. Blood electrolytes exhibit a strong influence on the mobility of artificial catalytic microengines. *Phys. Chem. Chem. Phys.* **2013**, *15*, 17277-17280.
41. Zhao, G. J.; Sanchez, S.; Schmidt, O. G.; Pumera, M. Poisoning of bubble propelled catalytic micromotors: the chemical environment matters. *Nanoscale* **2013**, *5*, 2909-2914.
42. Wang, H.; Zhao, G.; Pumera, M. Blood metabolite strongly suppresses motion of electrochemically deposited catalytic self-propelled microjet engines. *Electrochem. Commun.* **2014**, *38*, 128-130.
43. Wang, H.; Zhao, G.; Pumera, M. Blood Proteins Strongly Reduce the Mobility of Artificial Self-Propelled Micromotors. *Chem-Eur J* **2013**, *19*, 16756-16759.
44. Morales-Narváez, E.; Guix, M.; Medina-Sánchez, M.; Mayorga-Martinez, C.C.; Merkoçi, A. Micromotor Enhanced Microarray Technology for Protein Detection. *Small* **2014**, *10*, 2542-2548.
45. Kagan, D.; Campuzano, S.; Balasubramanian, S.; Kuralay, F.; Flechsig, G.U.; Wang, J. Functionalized Micromachines for Selective and Rapid Isolation of Nucleic Acid Targets from Complex Samples. *Nano Lett.* **2011**, *11*, 2083-2087.
46. Wang, W.; Castro, L A.; Hoyos, M.; Mallouk, T. E. Autonomous Motion of Metallic Microrods Propelled by Ultrasound. *Acs Nano* **2012**, *6*, 6122-6132.
47. Rao, K. J.; Li, F.; Meng, L.; Zheng, H.; Cai, F.; Wang, W. A Force to Be Reckoned With: A Review of Synthetic Microswimmers Powered by Ultrasound. *Small* **2015**, *11*, 2836-2846.
48. Xu, T.; Soto, F.; Gao, W.; Dong, R.; Garcia-Gradilla, V.; Magan, E.; Zhang, X.; Wang, J. Reversible Swarming and Separation of Self-Propelled Chemically Powered Nanomotors under Acoustic Fields. *J Am Chem Soc* **2015**, *137*, 2163-2166.
49. Garcia-Gradilla, V.; Orozco, J.; Sattayasamitsathit, S.; Soto, F.; Kuralay, F.; Pourazary, A.; Katzenberg, A.; Gao, W.; Shen, Y.; Wang, J. Functionalized ultrasound-propelled magnetically guided nanomotors: Toward practical biomedical applications. *Acs Nano* **2013**, *7*, 9232-9240.
50. Garcia-Gradilla, V.; Sattayasamitsathit, S.; Soto, F.; Kuralay, F.; Yardimci, C.; Wiitala, D.; Galarnyk, M.; Wang, J. Ultrasound-Propelled Nanoporous Gold Wire for Efficient Drug Loading and Release. *Small* **2014**, *10*, 4154-4159.
51. Kiristi, M.; Singh, V. V.; Esteban-Fernández de Ávila, B.; Uygun, M.; Soto, F.; Uygun, D. A.; Wang, J. Lysozyme-Based Antibacterial Nanomotors. *Acs Nano* **2015**, *9*, 9252-9259.
52. Wang, W.; Li, S.; Mair, L.; Ahmed, S.; Huang, T. J.; Mallouk, T. E. Acoustic Propulsion of Nanorod Motors Inside Living Cells. *Angew. Chem. Int. Ed.* **2014**, *53*, 3201-3204.

53. Wu, Z.; Li, T.; Li, J.; Gao, W.; Xu, T.; Christianson, C.; Gao, W.; Galarnyk, M.; He, Q.; Zhang, L.; Wang, J. Turning Erythrocytes into Functional Micromotors. *Acs Nano* **2014**, *8*, 12041–12048.
54. Wu, Z.; Esteban-Fernández de Ávila, B.; Martín, A.; Christianson, C.; Gao, W.; Thamphiwatana, S. K.; Escarpa, A.; He, Q.; Zhang, L.; Wang, J. RBC micromotors carrying multiple cargos towards potential theranostic applications. *Nanoscale* **2015**, *7*, 13680-13686.
55. Kagan, D.; Benchimol, M. J.; Claussen, J. C.; Chuluun-Erdene, E.; Esener, S.; Wang, J. Acoustic Droplet Vaporization and Propulsion of Perfluorocarbon-Loaded Microbullets for Targeted Tissue Penetration and Deformation. *Angew. Chem. Int. Ed.* **2012**, *51*, 7519-7522.
56. Li, J.; Sattayasamitsathit, S.; Dong, R.; Gao, W.; Tam, R.; Feng, X.; Ai, S.; Wang, J. Template electrosynthesis of tailored-made helical nanoswimmers. *Nanoscale* **2014**, *6*, 9415-9420.
57. Schamel, D.; Pfeifer, M.; Gibbs, J. G.; Miksch, B.; Mark, A. G.; Fischer, P. Chiral Colloidal Molecules And Observation of The Propeller Effect. *J. Am. Chem. Soc.* **2013**, *135*, 12353-12359.
58. Breger, J. C.; Yoon, C.; Xiao, R.; Kwag, H. R.; Wang, M. O.; Fisher, J.P.; Nguyen, T.D.; Gracias, D. H. Self-Folding Thermo-Magnetically Responsive Soft Microgrippers. *ACS Appl. Mater. Interfaces* **2015**, *7*, 3398-3405.
59. Li, Y.; Wu, J.; Xie, Y.; Ju, H. An efficient polymeric micromotor doped with Pt nanoparticle@carbon nanotubes for complex bio-media. *Chem. Commun.* **2015**, *51*, 6325-6328.
60. Yao, K.; Manjare, M.; Barrett, C. A.; Yang, B.; Salguero, T. T.; Zhao, Y. Nanostructured Scrolls from Graphene Oxide for Microjet Engines. *J. Phys. Chem. Lett.* **2012**, *3*, 2204-2208.
61. Hu, C.; Zhao, Y.; Cheng, H.; Wang, Y.; Dong, Z.; Jiang, C.; Zhai, X.; Jiang, L.; Qu, L. Graphene Microtubings: Controlled Fabrication and Site-Specific Functionalization. *Nano Lett.* **2012**, *12*, 5879-5884.
62. Wang, H.; Sofer, Z.; Eng, A. Y. S.; Pumera, M. Iridium-Catalyst-Based Autonomous Bubble-Propelled Graphene Micromotors with Ultralow Catalyst Loading. *Chem.-Eur. J.* **2014**, *20*, 14946-14950.
63. Feng, X.; Zhang, Y.; Li, Y.; Huang, Z.; Chen, S.; Ma, Y.; Zhang, L.; Wang, L.; Yan, X. Graphene-based Highly Efficient Micromotors. *Chem. Lett.* **2015**, *44*, 399-401.
64. Chen, X.; Wu, G.; Lan, T.; Chen, W. Autonomous micromotor based on catalytically pneumatic behavior of balloon-like MnOx-graphene crumples. *Chem. Commun.* **2014**, *50*, 7157-7159.

IV.2. Chemically powered graphene micromotors



IV.2.1. Introduction and objectives

As it has been stated in the previous section **IV.1**, the motion of synthetic microscale objects has inspired considerable research efforts over the past decade.¹⁻¹⁰ Particular attention has been given to chemically powered micromotors that exhibit self-propulsion in the presence of hydrogen peroxide fuel.^{1,2,5,9} Several approaches have been explored to prepare different tubular micromotors^{5,6,11,12} and Janus microparticles,^{13,14} including top-down photolithography, e-beam evaporation and stress-assisted rolling of functional nanomembranes on polymers. The complexity and high cost of these fabrication processes led to the development of template electrodeposition methods for preparing catalytic nanowire motors^{1,15} and microtubular motors.¹⁶⁻¹⁹ Bubble-propelled microtube motors are particularly attractive for diverse real-life applications owing to their efficient locomotion in diverse (salt-rich) matrices. Particular attention has been given to the template-assisted electrodeposition of polymer-Pt tubular micromotors¹⁶⁻¹⁹ or bimetallic Cu-Pt microwires.¹⁷ The versatility of template electrosynthesis methods allows explorations of micromotors based on new compositions and structures, with improved catalytic performance and new functionalities essential for diverse new practical applications.

In addition, it has been widely commented in this Thesis that graphene has captured the attention of the scientific community because of its outstanding material's properties, already described in section **II.1**, including high electrical and thermal conductivities, large surface area, extraordinary elasticity and mechanical strength.²⁰⁻²² Due to these material characteristics, graphene is an attractive candidate for advanced micromachines applications. Yao et al. described a multilayered GO/Ti/Pt tubular micromotor, using e-

beam evaporation to coat the previously deposited GO with Ti and Pt that spontaneously roll into full or partial scrolls of 1-2 μm diameter and 10-20 μm length.²³ Hu et al. illustrated millimeter size graphene tubes, in which GO is hydrothermally reduced and confined on a Cu wire contained in a glass pipeline and selectively functionalized with metals in the outer of inner walls of the previously synthesized graphene tube.²⁴ Pumera's team described a Janus particle micromotor based on graphene-iridium²⁵ and Chen and coworkers showed balloon-like MnOx-graphene crumples synthesized via an ultrasonic spray pyrolysis method.²⁶ Graphene tubes of larger sizes were prepared using CVD²⁷⁻³¹ and other complex strategies.³¹ However, these last examples involving costly preparation of graphene tubes (without inner metal layers) have focused mainly on applications involving flexible actuators, robots, photovoltaic cells and supercapacitors.³²

In this chapter, the main objective has been to demonstrate a greatly simplified template electrodeposition approach for the mass production of highly efficient graphene-based microtubular motors as well as the role of graphene micromotor propulsion. The template-assisted approach for preparing the graphene-based tubular micromotors relies on the electrodeposition of graphene oxide on the inner wall of a polycarbonate membrane by a cyclic voltammetry technique, followed by deposition of the inner porous metal layer (**Figure IV.7**).

IV.2.2. Synthesis and characterization of chemically powered graphene micromotors

A new template electrodeposition protocol for the fabrication of electrochemically reduced graphene oxide (erGO)/metal (platinum (Pt) or gold (Au)) bilayer micromotors was designed as illustrated in **Figure IV.7A**. In a first step (a), GO was electrodeposited on the inner wall of a polycarbonate (PC) membrane by a CV technique, leading to a rapid formation of an electrochemically reduced GO film. GO was electrochemically reduced with a potential cycling at 50 mV s⁻¹ in 0.1 M H₂SO₄ (+0.30 to -1.50 V vs. Ag/AgCl). **Figure IV.7B** shows the cyclic voltammograms obtained during the reduction process (n= 2, 3 and 5 scans, respectively). As it can be seen, the current reduction peak decreases while the potential cycling proceeds, implying a reduction in the graphene structure. The resulting erGO structure is partially modified and the oxygen functionalities are mainly removed.³³ This reduction of oxygen moieties in the graphene surface implies a change in its structure, increasing the sp²-carbons and thus the hydrophobicity of the graphene film. Under these conditions, graphene layers tend to aggregate between them via π - π interactions and within the walls of the PC membrane via hydrophobic interactions.³⁴ This erGO film has higher conductivity than the pure GO, and favors the electrodeposition of a second metallic layer (platinum or gold) using a galvanostatic method (step b in **Figure IV.7A**). The most favorable electrochemical growth conditions of erGO/Pt and erGO/Au micromotors (number of cyclic scans, n=5; Pt deposition, -2 mA, 500 s; Au deposition, -0.90 V to a total charge of 1 C) were optimized for their microtubes bilayer structures.

Figures IV.7B (inset) and **IV.7C** display side-view and cross-view SEM images of the typical 10 μm -length conical erGO/Pt microtubes under the optimized conditions. These images indicate that the resulting micromotors have outer diameters of 5.0 and 4.0 μm and inner opening of 3.8 and 3.2 μm , with a semi-cone angle (δ) of 3.2° . A close examination of such bilayer structure (**Figure IV.7D**) reveals that, unlike common micromotors that exhibit a Pt smooth surface,¹⁶ the Pt layer is composed of granular nanoparticles with average diameters of ~ 200 nm. As will be illustrated below, such Pt structure leads to a dramatically increased catalytic surface area and to an improved propulsion behavior. This nanoparticle-based porous Pt structure can be directly related to the presence of higher boundaries and defects in the graphene thin shell-layer. Similarly, a gold inner layer can be electrodeposited inside the outer erGO tube layer for immobilizing oxygen-generating biocatalytic layers (such as catalase). **Figure IV.7E** displays a SEM image of five template-prepared erGO/Au microtubes. This image illustrates the reproducibility of the method, along with the characteristic conical morphology of the resulting erGO/Au microtubes and an inner opening of 3.9 μm .

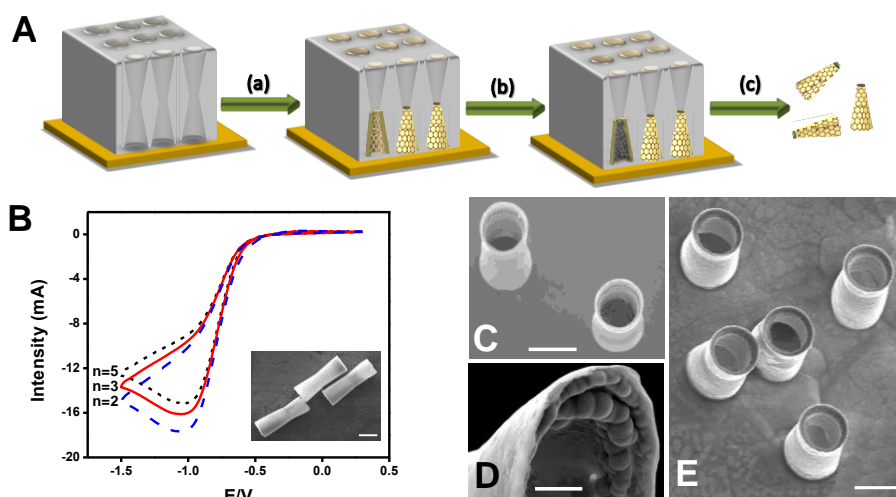


Figure IV.7. Template electrodeposition of graphene/metal tubular micromotors. **(A)** Schematic of the template-based fabrication procedure: (a) electrodeposition of reduced graphene oxide, (b) deposition of Pt or Au layers, (c) removal of the membrane template. **(B)** CVs corresponding to the electrochemical reduction of GO, scans $n = 2$ (dash line), $n = 3$ (solid line) and $n = 5$ (dotted line) and SEM images of the side view of erGO–Pt (inset). **(C)** SEM of top view and **(D)** Pt roughness in erGO–Pt and **(E)** top view in erGO–Au microtubes. Scale bars: (C,E) $5 \mu\text{m}$ and in (D) $1 \mu\text{m}$

The synthesis conditions have a profound effect on the thickness and length of the erGO-based microtubes. From the SEM images displayed in **Figure IV.S1**, it can be seen that the Pt layer plays a critical role in maintaining the shape and mechanical stability of the erGO microtubes. At lower Pt deposition times (100 s, **Figure IV.S1 a**) the graphene tube collapsed because the thin layers lack the strength to retain the open tubular shape after removal of the template. However, when the platinum content is increased, the

resulting bilayer microtube structure is preserved after the template dissolution (**Figure IV.S1 b**). Longer deposition times (1000 s) results in the overgrowth of platinum, which form wires, filling the pores completely and overgrowing over the top of the tubular structure (**Figure IV.S1 c**). Similar results were observed after deposition of different Au layers (not shown). Furthermore, the effect of GO electrodeposition time was evaluated by varying the number of cyclic CV scans from 1 to 10. After two redox scans, a low percentage of the GO is reduced, therefore, a lower content of graphene is deposited on the PC membranes; this leads to less uniform, rougher tubular structures with thicker walls (**Figure IV.S1 d**). erGO/Pt microtubes prepared using 5 scans (**Figure IV.S1 e**) are characterized with a more regular surface morphology and defined conical bilayer microtube structure, which contains a wider opening pore essential to achieve an optimal bubble evolution and speed for practical applications.

Further characterization of the unique surface morphology of the nanoporous metallic layer deposited on erGO was carried out using SEM. **Figure IV.8A, 8B** and **8C** shows the cross-views (a) of the bilayer erGO/Pt, erGO/Au and PANI/Pt structures, respectively. Higher magnification images (b) illustrate that the inner Pt or Au layers display a very rough morphology, as compared to the smooth surface obtained after depositing the metals on common polymer (PANI)-based microtubes prepared under similar conditions (**Figure IV.8B (b)**). Such close examination of the catalytic Pt layer on the outer erGO tube reveals that the Pt surface is composed of granular metal nanoparticles. Similarly, the inner Au layer (shown in **Figure IV.8B**) is characterized with a porous structure, composed of smaller, fine-grain size gold nanoparticles. TEM was carried out to further characterize the size and morphology of the Pt nanoparticles

in erGO microtubes, as displayed in the two images of **Figure IV.8D** and **Figure IV.S2, a**. It is observed that the Pt layer is composed of granular metal nanoparticles with average sizes ranging from 10 to 50 nm. For comparison, TEM images PANI/Pt micromotors (See **Figure IV.S2, b**) reveal the thin film structure of the Pt layer, with the absence of nucleation sites. This structure can be attributed to the presence of a high density of intra-grain and grain-boundary defects in the erGO layer. The intermittent layers of erGO that form the shell of the micromotor implies the presence of large number of edges and defects in this thin carbon film. Pt and Au layers thus tend to nucleate and grow from the defects of erGO sheets, leading to such porous structures.³⁵⁻³⁷ Previous reports also suggest that carbon atoms with dangling bond or oxygen functional groups (such as that one existing in our erGO layer) enhanced the interaction between graphene and Pt clusters, stabilizing the porous structure and improving its catalytic properties. Anchoring metallic nanocatalysts onto erGO porous structure has been shown to enhance the active surface area and increase the effective transport of the reactants.³⁸ The energy dispersive X-ray spectroscopy (EDX) mapping analysis, depicted in **Figure IV.8D**, clearly shows the presence of either Pt or Au (metals) and carbon (from erGO) within the tubular erGO/Pt and erGO/Au microtubes, respectively.

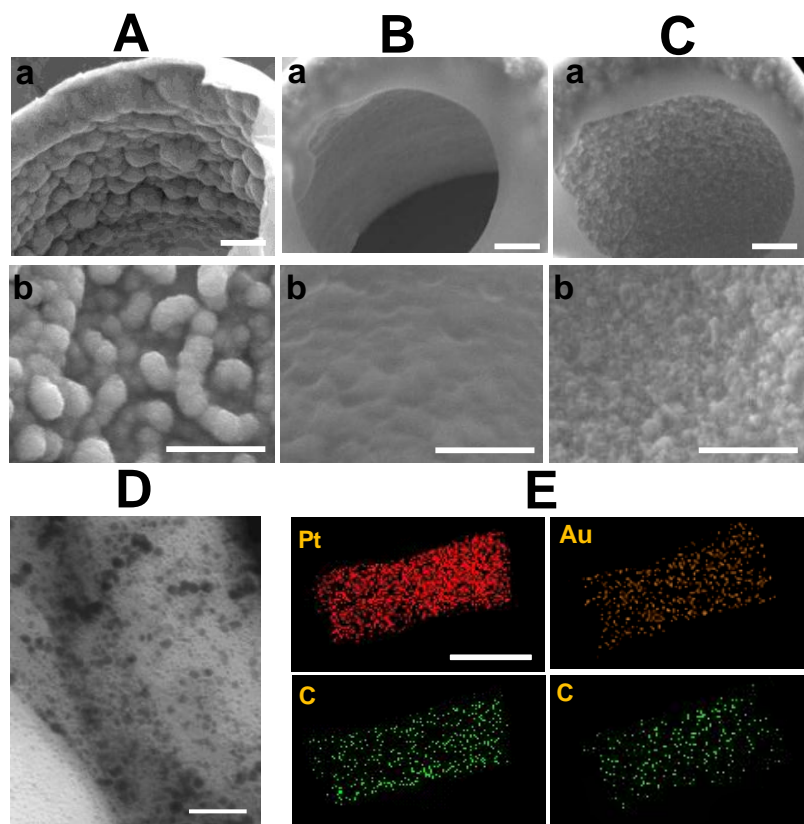


Figure IV.8. SEM images of the cross view of the bilayer tube structure (a) and magnification images showing the different inner metal layer structures (b) of **(A)** erGO-Pt, **(B)** PANI-Pt and **(C)** erGO-Au micromotors. Scale bars, 500 nm. **(D)** TEM image of Pt nanoparticles in the erGO layer. Scale bar, 50 nm. **(E)** EDX spectroscopy images of an erGO-Pt (left) and erGO-Au (right) micromotor illustrating the distribution of carbon, Pt, and Au. Scale bars, 5 μm

IV.2.3. Propulsion of chemically powered graphene micromotors

Compared with normal smooth tubular micromotors, both erGO-metal bi-layers exhibited larger electrochemical active surface area, enhanced catalytic properties and high-density of binding sites for attaching biomolecules. Hierarchical porous Pt structures are expected to provide an enlarged catalytic surface area and improved fuel accessibility, and hence, lead to remarkably efficient propulsion.³⁷ The erGO/Pt micromotor displays an attractive propulsion behavior even at very low peroxide fuel levels. The microscopic images in **Figure IV.9A, a**, taken from **Video IV.1**, illustrate the fast propulsion of an erGO/Pt micromotor at a speed of over $37 \mu\text{ms}^{-1}$ using a peroxide fuel concentration of 0.1%. Control PANI/Pt micromotors (of similar size but a smooth catalytic surface) required a two-fold increase in the peroxide level for efficient propulsion at a diminished speed of $30 \mu\text{ms}^{-1}$ (see **Figure IV.9A, b** and corresponding **Video IV.1**). To further test the performance and advantages of the graphene/Au micromotors, we immobilized the enzyme catalase onto their inner porous gold layer surface, using an earlier protocol.³⁸ Catalase offers an attractive alternative to electrocatalytic metals for propelling peroxide-driven nano/microscale motors. **Figure IV.9A, c** (and corresponding **Video IV.2**) display the movement of graphene/Au/catalase micromotors at high speeds of $321 \pm 80 \mu\text{ms}^{-1}$ (32 bl/sec). (Note that the speed is given in bodylength per second (bl/sec) for comparative purposes with the literature). In comparison, control motors, PANI/Au/catalase micromotors (with a smooth inner gold layer), prepared under similar conditions, propelled at a significantly lower speed of $156 \pm 38 \mu\text{ms}^{-1}$ (11 bl/sec); see **Figure IV.9A, d** and

corresponding **Video IV.2**. The speed of the new graphene/Au/catalase micromotors is significantly higher than that reported for polypyrrole/Au/catalase (8 bl/sec in 0.5% H₂O₂)¹⁹ and rolled-up Ti/Au (6.8 bl/sec in 1.5% H₂O₂)³⁹ micromotors. Such remarkable speed of graphene/Au/catalase micromotors can be attributed to the very rough Au surface of the graphene based micromotors (**Figure IV.8C**) which increases the specific surface area for immobilizing large amounts of the enzyme.

Figure IV.9B displays the dependence of the speed of the erGO/Pt and PANI/Pt micromotors upon the hydrogen peroxide concentration (from 0.1 to 3.0% fuel, for n=50 micromotors). As expected, the speed of the micromotors is strongly dependent on the concentration of the peroxide fuel, which influences the frequency of the generated oxygen bubbles. For example, the bubble frequency of the erGO/Pt micromotors increases greatly from 25 to 227 Hz upon raising the peroxide level from 0.1 to 0.5%. As expected, the higher bubble frequency led to an increased speed, e.g., 37 μms^{-1} in 0.1 % H₂O₂ as compared to 170 μms^{-1} in 0.5% H₂O₂. In contrast, no bubble evolution is observed for the control PANI/Pt micromotors at the 0.1% H₂O₂ solution. In addition, a lower bubble frequency (188 Hz) is observed for these control micromotors at the 0.5 % H₂O₂ level, resulting in a substantially lower speed of 96 μms^{-1} compared to that (170 μms^{-1}) observed for the erGO/Pt at the same conditions.

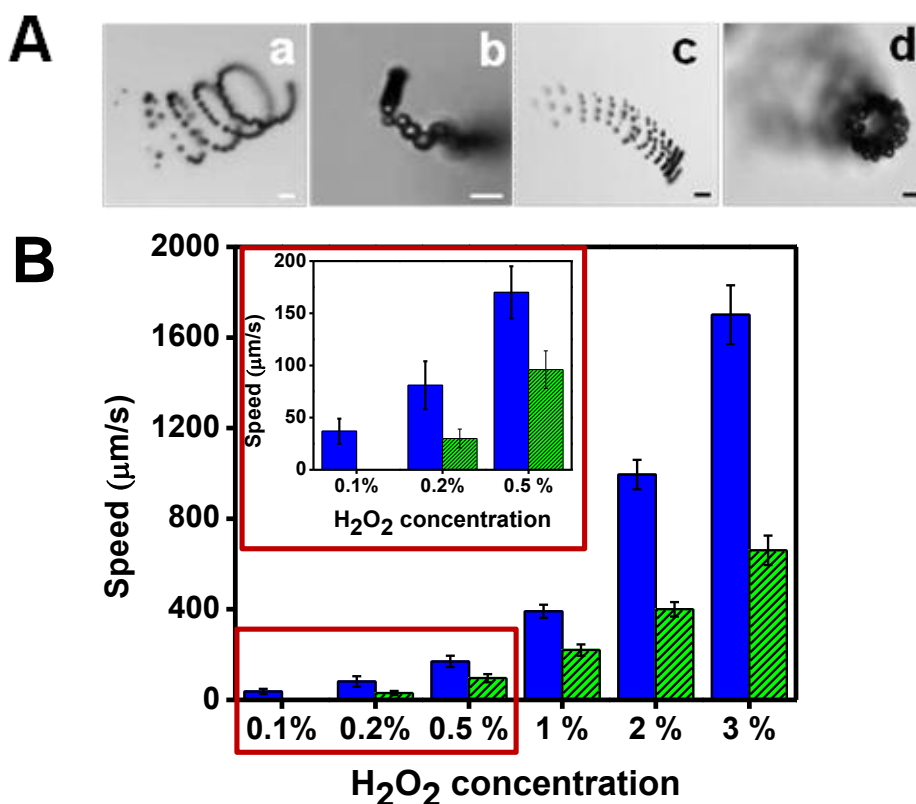


Figure IV.9. Ultrafast propulsion of erGO–Pt and erGO–Au micromotors. **(A)** Propulsion images of erGO–Pt-based micromotor, based on **Video IV.1**, in 0.1% H₂O₂ solution (a), as compared with a control polyaniline (PANI)–Pt micromotors in 0.2% H₂O₂ (b); propulsion images of erGO–Au-catalase micromotors, based on **Video IV.2**, in 1.0% H₂O₂ solution (c), compared with control PANI–Au-catalase micromotors (d). **(B)** Comparison of the speed profile of erGO–Pt micromotors (blue bars) and PANI–Pt micromotors (lined bar graphs) over the 0.1%–3.0% peroxide range, in the presence of 1.5% sodium cholate surfactant ($n = 50$). Inset: magnified speed dependence over the 0.1%–0.5% peroxide range. Scale bars, 10 μm

Previous reports ⁴⁰⁻⁴² indicate that, for a tubular cavity with a defined radius R_j and length L , the rate of oxygen generation is linearly proportional to the area of the Pt surface and to the H_2O_2 concentration. The oxygen bubble expelling frequency (f) can be thus deduced using the average bubble radius (R_b), as described in **Equation IV.1**.

$$f = \frac{nC_{H_2O_2}2\pi LR_j}{V_{bubble}} = \frac{3nC_{H_2O_2}LR_j}{2R_b^3} \quad (\text{Equation IV.1})$$

Based on the previous equation, the average velocity (v_j) of erGO/Pt and PANI/Pt tubular micromotors can be theoretically predicted from **Equation IV.2**.

$$v_j^{ave} = \frac{9nC_{H_2O_2}LR_j}{3R_b^2 + LR_b / \left(\ln\left(\frac{2L}{R_j}\right) - 0.72 \right)} \quad (\text{Equation IV.2})$$

These equations are valid for cylindrical motors. A more recent model ⁴¹ introduces slight modifications for a conically-shaped motor.

Figure IV.10 depicts the calculated average velocities for erGO/Pt and PANI/Pt tubular micromotors, assuming the same geometric dimensions (length, L , 10 μm and inner opening radius, R_j 2.2 μm) as a function of H_2O_2 concentration. The solid curves represent the calculated speed assuming bubble radius (R_b) with values ranging from R_j to $R_j/5$. The triangular and circular symbols are derived from

our experimental results for PANI/Pt and erGO/Pt-based micromotors ($n=50$), respectively. As can be seen, the experimental results for PANI/Pt micromotors fit well with the curve $R_b=R_j/2$. This data deviates slightly from the adopted model, which assumed that the equivalent bubble radii should be equal or slightly larger than the radius of the micromotors. Surprisingly, a much higher deviation is found for erGO/Pt micromotors, which fit well with the curves $R_b=R_j/4$ at low peroxide levels (0.1-1.0%) and $R_b=R_j/5$ in 2.0 and 3.0% H_2O_2 solutions. According to the equation adopted in our model, such small bubble size leads to a higher bubble expelling frequency, resulting in a faster micromotor movement, as indicated by our experimental results. Both the large surface area of the platinum catalyst and higher oxygen microbubble generation frequency are responsible for the highly efficient propulsion behavior of graphene/Pt micromotors, compared to the smooth (control PANI) micromotors. The high bubble expelling frequency at low peroxide fuel levels leads to small size O_2 bubbles and results in a faster micromotor movement compared to the control PANI-based controls.^{16,37,40} The dynamics of microtube motors has been described quantitatively by the body-deformation model that considers the micromotor and the microbubble to be one system.⁴⁰ The average speed of tubular micromotor is approximately equal to the product of the bubble radius and expelling frequency.^{12,40} The role of the geometric dimensions of the micromotor, such as length and radius, on its dynamic characteristics was also investigated. The average motor speed depends also strongly on the micromotor length. The length of our erGO-based micromotors can be controlled by varying the number of CV scans during the GO reduction. Longer micromotors (up to 20 μm length) can thus be prepared, leading to micromotors with a large inner Pt surface. This results in a higher

bubble expelling frequency and an increased speed. However, the increase is not so pronounced since is counteracted by the larger drag force, thus slowing down the micromotor.⁴⁰

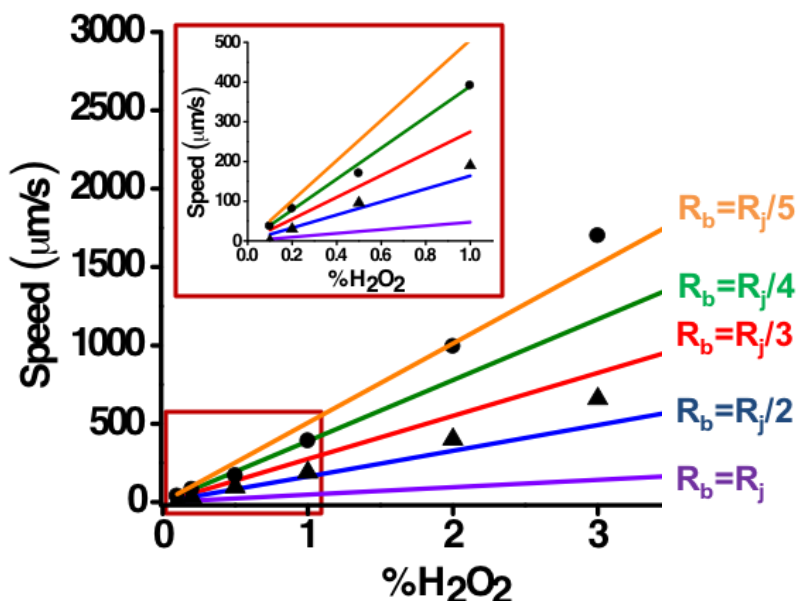


Figure IV.10. Dependence of the average micromotor speed upon the H_2O_2 concentration (0.1%–3.0%). For calculations, micromotors were assumed to have the same geometric dimension (length, L , $10\ \mu\text{m}$, and inner opening radius, R_j $2.2\ \mu\text{m}$). The solid curves represent the calculated speed bubbles radii (R_b) with values from R_j to $R_j/5$. The triangular and circular symbols are derived from our experiment results for PANI-Pt and erGO-Pt-based micromotors, respectively. Inset: magnified speed dependence over the 0.1%–1.0% peroxide range

Such ultrafast speed is attributed to the increased catalytic reactivity of the inner platinum surface, associated with the higher surface roughness, compared to the smooth platinum surface of common micromotors. Thus, erGO/Pt micromotors can propel at high speeds of 37 ± 10 , 81 ± 23 , 170 ± 40 , 390 ± 80 and $1700 \pm 200 \mu\text{ms}^{-1}$ at H_2O_2 levels of 0.1, 0.2, 0.5, 1.0 and 3.0%, respectively. Such speed is remarkably high compared to those reported for the common polymeric-based PANI/Pt, PPy/Pt and PEDOT/Pt micromotors, e.g., 660, 435 and 932 μms^{-1} , respectively, at 3.0% H_2O_2 .¹⁹ Graphene-based motors, prepared previously using different synthetic routes, displayed much lower speeds even using higher fuel concentrations, e.g., 138 $\mu\text{m s}^{-1}$ at 10 % H_2O_2 for rolled-up GO/Ti/Pt catalytic micromotors,²³ 40 μms^{-1} for graphene Janus motors in 3.0 % H_2O_2 ²⁵ or 24 cm in 6 seconds for graphene millitubes operated at a very high (20%) peroxide concentration.²⁴ The fast catalytic locomotion and hence high power of the template-electrodeposited erGO/Pt micromotors make them excellent candidates as efficient micromachines for a wide range of practical applications.

The combination of Pt microparticles with the graphene layer has demonstrated efficient catalytic effect, a powerful propulsion thrust and distinct moving trajectories. The optical images (and corresponding tracking lines) of **Figure IV.11** illustrate representative trajectories of autonomous motion of erGO/Pt based micromotors. The microbubble tails resulting from the hydrogen-peroxide decomposition reaction reveal unique trajectories with (a) linear, (b) circular, (c) flower-like, (d) helical, (e) self-rotation and (f) snake-like motions. Although, some similar motion trajectories (linear, circular, helical and self rotating ones) were reported previously for larger rolled-up micromotors,¹² the erGO/Pt micromotors display unique moving trajectories, such as flower and

snake-like motions (c and f, respectively) that were not reported earlier. The enhanced catalytic activity and ultrafast-bubble production of the erGO tubular micromotors lead to a unique combination of bubble recoil and fluid pumping into the tubular structure, resulting in a new torque and distinct flower and snake-like moving behaviours. It was reported that the motion of the microtube motors is strongly influenced by the tubular geometry.¹² The erGO/Pt micromotors, due to the asymmetric inner porous Pt catalyst structure, provide anisotropic distribution of drag forces along the axial and radial directions. This inner asymmetry in the structure causes unbalanced oxygen production along the tube, leading to the distinct motion patterns shown in **Figure IV.11**.

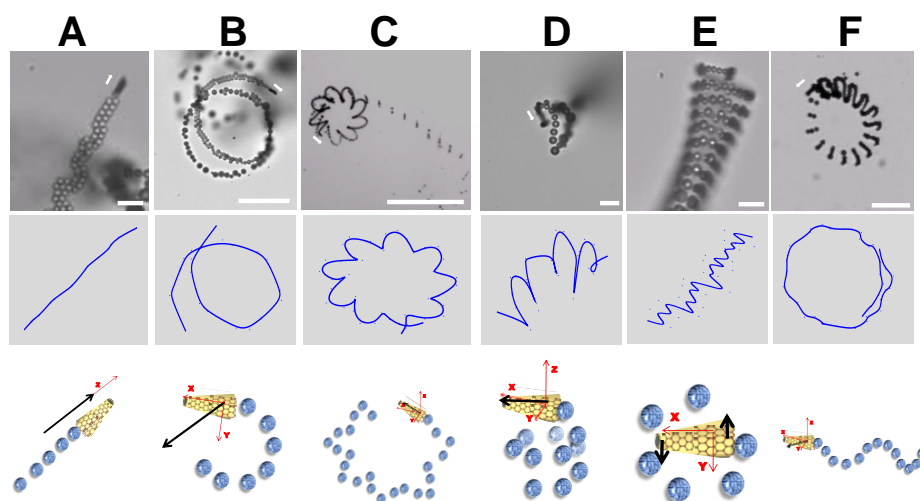


Figure IV.11. Propulsion images showing the motion trajectories and corresponding tracking lines of erGO–Pt-based micromotors (taken from **Videos IV.3, IV.4**). The lower schematic diagrams sketch the corresponding moving behaviors. Movements: **(A)** linear, **(B)** circular, **(C)** flower-like, **(D)** helical, **(E)** self-rotation, and **(F)** snake-like motions. Conditions: a 2.0% H_2O_2 solution containing 1.5% sodium cholate. Scale bars, 20 μm

IV.2.4. Conclusions

We described a greatly simplified, low-cost membrane template electrodeposition of erGO/Pt and erGO/Au tubular micromotors with an efficient propulsion performance. Unlike earlier graphene-based micromachines, the micromotors described here are based on the electroreduction of GO followed by deposition of a porous inner metal layer. The effective movement of such template-prepared graphene-based has been attributed to the porous metallic surface that offers a greatly enhanced catalytic activity and efficient bubble evolution compared with common smooth tubular micromotors. This nanoporous metallic structure can be directly related to the presence of higher boundaries and defects in the thin graphene shell-layer. Such enhanced catalytic activity along with improved reactant accessibility and larger surface area enabled a dramatic acceleration of the fuel catalytic reaction. In addition, the aromatic character of the outer graphene layer could be used for *on-the-move* removal of polyaromatic compounds via π - π interactions (removal of interferences).

The electrodeposition protocol was highly versatile, allowing control of the graphene micromotors dimensions by using membrane templates with different pore sizes, or by variation of the number of cyclic scans. Furthermore, in order to remote control the motion of the micromotors, an intermediate magnetic layer can be easily incorporated, providing magnetically-guided propulsion for future on-chip applications. In addition to the preparation of graphene-based micromotors, the template electrodeposition route holds considerable promise for creating a wide range of graphene-based core-shell materials and composite nanostructures for diverse applications.

IV.2.5. Experimental section

IV.2.5.1. Electrochemical synthesis of reduced graphene oxide micromotors and control micromotors

The erGO micromotors were prepared by electrochemical reduction of graphene oxide (GO, graphene supermarket, New York, USA) into 5 μm -diameter conical pores of a polycarbonate membrane (Catalog No. 7060–2513; Whatman, Maidstone, UK). A thin gold film was first sputtered on the branched side of the membrane to serve as a working electrode. The membrane was assembled in a Teflon plating cell with aluminum foil serving as an electrical contact for the subsequent electrodeposition. GO, 0.10 mg mL⁻¹ was first dispersed in a solution containing 0.10 M H₂SO₄ and 0.50 M Na₂SO₄ by ultrasonication for 15 min. The resultant homogeneously dispersed yellow-brown GO can be stable for several weeks because of the high presence of oxygen functionalities. The simultaneous electrochemical reduction and deposition of GO was carried out using CV, over +0.30 to -1.50 V vs. Ag/AgCl/Cl⁻ (3 M), at 50 mV s⁻¹, for five cycles ($n = 5$), using a Pt wire as counter electrode. Subsequently, a metal tube layer was plated inside the erGO layer. For erGO–Pt, the inner Pt layer was galvanostatically deposited at -2 mA for 500 s from a commercial platinum plating solution (Platinum RTP; Technic Inc, Anaheim, CA); for erGO–Au microtubes, the gold was plated at -0.90 V for 1 C from a commercial gold plating solution (Orotemp 24 RTU RACK; Technic Inc.). The control PANI-Pt micromotors were prepared in a similar fashion. Briefly, aniline was freshly distilled before use at a vapor temperature of 100 °C and a pressure of 13-mm Hg. PANI microtubes were electropolymerized by CV, +1.50 to -1.50 V vs. Ag/AgCl (KCl 3 M), 50 mV s⁻¹, $n = 5$ from a plating solution

containing 0.10 M aniline, 0.10 M H₂SO₄ and 0.50 M Na₂SO₄. Subsequently, the inner Pt layer was deposited galvanostatically at -2 mA for 500 s. The sputtered gold layer was gently removed by hand polishing with 3–4 μm alumina slurry. The membrane was then dissolved in methylene chloride for 15 min to completely release the microtubes. The micromotors were collected by centrifugation at 7000 rpm for 3 min and washed repeatedly with isopropanol, ethanol and three times with ultrapure water (18.2 Ω cm), with a 3 min centrifugation following each wash. All microtubes were stored in ultrapure water at room temperature when not in use.

IV.2.5.2. Catalase Immobilization

The Au inner layer was first modified with an alkanethiol monolayer by overnight incubation in a mixture containing 7.5×10^{-3} M 6-mercaptohexanol and 2.5×10^{-3} M 11-mercaptoundecanoic acid, prepared in ethanol. The microtubes were rinsed with water for 5 min. Then, they were transferred to an eppendorf vial containing a 200 μL MES solution (25 mM, pH 6.50) containing the coupling agents, 1-ethyl-3-[3-dimethylaminopropyl]carbodiimide hydrochloride (0.4 M), N-hydroxysulfosuccinimide (0.1 M), and the catalase enzyme (2 mg mL⁻¹), and incubated for 7 h at 37 °C. This step was followed by two 15 min rinsing steps with phosphate buffer saline-Tween (pH 5.50). Finally, the microtubes were washed three times with water to remove the excess of catalase and then suspended in 5.5 pH buffer and stored at 4 °C.

IV.2.5.3. Equipments

Template electrochemical deposition of microtubes was carried out using an electrochemical station μ -Autolab Type III (Eco Chemie, Utrecht, Holland). SEM images were obtained with a Phillips XL30 ESEM instrument, using an acceleration voltage of 20 kV. Energy-dispersive X-ray mapping analysis was performed using an Oxford EDX detector attached to SEM instrument and operated by INCA software. TEM were taken using a Zeiss EM10C instrument. An inverted optical microscope (Nikon Eclipse Instrument Inc. Ti-S/L100), coupled with 10X and 20X objectives, and a Hamamatsu digital camera C11440 and NIS Elements AR 3.2 software, were used for capturing movies at a rate of 45 frames per second. The speed of the micromotors was tracked using a NIS Elements tracking module. Aqueous hydrogen peroxide solutions (Sigma-Aldrich, cat. 95313), with concentrations ranging from 0.1%–5.0%, were used as the chemical fuel. Sodium cholate (Sigma-Aldrich, cat. 270911) was used as surfactant in all propulsion experiments.

IV.2.6. Appendix

Videos, figures and tables

Video IV.1. Propulsion of erGO/Pt and control PANI/Pt micromotors in ultrapure water in the presence of 0.1% H₂O₂ and 0.2% H₂O₂, respectively; using 1.5% sodium cholate as surfactant

Video IV.2. Propulsion of erGO/Au/catalase and control PANI/Au/catalase micromotors in ultrapure water in the presence of 1.0% H₂O₂, using 1.5% sodium cholate as surfactant

Video IV.3. Linear, circular and flower-like motion of erGO/Pt micromotors in 2.0% H₂O₂ with 1.5% sodium cholate. For linear motion, the speed of the video has been slowed down 5 times for a better visualization of the micromotor trajectory

Video IV.4. Helical, self-rotating and snake-like motion of erGO/Pt micromotors in 2.0% H₂O₂ with 1.5% sodium cholate. For self-rotating motion, the speed of the video has been slowed down 5 times for a better visualization of the micromotor trajectory

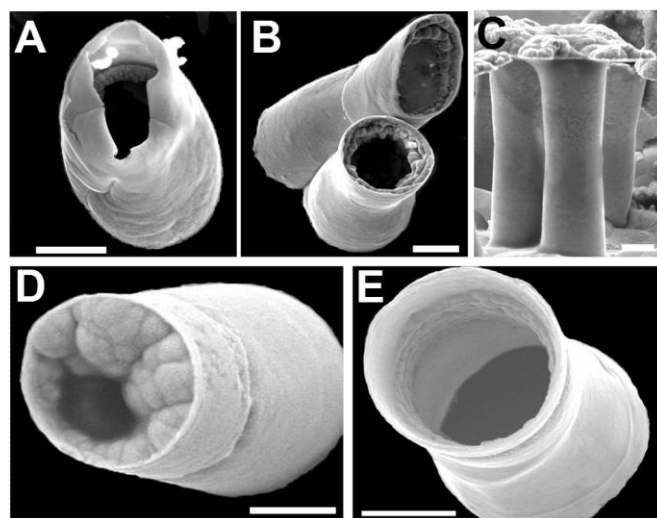


Figure IV.S1. SEM images of the morphology erGO-Pt based micromotors prepared under variable platinum deposition times: (A) 100 s, (B) 500 s and (C) 1000s and under different number of scans for the electrochemical reduction of GO (D) $n=2$ and (E) $n=5$. For the study of the influence of Pt, GO was deposited in 5 μm PC membranes fixing the scan number to 10. For the GO deposition times experiments, Pt was deposited for 500 s. Scale bars, 2 μm

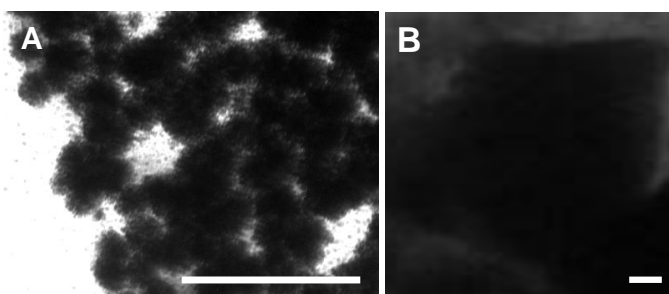


Figure IV.S2. TEM images revealing the size of the platinum nanoparticles in erGO-Pt based micromotors (A) and the thin platinum film in PANI-Pt micromotors (B). Scale bars, 50 nm

IV.2.7. References

1. Paxton, W. F.; Kistler, K. C.; Olmeda, C. C.; Sen, A.; St. Angelo, S. K.; Cao, Y.; Mallouk, T. E.; Lammert, P. E.; Crespi, V. H. Catalytic Nanomotors: Autonomous Movement of Striped Nanorods. *J Am Chem Soc* **2004**, *126*, 13424–13431.
2. Ozin, G.A.; Manners, I.; Fournier-Bidoz, S.; Arsenault, A. Dream Nanomachines. *Adv Mater* **2005**, *17*, 3011-3018.
3. Wang, J. *Nanomachines: Fundamentals and Applications*; Wiley- VCH: Weinheim, Germany, 2013.
4. Wang, W.; Duan, W.; Ahmed, S.; Mallouk, T. E.; Sen, A. Small power: Autonomous nano- and micromotors propelled by self-generated gradients. *Nano Today* **2013**, *8*, 531-554.
5. Mei, Y.; Solovev, A. A.; Sanchez, S.; Schmidt, O. G. Rolled-up nanotech on polymers: from basic perception to self-propelled catalytic microengines. *Chem. Soc. Rev.* **2011**, *40*, 2109-2119.
6. Sánchez, S.; Soler, L.; Katuri, J. Chemically Powered Micro- and Nanomotors. *Angew. Chem. Int. Edit.* **2015**, *54*, 1414-1444.
7. Fischer, P.; Ghosh, A. Magnetically actuated propulsion at low Reynolds numbers: towards nanoscale control. *Nanoscale* **2011**, *3*, 557-563.
8. Huang, G.; Wang, J.; Mei, Y. Material considerations and locomotive capability in catalytic tubular microengines. *J. Mater. Chem.* **2012**, *22*, 6519-6525.
9. Sánchez, S.; Pumera, M. Nanorobots: The Ultimate Wireless Self-Propelled Sensing and Actuating Devices. *Chem. –Asian J.* **2009**, *4*, 1402-1410.
10. Wang, J. Can Man-Made Nanomachines Compete with Nature Biomotors? *ACS Nano* **2009**, *3*, 4-9.
11. Mei, Y.; Huang, G.; Solovev, A. A.; Ureña, E. B.; Mönch, I.; Ding, F.; Reindl, T.; Fu, R. K. Y.; Chu, P. K.; Schmidt, O. G. Versatile Approach for Integrative and Functionalized Tubes by Strain Engineering of Nanomembranes on Polymers. *Adv Mater* **2008**, *20*, 4085-4090.

12. Solovev, A. A.; Mei, Y.; Bermudez Urena, E.; Huang, G.; Schmidt, O. G. Catalytic Microtubular Jet Engines Self-Propelled by Accumulated Gas Bubbles. *Small* **2009**, *5*, 1688-1692.
13. Howse, J. R.; Jones, R. A. L.; Ryan, A. J.; Gough, T.; Vafabakhsh, R.; Golestanian, R. Self-Motile Colloidal Particles: From Directed Propulsion to Random Walk. *Phys. Rev. Lett.* **2007**, *99*, 048102-048106.
14. Baraban, L.; Makarov, D.; Streubel, R.; Mönch, I.; Grimm, D.; Sanchez, S.; Schmidt, O. G. Catalytic Janus Motors on Microfluidic Chip: Deterministic Motion for Targeted Cargo Delivery. *ACS Nano* **2012**, *6*, 3383-3389.
15. Laocharoensuk, R.; Burdick, J.; Wang, J. Carbon-Nanotube-Induced Acceleration of Catalytic Nanomotors. *Acs Nano* **2008**, *2*, 1069-1075.
16. Gao, W.; Sattayasamitsathit, S.; Orozco, J.; Wang, J. Highly Efficient Catalytic Microengines: Template Electrosynthesis of Polyaniline/Platinum Microtubes. *J. Am. Chem. Soc.* **2011**, *133*, 11862-11864.
17. Zhao, G.; Pumera, M. Concentric bimetallic microjets by electrodeposition. *RSC Adv.* **2013**, *3*, 3963-3966.
18. Wang, J. Template electrodeposition of catalytic nanomotors. *Faraday Discuss.* **2014**, *164*, 9-18.
19. Gao, W.; Sattayasamitsathit, S.; Uygum, A.; Pei, A.; Ponedal, A.; Wang, J. Polymer-based tubular microbots: role of composition and preparation. *Nanoscale* **2012**, *4*, 2447-2453.
20. Stankovich, S.; Dikin, D. A.; Dommett, G. H. B.; Kohlhaas, K. M.; Zimney, E. J.; Stach, E. A.; Piner, R. D.; Nguyen, S. T.; Ruoff, R. S. Graphene-based composite materials. *Nature* **2006**, *442*, 282-286.
21. Lee, C.; Wei, X.; Kysar, J. W.; Hone, J. Measurement of the elastic properties and intrinsic strength of monolayer graphene. *Science* **2008**, *321*, 385-388.
22. Martín, A.; Escarpa, A. Graphene: The cutting-edge interaction between chemistry and electrochemistry. *Trends Anal. Chem.* **2014**, *56*, 13-26.

23. Yao, K.; Manjare, M.; Barrett, C. A.; Yang, B.; Salguero, T. T.; Zhao, Y. Nanostructured Scrolls from Graphene Oxide for Microjet Engines. *J. Phys. Chem. Lett.* **2012**, *3*, 2204-2208.
24. Hu, C.; Zhao, Y.; Cheng, H.; Wang, Y.; Dong, Z.; Jiang, C.; Zhai, X.; Jiang, L.; Qu, L. Graphene Microtubings: Controlled Fabrication and Site-Specific Functionalization. *Nano Lett.* **2012**, *12*, 5879-5884.
25. Wang, H.; Sofer, Z.; Eng, A. Y. S.; Pumera, M. Iridium-Catalyst-Based Autonomous Bubble-Propelled Graphene Micromotors with Ultralow Catalyst Loading. *Chem. - Eur. J.* **2014**, *20*, 14946-14950.
26. Chen, X.; Wu, G.; Lan, T.; Chen, W. Autonomous micromotor based on catalytically pneumatic behavior of balloon-like MnO_x-graphene crumples. *Chem. Commun.* **2014**, *50*, 7157-7159.
27. Li, X.; Zhao, T.; Wang, K.; Yang, Y.; Wei, J.; Kang, F.; Wu, D.; Zhu, H. Directly Drawing Self-Assembled, Porous, and Monolithic Graphene Fiber from Chemical Vapor Deposition Grown Graphene Film and Its Electrochemical Properties. *Langmuir* **2011**, *27*, 12164-12171.
28. Wang, R.; Hao, Y.; Wang, Z.; Gong, H.; Thong, J. T. L. Large-Diameter Graphene Nanotubes Synthesized Using Ni Nanowire Templates. *Nano Lett.* **2010**, *10*, 4844-4850.
29. Yang, C.; Xu, Y.; Zhang, C.; Sun, Z.; Chen, C.; Li, X.; Jiang, S.; Man, B. Facile synthesis 3D flexible core-shell graphene/glass fiber via chemical vapor deposition. *Nanoscale Res. Lett.* **2014**, *9*, 394.
30. Yu, P.; Li, Y.; Zhao, X.; Wu, L.; Zhang, Q. Graphene-Wrapped Polyaniline Nanowire Arrays on Nitrogen-Doped Carbon Fabric as Novel Flexible Hybrid Electrode Materials for High-Performance Supercapacitor. *Langmuir* **2014**, *30*, 5306-5313.
31. Sidorov, A.; Mudd, D.; Sumanasekera, G.; Ouseph, P. J.; Jayanthi, C. S.; Wu, S.Y. Electrostatic deposition of graphene in a gaseous environment: a deterministic route for synthesizing rolled graphenes? *Nanotechnology* **2009**, *20*, 055611.
32. Cheng, H.; Hu, C.; Zhao, Y.; Qu, L. Graphene fiber: a new material platform for unique applications. *NPG Asia Mater.* **2014**, *6*, e113.

33. Shao, Y.; Wang, J.; Engelhard, M.; Wang, C.; Lin, Y. Facile and controllable electrochemical reduction of graphene oxide and its applications. *J. Mater. Chem.* **2010**, *20*, 743-748.
34. Martín, A.; Hernandez-Ferrer, J.; Vazquez, L.; Martinez, M.; Escarpa, A. Controlled chemistry of tailored graphene nanoribbons for electrochemistry: a rational approach to optimizing molecule detection. *Rsc Adv.* **2014**, *4*, 132-139.
35. Zhou, Y.; Chen, J.; Wang, F.; Sheng, Z.; Xia, X. A facile approach to the synthesis of highly electroactive Pt nanoparticles on graphene as an anode catalyst for direct methanol fuel cells. *Chem. Commun.* **2010**, *46*, 5951-5953.
36. Yoo, E.; Okata, T.; Akita, T.; Kohyama, M.; Nakamura, J.; Honma, I. Enhanced Electrocatalytic Activity of Pt Subnanoclusters on Graphene Nanosheet Surface. *Nano Lett.* **2009**, *9*, 2255-2259.
37. Li, J.; Liu, Z.; Huang, G.; An, Z.; Chen, G.; Zhang, J.; Li, M.; Mei, Y. Hierarchical nanoporous microtubes for high-speed catalytic microengines. *NPG Asia Mater.* **2014**, *6*, e94.
38. Orozco, J.; Garcia-Gradilla, V.; D'Agostino, M.; Gao, W.; Cortes, A.; Wang, J. Artificial Enzyme-Powered Microfish for Water-Quality Testing. *Acs Nano* **2013**, *7*, 818-824.
39. Sanchez, S.; Solovev, A. A.; Mei, Y. F.; Schmidt, O. G. Dynamics of Biocatalytic Microengines Mediated by Variable Friction Control. *J. Am. Chem. Soc.* **2010**, *132*, 13144-13145.
40. Li, J.; Huang, G.; Ye, M.; Li, M.; Liu, R.; Mei, Y. Dynamics of catalytic tubular microjet engines: Dependence on geometry and chemical environment. *Nanoscale* **2011**, *3*, 5083-5089.
41. Li, L.; Wang, J.; Li, T.; Songa, W.; Zhanga, G. Hydrodynamics and propulsion mechanism of self-propelled catalytic micromotors: model and experiment. *Soft Matter* **2014**, *10*, 7511-7518.
42. Manjare, M.; Yang, B.; Zhao, Y. P. Bubble-Propelled Microjets: Model and Experiment. *J. Phys. Chem. C* **2013**, *117*, 4657-4665.

IV.3. Ultrasound powered graphene micromotors



IV.3.1. Introduction and objectives

“Magic bullets” that would drive drugs deep into diseased tissues have been a dream of biomedical researchers for over a decade.^{1,2} Such “magic bullet vision” has inspired and encouraged scientist to create efficient delivery devices towards the successful treatment of human diseases. Designing the right tool for efficient tissue penetration at small scales is essential for diverse applications in drug delivery and microsurgery applications. Novel micro/nanoscale ballistic could pave the way of deep tissue penetration on small scales, providing distinct advantages, due to their size and ability to reach places where catheters cannot. Powerful machinery, including ballistics, exists on the macroscopic scale to penetrate and cut through tissues. However, these large scale ballistic tools do not have analogous micro/nanoscale counterparts, hindering the ability to operate at this small scale and resulting in very limited tissue penetration. Traditional technology cannot just be scaled down due to the dominating viscosity effect (over inertia forces) at lower scales.³⁻⁵ Accordingly, small scale machinery tools need to be powered and actuated by fundamentally different approaches than macroscopic devices. New nanomachine strategies have been developed recently in this direction.⁶⁻¹⁰ Such tiny machines are capable of performing diverse applications,¹¹⁻¹⁴ including some initial reports of microsurgery^{15,16} and cell internalization.^{17,18} However, obtaining a stable, controlled, powerful, and directed means of penetrating tissue and delivering payloads at these small scales remains a major technological challenge. Although bullet-shaped microstructure materials have been designed¹⁹ and metallic bullets are reported as therapeutic tools,^{20,21} they do not offer penetration capabilities or motion but rather they are only incubated with the

target. Indeed, there are no earlier reports regarding the controlled firing of nanobullets (nBs) from a microstructure.

To address this challenge and fill this gap, our objective was to demonstrate the use of acoustically-triggered template-based graphene/Au micromotors and its use as novel tools towards advancing microscale tissue penetration of therapeutic payloads.

In this context, these micromotors would be named as microcannons (Mcs) in this epigraph. They are loaded with a gel matrix containing the nB and a PFC emulsion (**Figure IV.17A**). The US-triggered vaporization of the PFC emulsion,^{22,23} confined inside the Mc results in the rapid ejection of the nB, reaching remarkable speeds (on the scale of meters per second), analogous to the firing of a bullet through a barrel of a gun (**Figure IV.17B**).

Despite there are no reports of acoustic microcannons capable of firing nanobullets, US-triggered microbubble vaporization is an extremely attractive candidate for externally triggering the actuation of such micro/nanoscale ballistic tools, as it is biocompatible^{24,25} and can be used to enhance the permeation and delivery of therapeutics into blood vessels and tissue.²⁶⁻³⁶

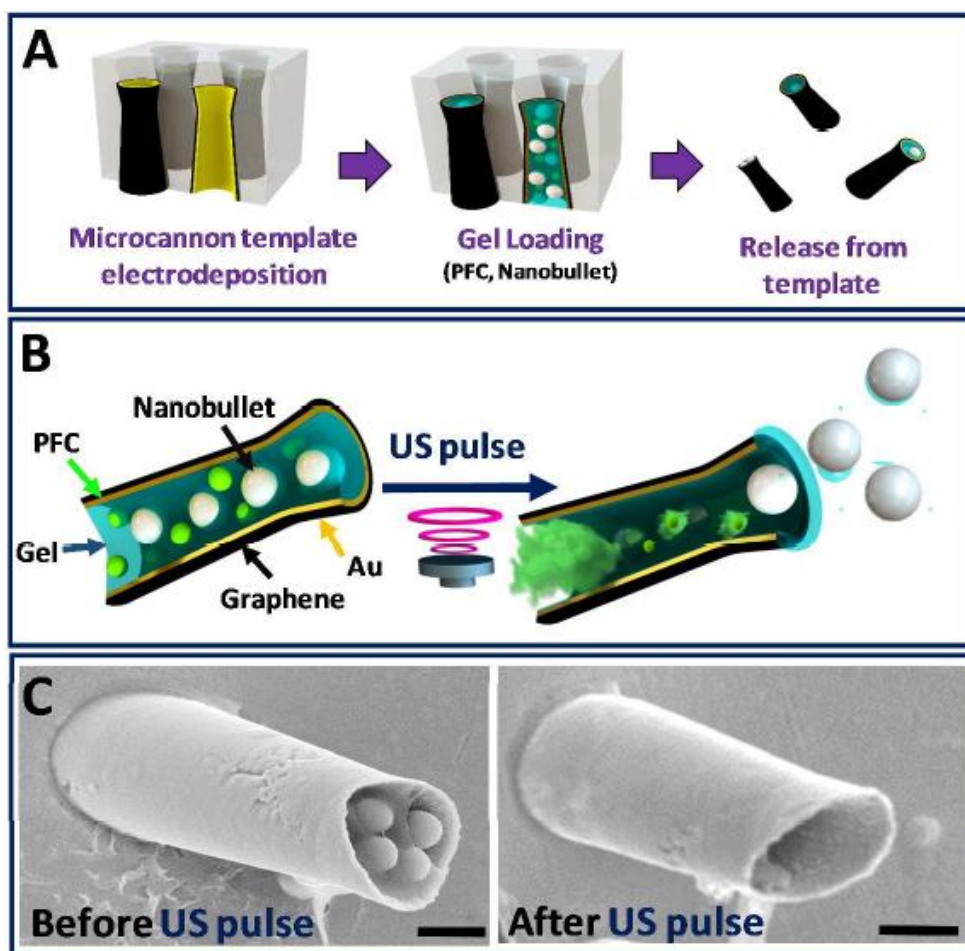


Figure IV.12. Ultrasound triggered nB firing based on vaporization of PFC droplets as a propulsion system. (A) Microcannon (Mc) fabrication by template electrodeposition, loading of cargoes by infiltrating them inside a gel matrix into the hollow Mcs interior and Mc release from the template. (B) Mc composition (left) and schematic illustrating the firing of nanobullets (nB) from Mc by the spontaneous PFC vaporization upon application of US pulse (right). (C) SEM images showing the nB-loaded Mc before (left) and after (right) the US-triggered firing. Micrographs are from microcannons of the same batch. Scale bar 20 μm

IV.3.2. Synthesis and characterization of US-propelled graphene-gold microcannons

A schematic of the synthesis of acoustically-powered graphene/Au Mcs is illustrated in **Figure IV.12A**. First, the hollowed cone structure of the Mc was fabricated using template electrodeposition of electrochemically reduced graphene oxide (erGO) and gold (Au) on the walls of micropores in a polycarbonate membrane, (see experimental section and further synthesis discussion in epigraph **IV.2.2**).³⁷ Afterwards, a liquid gel matrix (at 40 °C), containing 1 μm silica nBs and PFC emulsions, was infiltrated by gravity and capillarity forces into the hollow of the Mcs anchored in the template membrane.^{38,39} After cooling down to room temperature, the particles were entrapped in the solidified gel matrix, which served as a stabilizer and scaffold to protect and retain the loaded nB and PFC emulsion within the Mc interior.

The Mc components and operation is schematized in **Figure IV.12B**. Upon application of a focused ultrasound pulse by a piezoelectric transducer (see experimental and **Figure IV.S5**), the nBs are ejected rapidly from the Mc. The mechanism responsible for the propulsion thrust of the nB relies on the momentum associated with the ultrasound-induced vaporization of the PFC emulsion droplet into a rapidly expanding microbubble. Such vaporization events results from the collapse of the PFC gas microbubbles after the peak negative pressure exceeds its threshold, indicating that such event does not follow linear or exponential dependence on the applied ultrasound power. The subsequent expulsion of these microbubbles from one opening of the Mc structure, led to the ejection of nBs, and displacement of the Mc. The ejection of the nB

from the Mc structure by the acoustic energy is further supported by **Figure IV.12C** which shows SEM micrographs of Mc before and after the US pulse. While the nBs are initially packed in the gel within the Mc, the cannon is nearly empty after the ultrasound pulse, reflecting the PFC vaporization and the ejection of the nBs.

Figure IV.13 A and **Video IV.5** illustrate a vaporized PFC gas bubble, which is clearly visible after the US pulse. The rapid emulsion expansion during the vaporization process provides a sudden impulse that projects both Mc and nB out of the microscope field, leaving a PFC gas cloud. In this work, perfluorononane is used as the PFC fuel, and although it has a boiling point, of 125-126° C,⁴⁰ the US pulse generates enough energy for this PFC emulsion to cavitate and vaporize into a gas microbubble.³² Subsequent control experiments were performed using silica nB-loaded Mc structures without the PFC emulsion. No motion of Mc or ejection of bullets was produced, as illustrated in **Figure IV.13B** and **Video IV.5**, supporting the hypothesis that the firing is caused by vaporization of the PFC emulsion, as was demonstrated previously by Kagan et al.¹⁶

The number of nB loaded into the Mc can be adjusted by controlling the density of the nB embedded in the gel matrix, as shown in **Figure IV.14A**. These SEM micrographs demonstrate the efficient and tailored loading of different nB concentrations inside the Mc structure: from a gel matrix not containing nBs (**Figure IV.14A, a**) to a high packing density of nB (with minimal gaps) using the original commercial nB concentration (**Figure IV.14A, d**). Further (1:1000 and 1:100) dilutions of the original concentration result in low or medium nB loadings, respectively (**Figure IV.14A, b-c**).

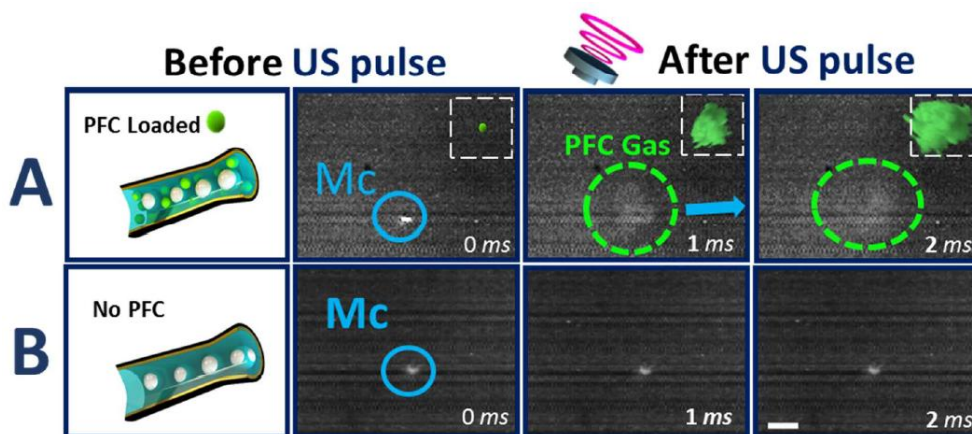


Figure IV.13. Mc loading schematic and time-lapse images of the Mc before (left) and after (right) application of US pulse, taken from **Video IV.5** at 1 ms intervals. **(A)** Images illustrating the US-triggered vaporization of the PFC-emulsion embedded inside the Mc. The rapid expansion of the PFC microbubble is responsible for the firing and propulsion thrust of the nB. **(B)** In the absence of PFC in the Mc, no firing, motion or ejection is produced. Schematic of the bubble expansion (Inset). Scale bar, 45 μ m

To obtain a better characterization and visualization of the firing mechanism, we evaluated static graphene/Au microcannons. These static microcannons consist in the same template electrodeposition protocol, without dissolving the polycarbonate template. Thus, it ends up in an array of multiple confined microcannons pointing in the same direction. The SEM images of **Figure IV.14B** illustrate the loading and ejection of nBs from the static Mcs (eight Mcs on top and a single one on bottom). Each micropore of the template membrane contains a bilayer graphene/gold Mc open-tube structure and is loaded with PFC emulsions and silica-nBs within the gel matrix. The loading mechanism of the cargo by a gel matrix is efficient, reproducible and essential to maintain the tightly-packed cargo inside the cannon as free nBs outside the micropore membrane

structure are removed during a thorough washing procedure (see **Figure IV.14B left**). After application of the US pulse, the silica nBs are ejected from the micropores and released toward the upper part of the membrane. A negligible number of silica bullets remain in the Mc structure (see **Figure 14B right**). Such ability to fire a large amount of nBs is essential for enhanced effectiveness (e.g., therapeutic efficacy in drug delivery).

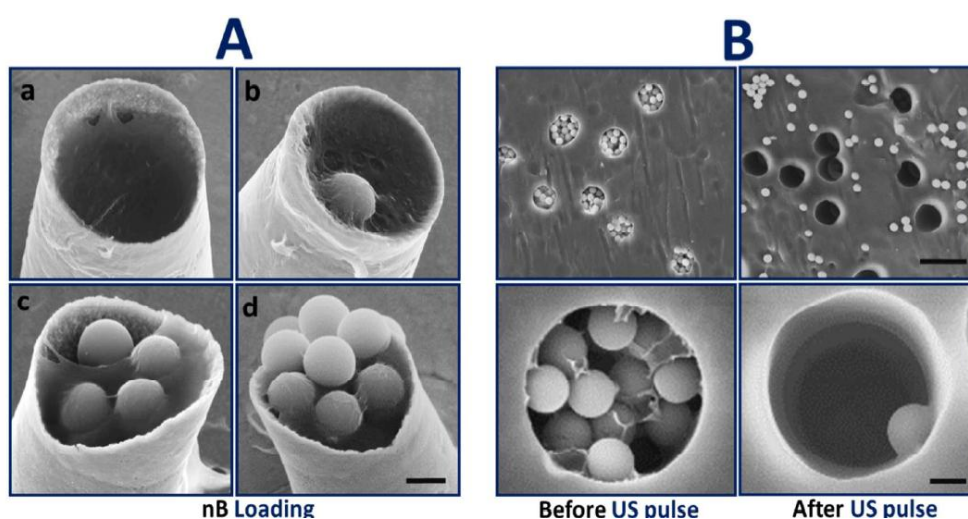


Figure IV.14. (A) SEM micrographs illustrating tunable nB loading density in the gel matrix: (a) no nB, (b) low nB concentration, (c) medium nB concentration and (d) high nB concentration (scale bar, 1 μm). (B) SEM micrographs showing firing characterization of static Mc confined within multiple micropores of the template membrane (top, scale bar 10 μm) and detail of single Mc. (bottom scale bar, 1 μm); before the US pulse (left) and the ejection of cargo nB after the US pulse (right)

IV.3.3. Penetration of nanobullets fired from graphene-gold microcannons

To further assess the distance reached by the nBs and demonstrate the versatility of the microballistic approach for loading and shooting different cargoes, static Mcs, confined in the template membrane (as in **Figure IV.14B**), were loaded with *Fluorospheres* that were fired towards a tissue phantom gel. The loading of the *Fluorosphere* nBs and the PFC was similar to the previous approach involving silica nBs (see experimental section for details). The tissue phantom gel has comparable acoustic and mechanical properties as real tissues,⁴¹ allowing for the measurement of the distance traveled by these fired nBs and the penetration capabilities of the presented microballistic approach. **Figure IV.15** shows the corresponding fluorescence images top and cross-section before and after the US pulse. The top view (**Figure IV.15A**) illustrates the graphene/Au Mcs filled with the fluorescent particles prior to the US pulse (left) with each point represents a Mc. A fluorescence ‘cloud’ is observed after the US-triggered firing (right), illustrating the *Fluorosphere* distribution on the tissue phantom and demonstrating the successful ejection of the *Fluorosphere* nBs from the static Mc upon application of ultrasound. The cross section view (**Figure IV.15B**) shows the nBs penetrating $17.5 \pm 3.7 \mu\text{m}$ into the tissue phantom after application of the ultrasound pulse.

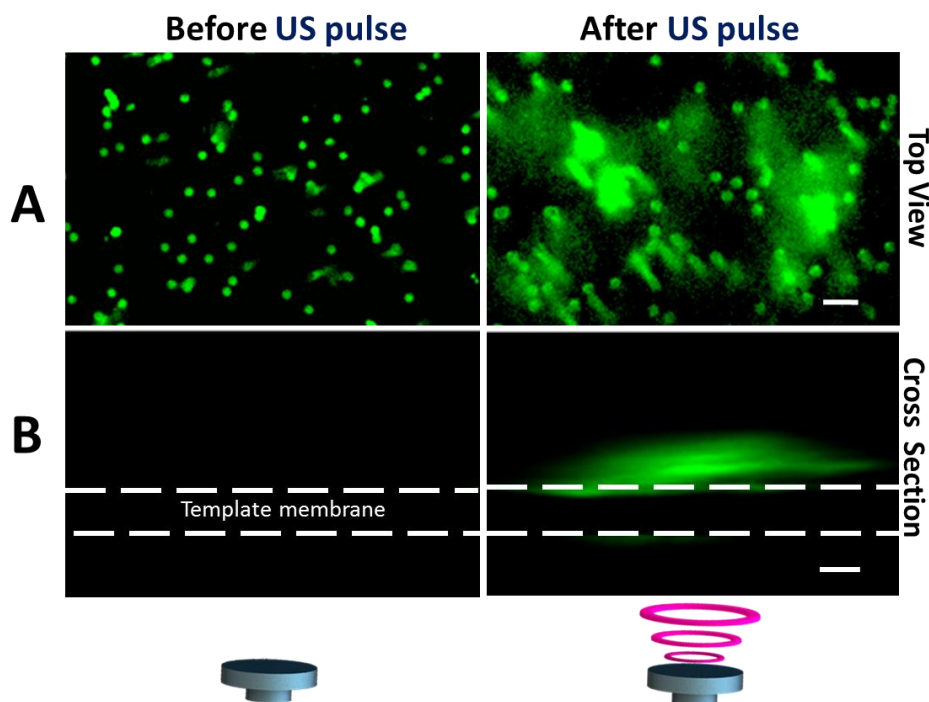


Figure IV.15. Fluorescence images of *Fluorosphere*-loaded static Mcs confined in the template membrane (**left**) and the distribution of the Fluorosphere bullets after the US-triggered firing inside a tissue phantom gel matrix (**right**). **(A)** Top view, where each point represents one microcannon loaded with Fluorosphere bullets. Scale bar 20 μm . **(B)** Cross section view showing the distance of the bullet penetration within the Agar. Scale bar 20 μm

Due to technological limitations for capturing the nB ejection from the graphene-based Mc (associated with their ultrafast ejection speed and size), a theoretical model was used to predict the nB behavior, see more information in the Appendix (**IV.3.7**). Taking into consideration that both the Mc and the nB are exposed to the same propulsion thrust of the PFC explosion, the speeds for nB could be modeled by measuring the displacement of the Mc (**Figure IV.16A**) and extrapolating the force to the nB. The Reynolds number, which

estimates the relation between viscous and inertial forces,^{4,8} was calculated to be 13.7 (see more information in appendix). This low Re means that the Mc moves in a laminar flow where viscous forces dominate the motion; thus the inertia of the objects is no longer important.^{3,42} **Figure IV.16B** shows a scheme of the forces acting in the two objects under study, the Mc and the nB. These include the force of friction (not considered for the calculation), the gravitational force and the hydrodynamic drag force. The latter is the primary force involved in the propulsion, defined by Stokes's law, and is proportional to the speed of the object. The proportionality constant, k depends on the shape of the object under study, so it differs from the Mc (cylinder) and the nB (sphere) as detailed in **Table IV.S1**. Since the drag force is responsible for the movement, the instantaneous and initial speeds for an object subject to this propulsion mechanism will be defined following **Equations IV.3** and **IV.4**, respectively, in which, v and v_0 are the instantaneous and initial speeds, respectively, the interval of time in which the object displaces by Δx and m is the mass of the object. The drag factors k for a cylindrical-shaped Mc and for a spherical nB⁴³ were calculated to be $8.8 \cdot 10^{-8} \text{ kg} \cdot \text{s}^{-1}$ and $1.9 \cdot 10^{-8} \text{ kg} \cdot \text{s}^{-1}$ respectively (see appendix in **IV.3.7**).

$$v = v_0 e^{-\frac{kt}{m}} \quad \text{Equation IV.3.}$$

$$v_0 = \frac{k \Delta x}{m (1 - e^{-\frac{kt}{m}})} \quad \text{Equation IV.4.}$$

The Mc displacement was captured using high-speed camera by considering the change in position of the microcannon in the time considered, resulting in $1.05 \pm 0.26 \text{ m/s}$ ($n=3$) average speed. Then, the initial Mc speed was estimated to be $9.0 \text{ m} \cdot \text{s}^{-1}$, according to **Equation IV.4**. This value was in accordance with other

microstructures propelled by perfluorocarbon.¹⁶ Consequently, an initial nB velocity of 42.2 m s^{-1} could be estimated, which is around 5 times faster than the speed of the Mc. The instantaneous speed-time profile was theoretically modeled for both the Mc and the nB, as shown in **Figure IV.16B**. For simplicity, these approximations were carried out considering that the force is applied only to a single nB; future studies will focus on developing a more precise theoretical simulation accounting for the ejection of multiple nBs. Overall, these theoretical predictions are in agreement with the experimental observations of the optical, fluorescence and SEM images, and indicate an ultrafast ejection of the nanobullet from the microcannon.

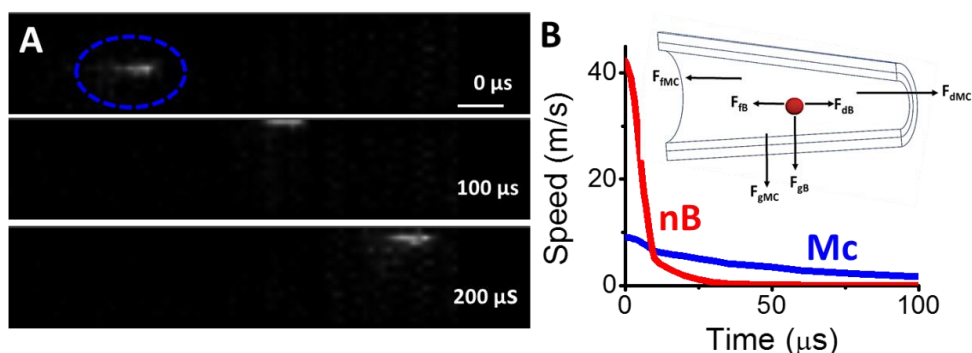


Figure IV.16. Experimental and theoretical behaviors of microcannon (Mc, blue) and nanobullet (nB, red) upon firing. **(A)** Time-lapse frames (0-200 μs) illustrating the displacement of the Mc (circled in blue) upon application of a US pulse recorded under high frame rate (nB ejection speed not shown). Scale bar 20 μm . **(B)** Theoretical speed profile of the Mc and nB upon firing; even though both experience the same initial drag force, they display distinct behavior based on geometry, design and density (see **Table IV.S1**). The inset shows schematic of the forces experienced by the Mc and nB, including force of friction (F_f), force of gravity (F_g) and drag force (F_d), which is the dominant force

IV.3.4. Conclusions

In the framework of this Thesis, the presence of graphene, the outstanding physical properties allow in these Mcs, a light and resistant structure capable of supporting the vaporization of the PFC emulsions and light to penetrate and move in liquid media.

In addition, we have demonstrated the successful ballistic operation of acoustic graphene-based microcannons, which allow the versatile loading and firing of cargoes as nanoprojectiles. Such firing of nB has been modeled theoretically and demonstrated experimentally. The experimental data supports the theory that the ejection of nanobullets from the graphene/Au microcannon occurs due to PFC vaporization, presenting high power, fast displacement speed and a large biologically-relevant tissue penetration depth. These nanobullets could thus be used to drive drugs directly deep into diseased tissues or shoot genetic material into cell nuclei for gene therapy. Future work will thus aim at developing this microbullet platform technology for delivering a wide range of therapeutic payloads and expanding the practical utility of the acoustic microcannons, for use as single or array devices, revolutionizing drug delivery and the treatment of human diseases.

IV.3.5. Experimental section

IV.3.5.1. Perfluorononane emulsion preparation

Perfluorononane nanoemulsions purchased in Sigma Aldrich (St Louis) were prepared in phosphate buffer saline. 3:1:1 Volume ratio of phosphate buffer saline: anionic fluorosurfactant : perfluorononane was prepared through probe-type sonication. The tube containing phosphate buffer saline was immediately placed in a heating block at 90 °C for 5 minutes and 200 µL of Zonyl FSE (Sigma Aldrich, St Louis) anionic fluorosurfactant was added. The solution was vortexed until homogenized. A 200 µL aliquot of perfluorononane (from Sigma Aldrich, St Louis) was added to the phosphate buffer saline-Zonyl FSE mixture. The probe of the sonicator was lowered in the tube about 8 mm from the bottom. While still in the ice bath, the sonicator was operated with a LabVIEW program interfaced with the sonicator via a foot pedal input and a reed relay board. The program delivered three (0.5 second) bursts and was repeated 60 times. The short bursts prevented the solution from stirring violently and producing foam; a 2 sec delay between each set of 3 bursts served to prevent overheating. This process resulted in a 20 % vol. perfluorononane emulsion which was stable and turbid in appearance. Emulsion sizes and zeta potentials were measured by dynamic light scattering with a Zetasizer Nano-ZS (Malvern Instruments, Worcestershire, UK). The 20 % vol. perfluorononane emulsion was diluted to 1% vol. by a phosphate buffer saline pH 7.40 solution before incubating with the Mcs.

IV.3.5.2. Graphene/Au microcannon synthesis

The Mcs were prepared by electrochemical template synthesis of graphene and gold layers,³⁷ described in **IV.2**. The outer layer of electrochemically reduced graphene oxide (erGO) was prepared by the electrochemical reduction of graphene oxide (GO, graphene supermarket, New York, USA) into 5 μm diameter conical pores of a polycarbonate membrane (Catalog No. 7060–2513; Whatman, Maidstone, UK). A thin gold film was first sputtered on the branched side of the membrane to serve as a working electrode. The membrane was assembled in a Teflon plating cell with aluminum foil serving as an electrical contact for the subsequent electrodeposition. Graphene oxide (GO, 0.1 mg mL⁻¹) was first dispersed in a solution containing 0.10 M H₂SO₄ and 0.50 M Na₂SO₄ by ultrasonication for 15 min. The resultant homogeneously dispersed brown GO can be stable for several weeks because of the high presence of oxygen functionalities. The simultaneous electrochemical reduction and deposition of GO was carried out using cyclic voltammetry (CV, over +0.30 to -1.50 V vs. Ag/AgCl/Cl⁻ (3 M), at 50 mV s⁻¹, for five cycles; n = 5), using a Pt wire as counter electrode. Subsequently, a gold layer was plated inside the erGO layer acting as a scaffold or supporting layer for the graphene not to collapse. The gold layer was plated at -0.90 V for 1.5 C from a commercial gold plating solution (Orotemp 24 RTU RACK; Technic Inc.). The sputtered gold layer was gently removed by hand polishing with 3–4 μm alumina slurry.

Gelatin purchased in a local supermarket was prepared at 40 mg mL⁻¹ in water heating at 40–50 °C for having a solution, when it cools down it solidifies. In a total of 200 μL , 100 μL perfluorononane (dilution 1:100 from the synthesized), 50 μL silica particles (1 μm) and 50 μL gelatin were infiltrated in the resulted membrane and let it

cool down and dry until complete dryness and solidification of the gelatin in the pores. The extra-gelatin part was released on top of the membrane by thorough washing with a swab. The membrane was then dissolved in methylene chloride for 5 min to completely release the Mcs. The Mcs were collected by centrifugation at 7000 rpm for 3 min and washed repeatedly with ethanol and three times with ultrapure water (18.2 Ω cm), with a 3 min centrifugation following each wash. All Mcs were used after synthesis at room temperature.

For static Mc experiments, the same Mc synthesis and loading methodology cargo was used, but the polycarbonate template was not dissolved, allowing to end up with an array of statics Mc. Note that for the fluorescence experiments with static Mc, the Mc were loaded with a solution of 50 μ L of Fluorospheres microspheres (f8803 Invitrogen, USA) (0.5 mg/mL) was infiltrated instead of the silica particles. These fluorescence experiments were performed inside a tissue phantom gel made of 0.5% weight of Agarose (Sigma-Aldrich, USA).

IV.3.5.3. Acoustic-graphene-microcannon firing of nanobullets

Mc propulsion was initiated by exposure to a focused ultrasound pulse using a custom designed ultrasound and microscope system.⁴¹ A PCI-5412 arbitrary waveform (National Instruments, Austin, TX) was used to create a single 10 ms long US pulse at 2.25 MHz. A 300 W amplifier (Vox Technologies, Richardson, TX) was used to create a peak negative pressure of 1.9 MPa at the focal zone with a Panametrics V305-SU transducer (Olympus NDT Inc., Waltham, MA). A custom-designed LabVIEW 8.2 program was utilized to initiate the US pulses. The transducer was submerged in a water tank

while a Petri dish containing the sample was positioned at the water surface placing the sample in both the focal zone of the optics and the US transducer as previously described by Ibsen et. al.,⁴¹ and schematically represented in **Figure IV.S5**.

In order to capture the Mc propulsion, videos were acquired at 10,000 or 18,000 frames per second using a FASTCAM 1024 PCI high-speed camera (Photron, San Diego, CA) and a 20X objective. Frame rates of 45,000 and 109,500 frames per second were used for capturing the motion of bubbles resulting from emulsion vaporization. For static Mc experiments, the template membrane with the embedded motors was placed on a Petri dish. Experiments showing the ejection of silica nB from the Mc were performed in water in a Petri dish. The experiments showing the ejection of fluorescent *Fluorospheres* were performed with static Mc anchored in template membrane strips embedded at the bottom of a 0.5 % agarose tissue phantom that was placed inside. After applying the ultrasound pulse, the tissue phantom was sectioned and imaged in cross section using a Nikon Eclipse 80i upright microscope with a fluorescence B2-A FAM filter to determine the distance over which the fluorescent *Fluorosphere* nB had penetrated into the phantom. It should be noted that there is a small agar filled gap between the template membrane and the petri dish, generating a green fluorescent line at the bottom of the membrane after the US pulse (**Figure IV.15 (B)**). The SEM images were taken with a Phillips XL30 ESEM.

IV.3.6. Appendix

Video, figures and tables

Video IV.5. Acoustic droplet vaporization of PFC emulsions in a PFC/silica Nbs-loaded Mc and control experiments in Silica Nbs-Mc without PFC after applying US pulse.

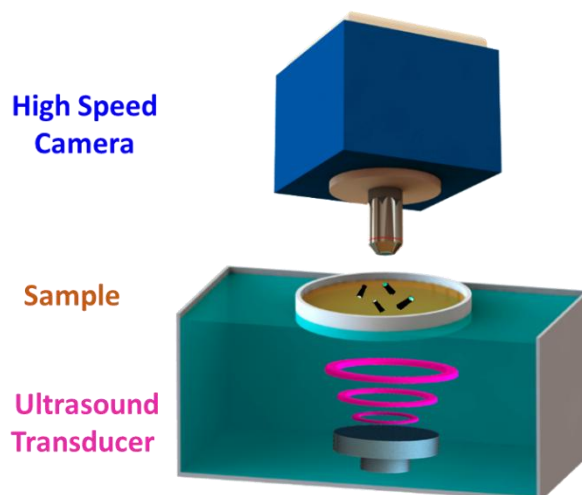


Figure IV.S5. Schematic of the ultrasound set up. The operation consists of a piezoelectric transducer submerged in water, a petri dish which contains the sample, and the firing of the microcannons is recorded by a high-speed camera on top

Table IV.S1. Microcannon and nanobullet features and initial speeds

	MICROCANNON	NANOBULLET
Length (μm) and Radius (μm)	13 and 5	1
Mass (kg)	2.72×10^{-13}	9.24×10^{-15}
k (kg/s)	8.8×10^{-8}	1.89×10^{-8}
V_0 (m/s)	9.0	42.2

Modelized speed of graphene-microcannon and nanobullet

Even though the Mc displacement was captured using high-speed camera with an average speed calculated for Mc to be 29 μm in 3 frames (recording at 109,500 frames per second). By considering the change in position of the microcannon, in the interval of time considered, lead to 1.05 ± 0.26 m/s average speed in for the microcannons. The visualization of nB firing presents a technological challenge to image and measure its average speed, in part due to their small size and high speed. Therefore, a theoretical approach was used to predict how the nB will react upon ultrasound-triggered firing of a Mc free in solution, taking into consideration the forces acting on the Mc, due to both Mc and nB are exposed to the same propulsion thrust of the PFC explosion.

In order to know which forces dominate in this movement, whether viscous or inertial forces, the Reynolds number was calculated as follows:

$$R_e = \frac{\rho v L}{\mu} \quad \text{Equation IV.S1}$$

Re is the Reynolds number that gives information about the type of flow of the object under study. Since the media of study is water and

considering ρ , density of the water, 10^3 kg/m^3 , μ , viscosity of the water, $1.0 \times 10^{-3} \text{ kg m}^{-1} \text{ s}^{-1}$, v the speed of the Mc 1.05 m s^{-1} and L , the length, in average $13 \text{ }\mu\text{m}$, Re was calculated to be 13.7. This low Reynolds number suggests that the Mc moves in a laminar flow where the viscous forces dominate the motion and the inertia of the microscale objects is no longer important. This fact was previously explored for other nano/micromachines ⁴² Thus, the Mc moves due to the vaporization of the perfluorononane and the expansion of the gas on the cavity, being this one the driving force, then, the primary force is the hydrodynamic drag force, the rest of the forces involved will not be considered. Furthermore, the nB is also experience by the same force, drag force. Consequently, the force applied to the Mc, F_{Mc} is the same that the one applied to the nB loaded in the Mc. The force of the nB will be defined as F_{nB} .

$$\vec{F}_{Mc} = \Sigma n_{nB} \cdot \vec{F}_{nB} \quad \text{Equation S2}$$

This force, defined by Stokes' law ⁴⁴ is proportional to the velocity being the constant, k dependent on the shape and size of the object under study, and it is the responsible of the movement of both Mc and nB, then, the speed equation can be obtained from the integration of the force term being m the mass for the object. The *Equation IV.3* expresses the speed of an object (Mc or nB), being the instantaneous and the initial speeds, v and v_0 ; the mass of the object, m ; the drag force constant, k ; and t the interval of time under study.

$$F = -m \frac{dv}{dt} = kv \quad ; \quad \frac{dv}{v} = -\frac{k}{m} dt \quad ; \quad \int_{v_0}^v \frac{dv}{v} = \int_0^t -\frac{k}{m} dt$$

$$\ln \left(\frac{v}{v_0} \right) = -\frac{k}{m} t ; v = v_0 e^{-\frac{kt}{m}}$$

$$v = v_0 e^{-\frac{kt}{m}} \quad \text{Equation IV.3.}$$

This *Equation IV.3* shows that the speed exponentially drops from the initial speed (v_0) achieved from the vaporization of the PFC. Considering that the speed is the rate of change in the position, the initial velocity of the Mc could be further described as follows:

$$v = \frac{dx}{dt} = v_0 e^{-\frac{kt}{m}} ; \int_0^x dx = \int_0^t v_0 e^{-\frac{kt}{m}} dt ; \Delta x = -\frac{1}{k/m} v_0 (e^{-\frac{kt}{m}} - 1)$$

Consequently, *Equation IV.4* defines the initial speed of the Mc considering the hydrodynamic drag force the responsible for the movement. This equation depends on the displacement that the Mc moves in a certain interval of time. Thus, *Equation IV.3* describes the Mc movement.

$$v_0 = \frac{k \Delta x}{m (1 - e^{-\frac{kt}{m}})} \quad \text{Equation IV.4}$$

The speed calculations, herein estimated, must be considered as an approximation because of the important instrumental limitations. Moreover, the measurement of the distance that the Mc moved in a short period of time should also be considered not completely accurate since it only possible to capture the bullet for 5 or 6 frames under 109,500 frames/s videos.

For calculation of the drag factor, the microcannon was modeled with a cylindrical shape, as in previous papers of nano/micromotors fabricated with the same template-based methodology, ⁴³ being the k factor obtained from the *Equation IV.S3*.

$$k_{Mc} = \frac{2\pi\mu L}{\ln\left(\frac{2L}{R}\right)^{-0.72}} \quad \text{Equation IV.S3}$$

Considering the dimension of the Mc, L, length 13 μm , R, radius of 5 μm , k_{Mc} was calculated to be 8.8×10^{-8} kg/s.

On the other hand, the mass of each Mc was calculated considering the mass of the gold deposited, being considered negligible the graphene mass contribution on each microtube. For that, as the charge, Q, deposited was 1 C, and considering 100% efficiency for the electrodeposition, the mass of gold deposited was estimated using the gold molecular mass, M_{mol} , the number of electrons involved in the electrodeposition, n, 3 for gold and the Faraday constant, F, 96485 C mol⁻¹.

$$W_{\text{metal}} = \frac{M_{\text{mol}} Q}{n F} \quad \text{Equation IV.S4}$$

The mass of gold deposited was 68 mg, considering that there are around 2.5×10^6 pores in each membrane template, the mass of each microcannon was estimated to be around 2.72×10^{-13} kg. The bullets are subjected to the same total force than the Mc, however, the sphere shape of the nB (silica particle) make that the drag constant, k_{NB} be calculated as follows,

$$k_{NB} = 6\pi\mu R \quad \text{Equation IV.S5}$$

Considering for a water medium, μ , the water viscosity (10^{-3} kg/m s) and R, the radii of the nB sphere, 1.0 μm , the drag constant, k had a value of $k_{NB} = 1.89 \times 10^{-8}$ kg/s. Knowing that the density of the silica particles is 2.2 g/cm³ and the volume of a sphere, 4.2×10^{-18} m³, thus the mass of a particle is 9.24×10^{-15} kg.

The bullet direction and movement with the camera limitations cannot be determined, but the initial speed of the bullet can be estimated and calculated using *Equation IV.4* and the calculated mass and drag force constant.

Another approximation should be required since the M_c and n_B are propelled by the same force, drag force, which causes the movement of both objects, thus the initial velocity of the bullet was 42.2 m/s around 5 times faster than the M_c . This approximations were carried out considering the force is only applied to a single n_B for simplicity, future studies will focus on developing a more precise theoretical simulation considering the greatest fraction of space occupied by spheres defined by Gauss to be a close-packing of equal spheres with a value of $\frac{\pi}{3\sqrt{2}}$ the maximum number of spheres which could be loaded will be 45 spheres.

IV.3.7. References

1. Sanhai, W. R.; Sakamoto, J. H.; Canady, R.; Ferrari, M. Seven challenges for nanomedicine. *Nature Nanotechnology* **2008**, *3*, 242-244.
2. Wang, J. *Nanomachines: Fundamentals and Applications*; Wiley- VCH: Weinheim, Germany, 2013.
3. Purcell, E. M. Life at low Reynolds number. *Am. J. Phys* **1977**, *45*, 3-11.
4. Feynman, R. P. There's plenty of room at the bottom. *Engineer sci* **1960**, *23*, 22-36.
5. Walker, D.; Kübler, M.; Morozov, K. I.; Fischer, P.; Leshansky, A. M. Optimal length of low Reynolds number nanopropellers. *Nano Lett.* **2015**, *15*, 4412-4416.
6. Nelson, B. J.; Kaliakatsos, I. K.; Abbott, J. J. Microrobots for minimally invasive medicine. *Ann. rev. biomed. eng.* **2010**, *12*, 55-85.
7. Solovev, A. A.; Sanchez, S.; Pumera, M.; Mei, Y. F.; Schmidt, O. G. Magnetic Control of Tubular Catalytic Microbots for the Transport, Assembly, and Delivery of Micro-objects. *Adv. Funct. Mater.* **2010**, *20*, 2430-2435.
8. Wang, W.; Duan, W.; Ahmed, S.; Mallouk, T. E.; Sen, A. Small power: Autonomous nano- and micromotors propelled by self-generated gradients. *Nano Today* **2013**, *8*, 531-554.
9. Wang, H.; Pumera, M. Fabrication of Micro/Nanoscale Motors. *Chem. Rev.* **2015**, *115*, 8704-8735.
10. Chalupniak, A.; Morales-Narváez, E.; Merkoçi, A. Micro and nanomotors in diagnostics. *Adv. Drug Deliv. Rev.* **2015**, *1*, 104-116.
11. Soler, L.; Magdanz, V.; Fomin, V. M.; Sanchez, S.; Schmidt, O. G. Self-Propelled Micromotors for Cleaning Polluted Water. *Acs Nano* **2013**, *7*, 9611-9620.
12. Singh, V. V.; Soto, F.; Kaufmann, K.; Wang, J. Micromotor-Based Energy Generation. *Angew. Chem. Inter. Ed.* **2015**, *54*, 6896-6899.
13. Cheng, R.; Huang, W.; Huang, L.; Yang, B.; Mao, L.; Jin, K.; ZhuGe, Q. ; Zhao, Y. Acceleration of Tissue Plasminogen Activator-Mediated Thrombolysis by Magnetically Powered Nanomotors. *ACS Nano* **2014**, *8*, 7746-7754.
14. Gao, W.; Dong, R.; Thamphiwatana, S.; Li, J.; Gao, W.; Zhang, L.; Wang, J. Artificial Micromotors in the Mouse's Stomach: A Step toward *in Vivo* Use of Synthetic Motors. *ACS Nano* **2015**, *9*, 117-123.

15. Xi, W.; Solovev, A. A.; Ananth, A. N.; Gracias, D. H.; Sanchez, S.; Schmidt, O. G. Rolled-up magnetic microdrillers: towards remotely controlled minimally invasive surgery. *Nanoscale* **2013**, *5*, 1294-1297.
16. Kagan, D.; Benchimol, M. J.; Claussen, J. C.; Chuluun-Erdene, E.; Esener, S.; Wang, J. Acoustic Droplet Vaporization and Propulsion of Perfluorocarbon-Loaded Microbullets for Targeted Tissue Penetration and Deformation. *Angew. Chem. Inter. Ed.* **2012**, *51*, 7519-7522.
17. Wang, W.; Li, S.; Mair, L.; Ahmed, S.; Huang, T. J.; Mallouk, T. E. Acoustic Propulsion of Nanorod Motors Inside Living Cells. *Angew. Chem. Inter. Ed.* **2014**, *53*, 3201-3204.
18. Esteban-Fernandez de Avila, B.; Martin, A.; Soto, F.; Lopez-Ramirez, M. A.; Campuzano, S.; Vasquez-Machado, G. M.; Gao, W.; Zhang, L.; Wang, J. Single Cell Real-Time miRNAs Sensing Based on Nanomotors. *ACS Nano* **2015**, *9*, 6756-6764.
19. Gautam, U. K.; Panchakarla, L. S.; Dierre, B.; Fang, X.; Bando, Y.; Sekiguchi, T.; Govindaraj, A.; Golberg, D.; Rao, C. N. R. Solvothermal Synthesis, Cathodoluminescence, and Field-Emission Properties of Pure and N-Doped ZnO Nanobullets. *Adv. Funct. Mater.* **2009**, *19*, 131-140.
20. Pissuwan, D.; Valenzuela, S. M.; Miller, C. M.; Cortie, M. B. A Golden Bullet? Selective Targeting of *Toxoplasma gondii* Tachyzoites Using Antibody-Functionalized Gold Nanorods. *Nano Lett.* **2007**, *7*, 3808-3812.
21. Elinav, E.; Harnessing, D. P. Nanomedicine for Mucosal Theranostics—A Silver Bullet at Last? *ACS Nano* **2013**, *7*, 2883-2890.
22. Giesecke, T.; Hynynen, K. Ultrasound-mediated cavitation thresholds of liquid perfluorocarbon droplets in vitro. *Ultrasound Med. Biol.* **2003**, *29*, 1359-1365.
23. Reznik, N.; Shpak, O.; Gelderblom, E. C.; Williams, R.; de Jong, N.; Versluis, M.; Burns, P. N. The efficiency and stability of bubble formation by acoustic vaporization of submicron perfluorocarbon droplets. *Ultrasonics* **2013**, *53*, 1368-1376.
24. Litvak, E.; Foster, K. R.; Repacholi, M. H. Health and safety implications of exposure to electromagnetic fields in the frequency range 300 Hz to 10 MHz. *Bioelectromagnetics* **2002**, *23*, 68-82.
25. Zanelli, C. I.; Hennige, C. W.; Kadri, M. M. In *In Beamforming for therapy with high intensity focused ultrasound (HIFU) using quantitative schlieren*; Ultrasonics Symposium, 1993. Proceedings., IEEE 1993; 1993; , pp 1233-1238 vol.2.
26. Ibsen, S.; Benchimol, M.; Simberg, D.; Schutt, C.; Steiner, J.; Esener, S. A novel nested liposome drug delivery vehicle capable of ultrasound triggered release of its payload. *J. Controlled Release* **2011**, *155*, 358-366.

27. Rosenthal, I.; Sostaric, J. Z.; Riesz, P. Sonodynamic therapy—a review of the synergistic effects of drugs and ultrasound. *Ultrason. Sonochem.* **2004**, *11*, 349-363.
28. Tachibana, K.; Feril Jr., L. B.; Ikeda-Dantsuji, Y. Sonodynamic therapy. *Ultrasonics* **2008**, *48*, 253-259.
29. Okada, K.; Kudo, N.; Niwa, K.; Yamamoto, K. A basic study on sonoporation with microbubbles exposed to pulsed ultrasound. *J. Med. Ultrason.* **2005**, *32*, 3-11.
30. Zarnitsyn, V.; Rostad, C. A.; Prausnitz, M. R. Modeling Transmembrane Transport through Cell Membrane Wounds Created by Acoustic Cavitation. *Biophys. J.* **2008**, *95*, 4124-4138.
31. Skyba, D. M.; Price, R. J.; Linka, A. Z.; Skalak, T. C.; Kaul, S. Direct In Vivo Visualization of Intravascular Destruction of Microbubbles by Ultrasound and its Local Effects on Tissue. *Circulation* **1998**, *98*, 290-293.
32. Ibsen, S.; Schutt, C. E.; Esener, S. Microbubble-mediated ultrasound therapy: a review of its potential in cancer treatment. *Drug Des Devel Ther.* **2013**, *7*, 375-388.
33. Duncanson, W. J.; Arriaga, L. R.; Ung, W. L.; Kopechek, J. A.; Porter, T. M.; Weitz, D. A. Microfluidic Fabrication of Perfluorohexane-Shelled Double Emulsions for Controlled Loading and Acoustic-Triggered Release of Hydrophilic Agents. *Langmuir* **2014**, *30*, 13765-13770.
34. Lentacker, I.; De Smedt, S. C.; Sanders, N. N. Drug loaded microbubble design for ultrasound triggered delivery. *Soft Matter* **2009**, *5*, 2161-2170.
35. Wang, C.; Kang, S.; Lee, Y.; Luo, Y.; Huang, Y.; Yeh, C. Aptamer-conjugated and drug-loaded acoustic droplets for ultrasound theranosis. *Biomaterials* **2012**, *33*, 1939-1947.
36. Huang, H.; Liu, H.; Hsu, P.; Chiang, C.; Tsai, C.; Chi, H.; Chen, S.; Chen, Y. A Multitheragnostic Nanobubble System to Induce Blood-Brain Barrier Disruption with Magnetically Guided Focused Ultrasound. *Adv. Mater.* **2015**, *27*, 655-661.
37. Martín, A.; Jurado-Sánchez, B.; Escarpa, A.; Wang, J. Template Electrosynthesis of High-Performance Graphene Microengines. *Small* **2015**, *11*, 3568-3574.
38. Wu, Z.; Lin, X.; Zou, X.; Sun, J.; He, Q. Biodegradable Protein-Based Rockets for Drug Transportation and Light-Triggered Release. *ACS Appl. Mater. Interfaces* **2015**, *7*, 250-255.
39. Daglar, B.; Demirel, G. B.; Khudiyev, T.; Dogan, T.; Tobail, O.; Altuntas, S.; Buyukserin, F.; Bayindir, M. Anemone-like nanostructures for non-lithographic, reproducible, large-area, and ultra-sensitive SERS substrates. *Nanoscale* **2014**, *6*, 12710-12717.

40. Lugert, E. C.; Lodge, T. P.; Bühlmann, P. Plasticization of amorphous perfluoropolymers. *J. Polym. Sci Part B* **2008**, *46*, 516-525.
41. Ibsen, S.; Benchimol, M.; Esener, S. Fluorescent microscope system to monitor real-time interactions between focused ultrasound, echogenic drug delivery vehicles, and live cell membranes. *Ultrasonics* **2013**, *53*, 178-184.
42. Gibbs, J. G.; Zhao, Y. -. Design and Characterization of Rotational Multicomponent Catalytic Nanomotors. *Small* **2009**, *5*, 2304-2308.
43. Li, L.; Wang, J.; Li, T.; Songa, W.; Zhanga, G. Hydrodynamics and propulsion mechanism of self-propelled catalytic micromotors: model and experiment. *Soft Matter* **2014**, *10*, 7511-7518.
44. Howard, J.; Howard, B. Reynolds Number hydrodynamics with special applications to particulate media. Englewood Cliffs, NJ: Prentice Hall, **1965**

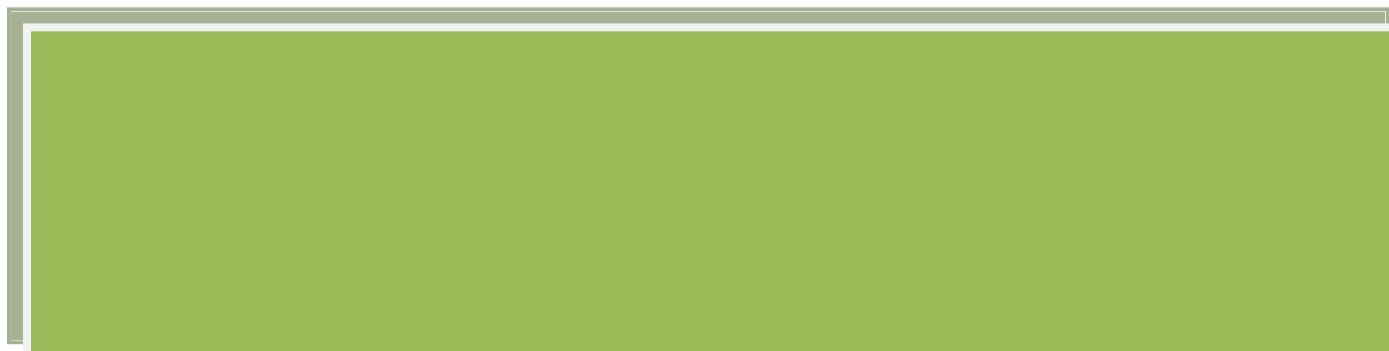
Chapter V

Conclusions

Un científico debe tomarse la libertad de plantear cualquier cuestión, de dudar de cualquier afirmación, de corregir errores. (Robert Oppenheimer)



V. General conclusions



At the light of the unifying thread of this Doctoral Thesis relying on the exploration of the graphene properties as a new tool in the electrochemical (bio-)-sensing using screen-printed technology and microfluidics as well as in the design and development of cutting-edge micromotors as new autopropelled analytical tools, in the framework of the present analytical nanoscience and nanotechnology. The general conclusions of this Thesis have been divided into three bullet points considering the main three chapters.

1. Graphene nanoribbons (graphene oxide and chemically reduced one), obtained after opening carbon nanotubes by chemical oxidation have demonstrated that (i) they are suitable nanomaterials because of the rich edge chemistry compared to pristine graphene (ideal graphene) and (ii) there are nanoribbons with a more suitable functionalization than others for electrochemical detection, depending on the chemical structure of the target molecule. This later fact paves the way to the tailored-designed graphenes for improving the analytical detection according to the chemical structure of the target molecule.

Indeed, the reactivity (abundance in defects and Csp^2/Csp^3 ratio) and the inherent properties of graphene nanoribbons (high surface area and excellent electrical conductivity), have demonstrated to play an important role in the design and development of electrochemical (bio-)-sensing strategies with enhanced analytical features in terms of selectivity, sensibility and reproducibility.

All in sum, the research and examination of the synergies between the analytical performance found for the graphene nanoribbons and those inherent to the screen-printed technologies have permitted to develop fast response, disposable and portable analytical innovative tools, which require

low sample volumes and reagent consumption. Indeed, these graphene nanoribbons have been successfully employed in the development of electrochemical sensors (reduced graphene nanoribbons) and in the development of biosensing strategies (graphene oxide nanoribbons) for the detection of clinical and relevant markers in illnesses such as uric acid and D-amino acids, respectively.

2. The features derived from graphene have been creatively explored with the inherent advantages of microfluidic systems (fast analysis with low sample and reagent consumption, portability and flow control in the microscale), because of their compatibility between the micro and nano scales as well as in between the micro and nanotechnologies.

Certainly, graphene (chemically reduced graphene) has demonstrated to be an excellent nanomaterial for the development of electrochemical transducers coupled to microfluidic systems. In the framework of the electrochemical detection coupled to microfluidic systems, it has exhibited remarkable electrocatalysis, enhanced sensitivity and high reproducibility due to its also high surface area and conductivity. So, these evidences confer to graphene an extra value in electrochemical microfluidics because of the low sensitivities usually presented by these platforms.

All these reasons have permitted, on the one hand, the development of innovative biosensing applications, using thin film approaches on conductive surfaces in the fabrication of electrochemical detectors, for the enantiomeric resolution and selective detection of D-amino acids with clinical relevancy in important illnesses such as *Vibrio Cholerae*.

On the other hand, in order to explore the mentioned electrocatalytic properties of graphene, new electrochemical detectors based on exclusive nanomaterials such as graphene and also extended to carbon nanotubes,

have been designed, characterized and developed. The simple filtration of the nanomaterial and its disposition on flexible and non-conductive wafers has permitted the development of new nanomaterial-exclusive transducers for electrochemical microfluidics, which has been the starting point in the development of important applications in the agro-food sector such as the fast and reliable detection of phenolic markers in olive oil.

3. The exceptional contribution of graphene (graphene oxide and electrochemically reduced graphene oxide) in the design and development of catalytic micromotors, which have been electrosynthesized on the pores of a polycarbonate membrane, has been demonstrated. Clearly, the high surface area of graphene, suitably functionalized, could improve from the chemical reaction responsible for the propulsion of the micromotor to the interaction with target molecules with analytical (bio-)-sensing purposes.

The found results have underlined graphene to be the responsible for the improved propulsion in micromotors yielding fast and efficient micromotors with propulsion mechanisms relying on the generation of bubbles from a chemical reaction and assisted by acoustic energies. These finds foresees a promising future in the development of movable sensors capable of *in situ* perform analytical tasks, swimming in small sample volumes without the use of external fluid forces.

In sum, the general conclusion of this Doctoral Thesis is that graphene –in all its different chemical forms and variants- has demonstrated to be an extraordinary material in the design and development of analytical vanguard tools such as (bio-)-sensors and microfluidic electrochemical systems and in other new generation of cutting-edge tools such as micromotors in the present framework of analytical nanoscience and nanotechnology.

V. Conclusiones generales



A la luz del hilo conductor de esta Tesis Doctoral –exploración de las propiedades del grafeno como nueva herramienta en el (bio)-sensado (microfluídico) electroquímico y en el diseño y desarrollo de micromotores– y todo ello dentro del marco más actual de la nanociencia y nanotecnología analíticas, se describen con arreglo a los tres capítulos donde se han agrupado y discutido los resultados, las conclusiones generales de esta Tesis Doctoral.

1. Las nanocintas de grafeno (oxidadas y reducidas químicamente), obtenidas tras apertura por oxidación química de los nanotubos de carbono, han demostrado ser unos nanomateriales muy adecuados debido a su química rica en defectos en comparación con el grafeno ideal (conceptualmente constituido por una lámina carbonácea perfecta). Asimismo, se han encontrado evidencias de la influencia que ejerce la química de funcionalización en la detección electroquímica de las moléculas diana con arreglo a su estructura química. Este hecho conduce al diseño de nanocintas de grafeno con química de funcionalización dirigida a una detección electroquímica mejorada dependiendo de la estructura química del analito.

En efecto, la reactividad (abundancia de defectos y la relación C_{sp^2}/C_{sp^3}) y las propiedades inherentes de las nanocintas de grafeno (elevada superficie específica y excelente conductividad eléctrica), han demostrado ejercer un papel predominante en el diseño y en el desarrollo de estrategias de (bio)-sensado electroquímicas con propiedades analíticas muy mejoradas en términos de selectividad, sensibilidad y reproducibilidad de los análisis.

Por todo ello, la búsqueda y exploración de sinergias entre las prestaciones analíticas encontradas para las nanocintas de grafeno y aquellas inherentes a la tecnología serigrafiada han permitido desarrollar y proponer herramientas

analíticas innovadoras de respuesta rápida, desechables y portables que exigen bajos volúmenes de muestra y bajo consumo de reactivos. En efecto, estas nanocintas de grafeno se han empleado con éxito en la construcción de sensores electroquímicos (nanocintas de grafeno ricas en Csp^2) y en el desarrollo de estrategias biosensoras (nanocintas de grafeno ricas en Csp^3) para la detección de marcadores de enfermedades de elevada importancia clínica como son el ácido úrico y los D-amino ácidos, respectivamente.

2. Las propiedades del grafeno han sido creativamente exploradas junto con las inherentes ventajas de los sistemas microfluídicos (análisis rápidos, bajo consumo de muestra y reactivos, portabilidad y control de fluidos en la microescala) debido a la compatibilidad entre la micro y la nano escala, así como entre las micro y las nanotecnologías.

En efecto, se ha demostrado que el grafeno (grafeno reducido químicamente) es un nanomaterial excelente para la construcción de transductores electroquímicos acoplados a sistemas microfluídicos debido a que ha exhibido –en el marco de la detección electroquímica acoplada a estos sistemas microfluídicos– una marcada electrocatálisis, un aumento de sensibilidad y una elevada reproducibilidad debido también a su elevada superficie específica y conductividad. Estos hallazgos confieren al grafeno un valor añadido dentro de la microfluídica electroquímica dado que ésta presenta muy frecuentemente bajas sensibilidades.

Todo ello ha permitido, por una parte, el desarrollo de aplicaciones innovadoras de biosensado –empleando métodos de formación de película delgada sobre superficies conductoras para la construcción de los detectores electroquímicos– basadas en la resolución enantiomérica y detección selectiva de los D-amino ácidos con relevancia clínica en enfermedades importantes como el *Vibrio cholerae*.

Por otra parte, y en aras de explotar esas propiedades electrocatalíticas del grafeno, se han diseñado, caracterizado y desarrollado nuevos detectores electroquímicos constituidos exclusivamente por grafeno, que se han extendido de forma natural a otros nanomateriales de carbono como son los nanotubos. La simple filtración del nanomaterial y su adecuada disposición sobre soportes flexibles no conductores, ha permitido desarrollar nuevos transductores para microfluídica electroquímica constituidos exclusivamente por el nanomaterial y ha supuesto ser el punto inicial para el desarrollo de aplicaciones tal y como es la detección rápida y fiable de marcadores fenólicos en aceite de oliva.

3. Se ha demostrado la excepcional contribución del grafeno (grafeno oxidado y electroquímicamente reducido) dentro del ámbito del diseño y construcción de micromotores catalíticos electrosintetizados sobre poros de membranas de policarbonato. La elevada superficie del grafeno, adecuadamente funcionalizada, puede mejorar tanto las reacciones químicas en las cuales se basa la propulsión de estos micromotores como las interacciones con otras moléculas con fines analíticos de (bio-)-sensado.

En efecto, se han encontrado resultados conducentes a que el grafeno ha dotado a los micromotores de propiedades propulsoras mejoradas que han permitido la obtención de micromotores mucho más rápidos y eficaces, tanto en aquellos cuyo mecanismo de propulsión es la generación de burbujas a través de reacciones químicas como en aquellos asistidos por aplicación de pulsos de ultrasonidos. Estos hallazgos hacen prever un futuro muy prometedor para el desarrollo de nuevos sensores móviles capaces de realizar operaciones analíticas *in situ*, navegando en pequeñas cantidades de muestra y sin necesidad del empleo de fuerzas impulsoras de fluidos.

Por todo ello, finalmente se podría establecer como conclusión general de esta Tesis Doctoral que el grafeno –en sus distintas variantes y formas químicas– ha demostrado ser un material extraordinario en el diseño y desarrollo de herramientas analíticas de vanguardia tales como los (bio)-sensores y sistemas microfluídicos electroquímicos así como en otras que podrían decirse de nueva generación como son los micromotores, todo ello dentro del marco más actual de la nanociencia y nanotecnología analíticas.

Chapter VI

General Appendix

Todo cuanto hacemos debe tender al progreso y al perfeccionamiento.

(Baruch Spinoza)



List of Figures and Tables



List of Figures

Chapter II

Fig. II.1 Multidimensional carbon allotrope family	14
Fig. II.2. Representation of single, few and multi-layer graphenes	15
Fig. II.3. Schematic model of graphene oxide	25
Fig. II.4. Schematic model of reduced graphene oxide	30
Fig. II.5. Synthetic routes of GNRs from unzipping of nanotubes	38
Fig. II.6. AFM images and height profiles of GNRox and GNRred	71
Fig. II.7. TEM images of MWCNTs, GNRox, and GNRred	72
Fig. II.8. X-Ray diffractograms of MWCNTs, GNRox and GNRred	73
Fig. II.9. Raman spectra of the MWCNTs GNRox and GNRred	74
Fig. II.10. C1s XPS spectra and binding energies of GNRox and GNRred	75
Fig. II.11. IR spectra of the MWCNTs, GNRox and GNRred	76
Fig. II.12. CV of $K_3Fe(CN)_6$ on GNRred with and without tip sonication	78
Fig. II.13. Chronocoulometric charge-time and charge- time square root plots	79
Fig. II.14. FE-SEM images of non-modified and GNR modified CSPeS	80
Fig. II.15 DPVs of HQ, CT, and RS in non-modified, MWCNT and GNRs modified GCE. Scheme of the interactions between molecules and GNRs	82

Fig. II.16 DPVs of AA, LD, UA, L-Tyr in non-modified, MWCNT and GNRs modified GCE. Scheme of the interactions between molecules and GNRs	83
Fig. II.17 DPVs of (a) HQ-CT-RS. (b) AA-LD-UA. (c) UA-Tyr with GNRs	85
Fig. II.18 DPVs for HQ in a cosmetic sample and UA in a urine sample	87
Fig. II.19 DPVs of AA-LD-UA in bare, MWCNTs and GNRs modified CSPE	89
Fig. II.20 Simultaneous calibration of AA, LD and UA	91
Fig. II.21 DPV of diluted urine samples and spiked with AA-UA-LD	92
Fig. II.22 DPVs for enantiomeric analysis of L,D AAs: Tyr and Met	112
Fig. II.23 DPV for L-Tyr and D-Tyr using GNRs and non-modified CSPE	113
Fig. II.24 FE-SEM micrograph for modified GNRox and bare CSPE	114
Fig. II.25. Plot for extinction of D-Tyr and apparition of enzymatic product, (A) H ₂ O ₂ intensity current vs. enzyme and (B) vs. D-Tyr concentrations	116
Fig. II.26. Simultaneous calibration of D and L-Tyr and urine analysis	118

Chapter III

Fig. III.1 Microfluidic chip schematic layouts: single and double-T models	132
Fig. III.2 Non-pinched electrokinetic protocol for injection and separation of the analytes	135
Fig. III.3 Design configuration of MCs and electrochemical detection coupling	136

Fig. III.4 MC strategy: enzyme and D-AAs electrokinetic injection, electrofocusing, D-AAs separation, in-channel enzymatic reaction and H ₂ O ₂ detection	166
Fig. III.5 Effect of DAAO concentration on D-Met amperometric signal	168
Fig. III.6 Estimation of electrochemical surface area of the different electrodes	169
Fig. III.7 HDVs for H ₂ O ₂ on GNRred/PEI and CSPE	170
Fig. III.8 MC electropherograms for D-Leu and D-Met separation using DAAO	171
Fig. III.9 Design of the carbon nanomaterial-based TFEs: three and line-electrode configuration for off and on-chip measurements, respectively	184
Fig. III.10 CV and DPVs of DA and CT using SW, MW and GP-TFEs	184
Fig. III.11 Hydrodynamic voltammograms for DA and CT using TFEs	187
Fig. III.12 DA and CT sensing using MC coupled to SW, MW and GP-TFEs	188
Fig. III.13 Morphological characterization. FE-SEM micrographs for TFEs	191
Fig. III.14 Current sensing AFM: topographical and resistance data	193
Fig. III.15 Electrochemical characterization of TFEs by impedance	194
Fig. III.16 Interpretation of the disposition of the nanomaterials in the TFE	194
Fig. III.17 Chemical structures and HDVs of TY, OL and HTY in MW-TFE, and MW-CSPE and bare CSPE	197
Fig. III.18 TFE coupling with MC in real samples. Electropherograms for the separation of TY, OL and HTY in MW-TFE and in olive oil	199

Chapter IV

Fig. IV.1 Micromotors classification attending to the propulsion method	219
Fig. IV.2 Self-electrophoresis propulsion of bimetallic structures	220
Fig. IV.3 Electrosynthesis of nanowire motors on alumina membrane template	223
Fig. IV.4. Electrosynthesis of tubular motors on PC membrane template	225
Fig. IV. 5 Schematic of bubbling principle. Growth, migration and recoiling.	227
Fig. IV.6 US propelled micromotors. Principle of acoustophoresis mechanism	230
Fig. IV.7 Template electrodeposition of erGO/Pt or Au tubular micromotors. CV of erGO and SEM of erGO–Pt and erGO–Au micromotors	249
Fig. IV.8 SEM and EDX images of erGO–Pt/Au and PANI-Pt/Au. TEM of Pt.	252
Fig. IV.9 Propulsion of erGO–Pt and Au/catalase micromotors vs. PANI-Pt	255
Fig. IV.10 Dependence of the micromotor speed upon the H ₂ O ₂ concentration	258
Fig. IV.11 Propulsion images showing trajectories and tracking lines of erGO–Pt micromotors	260
Fig. IV.12 Microcannon fabrication, composition and SEM after US-pulse	275
Fig. IV.13 Scheme and time-lapse images of the Mc with(out) PFC before/after US-pulse	278
Fig. IV.14 SEM images with different nB loading before/after US pulse	279
Fig. IV.15 Fluorescence images of fluorosphere-loaded static Mcs after firing	281
Fig IV.16 Experimental and theoretical behavior of microcannon and nanobullet	283

List of Tables

Chapter II

Table II.1. Terminology and synthesis of graphene in electroanalysis	45
Table II.2. Analytical techniques for characterization of graphene	17
Table II.3. HET rate for carbon material-based electrodes	22
Table II.4. Graphene oxide applications in electrochemistry	47
Table II.5. Reduced graphene oxide applications in electrochemistry	48
Table II.6. Graphene nanoribbons applications in electrochemistry	52
Table II.7. Electrochemical detection with graphenes	44
Table II.8. Volume optimization. Current intensities for GNRox/GCE.	92
Table II.9. Determination of AA, LD and UA in urine samples	115
Table II.10. Optimization of the enzymatic reaction time	12

Chapter III

Table III.1. Analytical remarks of the coupling MC-CNTs	153
Table III.2. Analytical remarks of the coupling MC-graphene	154
Table III.3. Electrochemical sensing of DA and CT using three-electrode TFEs	185
Table III.4. Analytical evaluation of the TFEs	186
Table III.5. Calibration analytical features MC-TFEs detection	189
Table III.6. Analytical evaluation of the MW-TFE	198
Table III.7. Calibration analytical features of TY, OL and HTY	200

Acronyms



Acronyms

AA	ascorbic acid	GCE	glassy carbon electrode
AE	auxiliary electrode	GNRs	graphene nanoribbons
L/D-AAAs	(L-D)-amino acids	GNRox	oxide graphene nanoribbons
AFM	atomic force microscopy	GNRred	reduced graphene nanoribbons
CE	capillary electrophoresis	GO	graphene oxide
CNT	carbon nanotubes	GP	graphene
CSPE	carbon screen-printed electrode	LD	levodopa
CT	catechol	LOD	limit of detection
CTAB	cetyltrimethyl ammonium bromide	L-Tyr	L-tyrosine
CV	cyclic voltammetry	MC	microfluidic chips
CVD	chemical vapor deposition	Mcs	microcannons
DA	dopamine	MES	2-(N-morpholino) ethanesulfonic acid
DAAO	D-amino acid oxidase	MWCNTs	multi-walled carbon nanotubes
D-Leu	D-Leucine	Nb	nanobullet
D-Met	D-Methionine	NMR	nuclear magnetic resonance
D-Tyr	D-Tyrosine	OL	oleuropeine
DMF	dimethylformamide	PAA	polyallylamine
DPV	differential pulse voltammetry	PANI	polyaniline
DR	detection reservoir	PC	polycarbonate
EDX	energy dispersive X-ray spectroscopy	PDMS	polydimethylsiloxane
ER	enzymatic reservoir	PEDOT	poly(3,4-ethylenedioxy thiophene)
erGO	electrochemically reduced graphene oxide	PEI	polyethyleneimine
HDVs	hydrodynamic voltammograms	PET	polyethylene terephthalate
HET	heterogeneous electron transfer	PFC	perfluorocarbon
HQ	hydroquinone	PMMA	polymethyl methacrylate
HPLC	high-performance liquid chromatography	PPy	polypyrrol
HTY	hydroxytyrosol	rGO	reduced graphene oxide
IR	infrared	RB	running buffer reservoir
ITO	indium tin oxide	RE	reference electrode
FE-SEM	field emission scanning electron microscopy	RS	resorcionol
		RSD	relative standard deviation

SDBS	sodium dodecylbenzene sulfonate
SDS	sodium dodecyl sulfate
SEM	scanning electron microscopy
SR	sample reservoir
SWCNTs	single walled carbon nanotubes
TEM	transmission electron microscopy
TFE	teflon filter electrode
TGA	thermal gravimetric analysis
TY	tyrosol
UA	uric acid
US	ultrasound
WE	working electrode
WR	waste reservoir
XPS	X-ray photoelectron spectroscopy
XRD	X-ray diffraction

VII. Publications and conferences



International publications

- **A. Martín**, A. Escarpa. Graphene: the cutting-edge interaction between chemistry and electrochemistry. *Trends in Analytical Chemistry*, **2014**, 56, 13-26. (In section **II.1**)
- **A. Martín**, J. Hernández-Ferrer, L. Vázquez, M.T. Martínez, A. Escarpa. Controlled chemistry of tailored graphene nanoribbons for electrochemistry: a rational approach to optimizing molecule detection. *RSC Advances*, **2014**, 4, 132-139. (In section **II.2**)
- **A. Martín**, P. Batalla, J. Hernández-Ferrer, M.T. Martínez, A. Escarpa. Graphene oxide nanoribbons-based sensors for the simultaneous bio-electrochemical enantiomeric resolution and analysis of amino acid biomarkers. *Biosensors and Bioelectronics*, **2015**, 68, 163-167. (In section **II.3**)
- **A. Martín**, J. Hernández-Ferrer, M.T. Martínez, A. Escarpa. Graphene nanoribbons-based electrochemical sensors on screen-printed platforms. *Electrochimica Acta*. **2015**, 172, 2-6. (In section **II.2**)
- **A. Martín**, M.A. López, M.C. González, A. Escarpa. Multidimensional carbon allotropes as electrochemical detectors in capillary and microchip electrophoresis. *Electrophoresis*, **2015**, 36, 179-194. (In section **III.1**)
- P. Batalla‡, **A. Martín**‡, M.A. Lopez, M.C. Gonzalez, A. Escarpa. Enzyme-based microfluidic chip coupled to graphene electrodes for the detection of D-amino acid enantiomer-biomarkers. *Analytical Chemistry*, **2015**, 87, 5074-5078. (ACS Editors' Choice). (In section **III.2**)
- **A. Martín**, A. Escarpa, Graphene and carbon nanotubes teflon-filtered electrodes tailor-designed on adaptable non-conductive substrates for electrochemical (microfluidic) sensing. **2015**. (Submitted). (In section **III.3**)
- **A. Martín**, L. Vázquez, A. Escarpa. Porous electrodes based on exclusive multi-walled carbon nanotubes in Food Microfluidics. **2015**. (Under revision in *Analytical Chemistry*). (In section **III.3**)
- **A. Martín**‡, B. Jurado-Sánchez‡, A. Escarpa, J. Wang. Template electrosynthesis of high performance graphene microengines. *Small*, **2015**, 11, 3568-3574. (In section **IV.2**)
- F. Soto‡, **A. Martín**‡, S. Ibsen, M. Vaidyanathan, V. García-Gradilla, Y. Levin, A. Escarpa, S.C. Esener, J. Wang. Acoustic microcannons: towards advanced microballistics. **2015**. (Accepted with minor revision in *ACS Nano*). (In section **IV.3**)

‡ Equal contribution of authors

Patents (pending)

- **A. Martín**, A. Escarpa. Disposable electrodes based on filtered nanomaterials. (Spanish Patent+ International PTC extension). Reference: PTC/ES2014/070946. (University of Alcalá). June 2014.

Conferences and poster presentations

Invited oral presentation

- **A. Martín**, A. Escarpa. Graphene and carbon nanotubes in electrochemical sensing on microfluidic chips. International Workshop on Graphene Nanobiosensors. June 2015. Barcelona. Spain.
- **A. Martín**, M.A. López, M.C. González, A. Escarpa. Graphene nanoribbons: novel materials for electrochemical sensing on microfluidic chips. International IV Workshop on Analytical Miniaturization and Nanotechnologies. Copenhagen. June 2014. Denmark.
- **A. Martín**, J. Hernández, L. Vázquez, M.A. López, M. C. González, M.T. Martínez, A. Escarpa. Graphene nanoribbons in sensing and biosensing: synthesis, characterization and applications. International VI Workshop: Nanoscience and Analytical Nanotechnologies. June 2013. Madrid. Spain.

Poster presentation

- **A. Martín**, B. Jurado-Sanchez, A. Escarpa, J. Wang. Template electrosynthesis of high performance graphene microengines. International VII Workshop: Nanoscience and Analytical Nanotechnologies. June 2015. Salamanca. Spain. (Poster Award)
- **A. Martín**, B. Jurado-Sanchez, J. Wang. Bubble-propelled micromotors powered with ultralow catalyst loading. MRS Congress. March 2015. San Francisco. USA.
- P. Batalla, **A. Martín**, M.A. López, M.C. González, A. Escarpa. D-amino acid detection using a microfluidic enzymatic strategy with graphene-based electrodes. Lab-on-a-chip European Congress. March 2014. Berlin Germany.
- **A. Martín**, A. Escarpa. Disposable graphene nanoribbons electrodes for simultaneous determination of ascorbic acid, L-dopa and uric acid in urine samples. International VI Workshop: Nanoscience and Analytical Nanotechnologies. June 2013. Madrid. Spain.
- P. Batalla, **A. Martín**, M.A. López, M.C. González, A. Escarpa. Detection of D-amino acids of clinical relevance using a microfluidic enzymatic strategy with graphene-based electrodes. International VI Workshop: Nanoscience and Analytical Nanotechnologies. June 2013. Madrid. Spain.
- **A. Martín**, J. Hernández, M. C. González, M.T. Martínez, A. Escarpa. Grafeno como transductor electroquímico: estudios voltamétricos. XXXIII Reunión del Grupo de Electroquímica de la RSEQ. July 2012. Madrid. Spain.

